INTRACEREBRAL IMPLANTATION OF ECM HYDROGEL FOR THE TREATMENT OF STROKE

by

Harmanvir Ghuman

Bachelor of Science in Biomedical Engineering, University of Arizona, 2013

Submitted to the Graduate Faculty of

Swanson School of Engineering in partial fulfillment

of the requirements for the degree of

Doctor of Philosophy

University of Pittsburgh

2018

UNIVERSITY OF PITTSBURGH

SWANSON SCHOOL OF ENGINEERING

This dissertation was presented

by

Harmanvir Ghuman

It was defended on

September 10, 2018

And approved by

Bryan Brown, PhD, Assistant Professor, Department of Bioengineering

Mark Richardson, MD, PhD, Associate Professor, Department of Neurological Surgery

Tracy Cui, PhD, William Kepler Whiteford Professor, Department of Bioengineering

Yadong Wang, PhD, William Kepler Whiteford Professor, Department of Bioengineering

Dissertation Director: Michel Modo, PhD, Professor, Department of Radiology

INTRACEREBRAL IMPLANTATION OF ECM HYDROGEL FOR THE TREATMENT OF STROKE

Harmanvir Ghuman, Ph.D.

University of Pittsburgh, 2018

Stroke is the leading cause of serious, long-term disability affecting nearly 15 million people worldwide each year. One of the key challenges in treating chronic stroke is the dramatic loss of brain tissue, and the formation of a cavity filled with extracellular fluid (ECF). Physical therapy and intracerebral implantation of cells has shown limited success in improving motor dysfunction, however there is no replacement of the lost tissue and hence a large tissue cavity remains in the brains of stroke survivors. Extracellular matrix (ECM), which fills the space between the cells, makes up 20% of the whole brain tissue volume and contains proteins such as laminin, fibronectin, myelin and growth factors. The objectives of this work were to determine if hydrogels composed of decellularized mammalian ECM implanted in a stroke cavity promotes cellular infiltration and constructive tissue remodeling, as well as optimization of 19F MR imaging to visualize the peripheral macrophages invading the lesion cavity.

At ECM concentrations that have similar rheological properties as brain tissue, the ECM exists in fluid phase at room temperature, while forming hydrogels at body temperature. However, large volumes of hydrogel injection into the lesion cavity will increase the intracerebral pressure and further damage brain tissue. Using non-invasive magnetic resonance imaging (MRI)-guidance, the hydrogel can be reliably delivered to

the lesion cavity, while draining the ECF through another cannula. We evaluated histologically 0, 3, 4 and 8 mg/mL of porcine-derived urinary bladder matrix (UBM)-ECM hydrogel concentrations implanted in a 14-day old stroke cavity. Less concentrated hydrogels (3 and 4 mg/mL) were efficiently degraded with a 95% decrease in volume by 90 days, whereas only 32% of the more concentrated and stiffer hydrogel (8 mg/mL) was resorbed. The less concentrated hydrogels showed a robust invasion of endothelial cells that supported neovascularization. No neovascularization occurred with the stiffer hydrogel. Invasion of neural cells increased with time in all hydrogel concentrations. Differentiation of neural progenitors into mature neurons with axonal projections was evident, as well as a robust invasion of oligodendrocytes. Macrophage infiltration and density within the bioscaffold affected the hydrogel biodegradation and progressively increased in the less concentrated hydrogels and decreased in the 8 mg/mL hydrogels.

Optimization of 19F imaging parameters revealed fast imaging with steady state precession (FISP) sequence being the most efficient for the detection of perfluorocarbons (PFCs). In vivo 19F MRI shows robust visualization of peripheral macrophages invading the lesion cavity implanted with 4 mg/mL ECM hydrogel. Intravenous administration of PFCs results in accumulation of 19F labeled cells within the ECM hydrogel and in the peri-infarct tissue. Histological analysis at 1 day post-injection revealed all infiltrating Iba1+ cells to also be 19F labeled, indicating that these are peripheral macrophages rather than brain derived microglia. This body of work demonstrates that implantation of an ECM hydrogel induced neural tissue regeneration, but a more complete understanding is required to evaluate its potential therapeutic application.

TABLE OF CONTENTS

LIST OF TABLES

LIST OF FIGURES

PREFACE

My time here at Dr. Michel Modo's laboratory has been one of growth and development that provided me with experiences and training that are invaluable for my development as a scientist. Dr. Modo, is an exceptional mentor who taught me more than I could have imagined when I started my doctoral studies at the University of Pittsburgh, and I owe Dr. Modo my sincerest gratitude for taking me into his laboratory and providing me with his valuable time and mentorship. I am grateful to be given the opportunity to work in his laboratory and fostering a sense of collaboration, strong work ethic, commitment, and hard work that drives me to emulate this in my future career.

I would also like to thank my committee members: Dr. Bryan Brown, Dr. Mark Richardson, Dr. Tracy Cui, and Dr. Yadong Wang who have been exceptional mentors providing me with guidance and support throughout my doctoral studies. I am grateful for their invaluable help and insights which developed my capabilities as a researcher.

I would also like to thank everyone in Dr. Modo's laboratory who has been there for guidance, experimental support, and anything else I needed. Dr. Francesca Nicholls and Dr. Tony Chou were always supportive doctoral students who gave me training and direction during my early years in lab. I am truly grateful for providing me with much of the technical knowledge of surgeries and MRI imaging. My accomplishments in the Modo lab to a great extent were facilitated by undergraduate students and postdocs. I have had the

opportunity to mentor several students who ultimately made invaluable contributions to my work. Dr. Ximena Castillo, Dr. Franziska Nitzsche, Jessie Liu, Madeline Gerwig, Reem Azar, Carrinton Mauney, Alexandra Tompkins, Nikhita Perry, and Lauren Grice are all exceptional and enthusiastic young scientists who are going to have stellar careers of their own.

This dissertation is dedicated to my late parents Mahesh and Surinder Ghuman, my brother Karan Ghuman, my uncle Harinder and late aunt Jaswinder Ghuman. I owe all my opportunities and accomplishments to them and I am forever grateful for their love, encouragement and the values they have instilled in me.

1.0 INTRODUCTION

Work in this chapter has been adapted from the following manuscript:

***Ghuman H**, Modo M. Biomaterial applications in neural therapy and repair. Chinese Neurosurgical Journal. 2016; 2:34.*

1.1 CLINICAL MANIFESTATION OF STROKE

Stroke or a cerebrovascular accident (CVA) is the leading cause of adult disability affecting nearly 800,000 Americans (15 million worldwide) each year, with ischemic stroke accounting for 80% of all cases [1]. This injury is characterized by occlusion of blood flow to brain tissue, cell death, and blood-brain barrier disruption, resulting in transmigration of leukocytes into the surrounding brain tissues [2]. Disruption of the blood-brain barrier and release of various proteases and reactive oxygen species (ROS) by leukocytes into the brain tissue results in cerebral edema and irreversible damage to the viable cells in the ischemic core. These mechanisms may clinically manifest as significantly worsened sensory, motor, or cognitive functions, or even death. The only approved treatment for acute ischemic stroke is the intravenous administration of recombinant tissue plasminogen activator (rtPA) to dissolve the clot [3], with the therapeutic windown open for up to 4.5 hours after stroke, and thus applicable to a very small proportion of all stroke patients (up to 5%) [4].

With the increasing incidences of stroke, and declining mortality, the number of disabled stroke survivors is expected to increase [5]. While patients currently rely on physical therapy to restore motor function after stroke, these improvements are modulated through existing brain circuitry [6], and not through replacing lost cells and tissue, with one-third of all stroke patients remaining permanently disabled even with intensive task specific training [7, 8]. In other words, there is a loss of functional tissue after stroke, and thus the physical therapy and rehabilitation is limited in restoring the lost cognitive and physiological functions. The lack of effective treatments for stroke and other neurological diseases can also be explained by the limited regenerative potential of the central nervous system [9].

1.2 ANIMAL MODELS OF STROKE

Over the past four decades, a variety of animal models of stroke have been developed to identify mechanisms that underlie ischemia and develop strategies for therapy. The majority of the stroke experiments are carried out in small animals (ex. mice, rats etc) since these present lower costs and greater acceptability from an ethical perspective.

Photothrombosis model: The photothrombotic stroke model is based on intravascular photo-oxidation, which leads to well defined and reproducible lesions in the cortex [10]. To achieve this, a photoactive dye (eg. Rose Bengal, erythrosine B) is injected i.p. or i.v. and the intact cortex is irradiated by a light beam [10, 11], which generates oxygen radicals leading to endothelial damage, platelet activation, and aggregation in all vessels within the irradiated light beam. This techniques enables cerebral ischemia to be induced

in a desired region (eg. motor, sensory cortex), as well as high reproducibility of the lesion, and low mortality. However, the endothelial damage and ischemic injury using this model leads to vasogenic (extracellular) edema formation [12], with no ischemic penumbra and reperfusion possible in this model.

Endothelin-1 model: ET-1 is a potent vasoconstrictive peptide, produced by vascular endothelium [13]. It can be applied directly onto the exposed middle cerebral artery (MCA) [14], or injected intracerebrally [15], to produce dose-dependent ischemic lesions with some edema [16]. After ET1 administration, a rapid and severe CBF reduction (up to 90%) is seen, followed by reperfusion over several hours [17]. This technique offers low mortality and the choice of inducing ischemia in deep brain regions. However, ET1 has been shown to induce astrocytosis and axonal sprouting [18], making it difficult to interpret neural tissue repair experiments.

Embolic stroke model: The embolic stroke model involves injection the of microspheres/macrospheres (20-400 μm in diameter) [19], or homologous clots into the internal carotid artery (ICA) or MCA to mimic human infarcts [20, 21]. Microphere-induced stroke results in multifocal and heterogenous infarcts [22], with the extent and severity of lesions dependent on the size and dose of microspheres [23]. For the thromboembolic clot model, the mechanism of vascular occlusion mimics very closely to human stroke with volume of the infarts dependant on the size and elasticity of the clot [24]. However, lesion volume in this model is much more variable compared to the suture MCA occlusion model [25].

Intraluminal suture MCAo model: The middle cerebral artery (MCA) is one of the cerebral vessels most often affected in human ischemic stroke, accounting for nearly 70% of all

infarcts [26]. The transient MCA occlusion (MCAo) is one of the models that most closely resembles human ischemic stroke and is characterized by reliable and reproducible infarcts. This model involves blocking the common carotid artery (CCA), introducing a suture into the internal carotid artery (ICA), and advancing the suture until it interrupts blood flow to the MCA. This technique offers transient ischemia with reperfusion, but also the choice of permanent MCAo. Depending on the duration of occlusion, this model leads to territorial infarction involving striatum, somatosensory cortex, as well as some portion of the occipital cortex and thalamus [27]. Thus, the MCAo model is considered the most suitable for mimicking human ischemic stroke and subsequent cell death, inflammation, blood brain barrier disruption, as well as producing reliable behavioral results [28].

1.3 DISTINGUISHING PATHOLOGY MICROENVIRONMENTS

In the very early stages of ischemic stroke, adenosine triphosphate (ATP) consumption continues despite insufficient synthesis due to reduced glucose and oxygen flow in the tissue. This leads to a drop in total ATP available to the cells and ionic homeostasis. Severe ischemia results in an excess release of the main excitotoxic neurotransmitter called glutamate, which promotes a major influx of calcium into the cells and activates the phospholipases and proteases to degrade proteins and membranes in neuronal cells [29]. The core of the infarct results in an area of complete cell death leading to irreversibly damaged tissue [30] (**Figure 1.1**). Cerebral blood flow (CBF) is highly compromised in this region with < 20% of baseline blood flow levels [31]. With fast degradation (7-10 days) of the damaged host tissue extracellular matrix (ECM), the cavity is filled with extracellular

fluid after liquefactive necrosis [32], and transplantation of cells in this region would result in severe loss of the injected graft [33, 34].

The brain tissue surrounding the core, or the ischemic penumbra (IP), contains partially dying cells as well as activated microglia, peripheral macrophages and astrocytes.

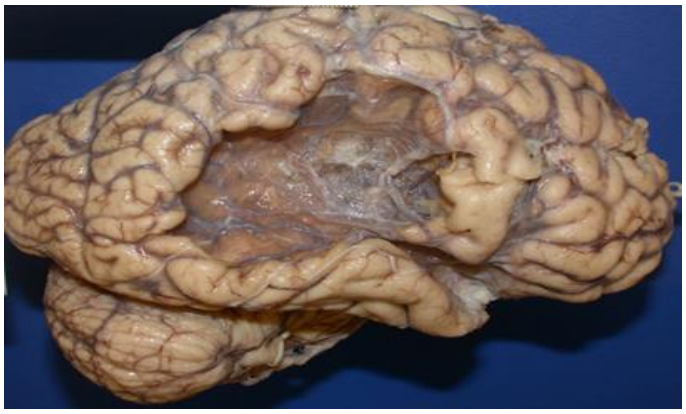

Figure 1.1. Right human MCA infarct shows a collapsed cavity void of all cells and tissue.

Microglia, the resident immune cells of the brain constantly monitor the microenvironment and respond to the insult with typical macrophagic roles, such as secretion of cytokines, phagocytosis and antigen presentation. Microglia are activated within minutes of the stroke onset and accumulate surrounding the lesion cavity in the peri-infarct tissue. The proliferation of these immune cells peaks at 48-72 hours after ischemia and may last for several weeks depending on the extent of damage [35, 36]. While traditionally these cells were considered to be deleterious and neurotoxic by releasing pro-inflammatory cytokines, such as tumor necrosis factor (TNF)-alpha and Interleukin (IL)-1 [37-39], it has been shown that activated microglia can maintain and support neuronal survival [40, 41]

by releasing anti-inflammatory and neurotrophic factors. Microglia have also been shown to promote neurogenesis by guiding stem cells to the site of injury [42-44].

The astrocytic response after the injury, or reactive gliosis, is characterized by excessive expression of glial fibrillary acidic protein (GFAP), cellular hypertrophy and process extension, creating a glial scar tissue surrounding the lesion [45-47] (**Figure 1.2**). It is well known that astrocytes are more resistant to oxygen and glucose deprivation [45], which enables them to survive for a prolonged period in the IP, where the vasculature is partially maintained [48].

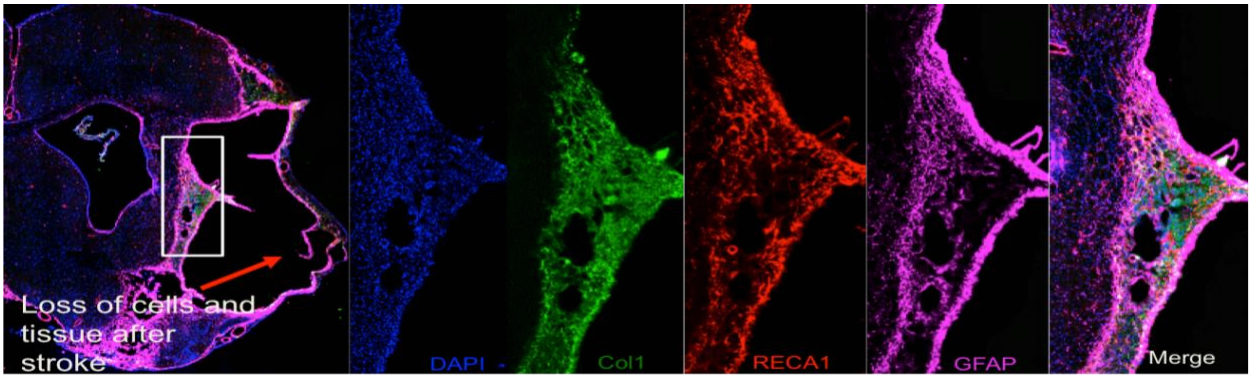

Figure 1.2. Peri-infarct cavity in a rat brain shows active tissue remodeling with upregulation of ECM proteins (eg. collagen), endothelial marker protein RECA1, and expression of GFAP reslting in a reactive glial scar around the cavity.

Astrocytes are involved in a number of activities during ischemia, including regulating the blood brain barrier (BBB), CBF regulation, glutamate and ion homeostasis [48-52]. Although astrocytes limit axon outgrowth by expressing inhibitory molecules (e.g. proteoglycans) and forming a glial scar [53], they are also known to release extracellular

matrix proteins, such as thrombospondins 1 and 2, which have been shown to increase the number of synapes and axonal sprouting in stroke-damaged brains [54]. In the days to weeks following brain tissue damage, microglia and astrocyte activation shifts its cytokine release profile through the secretion of anti-inflammatory and neurotrophic factors, such as TGF-β, BDNF and NGF [55].

1.4 CELL THERAPY TO SUPPLEMENT ENDOGENOUS REPAIR RESPONSES

Cellular and molecular approaches to achieve tissue repair includes cell therapy [56-58], using molecular mechanisms to induce axonal growth [59, 60], modulating the neural responses using light (optogenetics) [61], and immunotherapy [62, 63]. With a limited endogenous neurogenesis and capacity to regenerate following injury, delivery of exogenous cells to the site of injury has been shown to modulate the inflammatory response, stimulate endogenous stem cells and promote neuroprotection and plasticity [64]. These transplanted cells can help in the tissue repair process by directly integrating into the host tissue or by secreting factors that promote neurogenesis [65]. Indeed, human NSCs transplanted in the ischemic parenchyma in rats have been shown to release factors, such as VEGF and FGF-2, which are effective in stimulating endogenous neurogenesis [66, 67]. In addition, transplanted NSCs have been shown to induce a downregulation of pro-inflammatory cytokines, such as interleukin-1B and tumor necrosis factor alpha, in ischemic mice's brains [68], drastically decreasing the microglia driven inflammatory response. Studies have also shown that injecting cells directly into the lesion cavity results in their migration into the existing parenchyma with poor survival [69]. One

key parameter that has been shown to affect cell survival is the regulation of inflammatory cytokines. The stroke cavity is surrounded by resident immune cells, i.e. microglia, as well as perivascular macrophages who respond to the injury by releasing inflammatory cytokines [70], that have a detrimental effect on the cells transplanted in a close proximity to the cavity [33]. These exogenously delivered cells by themselves do not replace lost tissue. To achieve a retention of injected cells within the lesion cavity, it is essential to provide a permissive structural and functional microenvironmental niche [69, 71-73]. Such niche support may be achieved by biomaterials specifically engineered to be compatible with neural tissue and amenable to delivery through a small gauge needle for intracerebral injections, with minimal damage to healthy tissue [74, 75]. Matrigel, a commonly used biomaterial derived from a mouse sarcoma with ECM components collagen, entactin and laminin has been shown to reduce the infarct size after injury, only when used in combination with transplanting cells [72]. Also, transplantation of NPCs mixed with HA/collagen hydrogel into the stroke cavity 7 days post-stroke improved the survival of NPCs and reduced the infiltration of inflammatory cells to the graft [76]. These attributes allow biomaterials to not only benefit the transplanted cells, but also supports the invasion and migration of endogenous host cells surrounding the implant. With the ability to protect the cells to improve survival and promote neural cell integration, more studies on cell therapy in combination with protective hydrogels would greatly advance the neural tissue engineering.

1.5 BARRIERS TO TISSUE REPAIR AND REGENERATION

Regenerative strategies, such as stem cell therapy have shown limited success in improving behavioral outcomes, but there is no replacement of the lost tissue [57, 77], and hence a large tissue cavity remains in the brains of stroke survivors [78]. There are 2 major limitations with stem cell therapy. Firstly, there is a large scale loss of the transplanted cells in the days following intracerebral implantation, with survival ranging from 1% to 32% [79]. Similarly, systemic administration of cells in ischemic rats accumulates cells primarily in internal organs instead of brain [80]. Secondly, intracerebral cell injection requires transplantation into the peri-infarct region, which is considered to be an active site for cerebral reorganization after stroke [81], and multiple injections into this site can potentially damage the tissue even further. Pro-aniogeneic growth factors like VEGF have also been been administered to stroke rats using systemic and intracerebral routes. Results suggest that early delivery of VEGF after stroke increases the formation of disorganized and immature blood vessels, worsens edema and disrupts the blood brain barrier while its antagonist reduces the tissue damage [82].

In addition, the ECMs (specifically chondroitin sulfate proteoglycans) produced by reactive astrocytes are known to impede axonal regeneration by forming a physical barrier along the lesion cavity [83]. The glial scar provides a biochemical and mechanical barrier to neuronal regeneration [84, 85], consitituing a stiff barrier that neurons cannot penetrate [85]. In order to modulate the immune and glial cell responses, an ideal

treatment strategy will be to protect the implanted or infiltrating host cells from the inflammatory response and allow the host cells to cross the glail scar into the lesion cavity.

1.6 PROVIDING SCAFFOLDING SUPPORT FOR TISSUE REPAIR

Biomaterial scaffolds are natural or synthetic 3D polymer networks that provide an appropriate environment for cells to attach, proliferate, and differentiate to facilitate the formation of extracellular matrix (ECM) [86]. Although biomaterials based tissue repair strategies have been studies for at least two decades, they have not been extensively applied to repair the post-stroke brain. It is important to note that the chemical and mechanical properties of a biomaterial determine the fate of transplanted cells, as well as the drug release profile. The extent of cross-linking and rate of degradation are directly affected by the chemical characteristics of the preparation and determine the overall functionality of the biomaterial.

1.6.1 Natural versus synthetic scaffolds

Extracellular matrix makes up 20% of the whole brain tissue volume and plays a role in maintaining key cellular functions [87]. Hydrogels derived from ECM may provide the mechanical properties and signaling molecules to attract host cells into the lesion cavity and obviating the need for exogenous cells [71, 77, 88, 89]. The decellularized biomaterial contains ECM proteins like laminin and fibronectin, myelin and growth factors including VEGF and fibroblast growth factor-2 [90, 91].

ECM harvested from different organ systems, such as the brain, spinal cord or urinary bladder, influence neural stem cell phenotypic fate and the extent of cell invasion [92]. While the ECM in the peripheral tissue contains high amounts of structural proteins, such as collagen, fibronectin and laminin, the adult CNS is mainly composed of glycosaminoglycans and proteoglycans [93, 94]. In an in vitro comparison study of ECM derived from brain, spinal cord and urinary bladder, all ECMs increased the number of cells expressing neurites, but only the brain ECM increased neurite length [95].

In addition to ECM hydrogels, natural polymers like hyaluronic acid (HA) [96, 97], fibrin [98], HA-methylcellulose (HAMC) [99], chitosan [100, 101] and collagen [102] have been used extensively to deliver cells or molecules in the CNS. Collagen is a popular material used in biomedical applications since it is the most abundant protein and main component of peripheral ECM in mammalian tissues. Collagen hydrogels have been used to encapsulate variety of stem cell types for tissue engineering applications because of its biocompatibility, mechanical strength and immunogenicity [103]. In a rodent model of cerebral ischemia, encapsulation of NSCs in collagen type I hydrogel showed an increase in cell survival (compared to injection of cells alone), formation of synapsis and facilitated the functional recovery of neural tissue following injury [86]. Another naturally occurring polysaccharide found in CNS and used for hydrogel formation is hyaluronan. It is known to have anti-inflammatory properties and has been shown to promote cell adhesion and survival [104]. Transplantation of a cross-linked hyaluronan and heparin sulfate hydrogel in a mice model of ischemia significantly promoted the survival of NPCs, and attenuated infiltration of immune cells into the graft compared with the cells delivered in suspension alone [76]. Also, injection of HA peptide hydrogels into the stroke cavity showed stiffness

dependent activation of macrophages, with stiffer hydrogels (~1300 Pa) showing an increased macrophage density at the host-hydrogel interface comepared to softer gels [97].

Synthetic biomaterials allow precise control over material properties and degradation rates slowing controlled release of small molecules or drugs into the surrounding tissue. The commonly used biomaterials for controlled drug delivery are the polymeric agents polylactide (PL), polyglycolide (PG), and the copolymers of lactide and glycolide (PLGA). PLGA particles are loaded with bioactive molecules and delivered to the site of injury or embedded in hydrogels to further tune the location and rate of delivery. Synthetic biomaterials, unlike natural materials like collagen and Matrigel, are better chemically defined and biologically inert which reduces the variability and the host immune response. In normal untreated animals, injection of PLGA based microspheres evoked an inflammatory response no greater than just the needle tract [105, 106]. There was a peak in astrocyte activation at 1 week post-transplantation and diminished as the polymer degraded [105, 107, 108]. Like natural biomaterials, byproducts of synthetic materials can also be bioactive and influence the local microenvironment. In a recent study, application of lactic acid (a byproduct of PLGA) on cultured slices of developing mice cerebral cortex has shown to support oligodendrocyte development and myelination [109]. Nanoparticles and gels made from PGA, PLA and PLGA are primarily used for drug delivery since their degradation rate can be controlled by simply adjusting the PL:PG ratio.

Another synthetic polymer known to resist protein absorption and commonly used in biomaterial applications is poly (ethylene glycol) (PEG). Although cells do not directly attach to PEG hydrogels, it is most often mixed with other polymers like HA or gelatin to

support cell attachment and migration. Epi-cortical delivery of PEG modified epidermal growth factor (PEG-EGF) significantly increased tissue penetration and endogenous NSC stimulation compared to unbound EGF [110]. PEG based hydrogels are promising in the fields of drug and cell delivery for many reasons, including controlled drug delivery or degradation rate, low immunogenicity, non-toxicity and biocompatibility.

1.6.2 Injectable hydrogels

Since brain injuries, such as stroke, vary in size and shape, an ideal biomaterial will fill the cavity space and form gel to repopulate the lost tissue. Injectable biomaterials can be used as a scaffold to fill the stroke cavity and promote interactions between the transplanted material and host tissue [71, 88, 89, 111], deliver drugs or growth factors to the damaged tissue, promote the attachment and engraftment of transplanted cells and help recruit host cells to repopulate the lost tissue [112]. Protective hydrogels derived from natural and synthetic polymers can incorporate cells, growth factors, and other therapeutics to enhance the microenvironment and provide controlled release of bioactive molecules.

Crosslinking of water soluble polymers produces a hydrogel that has excellent nutrient and oxygen permeability, promoting cell survival inside the scaffold [113]. These biomaterials can be formulated to exist in liquid state at room temperature while forming gels in situ, allowing for minimal invasive delivery through a small-gauge needles, using MRI guidance [114]. For example, collagen, methylcellulose, and agarose are all temperature sensitive polymers and their gelation rates can easily be controlled by adding

other natural polymers, such as hyaluronic acid [115]. The high water content of hydrogels makes them very biocompatible and promising candidates for tissue engineering applications. It is an important consideration that large volume of hydrogel injection into the lesion cavity or into the peri-infarct area would cause tissue disruption and increased intracerebral pressure [116, 117], and therefore an innovating neurosurgical technique that allows for the drainage of ECF should be employed to avoid additional damage [114].

1.6.3 Gelation and retention

An ideal hydrogel chemistry would facilitate the gelation of the material and minimize permeation of scaffolding from the injection site into surrounding tissue. In order to achieve a complete coverage of the lesion cavity, rapid gelation of hydrogel is necessary to avoid leakage in the tissue and support the invasion of host cells into the cavity. Furthermore, mixing of the extracellular fluid (ECF) present in the stroke cavity with the injected hydrogel could change the chemical and mechanical properties and hence influence the extent of gelation and retention. Therefore, it is ideal to drain the ECF before or during the hydrogel injection to avoid mixing and increasing the intracerebral pressure. In experiments where partial diffusion into the host tissue is preferred such as drug delivery, the hydrogel can be formulated with lower concentrations that support diffusion as well as partial retention in the stroke cavity [114].

1.6.4 Biocompatible and non-toxic

Biocompatibility of a biomaterial refers to its biological compatibility with the host tissue, as well as all byproducts being non-toxic and avoiding any undesirable effects on the local tissue environment. The long term biocompatibility of the material with the host brain dictates the effectiveness of the implantation. Most commonly, the number and degree of reactivity of microglia and astrocytes surrounding the biomaterial is used as an indicator of immunorejection [118], or *in vivo* biocompatibility. The biocompatibility of byproducts from biomaterial degradation must also be considered, as the byproducts are often bioactive which can influence the surrounding environment. Another factor affecting the biocompatibility of a material is dependent on the method of polymerization. Photopolymerization of a hydrogel, i.e. crosslinking when exposed to light, can lead to formation of free-radicals which are toxic to the encapsulated cells [119, 120], as well as the host cells, which are already under high oxidative stress after the injury. However, polymerization processes that are dependent on changes in temperature or pH produce little to no free radicals and often polymerize at physiological conditions, making these polymers injectable using a minimally invasive procedure.

1.6.5 Biomaterial stiffness and cell invasion

As mentioned before, the chemical properties of the biomaterial affect the mechanical properties – especially the stiffness of material after polymerization. The compressive

modulus measures the stiffness of the biomaterial and can be easily varied by changing the proportion of monomers [121], or molecular weight of monomer [122, 123]. The stiffness of the prepared hydrogel is known to affect cell proliferation and differentiation in vivo. If microtubule compression forces determined scaffold stiffness is outside their sensitivity range, cells reinforce by increasing or decreasing actin filament building [124]. Rat NSCs grown on soft (<1 kPa) hydrogels differentiated primarily into astrocytes and neurons, however cells cultured on stiffer (> 7kPa) gels differentiated into oligodendrocytes [125]. In addition, cells cultured on intermediate stiffness (3.5 kPa) showed the most proliferation. Similarly, MSCs respond differently to varying mechanical properties with cells differentiating to neural like cells on soft gels (0.1-1 kPa), osteogenic cells on stiffer (25-40 kPa), and myogenic cells with intermediate stiffness [126]. It is important to note that an ideal biomaterial will closely resemble the mechanical properties of the host tissue to minimize the contact stresses and an aggravated response from the immune cells. However, some variability exists regarding the approximate stiffness of healthy brain tissue, which may be related to the different testing methods and brain regions used for the analysis. Using confined compession tests, a stiffness of 50 kPa has been reported for mouse and rat brains [127]. Using magnetic resonance elastography, a stiffness of 25 kPa was reported in a mouse brain [128]. Other groups have reported even lower compressive modulus of brain ranging from 300 Pa to 10 kPa [129] [130]. However the use of mechanics has not been fully explored in vivo to guide the differentiation of transplanted cells, likely since soft biomaterials needed for neuronal differentiation tend to degrade faster than desired. With biodegradation and loss of

collagen cross links over time, the compressive modulus of the implanted material decreases and results in the loss of mechanical integrity, leading to the influx of host cells.

1.6.6 Biodegradable

Biodegradation is a natural process during which the biomaterial is degraded by the invading cells, proteases or hydrolysis. After full biodegradation, the biomaterials are broken down into their components and released in the surrounding tissue. For successful integration into neural networks, it is necessary that the chemical properties of the material allow it to degrade over time. Permanent implants could lead to chronic inflammation and sustained activation of glial cells (i.e. a foreign body response) around the implant [131]. When designing a hydrogel, the degradation rate can have effects on both the functionality of the hydrogel, as well as the host response. For example, a slow degrading hydrogel would be preferred in order to support the transplanted cells to develop their own ECM, extend processes and integrate into neural networks. However, faster degradation could result in a reduced inflammatory response in vivo, and thus it is important to develop materials that balance the cell supportive nature of hydrogels, as well as the rate of degradation to avoid any additional immune response.

1.7. SPECIFIC AIMS

Aim 1: To establish the concentration-dependent rheological properties of an ECM hydrogel that influences its delivery and in vivo interaction with host tissue.

Hypothesis: The use of non-invasive MR imaging will guide the location and volume of injection, and affords efficient delivery of ECM hydrogel (3 – 8 mg/mL) to the stroke cavity.

a) Establish MRI-guided injection-drainage approach that minimizes tissue damage from ECM injection

b) Establish the gelation and retention properties of different ECM concentrations in a stroke cavity with characterization of infiltrating cells

Aim 2: To evaluate ECM biodegradation and behavioral impact in stroke rats implanted with ECM hydrogel.

Hypothesis: Biodegradation of 8 mg/mL ECM hydrogel will promote sensory and motor functional improvements by restoring tissue in the stroke cavity.

a) Quantify ECM biodegradation and cell invasion

b) Determine the phenotypes of invading cells

c) Evaluate the evolution of lesion volume and tissue deformations using MRI

d) Evaluate functional changes from ECM implantation

Aim 3: To evaluate the temporal evolution of cell invasion into ECM hydrogel injected in the stroke cavity. *Hypothesis: A significant concentration-dependent cell invasion will occur with microglia and macrophages being polarized toward a M2 phenotype, preceding nonimmune cells to follow and repopulate the tissue void.*

a) Establish gelation, retention and biodegradation of different ECM concentrations

b) Compare and quantify cell invasion for different ECM concentrations

c) Determine the phenotypes of invading cells

d) Determine the effect of ECM injection on host astrocytic response and tissue deformations in comparison to healthy and stroke groups.

Aim 4: To establish and validate the in vivo visualization of macrophage invasion into ECM hydrogel. *Hypothesis: Perfluorocarbon (PFC) nanoemulsions will afford a reliable discrimination of macrophages invading the ECM hydrogel from the peri-lesion parenchyma using ^{19}F MR imaging.*

a) Determine the optimal imaging parameters that achieve the greatest sensitivity for PFC nanoemulsion

b) Visualize and quantify macrophage invasion in stroke brain implanted with ECM hydrogel

c) Establish histological validation of PFC macrophage detection

2.0 INTRACEREBRAL DELIVERY OF ECM HYDROGEL USING MRI GUIDANCE AND CHARACTERIZATION OF HOST CELL INFILTRATE

Work in this chapter has been adapted from the following published manuscripts:

1. *Massensini AR*, **Ghuman H***, Saldin LT, Medberry CJ, Keane TJ, Nicholls FJ, Velankar SS, Badylak SF, Modo M. Concentration-dependent rheological properties of ECM hydrogel for intracerebral delivery to a stroke cavity. Acta Biomater. 2015; 27:116-30. *****Contributed equally*
2. ***Ghuman H**, Massensini AR, Donnelly J, Kim S, Badylak SF, Modo M. ECM Hydrogel injection for the treatment of chronic stroke: Characterization of the acute host cells invasion. Biomaterials. 2016; 91:166-181.*

2.1 INTRODUCTION

Therapeutic options for stroke remain very limited [75]. Most pharmacological agents are administered systemically during the acute phase to either resolve a thrombus or to provide neuroprotection. The focus of current therapy is the modulation of the remaining brain tissue response by systemic administration of agents or cells that putatively promote plasticity. In the absence of neuroprotection, cells in the infarct territory will die resulting in liquifactive necrosis and invading phagocytic cells will remove cellular debris and the surrounding tissue matrix [132]. A fluid-filled lesion cavity remains. A key challenge in the treatment of stroke is hence the removal of necrotic debris and access to the adjacent

viable or potentially viable tissue. The advent of regenerative medicine affords potentially novel strategies for integration of cells and/or therapeutic agents/materials into the damaged brain by intracerebral injection [74, 133]. Hydrogel forms of naturally occurring biomaterials composed of extracellular matrix (ECM) show in vitro chemoattraction and differentiation stimuli for neural stem cells and might obviate the need for exogenous cells [89, 91]. Alternatively, these materials may supply growth factors, mechanical properties, and/or signaling molecules to support delivered cells or surviving endogenous cells [134-136]. Rheologic characterization of an ECM hydrogel intended for CNS applications is essential for an effective evaluation of delivery, safety and efficacy of this therapeutic strategy.

ECM concentration affects rheological properties and determines if it will form a hydrogel or remain in a liquid phase [137]. Without the formation of a gel phase in situ, the ECM will diffuse and not provide a structural support within the lesion cavity [138]. Additionally, the stiffness of hydrogel will influence cell invasion and phenotypic choice of neural progenitors [139]. Determining the rheological properties of ECM hydrogels is therefore important to establish the retention of scaffolding material within the lesion cavity and the associated host response.As lesion cavities caused by ischemic stroke may consist of a large volume and irregular shape, it is essential to ensure that administration is indeed into the tissue void rather than intraparenchymally, where this volume would cause tissue disruption and potentially increased intracerebral pressure [116, 117]. The use of non-invasive imaging, such as magnetic resonance imaging (MRI), can guide the volume of injection, as well as its stereotactic location, to ensure the safety of this approach [140, 141].

The objective of the present study was to characterize the concentration-dependent rheologic properties of an ECM biologic scaffold material for the intended clinical application of minimally invasive intracerebral injection. To assay the in situ gel formation based on the concentration-dependent properties of the ECM, we also describe an innovative neurosurgical approach for its delivery in the liquid phase into the stroke cavity using MRI guidance.

2.2 MATERIALS AND METHODS

2.2.1 Extracellular matrix (ECM) based hydrogel

ECM hydrogel was produced by isolating the basement membrane and tunica propria of porcine urinary bladder (Tissue Source, Inc., Lafayette, IN) by mechanical delamination [137]. Decellularization was performed by immersing the isolated layers of the bladder in 0.1% peracetic acid in ethanol with agitation (4% v/v; 120 min; 300 rpm). A series of PBS and deionized water rinses removed cellular debris [137]. Decellularization was confirmed using Hematoxylin & Eosin, 4',6-diamidino-2-phenylindole (DAPI) staining, agarose gel electrophoresis, and quantification of remnant DNA [142]. ECM was then lyophilized, comminuted, and solubilized with pepsin (1 mg/mL) in 0.01 N HCl. pH neutralization was achieved by adding 0.1 N NaOH. Approximately 70% of the ECM material is collagen [95], but other prominent ECM proteins, such as fibronectin, decorin, laminin subunit γ1 are also present [143]. A variety of growth factors are also retained within the ECM preparation, including transforming growth factor-β, vascular endothelial growth factor-A,

basic fibroblast growth factor, and nerve growth factor [91], all of which are known to influence neuronal and endothelial cells. In addition, matrix-bound nanovesicles (MBV) enriched in miRNA and other signaling molecules are present within the ECM preparation [144]. Dilution to a desired concentration (3, 4 and 8 mg/mL) was attained by mixture with the appropriate volume of PBS [137]. Gelation of this preparation is concentration, pH and temperature-dependent. Concentrations <3 mg/mL do not readily form a hydrogel on the bench.

2.2.2 ECM hydrogel rheology

All rheological data was collected using a rheometer (AR2000, TA instruments, New Castle, DE) fitted with 40mm parallel plate geometry, as previously described [95, 137, 145]. Temperature was controlled within 0.1°C using a Peltier plate. The pre-gel at either 4 or 8 mg/mL was loaded onto the parallel plate rheometer at 10°C; a temperature substantially below which is required for ECM gelation readily occurs. Sample evaporation was minimized using mineral oil to seal the edges of the sample-plate interface.

A series of rheological tests were conducted in sequence for each sample. A creep test was performed to measure the steady shear viscosity of the pre-gel by applying a constant shear stress of 1 Pa. An oscillatory time sweep was performed to measure the gelation kinetics of the forming ECM hydrogel by rapidly raising the temperature to 37°C (a temperature at which ECM gelation occurs) and applying a small 0.5% oscillatory strain at a frequency of 1 rad/s. After 40-60 minutes after which the gelation was deemed

complete, an oscillatory frequency sweep was performed to measure the complex viscosity (|n*|) over a frequency range (0.1 rad/s – 100 rad/s) by applying 0.5% oscillatory strain. Samples were evaluated in triplicate. A two-tailed Student's *t-test* was performed to determine whether differences existed between the 4 and 8 mg/mL ECM sample means with the p-value set at 0.05 using SPSS Statistical Analysis Software (SPSS, IBM, Chicago, IL, USA).

2.2.3 Middle cerebral artery occlusion (MCAO)

All animal procedures complied with the US Animals Welfare Act (2010) and were approved by the University of Pittsburgh Institutional Animal Care and Use Committee (IACUC). Sprague-Dawley rats (male, 260±15g, Taconic Labs, USA) were maintained on a 12-hour light/dark schedule, with food and water available *ad libitum.* For transient intraluminal right middle cerebral artery (MCA) occlusion, a rat model of stroke, a 5-0 silicone rubber-coated monofilament (diameter 0.12 mm, length 30 mm, tip coating at 0.35 mm for 5-6 mm, Doccol, USA) was advanced to the ostium of the MCA in the circle of Willis, while the animal was under isoflurane anesthesia (4% induction, 1% maintenance in 30% O_2). The Middle cerebral artery was occluded for approximately 70 minutes prior to reperfusion by retracting the filament to the common carotid bifurcation, producing an occlusion similar to the scenario in 2/3 of all cases of human ischemic stroke. After recovery from anesthesia, animals were assessed for forelimb flexion and contralateral circling. Buprenorphine (0.05 mg/kg) was administered to the animals twice daily for 3 days for pain relief. Daily post-operative care and neurological assessment

were performed until they recovered pre-operative weight [146, 147]. Animals not exhibiting signs of MCA damage or who failed to recover weight were excluded from the study.

2.2.4 Magnetic resonance imaging (MRI) and infarct volume calculation

Acquisition. To assess the presence, location and volume of tissue loss, MCAo rats were anesthetized with isoflurane (4% induction, 1% maintenance in 30% O_2) and scanned using a T_2-weighted spin-echo MRI sequence (TR = 6000 ms, TE = 8 ms, 8 Averages, FOV 30x30 mm, 128x128 matrix, 42 slices at 0.5 mm thickness) on a horizontal bore 9.4 T Varian scanner 10 days post-infarction [114, 140].

Lesion volume and intensity measurements. Stroke damage was defined as tissue with a hyperintense signal on T_2-weighted images that were thresholded at 1 standard deviation above the mean of a rectangular region of interest (ROI) in the contralateral hemisphere, encompassing striatum, corpus callosum and neocortex [132, 148].

2.2.5 Simultaneous extracellular fluid drainage and intracerebral ECM injection in stroke brains

Injection of biomaterials into the lesion cavity has mainly been achieved by administering a high concentration of injectate that is then diluted by the extracellular fluid (ECF) present within the cavity. Solubilized extracellular matrix (ECM) and other materials are

dependent on a certain concentration to form a hydrogel in situ, otherwise the material will merely diffuse into the tissue parenchyma, rather than being retained within the cavity (**Figure 2.1.A**). Merely increasing the volume of injection is problematic, as this will lead to an increase in intracerebral pressure (ICP), compromising the remaining tissue. There is further a risk of biomaterial escaping the lesion cavity and, for instance, occluding ventricular space preventing normal flow of cerebrospinal fluid (Figure 2.1.B). In the brain, the trajectory of injection also needs to avoid damage to major anatomical structures and placement needs to be accurate to avoid damage to host tissue (**Figure 2.1.C**).

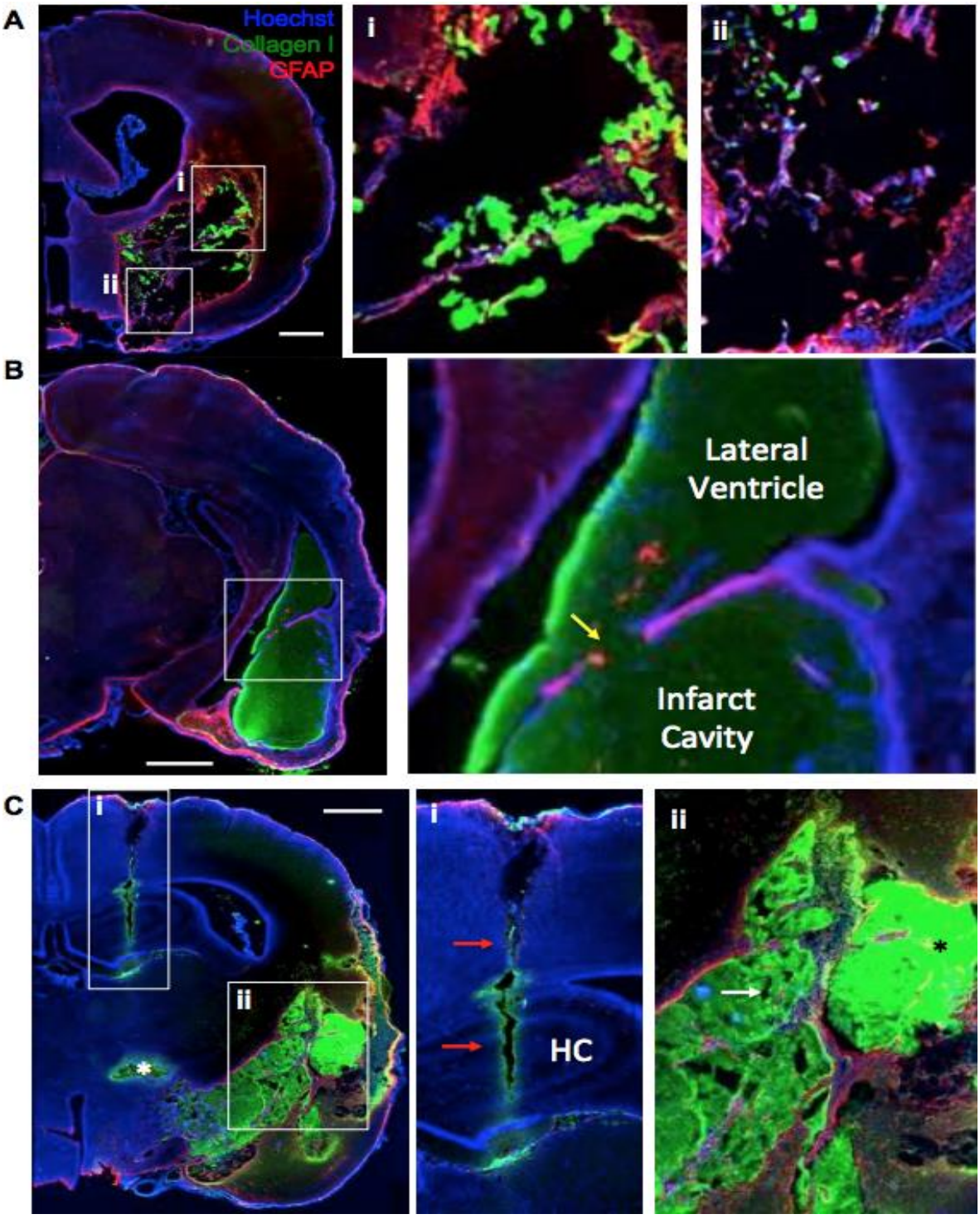

Figure 2.1. Considerations for the injection of biomaterials into a stroke cavity.

A*. Injection of an insufficient quantity or local concentration of an ECM preparation leads to a poor gelation within the cavity and hence does not afford a complete and homogenous coverage (2*

weeks post-MCAo, 24 hours post-injection). Although particles of ECM that formed accumulate at the border or remnants of tissue (i), vast areas of host tissue and the cavity do not show any accumulation of ECM material (ii) indicating that concentration and volume of material is important to ensure proper coverage of the cavity. ***B****. Trajectory for delivery through a needle requires careful planning based on in vivo non-invasive imaging. A trajectory for biomaterial delivery needs to avoid ventricular space, as it can lead to a puncture of the ventricular wall (yellow arrow) and the subsequent leakage of material into the ventricle. Such intraventricular leakage can lead to a decrease in biomaterial concentration in the cavity and an obstruction of cerebrospinal fluid movement through the ventricle with potential damage the choroid plexus.* ***C****. However, position of the injection tract avoiding the ventricle can damage critical neuroanatomical structures, such as the hippocampus, and lead to significant tissue tearing and backflow of biomaterial (i, red arrows). Placement of the cannula at the edge of the cavity can further damage already compromised tissue (white *), although it can deliver ECM material to the cavity. Nevertheless, an uneven distribution and heterogeneous concentration within the cavity (black *) can ensue with areas void of ECM containing extracellular fluid that has not been displaced (ii, white arrow). These examples indicate the need for appropriate neurosurgical planning of biomaterial delivery to ensure a homogenous and complete distribution of ECM throughout the stroke cavity.*

Intracerebral delivery of biomaterials can either be achieved by dilution of the material in the extracellular fluid available in the tissue cavity or this fluid can be drained during injection and a complete replacement of the milieu can be achieved (**Figure 2.2.A**). To define 3-dimensional coordinates for stereotactic injection of biomaterials and drainage of extracellular fluid, MR images were compared to the rat brain atlas (**Figure 2.2.B**).

Fourteen days post-stroke, rats underwent ECM implantation by placement into a stereotactic frame (Kopf, USA) under isoflurane anesthesia (4% induction, 1% maintenance in 30% O_2). A vertical skin incision exposed Bregma on the skull and provided guidance for the location of two Burr holes for 1) the placement of a 250 µL Hamilton syringe with a 24 G beveled tip metal needle (Hamilton) filled with solubilized ECM in PBS, as well as 2) a hole for a drainage cannula (24 G) [114]. MR images of

lesion location and volumes were used to define stereotactic coordinates for needle/cannula placements. Needles/cannula were advanced into the stroke lesion cavity.

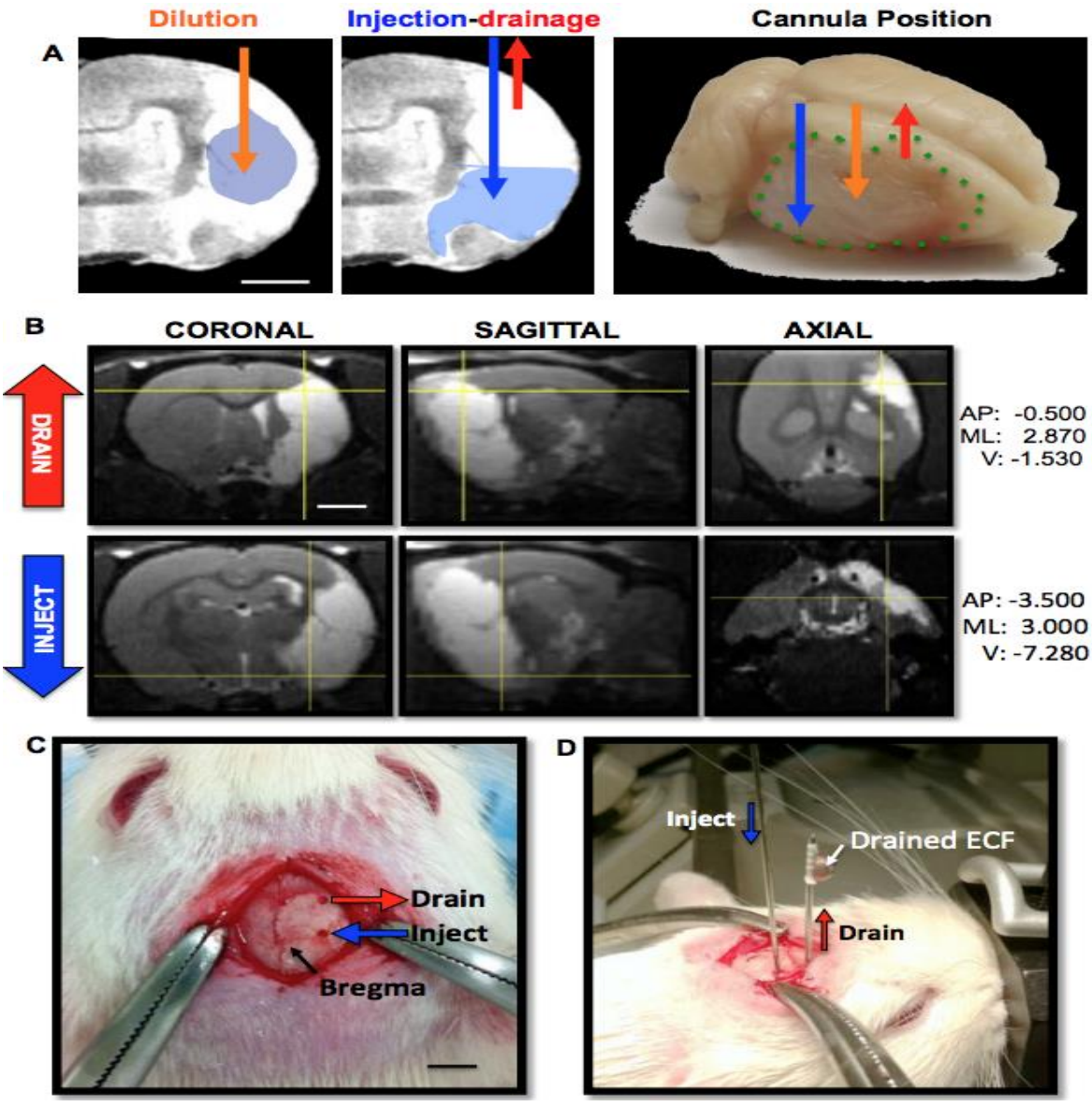

Figure 2.2. Injection-drainage of biomaterials and extracellular fluid.

A*. Delivery of material to the lesion cavity can be achieved by injection of a concentrate to be diluted in the extracellular fluid (ECF). For this, typically an injection site at the center of mass of*

the cavity is targeted (dotted green line = lesion cavity) [71, 140]. However, this delivery method can lead to variations in material concentration and especially in case of in situ gelation can produce areas void of biomaterial [89]. In contrast, the creation of a second burr hole allows displaced ECF to be drained while biomaterial is delivered. Placement of these ideally target the lower parts of the cavity for injection (to facilitate displacement) and crucially the drainage cannula needs to be positioned at the most dorsal part of the cavity to fully exploit the Archimedes principle of fluid displacement. ***B.*** *For injection-drainage, T_2-weighted MRI scans were used to calculate the volume of the lesion cavity (hyperintense area), as well as to define coordinates for injection and drainage (AP=Anterior-Posterior; ML=Medio-Lateral; DV=Dorso-Ventral).* ***C****. Based on these coordinates, Burr holes were drilled into the skull at the appropriate location in relation to Bregma.* ***D****. Injection of a liquid hydrogel composed of extracellular matrix (ECM) through a needle/syringe fixed to the stereotactic device allowed injection of a volume equal to the lesion volume. As the biomaterial was denser than extracellular fluid (ECF), its injection led to the displacement of ECF from the cavity through the drainage cannula. Gelation of the ECM occurred inside the cavity, allowing adaptation to the topology of the lesion.*

Lesion-equivalent volumes of solubilized ECM were injected into the ventral posterior region of the cavity to displace and drain the less dense necrotic debris from the stroke cavity. Injection of solubilized ECM (0, 3, 4, 8 mg/mL concentrations) was controlled using a frame mounted injection pump (World Precision Instruments, USA) at a constant speed of 10 µL/min until the total volume was delivered (4-24 min). The solubilized ECM formed a hydrogel in situ at 37 °C body temperature. Needle and cannula were left in place for 5 minutes to allow material to dissipate and form a gel before the needles were slowly withdrawn from the brain. Burr holes were filled with bone wax (Fisher) prior to suturing. LX4 (Ferndale, containing 4% Lidocaine) was topically applied as an analgesic, and buprenorphine (0.05 mg/kg) was administered via intraperitoneal injection to provide sustained pain relief

2.2.6 Intracranial pressure measurement

Injection of a large volume of biomaterial may cause an increase in intracranial pressure, which is known to have detrimental neurological effects. A comparison of the injection-drainage technique with no drainage (both 8 mg/ml ECM) was hence undertaken by monitoring intracranial pressure (ICP) during injections. A pressure sensor (WPI) attached to a fiber optic measurement system (RJC Enterprises) was used to measure ICP in mmHg. Before starting, the probe was calibrated to atmospheric pressure (=0) and allowed to stabilize. For ICP measurement, a burr hole was made on the contralateral side at coordinates equivalent to the injection site. The probe was slowly inserted into the contralateral hemisphere to a depth of 5mm. Bone wax was then used to seal the burr hole around the probe. The injection/drainage needles were inserted and ICP was recorded at 15 s intervals throughout the injection. After injections were completed, the needles were left in place for 5min with continued ICP measurement.

2.2.7 Histological assessment

2.2.7.1 Perfusion and immunohistochemistry. *Perfusion-fixation of tissue*. To determine the in-situ distribution of the ECM hydrogel and cell infiltration within the hydrogel, rats were transcardially perfused at 1, 14 or 90 days post-implantation with 0.9% saline followed by 4% paraformaldehyde (in 0.2 M PBS) to fix brain tissue prior to its removal from the skull. Brains were post-fixed in 4% paraformaldehyde for 24 hours prior to being cryopreserved in 30% sucrose with sodium azide (Sigma) at 4 °C. Histologic

sections (50 µm thickness) were prepared on a cryostat (Leica) maintained at – 25 C and placed directly onto microscopic slides to preserve tissue morphology and deformations.

Immunohistochemistry. Brain sections were washed 3x5 min with 0.01 M PBS, followed by 1 hr permeabilization in PBS + 0.1% Triton X-100 (Sigma) at room temperature (21 °C). Primary antibodies (**Table 1**) were applied, diluted in PBS + 0.05% Triton X-100, and incubated at 4 °C overnight. After rinsing off the primary antibodies (3x5 min PBS), appropriate secondary AlexaFluor 488, 555, or 660 antibodies (1:500; Life Technologies) were applied for 1 hour at room temperature followed by 3x5 min washes with PBS. Finally, sections were coverslipped with Vectashield for fluorescence containing Hoechst 33342 (1 µg/mL, Sigma) and stored at 4 °C prior to imaging. Visualization of antibodies was performed with a fluorescence microscope (Axioimager M2, Zeiss) interfaced with a monochrome camera driven by Stereo Investigator image capture software (MBF Bioscience) using a motorized stage [114].

Table 1. List of antibodies used for immunohistochemistry

Antibody	Concentration	Company	Cat. Ref.	Clone
Collagen-I	1:250	Abcam	Ab34710	Collagen I aa 1-1464
Iba-1	1:300	Abcam	Ab5076	Iba1 aa 135-147
GFAP	1:3000	Sigma	G3893	G-A-5
DCX	1:150	Abcam	Ab153668	CAA0661`7.1 and AAT58219.1
CNPase	1:200	Abcam	Ab6319	11-5B
Fox3	1:500	Abcam	Ab104224	1B7
RECA-1	1:100	Abcam	Ab9774	RECA-1
CD86	1:200	Abcam	Ab53004	EP1159Y
CD206	1:200	Santa Cruz	sc-34577	C-20

2.2.7.2 Cell invasion – quantification. To quantify the number and distribution of cells infiltrating the ECM hydrogel, a semi-automated script (Lux64R) was used. Collagen I was used to delineate the border between host and biomaterial [112, 114, 149, 150] to determine the number and phenotype of cells invading the injected ECM. Whole graft images were acquired at 20x magnification with brain sections stained for Hoechst (to identify cell nuclei) and Collagen I (to mask and delineate the host-ECM boundary to quantify cell invasion). A colorimetric scale ranging from blue, for cells most proximal, to red, indicating cells most distant from the adjacent host tissue, was used to create a color map of cell invasion (**Figure 2.3.C**), while providing measurements of distance of individual invading cells (**Figure 2.3.D**).

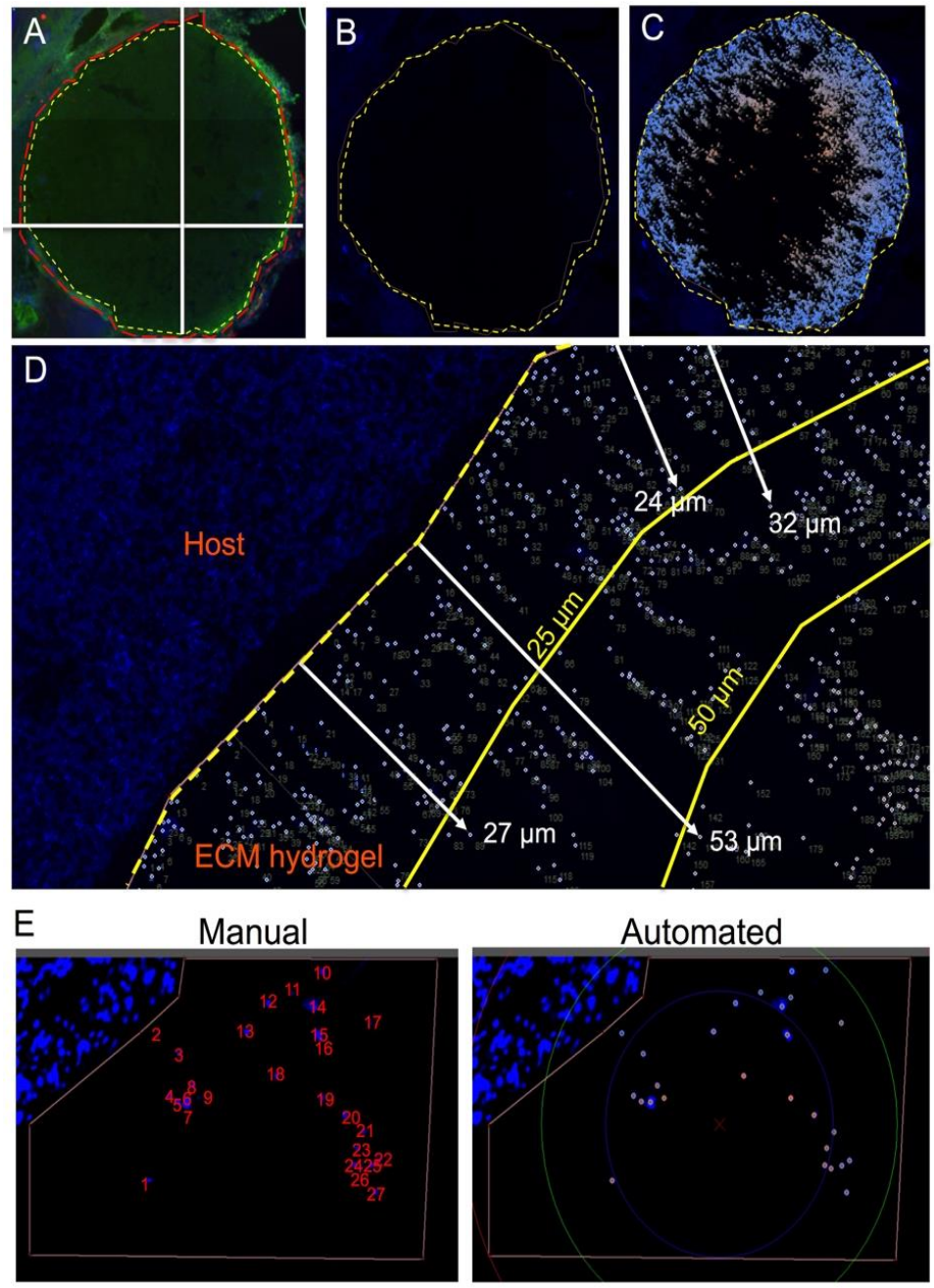

Figure 2.3. Measuring cell infiltration.

Overview of the cell infiltration quantification approach using Lux64R and DAPI stained fluorescent images. Using collagen I to stain the ECM biomaterial, the distinction between the lesion boundary and the ECM hydrogel interface is identified ***(A)****. Using Lux64R, the lesion boundary is then drawn and defined* ***(B)****. The cells inside the boundary are then labeled and counted* ***(C)****. A closer view in a region of interest shows that each cell is accurately identified and*

*labeled, while measuring its distance traveled from the previously defined lesion boundary **(D)**. Manual and automated cell counts using Lux64R shows cells being correctly identified for quantification of cell invasion **(E)**.*

The tangent distance of infiltration from the cavity boundary was measured for each cell using the cavity's center of mass as reference. To reveal a relationship between ECM hydrogel concentration and cell invasion, 25 μm concentric bins were used to compare the number and distance of invading cells in relation to center of mass for each defect. It is important to note that individual shapes of cavities were different, some more irregular than others. In some cases, the center of mass is hence not the most accurate point of reference towards which the cells infiltrated, but was still the most pertinent to afford a grouping of cell invasion and provide a comparison. Validation of this approach was shown by the high correlation (>95%) between manual counting and distance measurements against the semi-automated approach (**Figure 2.3.E**). All tissue sections containing ECM hydrogel was quantified (**Figure 2.4.A**).

2.2.7.3 Cell infiltration – cell phenotype analysis. To determine the phenotypes of cells invading the injected ECM, collagen I was used to delineate the border between host and biomaterial. Animals injected with concentrations >3 mg/mL resulted in a gelation and retention within the cavity. Due to differences in the extent of material present within a given defect, the number of FOVs counted ranged from 5 to 15 images to cover the material present within the cavity (**Figure 2.4.B**). Where ECM hydrogel covered the whole defect (i.e. concentrations of ≥3 mg/mL), FOVs were equally spaced throughout the material within a section and counted across all anterior-posterior slices. Images were

acquired at 20x magnification to determine the total number of cells (i.e. Hoechst+) within the ECM material and to determine the phenotype of cells [112, 149]. Five to eight images were acquired at equally-spaced distances throughout the material within a section and counted across all anterior-posterior slices containing ECM hydrogel. Phenotypic markers for neural progenitor cells (doublecortin, DCX), neurons (Fox3), astrocytes (glial fibrillary acid protein, GFAP), oligodendrocytes (2',3'-cyclic-nucleotide 3'-phospodiesterase, CNPase), endothelial cells (rat endothelial cell antigen 1, RECA-1), microglia (ionized calcium-binding adapter molecule 1, Iba-1), as well as macrophage activation (CD206 for the M2 phenotype, CD86 for M1 phenotype) were used for analysis.

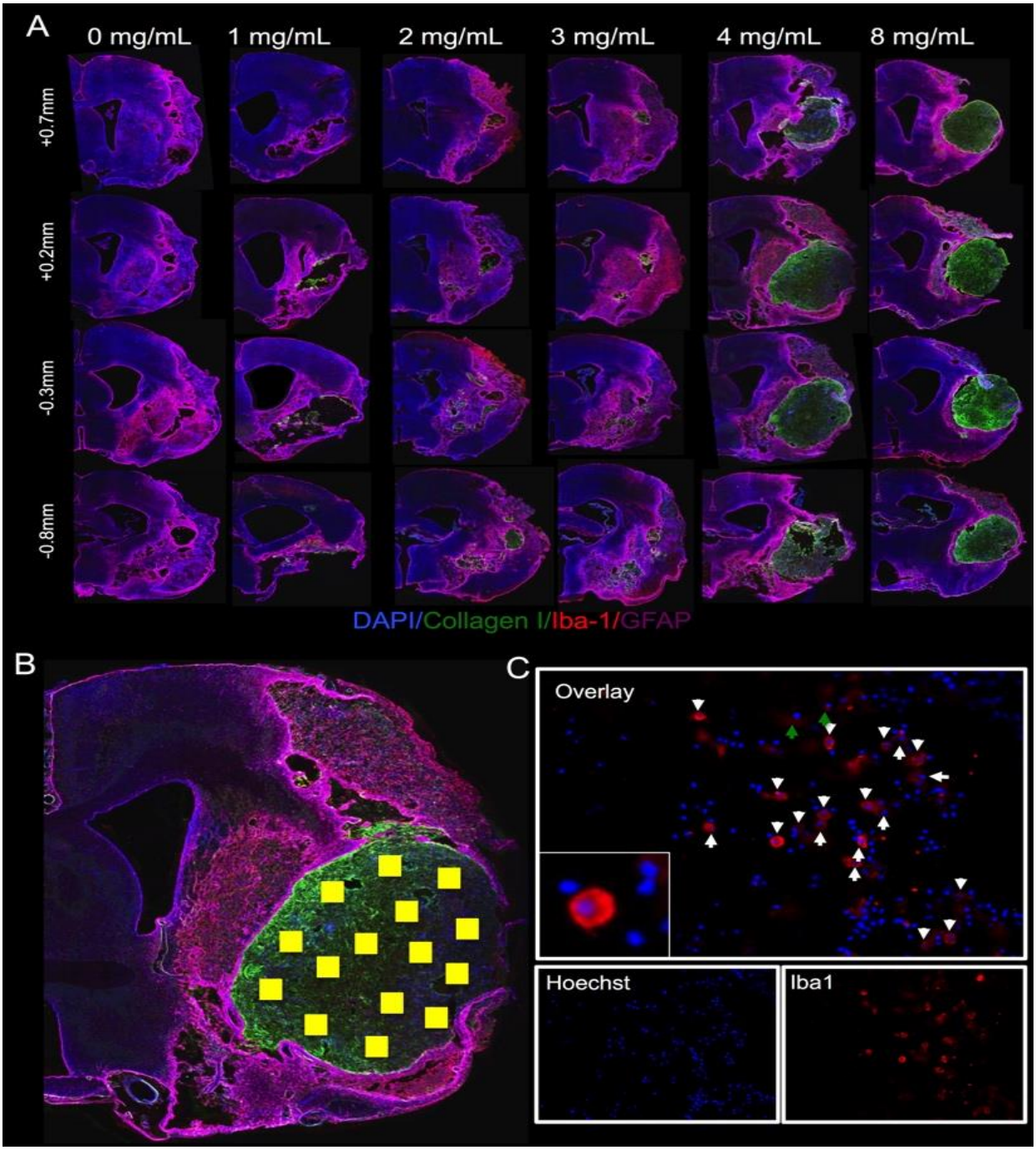

Figure 2.4. Concentration-dependent retention of ECM hydrogel in the lesion cavity.

(A) *Whole hemisphere images show the gelation and retention properties of the injected ECM hydrogel at different concentrations. Since the ECM contains high amounts of collagen I compared to the host brain tissue, it can be used for histological visualization of the injected material. A vehicle injection (0 mg/mL) of PBS indicated no collagen I detection inside the lesion*

cavity. At 1 and 2 mg/mL, the ECM material mostly permeated into the brain tissue, whereas at 3 mg/mL, hydrogel formed and was retained in the cavity with some permeation into the host tissue. At concentrations greater than 3 mg/mL, the ECM material shows gelation with little to no signs of permeation into the peri-infarct tissue, retaining both its morphology, as well as its shape. In order to accurately characterize the invading cells, multiple images were acquired inside the ECM material (as shown by the yellow boxes) ***(B)****. Once the images were acquired, manual counts of DAPI indicated the total number of cells in the field of view and co-staining with another marker (Iba-1 in this case) would result in characterization of the invading cells (as shown with white arrows)* ***(C)****.*

Although many mononuclear macrophages share histological markers, Iba-1 is a commonly used marker for brain microglia [151]. The phenotype of invading cells was determined by counting the number of cells positive for a given marker within a FOV (Figure 2C). Phenotypes were expressed as % of total cells present to account for differences in the number of invading cells.

2.2.8 Statistical analysis

Statistical analyses were performed in SPSS 17 for Mac (IBM) with significance set at $p<.05$. Specifically, a two-way ANOVA was used to compare cell invasion and the number of cells within each annulus, using a Bonferroni post-hoc test to validate significant comparisons. A one-way ANOVA with Bonferroni post-hoc testing was used to contrast the effects of ECM concentration on different cell phenotypes, as well as a comparison between lesion volumes and total cell invasion. The different ECM concentrations and the variance in MRI lesion volumes complied with a factorial design (also known as Design of Experiment, DoE) that is built on the foundation of analysis of variance by using

independent variables that allowed us to systematical determine their effect on measured data (i.e. the dependent variable), such as cell invasion, to generate contour plots (Minitab 8). These contour plots provided an overview of the entire experimental space of these variables allowing us to determine potential effects of intermediary concentrations or lesion volumes on the dependent variables. Graphs were drawn in Prism 6 (GraphPad) with data point representing the mean and bars reflecting the standard deviation.

2.3 RESULTS

2.3.1 Pre-gel viscosity and hydrogel stiffness

The rheological characteristics of the ECM hydrogel were determined before (10 °C) and after (37 °C) gelation was induced using a parallel plate rheometer. Before gelation, the viscosity of the 4 mg/mL ECM pre-gel was significantly ($p=0.001$) lower (0.084±0.008 Pa*s) than the 8 mg/mL ECM pre-gel (0.443±0.062 Pa*s) (**Figure 2.5.A**). The storage modulus G' and loss modulus G'' of the 4 and 8 mg/mL ECM gels changed sigmoidally over time after temperature was raised from 10°C to 37°C (**Figure 2.5.B**). At long times, the storage modulus at both concentrations far exceeded the loss modulus indicating substantially solid-like gels. The maximum storage modulus of the 8 mg/mL hydrogel (460.4±62.5 Pa) was significantly ($p\leq0.001$) higher than the 4 mg/mL hydrogel (76.6±10.4 Pa), as was the maximum loss modulus (66.4±9.3Pa, 11.0±1.5 Pa, $p=0.008$) (**Figure 2.5.C**). Half the maximum storage modulus ("50% gelation") marks the sharp increase in the storage modulus curve, and time to 50% gelation did not differ significantly between

the 4mg/mL (3.2±0.3 minutes) and 8mg/mL (3.0±0.5 minutes) groups (**Figure 2.5.D**). The fast gelation kinetics of the ECM hydrogel was further shown in that 15% of the final storage modulus was reached within 3-5 minutes for both gels (4 mg/mL in 3.9±0.5 minutes and 8 mg/mL in 4.4±0.5 minutes), and where final storage modulus is defined as the average storage modulus over the last 10 minutes of the time sweep test. The frequency sweep of the ECM hydrogel is shown for 4 mg/mL (**Figure 2.5.E**) and 8 mg/mL (**Figure 2.5.F**). Both moduli are only weakly dependent on frequency, and therefore the complex viscosity varies almost inversely with frequency, further confirming the predominantly solid-like nature of the gel.

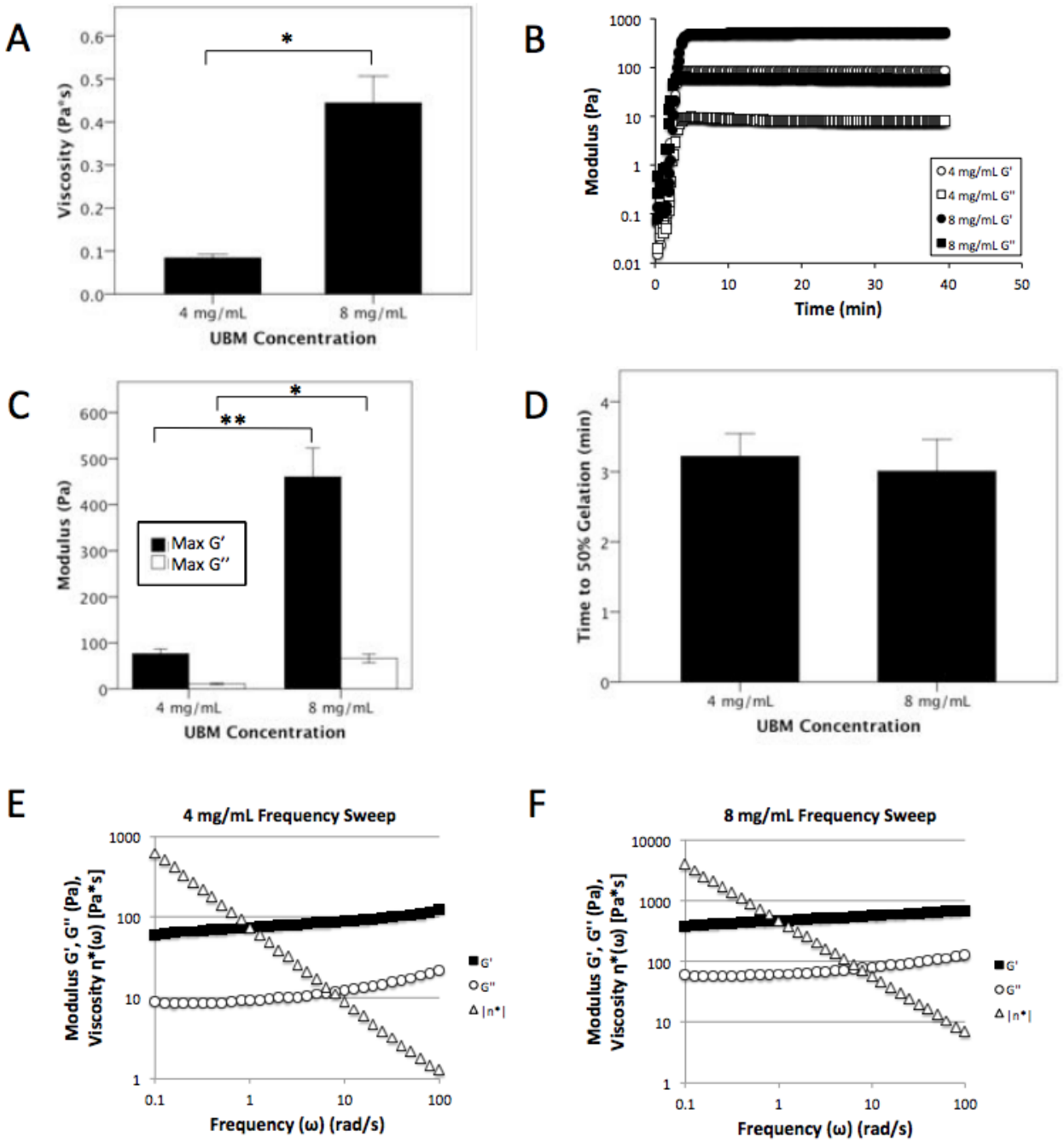

Figure 2.5. Rheological characterization of ECM hydrogels.

A. *Viscosity of the ECM pre-gel at 10 °C was measured by applying a constant shear stress of 1 Pa.* ***B****. Representative curves of the ECM hydrogel gelation kinetics show the storage and loss modulus increase sigmoidally over time. Temperature is rapidly raised from 10 °C to 37 °C, and a small 0.5% oscillatory strain at a frequency of 1 rad/s was applied.* ***C.*** *Maximum storage modulus*

and loss modulus of the ECM hydrogel after gelation was complete at 37°C. ***D.*** *Gelation time of the ECM hydrogels to 50% gelation, equal to 50% the maximum storage modulus.* ***E-F****. Representative graph of the storage modulus, loss modulus, and complex viscosity of the ECM hydrogels at 4mg/mL (E) and 8 mg/mL (F) plotted over angular frequencies on a log-log scale, measured at 37 °C by applying a small 0.5% oscillatory strain. *p≤0.01 **p≤0.001 (independent samples 2-sided t-test)*

Indeed, the storage and loss modulus of the 4mg/mL hydrogel was significantly lower than the 8 mg/mL hydrogel (p≤0.001) for the angular frequency range tested (0.1 -100 rad/s). Both 4 and 8 mg/ml hence produce stable hydrogels in the same amount of time, but differ in their pre-gel viscosity, as well as their substrate stiffness.

2.3.2 Injection-drainage affords efficient delivery of ECM hydrogel

The delivery of 8mg/ml hydrogel to the stroke cavity using a single injection point (i.e. no drainage) resulted in a 67% increase in intracranial pressure (ICP) with evidence of some material escaping the cranial vault past the needle used for injection. Using this no-drainage approach, it is hence difficult to control the exact concentration or volume of material being present within the cavity, as the injectate mixes with the fluid present in the cyst and it is not possible to control or monitor how much material seeps out. Injection with simultaneous drainage is hence proposed here as a superior method, where ICP only changed by 10% with excessive fluid from the cavity being displaced by the more dense injected biomaterial. Indeed, in this case, all excess fluid was drained extracranially through the additional cannula, rather than an uncontrolled escape along the injection needle. Importantly, in the injection-drainage condition, there was a negative correlation

(r=-0.98, p<.05) between lesion volume and change in ICP, i.e. the larger the volume of the lesion, the less change in ICP, due to a greater space for accommodating the hydrogel. The opposite trend was evident in the no drainage condition (r=0.97, p=0.07) with larger volume of injections leading to greater change in ICP. Although post-mortem (24hrs) there was no significant midline shift (2-5%) in either condition, drainage resulted in 10% less hemispheric volume shift compared to no drainage. The increase in ICP, as well as hemispheric volume shift, hence indicates that drainage reduces potentially adverse effects of intracerebral injections on brain tissue.

2.3.3 Histological detection of ECM hydrogel

A histologic visualization of the injected ECM material was used to investigate and validate the distribution and retention of material within the lesion cavity. As porcine (UBM-)ECM hydrogels contain a higher concentration of collagen I compared to brain tissue, a pig-specific mouse anti-collagen I antibody afforded the selective identification of the implanted hydrogel (**Figure 2.6.A**). In contrast, a non-specific rabbit anti-collagen I antibody detected both rat and pig collagen I. As ECM injection dramatically increased collagen I concentration, the exposure time used for image acquisition of the non-specific antibody can still selectively visualize the implanted materials (**Figure 2.6.B**). The non-specific rabbit anti-collagen I reliably stained host collagen I, as indicated by its localization in the basement membrane of host blood vessels and its peri-infarct localization in MCAo+vehicle animals. ECM also contains a variety of other molecules that putatively could serve for detection purposes inside the brain (**Figure 2.7**). ECM

contains notably high levels of collagen IV, which is readily detecting the injected material, but is also highly expressed in glial scar tissue in the peri-infarct region. The same applies to chondroitin sulfate, which is extensively present in the damaged hemisphere. Laminin also detects the injected material, but detection is not sufficiently specific as peri-infarct regions undergoing angiogenesis also express high levels. Although sensitivity is good for these markers, selectivity of ECM hydrogel visualization is poor. In contrast, Hyaluronic Acid contrasts sufficiently with host background and hence affords a specific macroscopic detection of the injected material akin to collagen I.

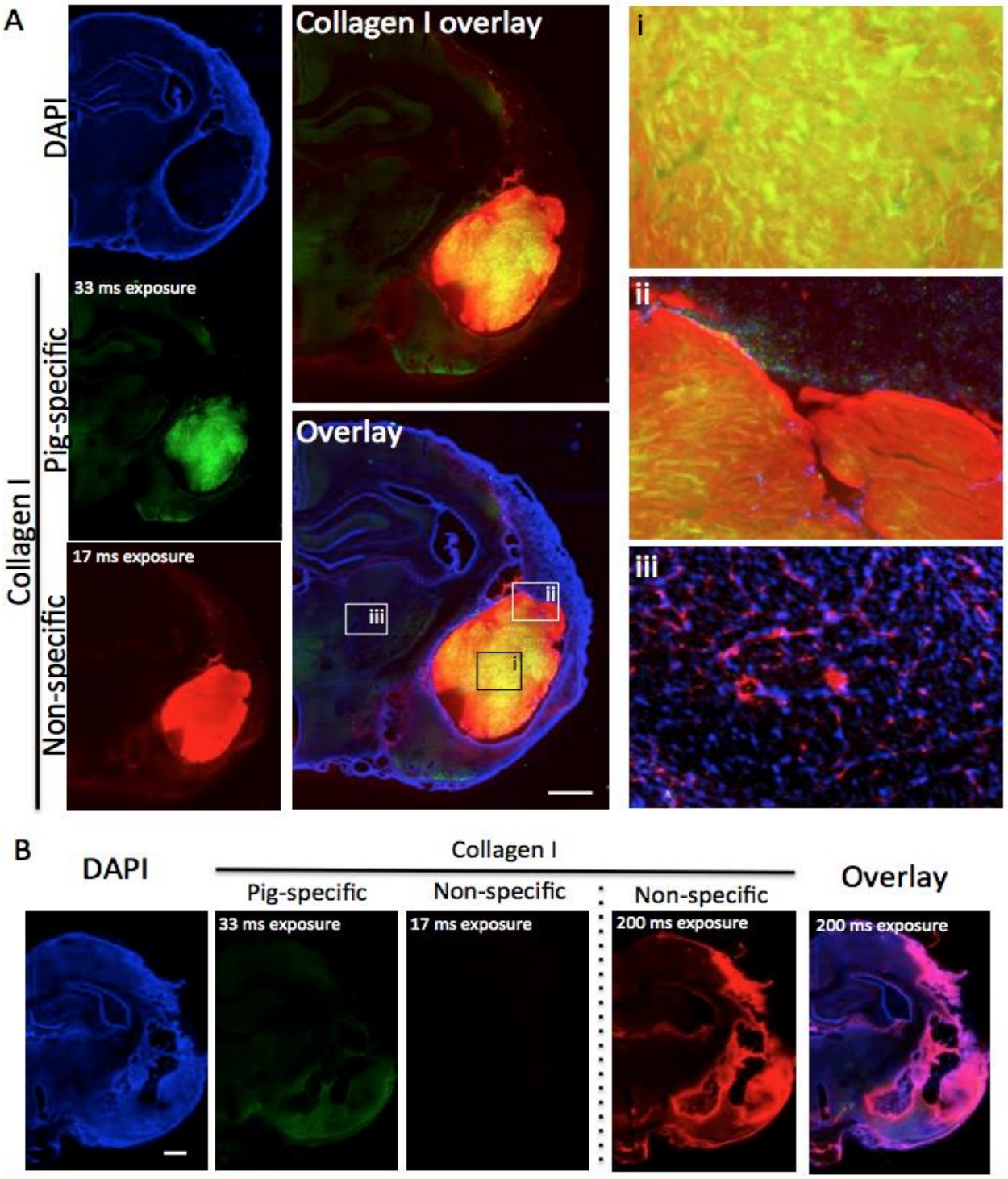

Figure 2.6. Detection of ECM hydrogel in the stroke cavity.

A*. The pig-specific collagen I antibody detects only the ECM hydrogel implanted into the stroke cavity, although there is some evidence of background autofluorescence and staining in damaged*

tissue. The non-specific collagen I antibody detects the implanted hydrogel with a very intense staining, but also stains host brain blood vessels as well as damaged tissue. The relatively high concentration of collagen I in the ECM hydrogel compared to the host brain is evidenced by the short exposure times required to acquire images. The core of the implant is detected equally by the pig-specific and the non-specific antibody, but there are difference in their staining pattern ***(i)****. Collagen I staining clearly allows a demarcation of the implant-host interface* ***(ii)****. Only the non-specific collagen I antibody detects rat collagen present in the basement membrane of host blood vessels in intact tissue* ***(iii)****.* ***B****. In a stroke brain injected with vehicle, there was no detection of pig-specific collagen I (only background fluorescence in the peri-infarct area). At the exposure time used for the ECM hydrogel (17ms) there was no detection of any fluorescence of the non-specific antibody, but at a longer exposure time (200ms), collagen I staining around the infarct cavity was evident. The pig-specific antibody can therefore be used to distinguish porcine-derived ECM implants versus rat host tissue with specific staining, but the ECM hydrogel can also be visualized macroscopically using the non-specific antibody by adjusting the exposure time for image acquisition.*

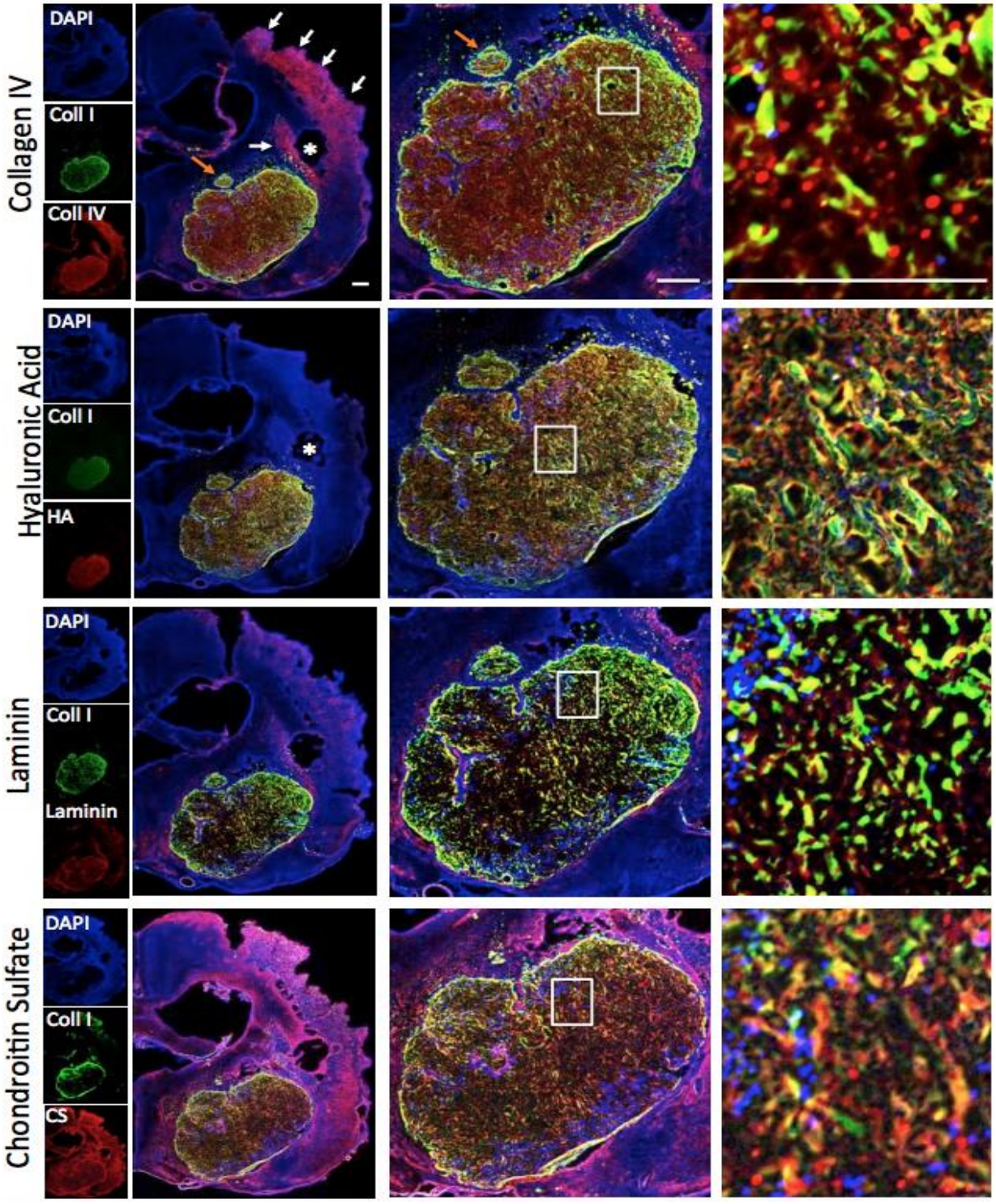

Figure 2.7. Detection of ECM hydrogel using ECM markers.

ECM contains a variety of molecules that can be detected using immunohistochemistry. The higher concentrations of molecules compared to brain tissue afford its detection using different

antibodies against collagen IV, Hyaluronic acid, laminin and chondroitin sulfate. It is evident here that ECM molecules associated with glial scarring (collagen IV, chondroitin sulfate) and angiogenesis (laminin) are also highly expressed in the peri-infarct area and hence not ideal for a selective detection of ECM hydrogel. However, hyaluronic acid also emerged as a potential alternative marker to collagen I, both of which are abundantly present with the (UBM-)ECM preparations compared to brain tissue.

2.3.4 Reliability of ECM hydrogel delivery

Using the injection-drainage approach, the delivery of ECM hydrogel (8mg/ml) to the stroke-induced lesion cavity successfully resulted in an extensive distribution of the biomaterial (as indicated by collagen I staining) throughout the lesion, while conforming to the topology of tissue loss (**Figure 2.8.A**). There was a good correspondence between pre-implantation MRI and post-mortem immunohistochemistry (**Figure 2.8.B**), indicating that the neurosurgical planning of the delivery location, as well as the volume were appropriate.

The formation of a hydrogel within the cavity at 8mg/ml further indicates that an appropriate concentration of injectate was delivered throughout the lesion. Gelation typically resulted in the retention of ECM within the area of tissue loss, rather than diffusion into the adjacent host brain tissue (**Figure 2.9.A**).

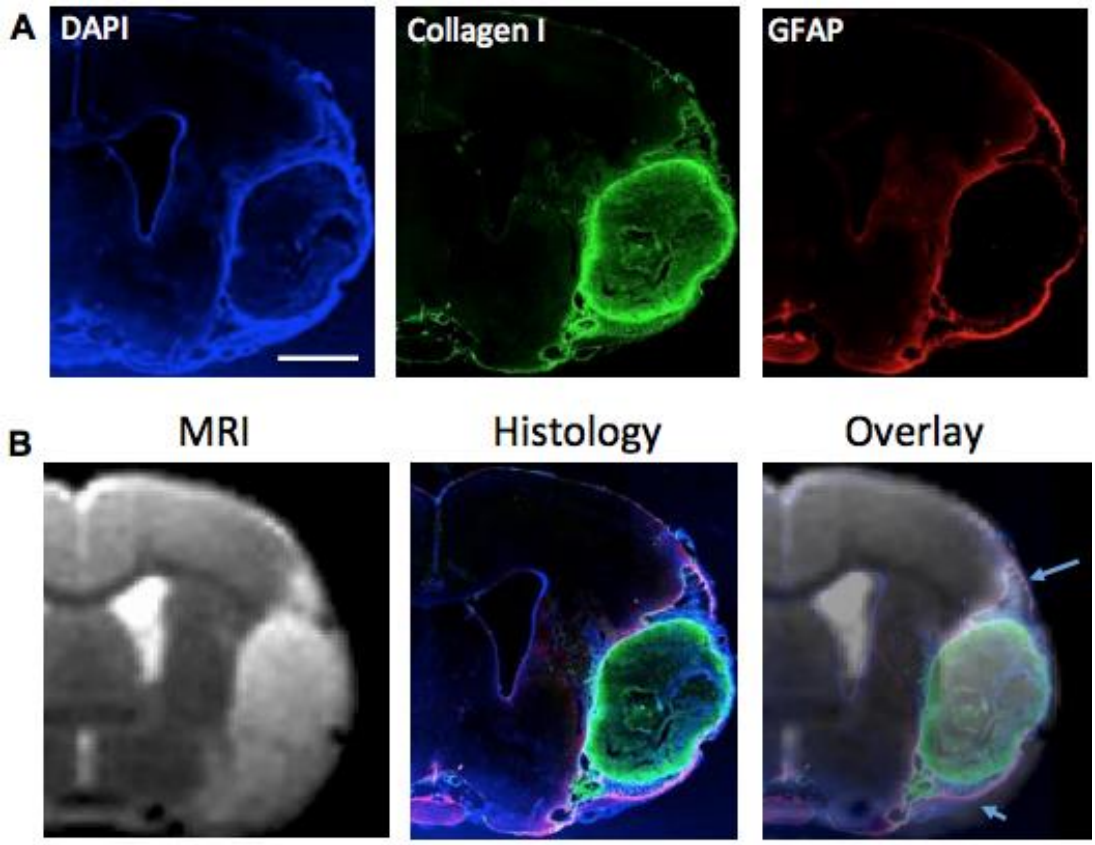

Figure 2.8. Correspondence between pre-implant MRI and post-mortem distribution of ECM hydrogel in the stroke cavity.

A*. Coverage of the lesion using this approach is demonstrated by immunohistochemistry 24 hours after injection. The lesion cavity is defined by glial scarring (GFAP), whereas the ECM hydrogel which contains high levels of collagen I can be detected using a collagen I antibody. It is remarkable that even within 24 hours there is cell invasion into the material from the host (DAPI).* ***B****. An overlay of the fluorescent histology images with the pre-implantation MRI indicates that indeed a good coverage of the cavity has been achieved. Nevertheless, it is noteworthy that the material did not completely cover the hyperintense area on the MRI, as tissue remnants were present in this region (blue arrows). This subtle difference is not evident based on the histologic assessment alone and indicates that further improvements in non-invasive imaging are required to better define microenvironments present within the infarct territory. However, if there is an overestimation of injection volume, the drainage of superfluous material will prevent a buildup in the cavity.*

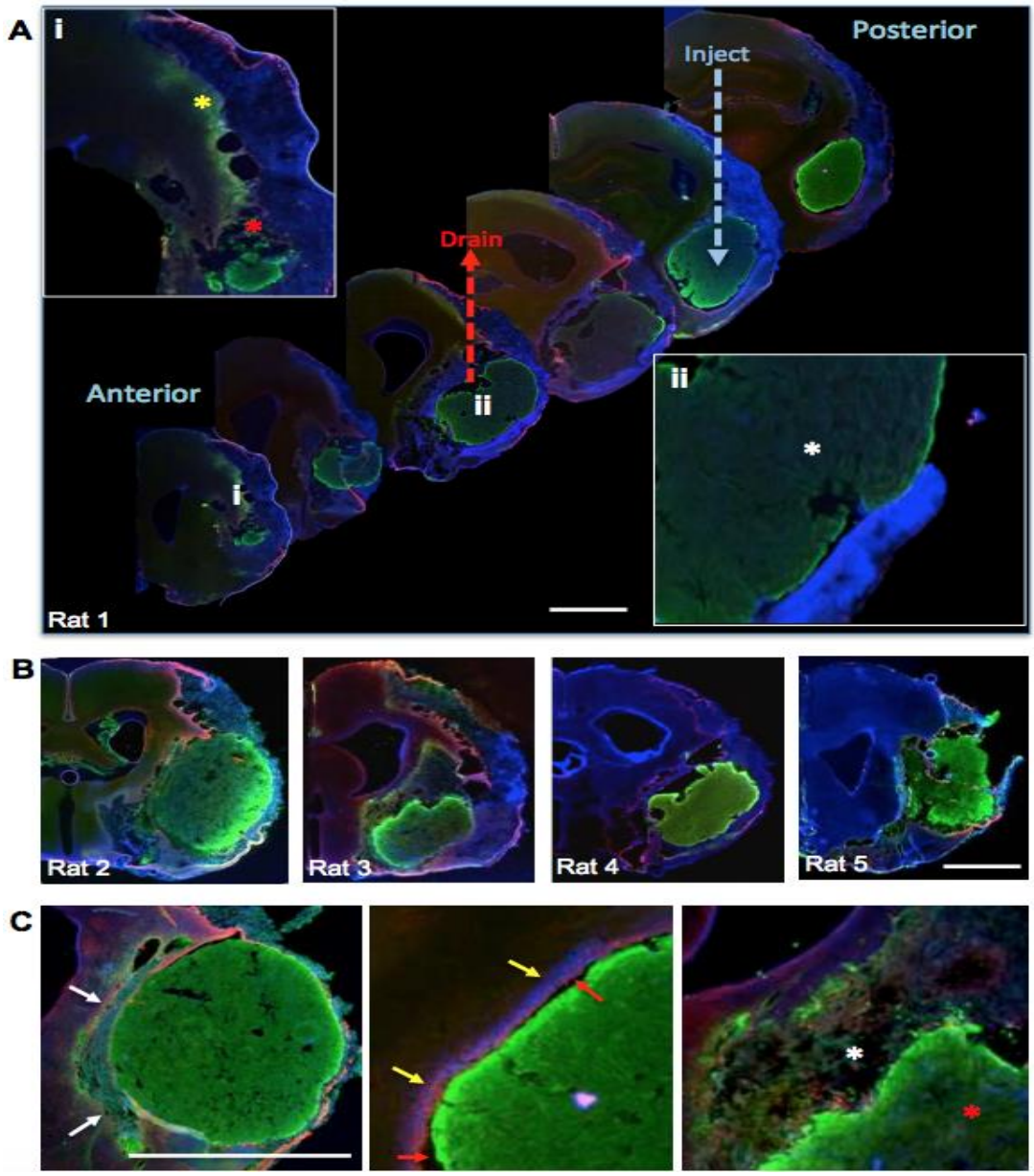

Figure 2.9. Anterior-posterior images covering the tissue cavity caused by middle cerebral artery occlusion. *A.* ***The ECM hydrogel (8mg/ml), as detected by collagen I staining (green), is fairly equally distributed throughout the cavity, defined by the lack of cells (DAPI staining in blue). Glial scarring (glial fibrillary acid protein in red) around the lesion cavity is also evident. The yellow dashed line indicates the point of injection, whereas the red dashed line depicts the position of the drainage cannula. In some areas, especially anteriorly*** *(i)*, ***some diffusion of ECM hydrogel into the host brain was evident (yellow *), whereas in in other areas (red *), small "particulates" of ECM were present within non-***

gelled areas of the cavity. A lack of hydrogel in some edge regions (white *) of the host-biomaterial interface was also evident indicating that some further optimization (e.g. speed of injection) of biomaterial distribution within the lesion can further improve coverage *(ii).* ***B. The described approach produces fairly consistent coverage of the cavity, as can be seen in a further 4 examples.*** *C.* ***Still, further challenges for intracerebral delivery are apparent. Notably, the fragile peri-infarct tissue can be impacted by large volume injections of a high concentration of material (white arrows), whereas a denser material could also create a "clump" of material, leaving voids between host and material (red arrows), while a glial scar is forming (yellow arrows). By focusing on the tissue cavity, the peri-infarct tissue that is severely damaged (white *), but not lost, is not receiving biomaterial (red *). These aspects further highlight the importance of determining appropriate concentrations and speed of delivery to potentially further improve the delivery of biomaterials to the damaged brain.***

Nevertheless, in small areas at the edge of the cavity, ECM material could be found in the host brain tissue where it gelled (**Figure 2.9.A i**). There was no evidence of additional glial scarring in these regions. It is also worth noting that small hydrogel accumulations were evident in a few edge regions, where the gel did not completely replace the liquefied necrotic debris. Although the hydrogel conformed to the lesion topology, it is important to note that the 8mg/ml ECM hydrogel was mostly distinct among the different ECM concentrations tested and did not invade adjacent brain tissue, with glial scarring being evident around most of the cavity. A small "bubble" without ECM hydrogel can occur (**Figure 2.9.A ii**) if the drainage point is not at the most dorsal part of the cavity. However, this approach is very reproducible across different lesion sizes and topology (**Figure 2.9.B**). Rheologic and turbidimetric characteristics of the biomaterial will also influence intracerebral distribution. For instance, a faster and stiffer polymerization in the cavity can displace small tissue fragments to the periphery of the cavity or provide a sharply defined

edge between ECM hydrogel and host tissue (**Figure 2.9.C**). Gelation properties defined by the concentration of the material therefore also define the interface with the host brain.

2.3.5 Concentration-dependent retention of ECM in stroke cavity

Using the injection-drainage method, it is possible to deliver a specific volume and concentration of ECM to the lesion cavity and determine the effect of these variables upon its distribution, interface with the host brain, as well as its retention within the cavity. Indeed, concentrations of <3mg/ml did not form a robust enough gel within the lesion cavity to afford retention, but rather showed diffusion of ECM into the adjacent host brain (**Figure 2.10.A**). Diffusion of ECM into the peri-infarct tissue results in a uniform extracellular distribution akin to tissue characteristics, such as striosomes, but is not associated with the basement membranes of blood vessels (**Figure 2.10.B**). It is likely that some injected ECM material remained within the cavity, but this could not be determined by histologic methods. At 2 mg/ml, some small ECM accumulations within the cavity were evident (range 3-26% coverage). At 3 mg/ml, diffusion into the host brain, as well as retention within the cavity, were evident (Figure 8C) with a more extensive coverage than the cavity (98-117% coverage). At concentrations >3mg/ml gelation and retention within the cavity occurred with little to no diffusion into the host brain (84-96%).

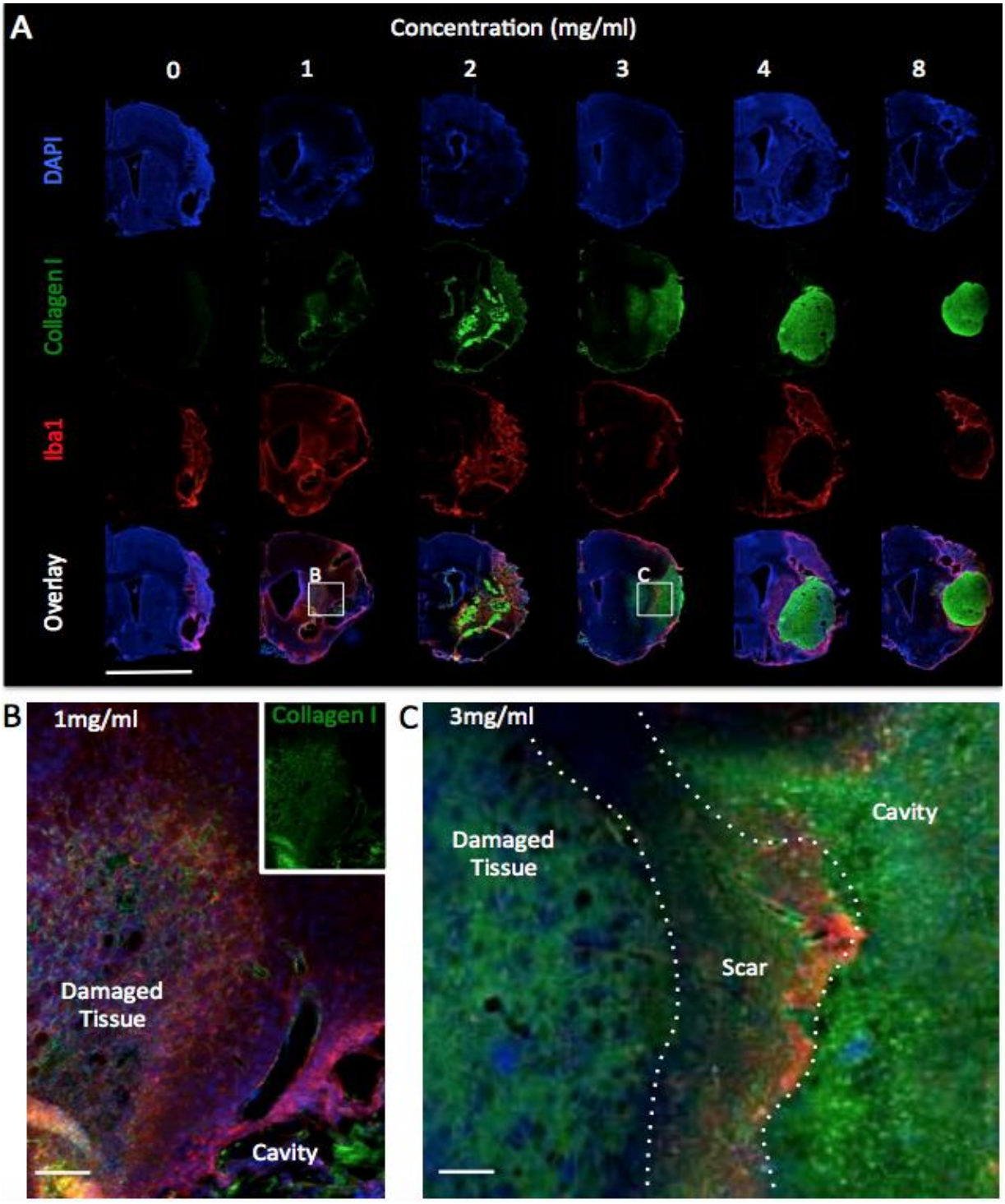

Figure 2.10. Concentration-dependent retention of ECM hydrogel in the lesion cavity.

A*. ECM hydrogel injection will only be retained within the lesion cavity if sufficient collagen I is present to afford gelation. Using the injection-drainage approach it is possible to inject accurate concentration of ECM into the cavity and determine retention the ECM hydrogel. A vehicle*

injection (0mg/ml) of PBS indicated no collagen I-dependent detection (33ms) of material inside the lesion cavity or the host brain. At 1 and 2mg/ml ECM material mostly dissipated into the host brain, whereas at 3 mg/ml, ECM hydrogel was formed and retained within the cavity with some material gelling in the peri-infarct tissue. Higher than 3mg/ml concentration resulted in a gelation within the lesion cavity and little to no ECM hydrogel diffusion into adjacent host tissue. ***B****. At 1mg/ml ECM injection, the injected material was only visible in the peri-infarct area. The pattern of distribution suggests diffusion from the cavity. However, it is likely that some material was still present within the cavity and was lost upon sectioning due to a lack of structure (i.e. no gelation).* ***C****. At 3mg/ml, gelation within the cavity occurred and this material was retained during sectioning, but it is also evident that some injected ECM material diffused into the damaged peri-infarct tissue potentially through the glial scar. Based on signal intensity it is also possible to see a clear difference in collagen I content between 1 and 3mg/ml. It is therefore important to note that not only is there a difference in "inductive" material being delivered, but the structural (i.e. gelation) properties of the ECM are also concentration dependent.*

2.3.6 Host tissue-ECM interface

Injection of ECM precursor gel into the lesion cavity resulted in gelation of material at concentrations >3 mg/mL. This *in situ* gelation resulted in the creation of an interface between the ECM hydrogel and the host tissue (**Figure 2.11**). However, stroke created a complex array of microenvironments of which cavitation is the most severe form of damage. Adjacent to the cavity, tissues void of neuronal cells and undergoing astrocytosis can be found. In some cases, an ongoing macrophage response can be seen that clears cellular debris and eventually removes extracellular matrix (i.e. the process of tissue cavitation). At concentrations >3 mg/mL a clear interface between the hydrogel and host tissue was evident and peri-cavity cortex was often severely damaged. ECM gel precursor in some instances permeated into these areas.

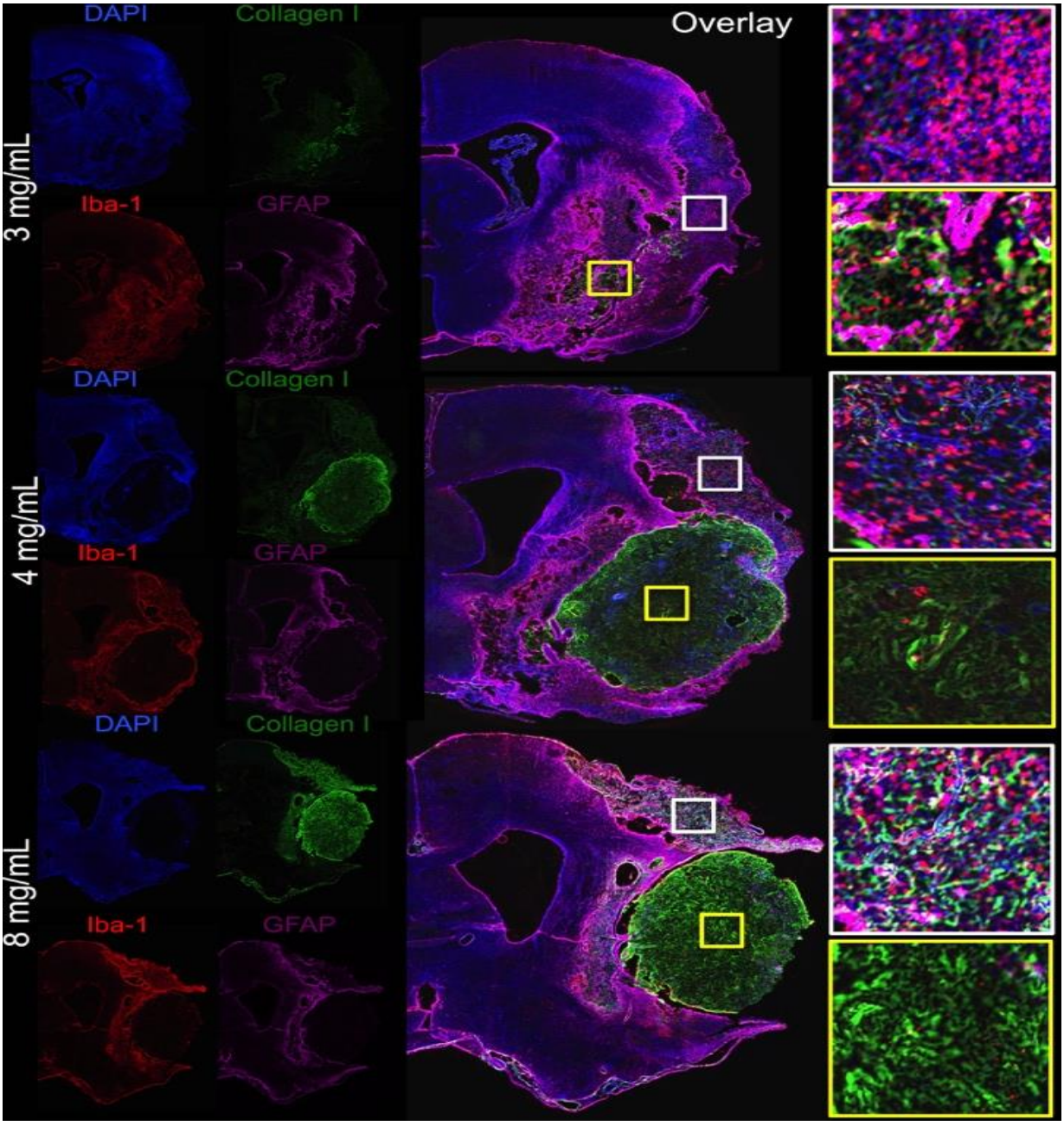

Figure 2.11. Interface between ECM hydrogel and host tissue.

Concentrations >3 mg/mL resulted in an in situ gelation and retention within the lesion cavity producing an interface where the ECM hydrogel contacts with the host brain tissue. It is important

to note two typical microenvironments within which ECM material can be found in these stroke-damaged brains: 1. the lesion cavity (yellow boxes); 2. severely damaged tissue that is not part of the lesion core (white boxes). Higher concentrations of 4 and 8 mg/mL typically completely filled the cavity, but also displaced some damaged tissue. The 3 mg/mL also permeated into damaged tissue directly adjacent to the cavity. In areas of cortical tissue damage, some permeation of ECM could be seen. These areas were mostly void of neurons, but significant amounts of microglia were present directly interacting with some of the permeating ECM.

Microglia, macrophages and astrocytes can be found in large abundance around the lesion cavity and in areas of tissue damage. With 0 mg/mL, a high cellular density of microglia and astrocytes can be seen around the lesion cavity forming a scar, i.e. glia limitans, that defines the boundary between tissue and cavity (**Figure 2.12**). This interface is somewhat preserved at the lower concentration of ECM precursor gel (1 & 2 mg/mL), with some ECM forming small patches of gel at the tissue boundary agglomerating around tissue remnants within the cavity. Small numbers of microglia and astrocytes can be found within this injected ECM. At higher concentrations, where gelation of ECM occurred within the cavity, a more distinct interface with host tissue can be identified. A significant infiltration of host cells was observed, especially in areas where cavitation was small.

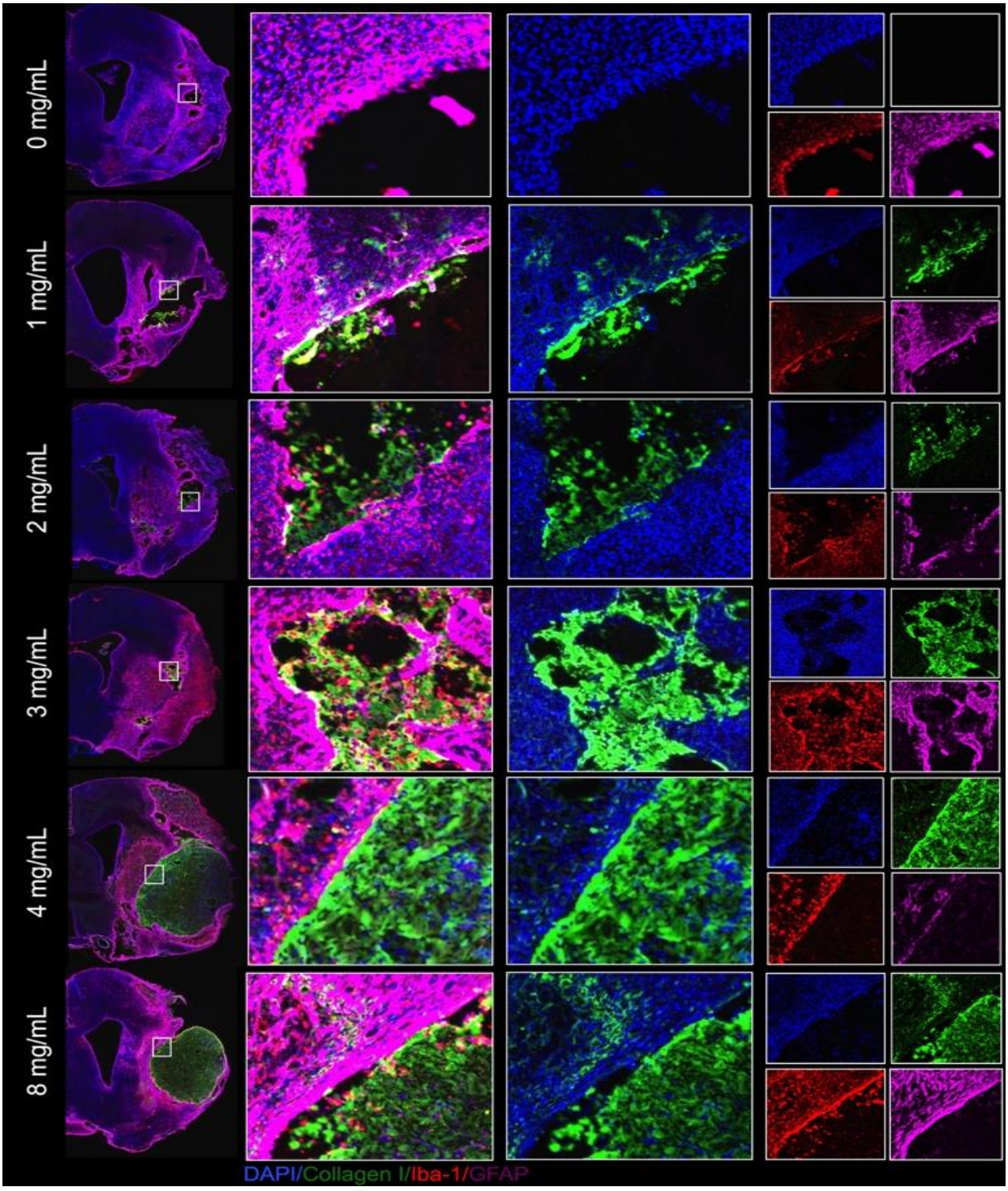

Figure 2.12. Gelation and permeation of the ECM material at the host tissue interface.

At 0 mg/mL (PBS injection), no exogenous collagen I is detected inside the lesion cavity (as delineated by Iba-1 staining for microglia and GFAP for astrocytes). At 1 and 2 mg/mL, injected

ECM material shows poor retention inside the lesion cavity, as significant diffusion of the ECM material into the peri-infarct area can be seen. At 3 mg/mL, the ECM material shows hydrogel formation and retention inside the cavity, with some diffusion into the surrounding tissue. At 4 and 8 mg/mL, a clear boundary can be seen at the interface between the host tissue and the ECM hydrogel. Concentrations >3 mg/mL resulted in complete gelation and retention of the hydrogel with minimal to no diffusion into the host tissue. The predominant cell phenotypes surrounding all cavities consist of microglia and astrocytes with evidence of cell invasion of these host cells into the injected material at all concentrations.

At concentrations of 4 and 8 mg/mL, a well-defined delineation between ECM hydrogel and tissue can be observed, but host cell invasion was also evident.

2.3.7 ECM hydrogel cell infiltration

Both structural support and inductive cues are necessary for cells to migrate into the ECM biomaterial. Where there is a close interface between ECM hydrogel and the host tissue (**Figure 2.13.A**), cells infiltrated the material and migrated inward. Host cell infiltration was also observed across small gaps between the ECM hydrogel and host tissue (**Figure 2.13.B**). However, these gaps are potentially artifacts of a differential fixation of tissue and hydrogel. Cell infiltration often followed a chain-like path that trailed channels within the collagen I staining found in the ECM hydrogel.

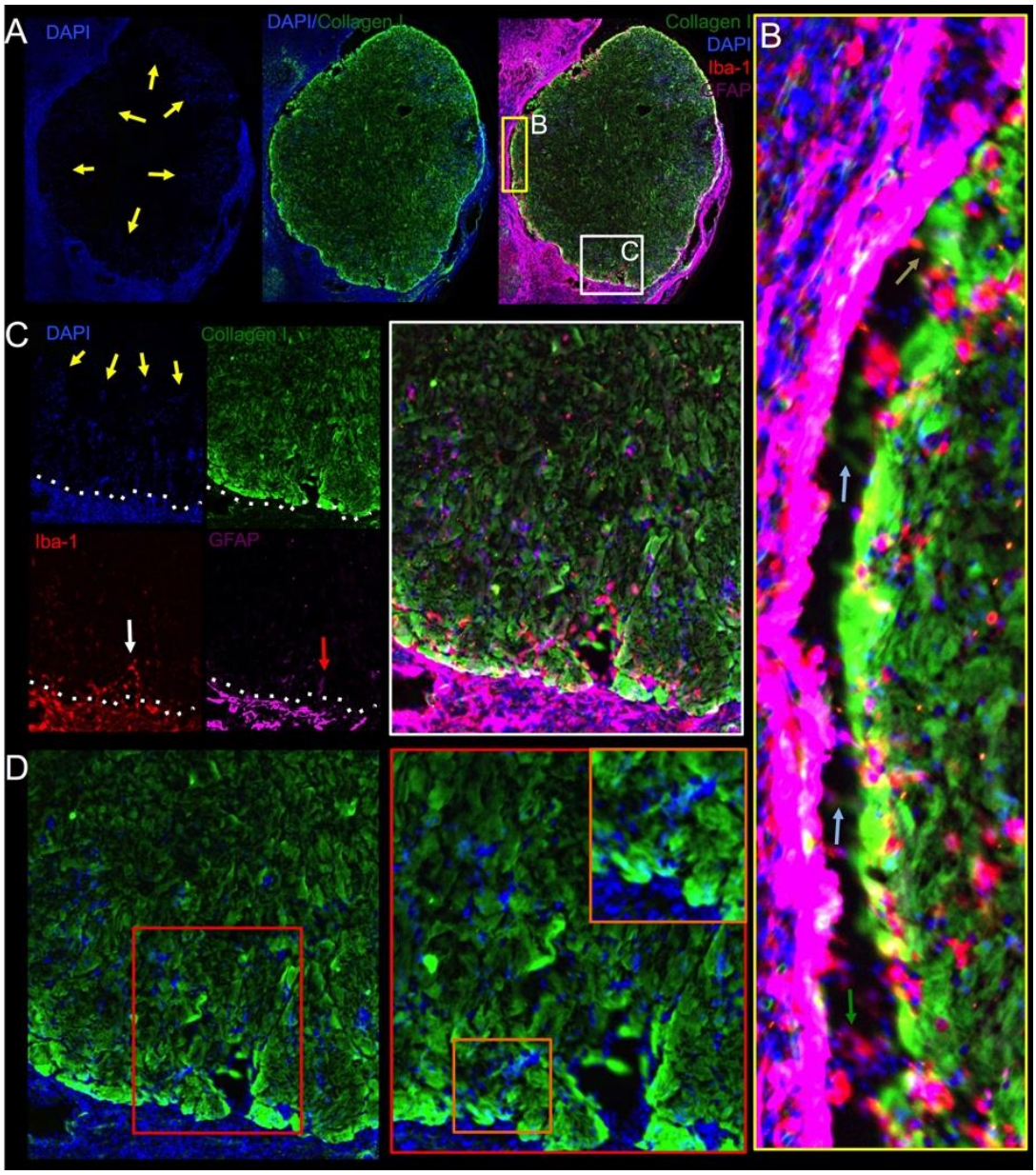

Figure 2.13. Patterns of cell invasion.

*A microscopic view of the lesion interface with the ECM hydrogel (collagen I+ area) indicates a higher density of DAPI+ cells surrounding the biomaterial with evidence of a concentric invasion of host cells (yellow arrows) into the acellular material. The predominant cellular phenotypes surrounding the ECM hydrogel, forming the glia limitans, are astrocytes (GFAP+ cells) and microglia (Iba-1+ cells) The injection-drainage approach produces a consistent coverage of the cavity **(A)**. A magnified view of the interface between the host tissue and the ECM hydrogel reveals invading microglia migrating from the host tissue to the hydrogel (green arrow). A collagen*

I negative staining area in some edge regions of the host-biomaterial interface was also evident (blue arrows), but this did not affect the invasion of some cells, although a close interface between host and hydrogel dramatically facilitated cell invasion (brown arrow) ***(B)****. In order for the cells to migrate into the damaged tissue, a structural support for the attachment and survival of the cells is favorable. Most commonly microglia are the cells that infiltrated the furthest into the hydrogel, whereas astrocytes were mostly present closer to the host tissue* ***(C).*** *Indeed, a guided chain-like migration along collagen I negative channels can be seen into the hydrogel, potentially indicating that hydrogel ultrastructure is also a contributing factor for initial cell invasion* ***(D)****.*

Commonly the cells with the deepest infiltration distance were microglia (Iba-1+), with astrocytes (GFAP+) being found closer to host tissue (**Figure 2.13.C**).

The availability of these cells at the tissue interface (i.e., the glial scar) may position these cells in a prime location for this acute (24 hrs) invasion. Infiltrating cells may form pathways along which other cells pursue their infiltration (**Figure 2.13.D**). It is unclear, however, if some cells remain in place or if all cells continue infiltration towards the center of mass (and beyond).

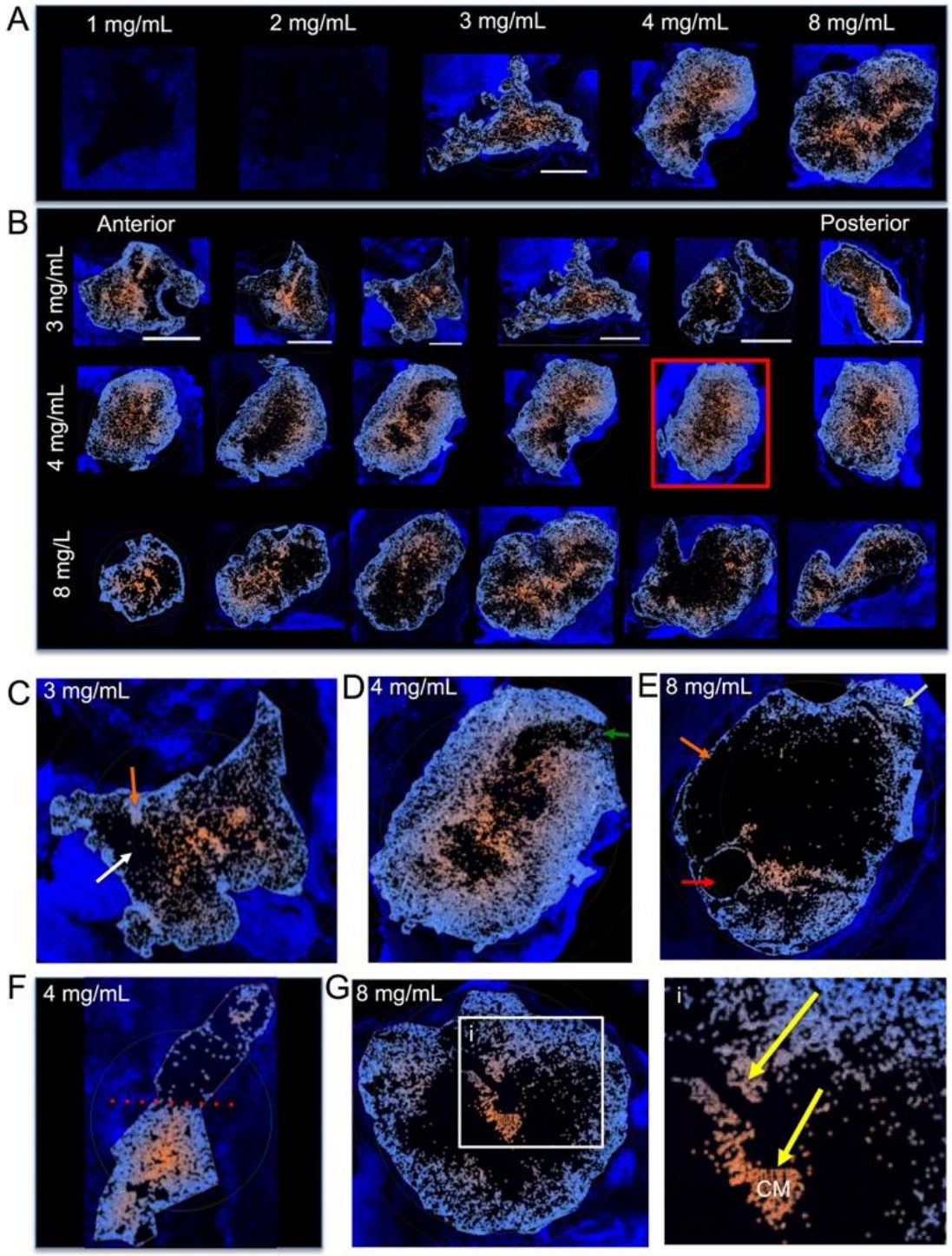

Figure 2.14. Cell invasion – Colorimetric maps.

Identification and labeling of cell invasion at different concentrations using Lux64R based on DAPI staining within a collagen I outline ROI. Using a colorimetric method ranging from light blue

(closest to the host boundary) to orange (furthest from host boundary), maps of cell invasion were created to highlight differences between ECM concentrations ***(A)****. These maps also allowed us to inspect the anterior-posterior invasion of cells within the ECM hydrogel. It was evident here that the smaller ECM hydrogel areas found at the poles of the cavity saw a more complete coverage of cell invasion compared to more central slices which occupied a large area* ***(B)****. Invasion typically followed a concentric pattern that saw cells migrating to the center of mass of the injected ECM hydrogel, in some cases leading to very homogenous distribution of host cells through the material (red box). Nevertheless, important qualitative differences in cell invasion were also noted on these colorimetric maps. Cell invasion in some instance followed a very densely packed channel with blind spots within the material hardly seeing any invasion* ***(C)****. In other cases, there was a no significant invasion (green arrow) in a very restricted region suggesting that potential host factors, such as scarring can influence invasion* ***(D).*** *Indeed, the varied pattern of invasion or the lack therefore indicates that technical factors, such as an air bubble (red arrow), as well as poor interface with host tissue (orange arrow) influence cell invasion, even though other areas of the gel are efficiently invaded (light green arrow)* ***(E)****. The differential patterns of cell invasion into the same hydrogel hence strongly suggest that the host microenvironment surround the ECM material has a significant influence on cell invasion* ***(F)****. Nevertheless even if there are blind spots within the hydrogel and areas of poor cell invasion at the host-gel interface, invading cells will find channels (yellow arrows) to move towards the center of mass* ***(i)*** *and are likely to continue their migration in the absence of encountering other cells* ***(G)****. Scale bars are 5000 µm.*

To illustrate the patterns of cell invasion, heat maps of individual nuclei and their distance of invasion were generated. It was evident here that lower concentrations, where no gelation and no significant retention of ECM material occurred, very few cells were present in the ECM material. Concentrations >3 mg/mL of ECM hydrogel resulted in large numbers of infiltrating cells (**Figure 2.14.A**). A comparison of anterior-posterior colorimetric maps indicated that cavity shape influenced cell invasion, with shorter distances between host tissue boundaries being more completely covered compared to greater distances, as found in the central slice of the cavity (**Figure 2.14.B**). Nevertheless,

this acute 24 hours infiltration pattern resulted in some cases with complete invasion of the material. A good interface between host and ECM material in itself is not the only determinant in the distance of infiltration. In some case, there was evidence of infiltration into the material, but patches within the ECM hydrogel were not uniformly infiltrated ("blind spots"), whereas other adjacent patches showed a strong infiltration (**Figure 2.14.C**). These "blind" patches were also evident where there was a good interface between host-ECM (**Figure 2.14.D**). Other cases showed that the adjacent host tissue might not respond to the ECM (**Figure 2.14.E & 2.14.F**). In some cases, small channels of cells migrated towards the center of mass without there being an equal distribution of cells throughout the material (**Figure 2.14.G**). Preferential routes of colonization of the ECM are hence potentially important considerations in how host cells invade the material (**Figure 2.14.G i**).

To provide a quantitative comparison of cell invasion, the number of cells contained in concentric 25 µm from the host tissue edge to the center of mass of the ECM hydrogel were plotted to reveal total cell invasion for each concentration. The highest number of invading cells was found with 8 mg/mL (average of 366,280 cells), followed by a similar amount of cells at 4 mg/mL, with significantly fewer cells invading at 3 mg/mL ($p<.05$). There were very few cells invading the cavity in concentrations <3 mg/mL and none in the 0 mg/mL (as there was no identifiable ECM material present for invasion) ($p<.001$). The distance of invasion within 24 hours revealed cells invading the 8 mg/mL ECM hydrogel by >1500 µm of which >5500 cells were within the first 25 µm of ECM hydrogel (**Figure 2.15.A**). A cellular infiltration speed of 62.5 µm/hr can hence be calculated. The degree and distance of cells infiltrating at 3 mg/mL was markedly less

than at 4 or 8 mg/mL ($p<.01$). Indeed, one animal showed very little infiltration at 3 mg/mL, but another showed an infiltration equivalent to those at higher concentrations (**Figure 2.15.B**).

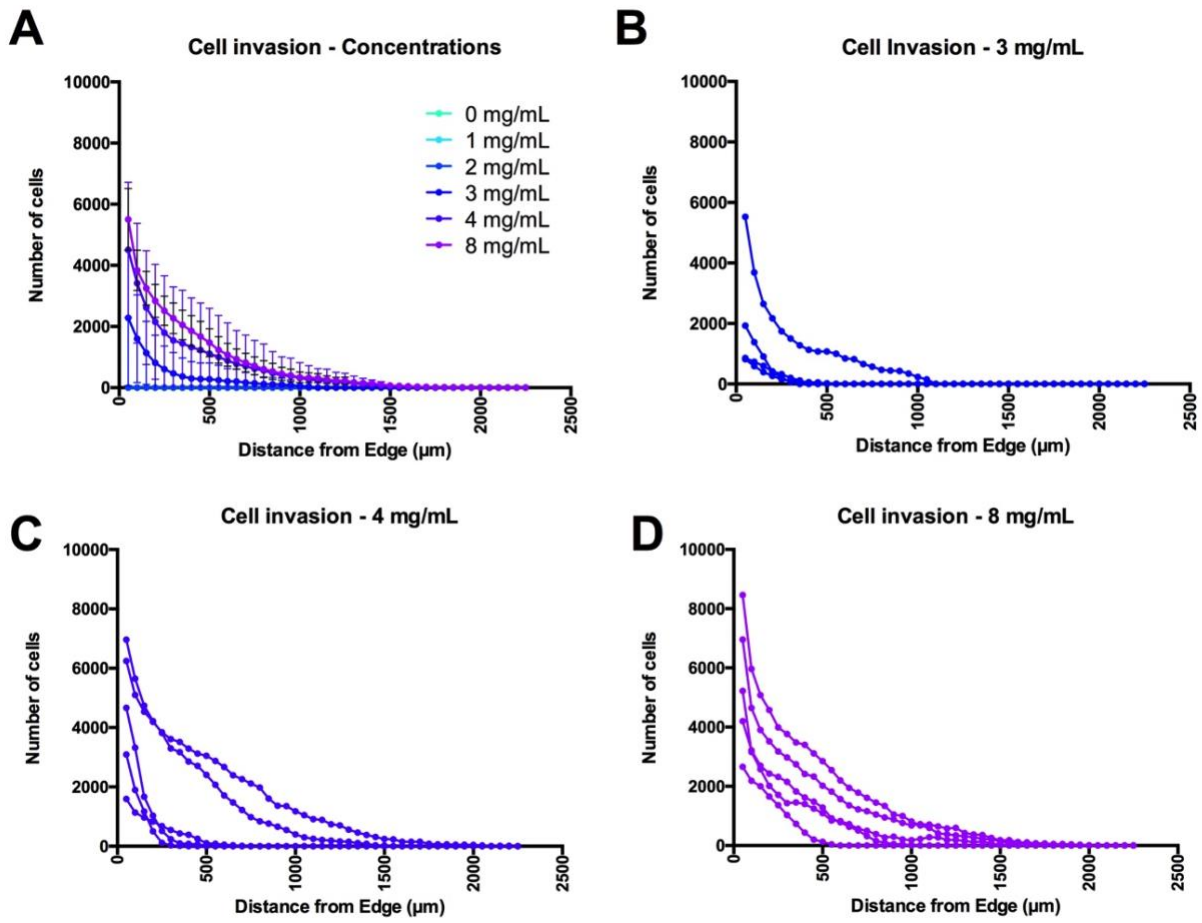

Figure 2.15. Cell invasion – Quantification.

(A) *Quantification of the cell infiltration into the infarct cavity afforded a comparison of all ECM concentration (mean±standard deviation) to determine how many cells invaded each 25 µm concentric circle from the center of the mass, as well as the total distance of invasion in relation to the ECM's interface with host tissue. Mapping of individual animals revealed a spread of cell invasion reflecting difference in the interface between host and ECM hydrogel, as well as ECM concentration for 3 mg/mL* ***(B)****, 4 mg/mL* ***(C)*** *and 8 mg/mL* ***(D)****.*

Also at 4 mg/mL, some variability in the degree and distance of cell infiltration was observed between different animals (**Figure 2.15.C**), further highlighting that factors beyond the concentration of the ECM and its gelation within the cavity influence cell invasion. The 8 mg/mL concentration performed the most consistently with all animals showing a good infiltration of cells (**Figure 2.15.D**), possibly reflecting a mass effect that this concentration exerts on host tissue, creating a more consistent and well defined interface.

2.3.8 Lesion volume and ECM concentration influence cell invasion

Although it is evident that concentration is a major determinant of cell invasion, lesion volume is also likely to be a major contributing variable. Indeed, all conditions, in which there was good retention of material within the lesion cavity (>3 mg/mL), showed a relationship between the size of defect and the number and distance of cells invading ($r>0.8$ for both). The larger the deficit (and hence the larger injected volume of ECM), the greater the number of cells that infiltrated the material and the greater the distance of infiltration. At lower concentrations, no relationship was evident, as insufficient material was available to warrant significant cell invasion.

To determine how different concentrations of ECM influence cell invasion, while accounting for differences in lesion volume, a contour plot was created and showed a more complex relationship between these factors (**Figure 2.16.A**). Concentrations <5 mg/mL, showed a poor invasion within 24 hours, apart for lesion volumes of 180-220 µL. A peak invasion of cells was observed with an 8 mg/mL concentration of ECM and a narrow lesion volume of 140-150 µL. Although total numbers of invading cells is an important indicator of inductive potential of ECM, larger lesions have more space for

greater numbers of cells to invade. Determination of cell density (i.e. invaded cells/µL volume) can mitigate this issue and provide a more accurate description of repopulation, but potentially can be higher in smaller lesions, as there is less space to fill (**Figure 2.16.B**).

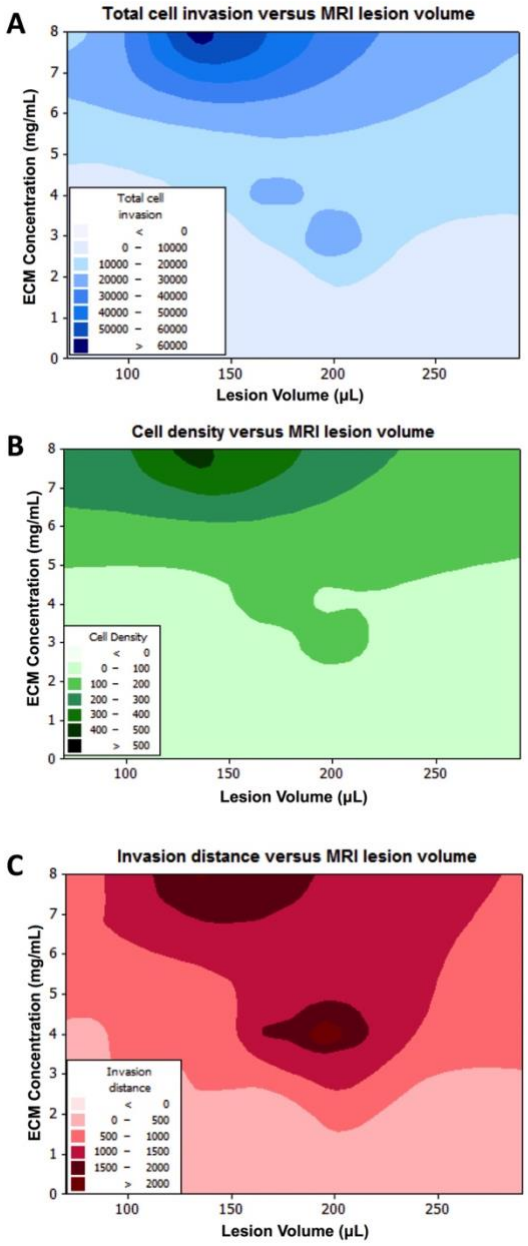

Figure 2.16. Contour plots.

*To determine an interaction between ECM concentration and lesion volume on the number of cells invading the ECM **(A)**, cell density within the ECM material **(B)**, as well as the distance of cell invasion **(C)**, contour plots were generated to illustrate which combinations would be the most and least combinations.*

Nevertheless, the overall interaction between ECM concentration and lesion volume was very similar between total cell invasion and cell density, with concentrations of <5 mg/mL having the lowest cell density per area of ECM, apart of the lesion volumes of 180-220 µL, where cell density was slightly elevated for concentrations as low as 3 mg/mL. Higher cell density per area of ECM was found with concentrations >6.5 mg/mL and lesion volumes <240 µL. A peak acute cell density of >500 cells/µL was also associated with an 8 mg/mL concentration and a narrow lesion volume of 140-150 µL.

Another factor affected by ECM concentration and lesion volume is the distance of cell infiltration. A simple correlational analysis indicated a very strong correlation between the lesion volume and the distance of cell infiltration. The distance was very similar for 3, 4 and 8 mg/mL (**Table 2**).

Table 2. Spearman correlations between MR volume and host cell invasion

	Lesion Volume			
	3 mg/mL	4 mg/mL	8 mg/mL	Combined
Invasion	r=0.8181 (p=0.0910)	r=0.8303 (p<0.05)	r=0.8793 (p<0.05)	r=0.55 (p<0.05)
Distance	r=0.87 (p=0.06)	r=0.92 (p<0.05)	r=0.94 (p<0.05)	r=0.61 (p<0.01)

Cell invasion distance was also strongly correlated with total cell infiltration for 3 mg/mL ($r=0.90$, $p<.05$), 4 mg/mL ($r=0.84$, $p=0.07$), and 8 mg/mL ($r=0.97$, $p<.01$), hence indicating a close relationship and interdependence between these different factors. A contour plot further highlighted this relationship (**Figure 2.16.C**), indicating that a concentration of >3 mg/mL is required for any infiltration to occur. Interestingly again, two separate peak spots for cell infiltration >2000 µm occurred, with larger lesions of 180-220 µL requiring lower ECM concentrations (4-5 mg/mL) and smaller lesions of 120-180 µL requiring a higher ECM concentration (>7 mg/mL).

2.3.9 Phenotypic characterization of cell infiltration

Considering the rapid infiltration of a large number of cells, it is essential to determine the phenotypes of the cells, as well as their participation in the remodeling and repopulation process. Indeed, the chain-like migration of cells along certain tracks within the injected ECM suggests that certain pioneering cells pave the way for others to follow.

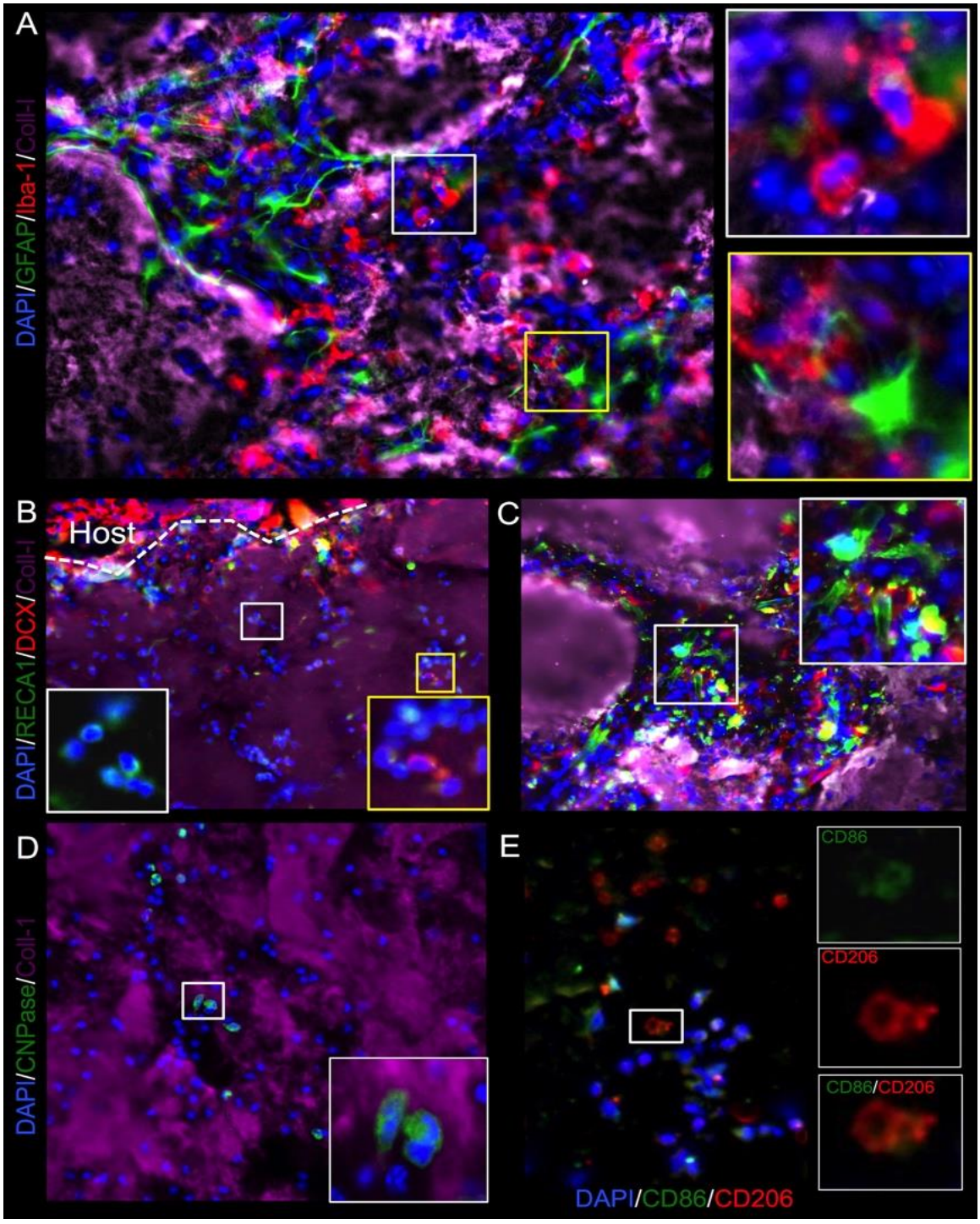

Figure 2.17. Cell invasion – phenotypic characterization.

Phenotypic characterization of cell invasion into injected ECM (collagen I+ area) was focused on cell phenotypes found in the brain: neural progenitors as revealed by doublecortin (DCX+), oligodendocytes (CNPase+), astrocytes (GFAP), microglia (Iba-1+) and endothelial cells (RECA-

*1+). There was noted invasion of microglia with a bulbar morphology pioneering a path for astrocytes to follow **(A).** A significant number of DCX+ neural progenitors also invaded the ECM, presumably these were already responding to the surrounding tissue damage **(B)**. A smaller number of endothelial cells was seen invading the ECM material. However, in some cases endothelial cells appeared to organize into tubules, but this was typically in areas where there were remnants of damaged tissue that were engulfed by the ECM hydrogel **(C)**. Oligodendrocytes were also found to invade deep into the ECM material, but cells were mostly of an uncharacteristic bulbar shape **(D)**. In addition to the "indigenous" brain cells, the infiltration of peripheral macrophages and their polarization towards an M1 (CD86+) or M2 (CD206+) phenotype were investigated **(E)**. Almost all CD206+ cells were also positive for CD86.*

Iba-1 microglia are very common amongst the cells infiltrating the furthest into the hydrogel (**Figure 2.17.A**), with GFAP+ astrocytes being located closer to the host tissue. Astrocytes and microglia within hydrogel have a more bulbar appearance within the ECM than in native tissue. Interestingly, significant numbers of DCX+ neural progenitors can be found to infiltrate the ECM hydrogel even during this acute phase, as do endothelial cells (**Figure 2.17.B**). As these infiltrate the gel, morphologically these appear bulbar and can be contrasted with areas where they show a more mature morphology. A more mature morphologies was typically associated with ECM hydrogel surrounding remnants of damaged tissue (**Figure 2.17.C**). Oligodendrocyte progenitors (CNPase+ cells) were also seen to infiltrate the ECM, hence indicating that all resident brain cells can be found to ininfiltrate ECM hydrogel within 24 hours (**Figure 2.17.D**). Nevertheless, the majority of cells found to infiltrate the ECM acutely were monocytes (mostly macrophages) that expressed markers for an M1 (CD86+) and/or M2 (CD206+) phenotype, presumably participating in the remodeling of the ECM (**Figure 2.17.E**).

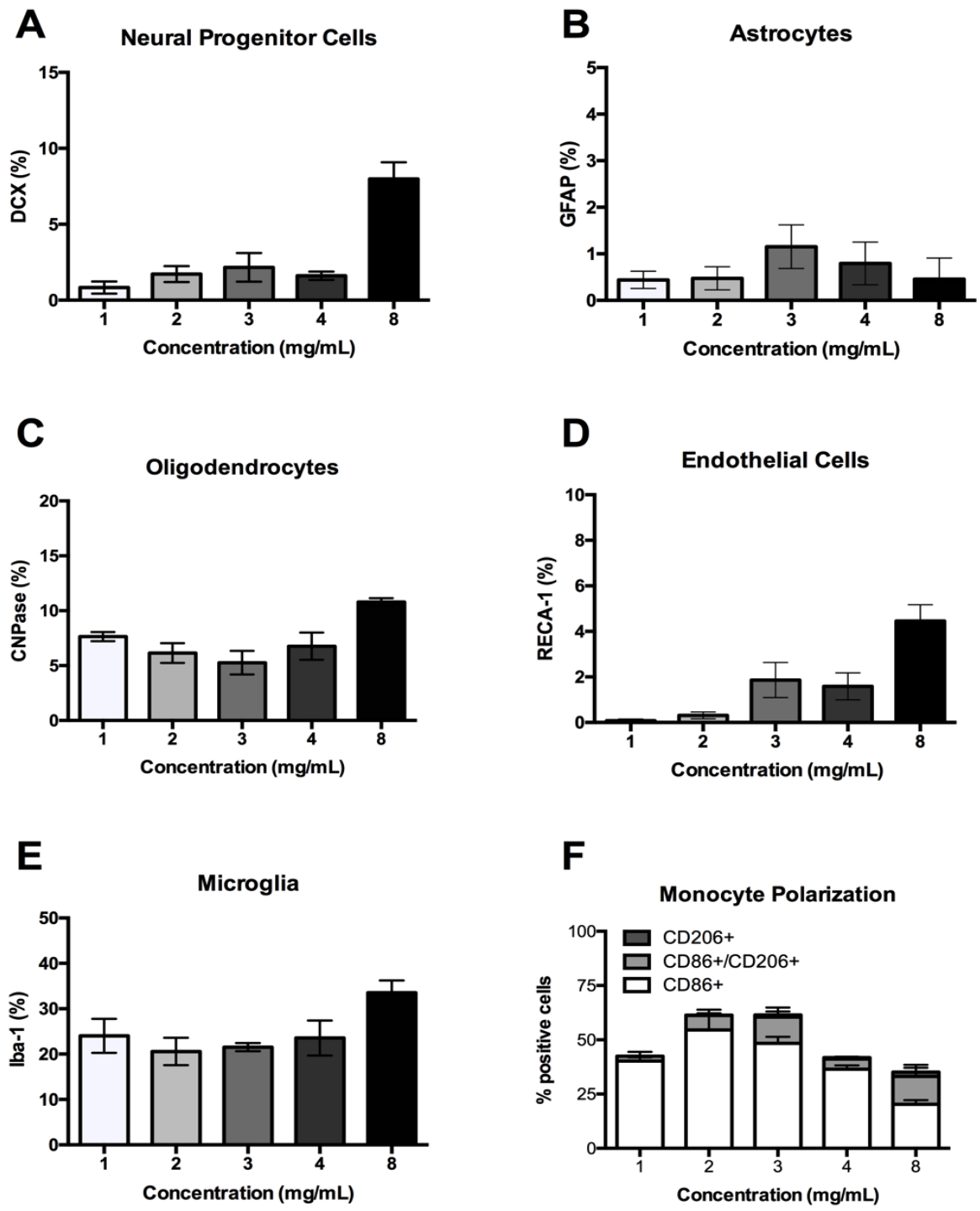

Figure 2.18. Cell invasion – Quantification of cell phenotypes.

An 8 mg/mL ECM concentration resulted in the most significant proportion of brain cells invading the material. Most significantly neural (DCX+ cells) and oligodendrocyte progenitors (CNPase+ cells) were among the first phenotypes to invade the ECM, with astrocytes (GFAP+ cells) and

endothelial (RECA-1+) cells being most negligible proportions. Nevertheless, as expected a high proportion of microglia (IBa-1+ cells) and macrophages invaded the material. Again, an 8 mg/mL ECM concentration produced the most significant shift from a M1 (CD86+ cells) towards an M2 (CD206+ cells) phenotype.

A quantification of the phenotypes and comparison across ECM concentrations showed that 8 mg/mL recruited the highest percentage of brain-derived cells (**Figure 2.18**). An average of 8% of invading cells at the 8 mg/mL concentration were DCX+ with all other concentrations recruiting <3% of neural progenitors ($p<.001$), i.e. the key phenotype required for repopulation of a neural tissue. Surprisingly, the recruitment of astrocytes was equivalent for all groups, as well as being very similar to neural progenitors at lower concentrations. The only slight rise (+1%) in astrocytes' infiltration was seen with 3 mg/mL, but this was statistically (and most likely biologically) insignificant. Oligodendrocytes were the most common "neural"-derived phenotype overall with >5% across all concentrations and a peak of 11% of infiltrating cells at 8 mg/mL ($p<.01$). In contrast, very few endothelial cells invaded (<3%), with a peak infiltration seen again with 8 mg/mL (4.5% of cells, $p<.05$). As expected, microglia were the most common phenotype of brain-derived cells that infiltrated the ECM with the highest proportion of cells being found at 8 mg/mL ($p<.05$). These results indicate that ~60% of cells at 8 mg/mL were derived from the brain, with the lowest proportion (~30%) invading from the surrounding tissue with a concentration of 3 mg/mL. A significant proportion of cells hence infiltrated from outside the brain. Monocyte (microglia/macrophage) polarization contrasting M2 (CD206+), M1 (CD86+), or M2/M1 (CD206+/CD86+) markers indicated that an M1-like phenotype was the most common across all concentrations, but was lowest at 8 mg/mL

(p<.01). The proportion of M2/M1 marker co-expression was also highest at 8 mg/mL (p<.05), although 3 mg/mL was equivalent. Only M2-like (i.e. CD206+) cells were very scarce with <2% being present at the 8 mg/mL concentration and no significant difference being evident across ECM concentrations.

2.4 DISCUSSION

The advent of cytocompatible and injectable biomaterials offers new opportunities to treat brain damage. However, access to the brain, as well as its rigid confinement within the skull [74, 75], pose technical challenges to define an adequate in situ hydrogel formation based on the concentration-dependent rheological characteristics of ECM. The use of non-invasive imaging, such as MRI [141], ensures an efficient delivery of appropriate concentrations to assay gelation properties and their influence of ECM distribution in vivo. Herein, we described the rheologic and turbidometric characteristics of an ECM hydrogel with the intended clinical application of minimally invasive intracerebral delivery and retention in stroke.

It is noteworthy that ECM's rheological characteristics are based on concentration, time, and temperature [137]. A high concentration of ECM here (>3mg/ml) afforded a robust and efficient formation of hydrogel that was retained within the lesion. These formulations are therefore desirable for delivery of agents without penetration of the host tissue, but their retention within the cavity could structurally support cell delivery or attract host cell invasion to recolonize areas where tissue has been lost [89]. Gradual degradation of the hydrogel and replacement by host tissue would be expected.

Alternatively, lowering the hydrogel ECM concentration (<3mg/ml) might improve integration with the peri-infarct tissue and promote better interaction with host cells. If diffusion of ECM hydrogel into the damaged peri-infarct proves to be of benefit, as with drug delivery, then concentrations of ECM that do not gel or show a protracted gelation time would be desirable to afford diffusion into tissue. There is some evidence that diffusion of ECM into damaged brain tissue can lead to behavioral improvements [138]. Indeed, a concentration of 3mg/ml in the present study resulted in both a diffusion of ECM into the peri-infarct areas, as well as gelation and retention within the cavity. The length of time required for hydrogel structural support for cell invasion and subsequent de novo tissue formation is unknown. As hydrogel stiffness, as well as inductive properties, can affect cell invasion and phenotype [92, 152, 153], it is essential to further characterize the short-term and long-term biological properties of the ECM formulations after injection in the stroke-damaged brain.

Although much effort is geared toward designing novel biomaterials or enhancing the biological effects of transplanted cells, little effort is devoted to the technical challenges associated with delivery of these therapeutics and its interaction with host tissue. Yet, there is ample evidence that biophysical considerations regarding delivery of therapeutics to the brain can dramatically influence their therapeutic effects [154]. Controlling cannula placement [155, 156] and size [157, 158], using an automated injection pump for consistent delivery [159, 160], as well as MRI guidance [140], have provided greater control over factors that can influence the delivery of therapeutics to the brain. The tuning of the rheological properties of ECM hydrogel that potentially can separate the stiffness of the gel from its inductive payload will provide further opportunities

for the refinement of the in situ structure-function relationships required for therapeutic success [161-163]. An efficient local delivery at an appropriate concentration will also be essential for the delivery of biomaterials that serve as local drug/cell delivery vehicles [72, 134, 135]. It was evident herein that the described approach mitigated potential adverse effects compared to injection of a large volume of a stiff material without drainage. Using the drainage-injection procedure, it will now be possible to better control the intra-cavity concentration of material and further optimize gelation parameters in situ in relation to the different biophysical and inductive properties of biomaterials. These steps are essential to provide a thorough preclinical evaluation of biomaterials, but also to define the technical challenges for clinical translation.

Foremost of all, recruitment of host cells into the injected material requires a gelation and retention of material within the cavity. At 1 day post-implantation, a robust formation of the hydrogel can be observed at concentrations >3 mg/mL [114]. However, small agglomerates of ECM at the border of the tissue, as demonstrated here, can also attract host cells, albeit at a smaller scale. Due to the lack of structural support throughout the cavity, no repopulation of the cavity with host cells occurs. In contrast, gelation of the ECM in situ resulted in a very dramatic acute infiltration of cells into the cavity in the order of ~360,000 for the 8 mg/mL ECM concentration. This concentration was rheologically comparable to uninjured brain tissue, which could explain why this concentration was so efficient in attracting host cells, specifically neural progenitors and oligodendrocytes. The mechanical properties of the hydrogel play an important part in cell invasion and phenotypic differentiation [139, 164] Stiffer gels (1,000-10,000 Pa) are associated with astrocytes, whereas softer gels (100-1,000 Pa) are more likely to promote neuronal

differentiation [165]. An intermediate stiffness (400-800 Pa) provides a mixtures of cells, as was seen here in the 8 mg/mL condition (460 Pa), and could provide mechanical properties that are conducive to neural tissue engineering requiring neurons, astrocytes, as well as oligodendrocytes.

A good interface with host tissue is nevertheless also important. A lack of interface did not result in a good cell infiltration. Even if there was a good interface, in some cases there was a poor invasion. It is conceivable that the density gradient at the interface influences cell infiltration [166], which potentially could be due to tissue characteristics, such as a glia limitans, or hydrogel characteristics, such as a higher material concentration at the cavity edge producing a higher elastic modulus [167]. Although very dense material can invoke a foreign body response in the brain that leads to an encapsulation of material by fibrotic scarring [118], injections of hydrogels typically exhibit a reduced microglia and astrocytes response compared to just needle track damage [167]. Although microglia and astrocytes are abundantly present in the peri-cavity tissue [168], more neurons and oligodendrocytes invaded the ECM hydrogels than astrocytes within 24 hours of injection. The reciprocity in interaction between hydrogel and host brain is essential to determine the host tissue response and guide cell invasion or induce further scarring and a foreign body response [169]. Further engineering of hydrogel potentially promises to provide a greater control over this interaction and influence the infiltration of specific cell phenotypes [170].

Apart from the rheological properties, inductive cues provided by the ECM material are thought to be the key mediator of cell infiltration [171]. The 8 mg/mL concentration in the current study was the highest concentration implanted and hence also provided the

greatest abundance of inductive cues to elicit a regenerative response [171, 172]. Indeed, the injected ECM contains growth factors, such as vascular endothelial growth factor, basic fibroblast growth factor, and nerve growth factor, which can be released from the injected material [91, 143]. The released proteins can permeate into host tissue, create a gradient, and facilitates infiltration of host cells, such as microglia/macrophages [173]. It is thought that these immune cells exert a pioneering function in that they invade the ECM, leading a constructive remodeling and in this process create trails of molecules that attract host tissue cells to gradually repopulate the material [169]. Microglia (Iba1+) cells were predominant amongst the cells that infiltrated the furthest into the ECM. Their infiltration appeared to follow a topological trail within the ECM. The chain-like infiltration suggests that there are particular trails within the material that these cells preferential follow, although at the tissue boundary a broader cell invasion into the material is observed. These invasion trails are likely to be a combination of abundant signaling molecules that attract particular cells, as well as conducive mechanical properties, such as gel surface curvature within the injected material, that interact reciprocally with pioneering cells [174].

Peripheral macrophages are infiltrating the ECM material and it is thought that both macrophages and microglia here exerted very similar functions, notably constructive remodeling of the ECM hydrogel and facilitating the invasion of host organ cells. All ECM concentrations (apart of 0 mg/mL) invoked a macrophage/monocyte infiltration. Proportionally this was lowest at the 8 mg/mL concentration. However, this is due to a greater number of host brain cells infiltration at this concentration, but in absolute numbers leads a similar number of macrophages than at 3 or 4 mg/mL. Although it is

conceivable that microglia and macrophage infiltration are a response to recognizing a foreign object, the difference in cell numbers and proportions across the different concentrations indicate that other factors are also important. The stiffness of the injected material, for instance, can influence macrophage infiltration and morphology of these cells, with higher stiffness being associated with a greater response [175]. Although macrophages are involved in a foreign body response to injected material [167], this typically involves macrophages of an M1-like phenotype only [176]. An M1-like phenotype response, in the absence of a polarization towards an M2-like phenotype, is associated with an insufficient decellularization of ECM material [177]. Although the M1-like response here was dominant overall, especially in the 1 mg/mL condition, polarization towards an M2 phenotype, especially at 3 and 8 mg/mL, using the same ECM material, indicates that this was not due to a insufficient decellularization. An M2-like phenotype polarization of invading macrophages has indeed been linked with peripheral nerve repair [178] and the constructive remodeling response of injected ECM [179]. It is this M2-like polarization that is thought to be crucial to attract cells from the host organ to repopulate the tissue defect and eventually replace the injected material with new tissue [171].

The infiltration of microglia and macrophages is thought to be an M1-like response with a shift towards an M2-like phenotype, occurring through juxtacrine or paracrine signaling within the ECM material [173]. It is important to stress that all infiltration into the material, i.e. even macrophage infiltration, was through host tissue, as there were no blood vessels contained within the cavity that would allow a direct infiltration of peripheral macrophages into the hydrogel. It is suggested that the mobilization of host brain cells (neurons, astrocytes, oligodendrocytes) and endothelial cells for infiltration followed a

chain-like migration of pioneering microglia and macrophages. This mobilization is a rapid process, as within 24 hours here, microglia and macrophages are seen at distances >1500 µm into the hydrogel. Moreover, a high proportion (~10%) of oligodendrocyte and neural progenitor cells was observed to follow these pioneering cells. Indeed, it is remarkable that within such a short time >60% of cells found within the hydrogel were cells required for tissue replacement. Still, it is unclear here why neural and oligodendrocyte progenitors were more abundant in their infiltration than astrocytes and endothelial cells. It is conceivable that this is due to ECM molecules required for migration [180]. Specifically, the abundance of ECM molecules, such as fibronectin and laminin, are thought to be pivotal in a repair response of neural stem cells [181, 182] and might explain the relative preferential infiltration of neural and oligodendrocyte progenitors. In contrast, the high collagen content of these ECM hydrogels might serve as a deterrent to astrocytes [183, 184], hence at this acute stage leading to a selective preference of neural progenitor infiltration. Nevertheless, the infiltration of a high proportion of neural progenitors is very encouraging to harness endogenous repair mechanisms into the lesion cavity and potentially promote the replacement of lost tissue using inductive biomaterials. Further investigations into the provision of appropriate paracrine and juxtacrine recruitment cues, as well as rheological conditions that are conducive to cell invasion of a neural cell population [125, 139, 164, 185] may enhance this potential.

2.5 CONCLUSIONS

Implantation of ECM gel precursor leads to the in situ formation of a hydrogel at concentrations >3 mg/mL, resulting in its retention within the lesion cavity. The ECM material induces a host response that is characterized by a rapid and robust cell infiltration that is concentration-dependent, but is also influenced by the size of the lesion. ECM concentration further influences the phenotype of cells, with an 8 mg/mL concentration resulting in ~60% of brain-derived cells. This concentration produced the most significant polarization towards an M2-like macrophage phenotype at this acute time point, whereas lower concentrations exerted a less significant M2-like polarization. These results hence suggest that an 8 mg/mL ECM concentration promotes a significant acute endogenous repair response. Nevertheless, a behavioral study characterizing cell infiltration, biodegradation, cell repopulation and its effect on host tissue is required to provide a more comprehensive framework to determine the potential of ECM hydrogel as a potential treatment for chronic stroke.

3.0 LONG TERM RETENTION OF ECM HYDROGEL REDUCES LESION VOLUME

The work in this chapter has been adapted from the following published manuscript:

***Ghuman H**, Gerwig M, Nicholls FJ, Liu JR, Donnelly J, Badylak SF, Modo M. Long-term retention of ECM hydrogel after implantation into a sub-acute stroke cavity reduces lesion volume. Acta Biomater. 2017; 63:50-63*

3.1 INTRODUCTION

The ECM hydrogel implanted into a chronic stroke lesion 1) induces a host tissue response that leads to a cell infiltration; 2) a structural support is required for cell infiltration into the cavity; 3) rheological properties akin to intact tissue promotes the most significant cell infiltration; 4) a significant portion of infiltrating cells are of a monocyte (i.e. microglia/macrophage) phenotype with a concentration-dependent polarization towards an M2-like phenotype and 5) a 8 mg/mL ECM concentration attracts large numbers of neural and oligodendrocyte progenitors within 24 hours.

To determine the impact of injecting large volumes of ECM hydrogel on behavioral functions, we investigated an ECM preparation (8 mg/mL) that is retained inside the stroke cavity to provide structural support [114, 150], but also provides a strong signaling environment to recruit large numbers of host cells that can promote structural remodeling

of the material [112]. The objective of the present study was to evaluate if this hydrogel formulation of ECM undergoes biodegradation inside a stroke cavity, akin to peripheral soft tissues, and if its continued presence or remodeling affects host tissue deformation, as well behavioral impairments after a stroke.

3.2 MATERIALS AND METHODS

3.2.1. Middle cerebral artery occlusion (MCAo)

Please see section 2.2.3. for details.

Rats (n=22) with lesion volume >40 mm^3 (i.e. 40 µL) were randomly assigned to either the untreated or the ECM treated group (Figure 1A), resulting in an equivalent distribution of lesion volumes across both groups. Lesion volumes ranged from 72-246 µL.

3.2.2. Magnetic resonance imaging (MRI) AND infarct volume calculation

Please see section 2.2.4. for details

3.2.3 Tissue deformation measurements

ROIs were defined based on anatomical definitions to segment host tissue and determine if ECM implantation affected the deformation of the brain due to stroke damage [149]. A midline shift is commonly observed due to the host tissue expanding due to the lack of sufficient structural support, resulting from the void of the lesion cavity [186, 187]. Midline

shift was determined by placing a vertical line from the longitudinal fissure to the median eminence at Bregma +0.7, which commonly is the central slice of MCAo damage [149]. In the middle of the vertical line, perpendicular lines are drawn to measure the distance to the edge of each hemisphere. A ratio is taken of these two measurements to define the relative midline shift. Ventricular enlargement is also often seen as a consequence of tissue deformations. Volume changes of tissue parenchyma were also calculated to determine if stroke and ECM implantation affected structural changes in these regions.

3.2.4 Behavior assessment

Establishing the efficacy of ECM hydrogel injection to recover behavioral deficits in an animal model of stroke requires evaluation of these deficits on a variety of tests that reflect damage to sensorimotor, motor, and cognitive systems. Researchers blinded to the condition of animals performed all acquisition of data, graphing and statistical analyses. Animals from different groups were mixed in cages.

3.2.4.1 Bilateral asymmetry test. The bilateral asymmetry test probed tactile extinction as a measure of sensory neglect [57, 146]. For this, two strips of equal size (6 cm long, 0.5-0.8 cm wide) were applied with equal pressure to the saphenous part of the forepaw. Four trials (180 seconds each) recorded the time to contact and removal for each paw. Sensorimotor bias was determined by subtracting the unaffected (right) from the affected (left) paw.

3.2.4.2 Footfault test. The footfault test evaluated the animals' ability to integrate motor responses by analyzing motor impairments of limb functioning and placing deficits during locomotion [57, 146]. The rats were placed in the Motorater System (TSE GmbH) with horizontal bars to record the placements of both unaffected and affected forelimbs over 8 trials (>60 placements). A comparison of total number of incorrect placements or % missed steps across groups measured performance on motor integration.

3.2.4.3 Rotameter. Amphetamine-induced rotations (2.5 mg/kg in saline, i.p.) were measured using an automated rotameter system (TSE Systems). Rotational bias is used as an index of striatal damage [57, 147]. Animals were harnessed into jackets tethered to the rotameter system and injected with amphetamine 30 minutes prior to assessment. Contralateral and ipsilateral rotations were recorded for 30 minutes.

3.2.5 Histological assessment

3.2.5.1 Perfusion and immunohistochemistry. Please see section 2.2.7.1

3.2.5.2 ECM hydrogel volume. The virtual tissue module (MBF Bioscience) tiled individual 20x magnification images to create a composite whole brain slice. Anterior-posterior whole biomaterial images (500 μm apart) were acquired to measure the area occupied by ECM (i.e. collagen I staining), and then multiplied by the distance between images to approximate total volume [149]. The rate of biodegradation was calculated by obtaining the average ECM hydrogel volume at a reference time point (1 or 14 days) and

dividing it with the volume at the target time point (14 or 90 days). Degradation rate was defined as the change in ECM hydrogel volume divided by number of days or µL/day.

3.2.5.3 Parenchyma and lesion volume. Regions of Interest (ROIs) were drawn on 8-bit whole brain histology images of DAPI in Fiji version 1.49 (https://fiji.sc) around the tissue for each hemisphere, including the ventricles. Based on the pixel intensity in the contralateral hemisphere, a threshold was applied to define parenchyma and create a binary map [149]. For each histological slice, contralateral parenchyma was defined by subtracting the lateral ventricle. Ipsilateral parenchyma volume was defined by subtracting lateral ventricle and lesion volume. Total volumes were calculated by multiplying area measurements by the distance to the next slice (500 µm). A ratio between ipsi- and contralateral parenchymal and ventricular volumes was calculated.

3.2.5.4 Scarring measurements. Brain tissue sections were immunolabeled for glial fibrillary acid protein (GFAP) before acquiring whole brain images at 10x magnification, as previously described [149]. Images were acquired with 100 ms exposure time for all animals to provide consistent signal intensity across all sections. The images were then processed through Fiji to define straight lines as ROIs starting from the lesion boundary and drawing away from the cavity. A plot of intensity versus distance determined thickness of the glial scar in both cortex and striatum. The average intensity of the GFAP signal was then averaged and binned for every 200 µm, starting from the lesion boundary. ROIs were drawn in all anterior-posterior brain sections containing the glial scar.

3.2.5.5 Peri-infarct astrocytosis. Whole brain GFAP stained images were first converted to 8-bit images before applying a threshold to mask GFAP+ cells and create a binary map to determine the area covered by astrocytes in both ipsilateral (i.e. right) stroke-affected and contralateral (i.e. left) unaffected hemispheres [149]. The same threshold value was used for all brain sections to maintain consistency. ROIs were then drawn around the parenchyma of the ipsilateral hemisphere to determine the area fraction (%) represented by astrocytes.

3.2.6 Statistical analysis. Statistical analyses were performed in SPSS 17 for Mac (IBM) with significance set at $p<0.05$. Specifically, a one-way ANOVA was used to compare cell invasion and phenotypes, using a Bonferroni post-hoc test to validate significant comparisons. A two-way ANOVA with Bonferroni post-hoc testing was used to contrast the comparison between lesion volumes, as well as behavioral data. Graphs were drawn in Prism 6 (GraphPad) with data points representing the mean and bars reflecting the standard deviation. A priori power calculations were performed in G*Power [188]. A power of 80% (Type II error) with a significance of $p<0.05$ (Type I error) is considered suitable [189]. With a medium effect size f of 0.25 for ANOVAs, a total sample size of N=36 is sufficient to achieve a power of 80% at the 5% significance level.

3.3 RESULTS

3.3.1 ECM implantation and evolution of lesion volume

The volume of implantation of ECM precursor was determined based on the hyperintense lesion volume, which was measured on pre-implantation T_2-weighted MR images (**Figure 3.1.A**) using tissue segmentation (**Figure 3.1.B**). After exclusion of animals with lesions <40 µL or no lesion, the remaining MCAo animals were randomly assigned to the untreated or treated MCAo groups, with both having equivalent mean lesion volumes of approximately 130 µL (**Figure 3.1.C**). Untreated and treated animals' lesion volume was significantly different from controls ($F=41.98$, $p<0.001$), with treated rats showing a significant reduction in lesion volume at 12 weeks ($p<0.05$). By accounting for pre-implantation volume, untreated animals revealed a 28% increase in volume, whereas lesion volume in treated rats was significantly reduced ($t=2.856$, $p<0.01$) in comparison to untreated animals (**Figure 3.1.D**). It is also noteworthy that there was a 10% decrease in volume compared to the 2 weeks post-infarct baseline volume, although this did not reach statistical significance. ECM implantation therefore attenuated the structural progression of stroke damage.

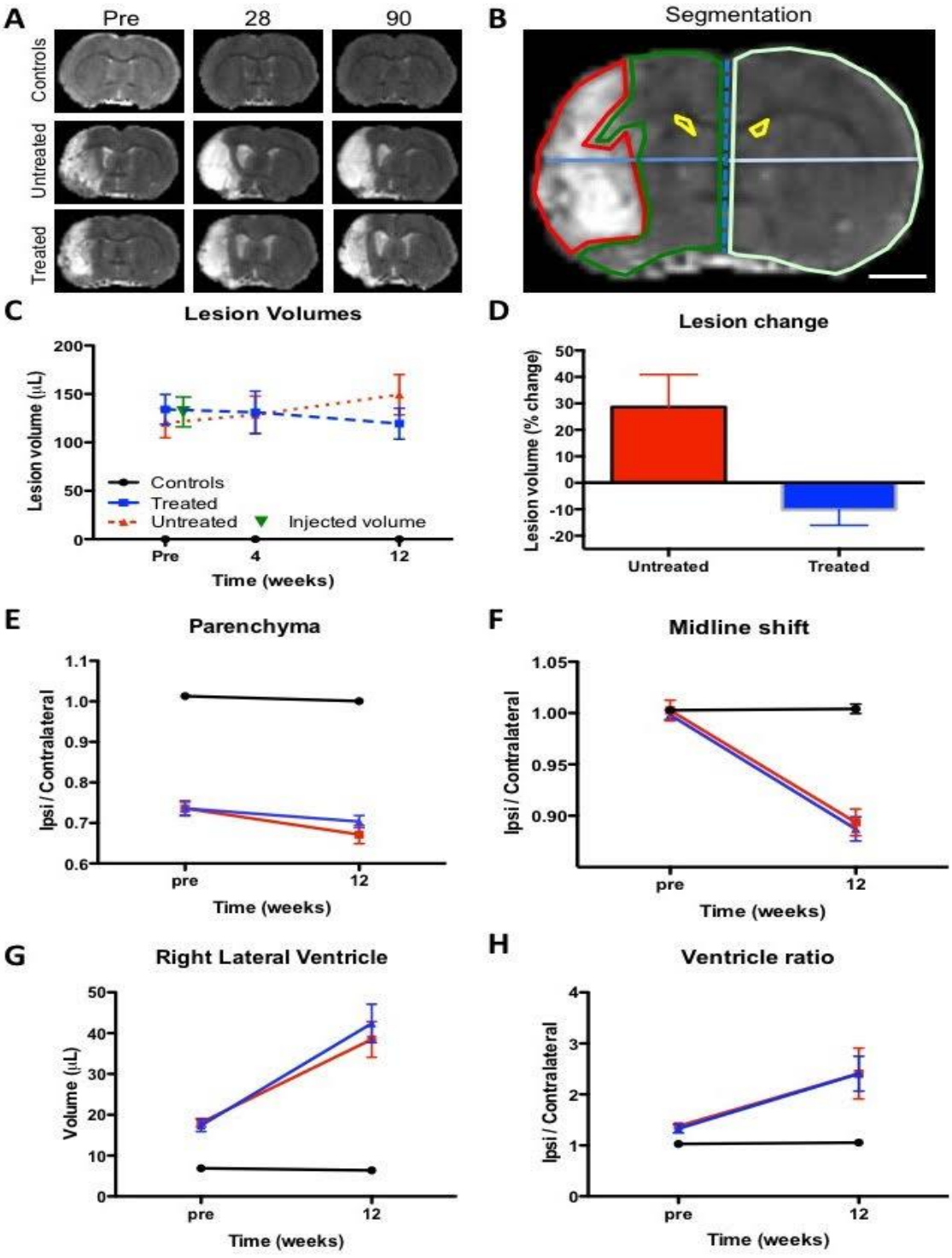

Figure 3.1. Evolution of lesion volume and tissue deformation.

A. *T_2-weighted MR images of experimental groups over time reveal the hyperintense lesion cavity in animals with stroke damage.* ***B.*** *Measurement of lesion volume (red region-of-interest) based*

on the hyperintense T_2-weighted signal on MR images defined by mean signal of the contralateral hemisphere + 1 standard deviation (scale bar 2 mm). Ipsilateral (green) and contralateral (light green) parenchymal tissue, lateral ventricles (yellow) were also segmented on MR images. Midline shift (blue line) was calculated by a ratio between distance of the ipsilateral and contralateral hemisphere midpoints. ***C.*** *Lesion volume was calculated for a baseline pre-implantation time point, as well as for 4 and 12 weeks post-implantation.* ***D.*** *To account for variations in lesion volume at baseline, % change between baseline and 12 weeks were calculated.* ***E.*** *A ratio of parenchymal volume revealed a significant loss of parenchyma in stroke animals, which further declined a little over 12 weeks.* ***F.*** *A gradual shift of the midline was evident in both stroke groups, but was not impacted by ECM hydrogel implantation.* ***G.*** *An equivalent dramatic increase in ipsilateral lateral ventricle was evident in both stroke groups.* ***H.*** *The ratio between the ipsilateral and contralateral ventricle further reflect these gradual long-term changes in tissue structure after stroke. ECM hydrogel did not affect these tissue deformations.*

3.3.2 ECM and tissue deformation

To quantitatively determine the impact of ECM implantation on host tissue structures, pre-implantation and final MR images were further segmented. Hemispheric parenchymal volume was measured to determine if the reduction in lesion volume translated into novel brain tissue. However, there was no significant difference between treated and untreated animals (**Figure 3.1.E**). This pattern of results was also evident for a midline shift (**Figure 3.1.F**), right lateral ventricular volume (**Figure 3.1.G**), and the ratio of left/right lateral ventricle (**Figure 3.1.H**). The lack of host tissue changes therefore suggests that changes in T_2-weighted lesion volumes is a reflection of an attenuation of the tissue-lesion interface (i.e. T2 signal in lesion), rather than the generation of new tissue per se or a slowing ventricular enlargement.

3.3.3 ECM hydrogel does not impact behavioral functions

To determine the impact of ECM hydrogel on the brain, a battery of behavioral tests was employed to evaluate functional changes associated with different brain regions affected by stroke. Sensorimotor functions are dependent on striatal and sensorimotor cortex, both affected by stroke, and readily assessed by the bilateral asymmetry test (BAT). The contralateral hemisphere is unaffected by stroke and serves as an internal control. The right forepaw here was unaffected by stroke and was equivalent in all 3 experimental groups (**Figure 3.2.A**). In contrast, the left affected forepaw exhibited a significant impairment in both untreated and treated MCAo animals compared to controls, with no evidence of ECM hydrogel altering this defect in a positive or negative fashion (**Figure 3.2.B**).

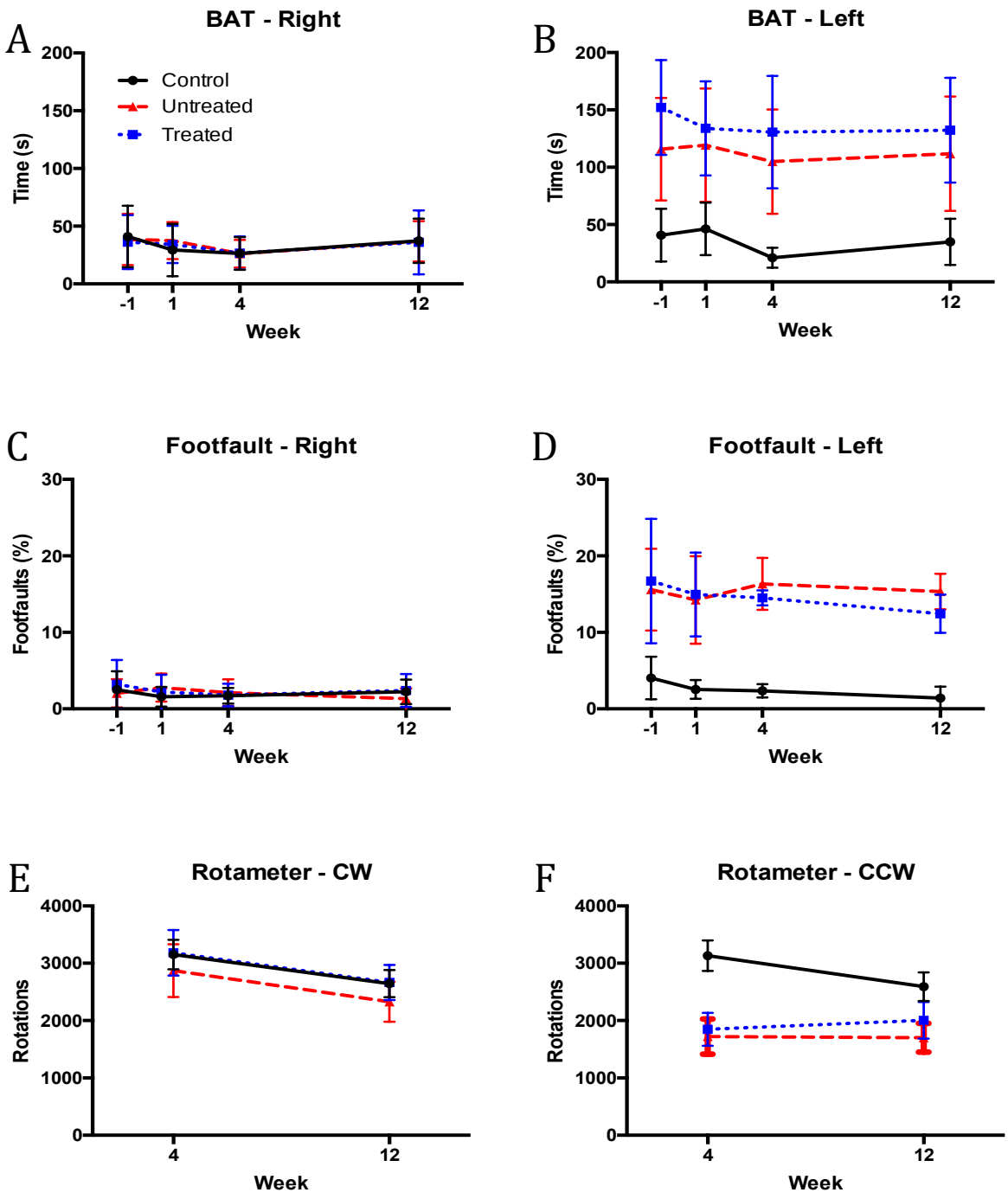

Figure 3.2. Behavioral assessment.

A. *Bilateral asymmetry test (BAT) analyses revealed a significant sensorimotor bias in the left forepaw, but not in the right forepaw in untreated and treated animals.* ***B.*** *Treatment did not affect sensorimotor bias compared to untreated animals. The footfault test measured motor integration,*

which was significantly impaired in the left affected forepaw. Treated animals performed comparably to untreated animals on this task. ***C.*** *Amphetamine-induced rotation bias on the rotameter reveals striatal integrity and dopamine responsiveness. Treated and untreated rats exhibited a comparable asymmetry in rotation.*

The footfault test is dependent on the motor loop of the striatum and motor cortex and demonstrates a robust long-term deficit after stroke. The right forepaw did not show any deficit walking over horizontal bars in any of the experimental groups (**Figure 3.2.C**), whereas the left forepaw contralateral to the stroke lesion exhibited a significant impairment pre-implantation ($p<0.001$), with no indication of change due to ECM hydrogel evident at any time point (**Figure 3.2.D**).

In contrast to the BAT and footfault, the rotameter evaluates pharmacologically induced rotations that probe the hemispheric dopamine-balance in the striatum (**Figure 3.2.E**), often considered a functional measure of the degree of striatal tissue loss. There was no bias in clockwise rotations between any of the experimental groups, but there was a significant bias in counterclockwise rotations in untreated and treated animals ($p<0.001$). No difference between untreated and treated animals was evident indicating that ECM hydrogel did not functionally affect host striatal tissue.

3.3.4 ECM hydrogel implantation decreases tissue cavitation

After completion of in vivo analyses, fixed tissue was processed for histological analyses. Stroke and the loss of brain tissue leads to the formation of a cavity that is delineated by a scar formed by glial cells, forming the edge of the tissue (**Figure 3.3.A**). Implantation of

8 mg/mL ECM hydrogel into the cavity indicates that it is contained within the cavity delineated by gliosis. Although stroke significantly reduced the amount of parenchyma in the ipsilateral stroke hemisphere ($F=67.58$, $p<0.001$), the presence of ECM hydrogel in the lesion cavity did not significantly increase parenchymal volume in comparison to untreated animals (**Figure 3.3.B**). There was also no evidence of a structural effect of ECM treatment on ventricular volume, although stroke significantly enlarged the ipsilateral ventricle in both groups relative to controls ($F=3.41$, $p<0.05$). A comparison of lesion volume between untreated and treated animals indicated that there was a 19.8% decrease in the cavity after ECM treatment ($t=2.143$, $p<0.05$).

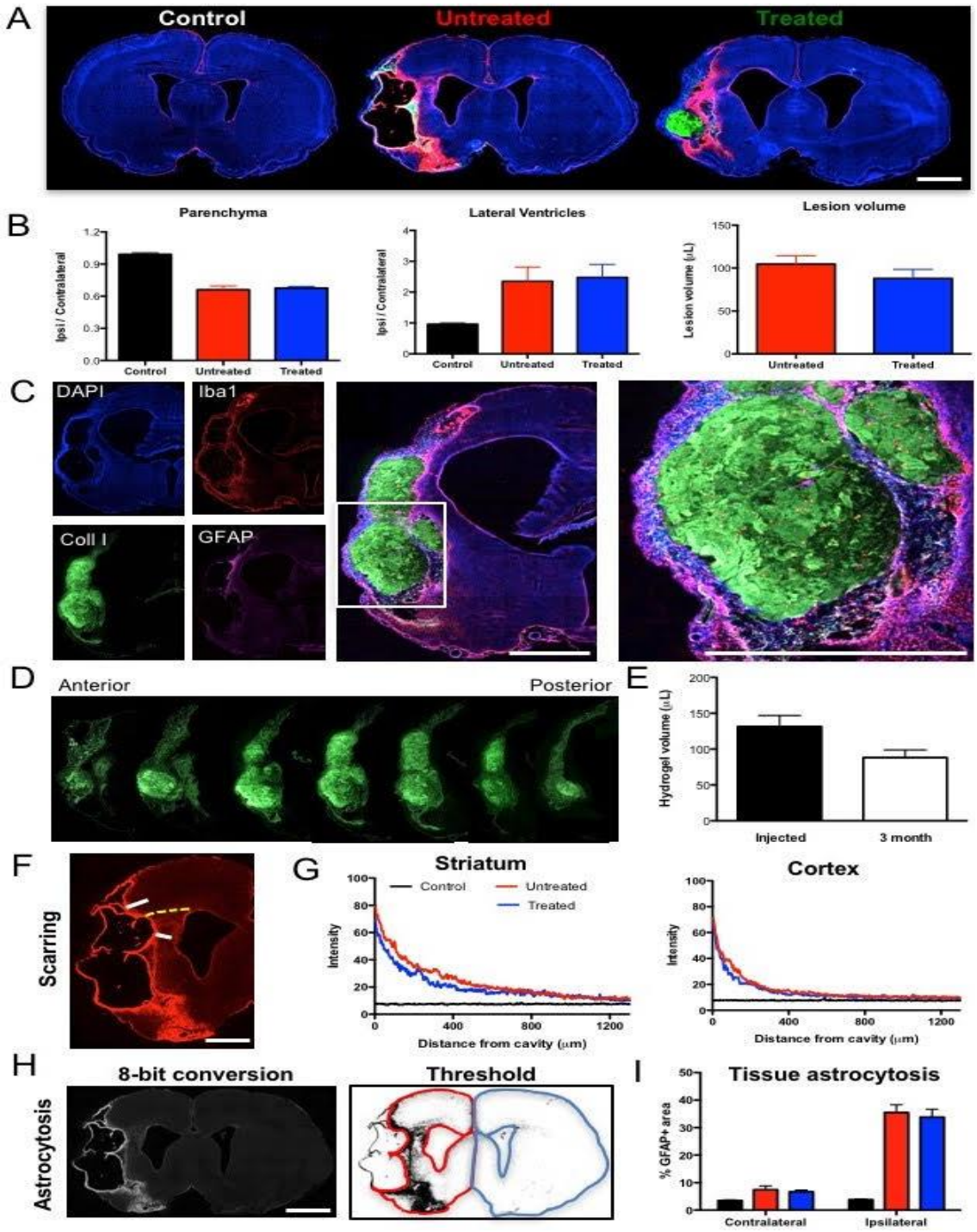

Figure 3.3. ECM hydrogel retention and glial scarring.

A. *A histological comparison between controls, untreated and treated stroke animals reveals a major tissue loss in the ipsilateral hemisphere, as well as the presence of ECM hydrogel within the lesion cavity.* ***B.*** *A quantification of parenchymal volume in these 3 groups indicated a 33%*

tissue loss in animals with stroke, as well as a dramatic increase in ipsilateral ventricular volume. A treatment effect was evident on stroke lesion volume with a 19.8% decrease in cavity volume. ***C.*** *ECM hydrogel was retained inside the lesion cavity in all treated animals as indicated by collagen I staining surrounded by host tissue.* ***D.*** *Along the anterior-posterior axis, ECM hydrogel was identifiable as a morphologically distinct entity aided by collagen I staining.* ***E.*** *A comparison between injection volume of ECM gel precursor and volume of hydrogel at 3 months revealed a decrease of 32%, but due to individual variability this did not reach statistical significance.* ***F.*** *To evaluate the impact of ECM hydrogel on glial scarring at the tissue interface, whole brain slice images covering the lesion cavity along the anterior-posterior axis were acquired for all 3 groups to measure the level of astrocytic (GFAP) reactivity inside striatal and cortical tissue.* ***G****. A marked increase in GFAP staining was evident at the border of the lesion cavity that gradually decreased further inside the tissue. GFAP reactivity in the stroke-damaged striatum was higher than in the cortex. However, there was no significant difference between untreated and treated animals.* ***H.*** *Peri-infarct astrocytosis (i.e. the area occupied by reactive astrocytes) in the ipsilateral and contralateral parenchyma was measured by an 8-bit conversion of whole slice images to apply a threshold that created a binary map.* ***I.*** *This binary image afforded quantification of area occupied and provided a comparison of the 3 experimental groups to indicate that there was no significant difference between untreated and treated animals, although both had significantly more astrocytosis than normal controls. Scale bar 2 mm.*

3.3.5 Slow biodegradation produces long term retention of ECM

A macroscopic evaluation of the presence of ECM hydrogel revealed that the bioscaffold, as indicated by collagen I staining, was distributed throughout the lesion cavity (**Figure 3.3.C**). Morphologically the ECM hydrogel appeared to reflect the pre-implantation MR lesion volume. Histological measurement of the ECM hydrogel volume along the anterior-posterior axis (**Figure 3.3.D**) afforded a volumetric comparison of injected and retained ECM. There was a significant 32% decrease ($t=6.737$, $p<0.001$) in ECM hydrogel volume by 12 weeks post-implantation compared to the injected precursor volume (**Figure 3.3.E**).

Despite some biodegradation, a large amount of ECM hydrogel remains (more than 60% of the implanted hydrogel) within the brain of all animals at 12 weeks post-implantation.

3.3.6 Glial scarring and astrocytosis is unaffected by ECM hydrogel

Using whole slice imaging of histological sections along the anterior-posterior axis allowed a quantitative determination of the extent of scarring in host tissue (**Figure 3.3.F**). The extent of scarring was highest at the edge of the tissue and gradually declined. The intensity of the glial scar indicates a scar that is much more pronounced in the striatum than cortex. A comparison between untreated and treated animals revealed no significant difference in scarring in striatum or cortex (**Figure 3.3.G**). Thresholding and quantification of the area of astrocytosis in the peri-infarct area (**Figure 3.3.H**) also did not reveal a significant effect of ECM in the ipsi- or contralateral hemisphere.

3.3.7 Presence of host cells is not correlated with injected and retained ECM volume

Host cells invaded the ECM hydrogel with cells scattered throughout the bioscaffold (**Figure 3.4.A**). Quantification of cells within the hydrogel (**Figure 3.4.B**) indicated some variability with a range of 44,820 to 78,740 cells (mean = 65,050) per animal. To investigate if this variability is associated with the volume of injected ECM, a correlation analysis between these was performed (**Figure 3.4.C**), but did not reveal a strong significant correlation (r=0.33, n.s.). Lesion volume did also not predict (r=0.35, n.s.) the

number of cells that were present within the ECM hydrogel (**Figure 3.4.D**). Cells within the ECM hydrogel were clustered, rather than distributed in a homogenous distribution. In some cases, an organization along grooves was observed in the hydrogel (**Figure 3.4.E**). In a few cases, the cellular organization consisted of endothelial cells forming tubules, but in most cases such cell accumulations consisted of other cell phenotypes.

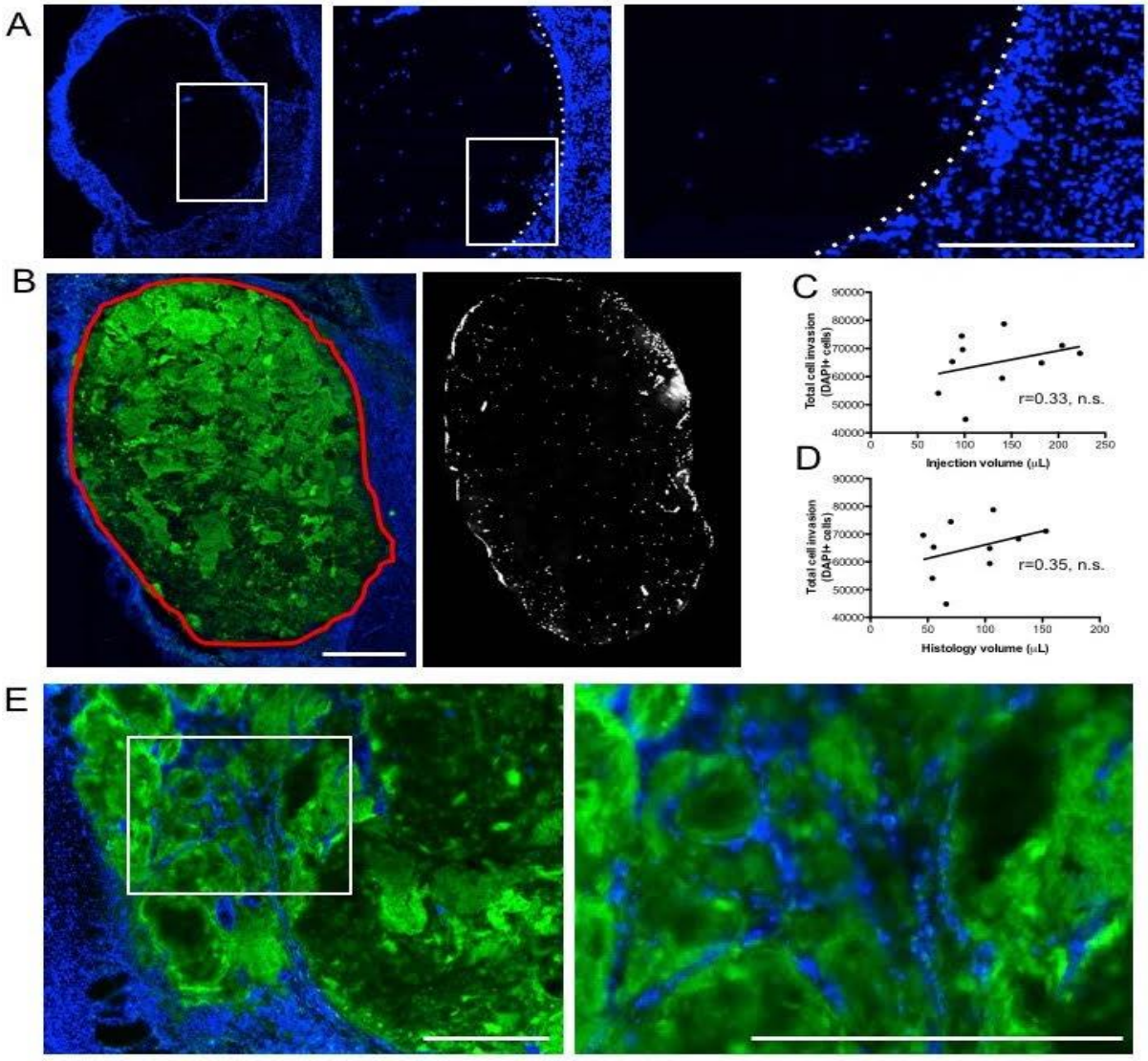

Figure 3.4. Presence of host cells in ECM hydrogel. *A.* ***A sharp boundary of DAPI cells defined the interface between biomaterial and host brain with some cells being present***

within the ECM hydrogel. *B.* ***Using collagen I staining, a region-of-interest for the ECM hydrogel was defined and applied to the DAPI image to provide a quantification of the number of cells present within the hydrogel at 12 weeks post-implantation. A mean invasion of 65,050 cells with a range of 44,820-78,740 cells was measured.*** *C.* ***A non-significant (n.s.) correlation between injection volume of ECM or histological volume of ECM at 12 weeks indicates that the number of invading cells was not directly related to the volume of ECM injected into the brain. The regression line in the scatter plot reflects the steepness of the correlation between the two data sets.*** *D.* ***There was also no significant association between the degree of stroke damage (i.e. lesion volume) and the number of invading cells, further highlighting that other factors play an important role in host cell invasion.*** *E.* ***Host cells that invaded and remained within the ECM hydrogel appear to be localized along topological grooves revealed by collagen I staining. Scale bars 100 μm.***

3.3.8 Microglia and oligodendrocytes predominantly invade the ECM

To assess the phenotypes of cells inside the ECM hydrogel, immunohistochemical markers for individual cell lineages (neural progenitors, neurons, astrocytes, oligodendrocytes, endothelial cells, and microglia) found in brain tissue were quantified (**Figure 3.5.A**). The vast majority of cells within the ECM were of a microglia (Iba1, 51%) phenotype ($F=130.6$, $p<0.001$; **Figure 3.5.B**), with fewer cells being oligodendrocytes (CNPase; 31%) and very few cells being endothelial (RECA1, 3.75) cells and astrocytes (GFAP, 1.3%).

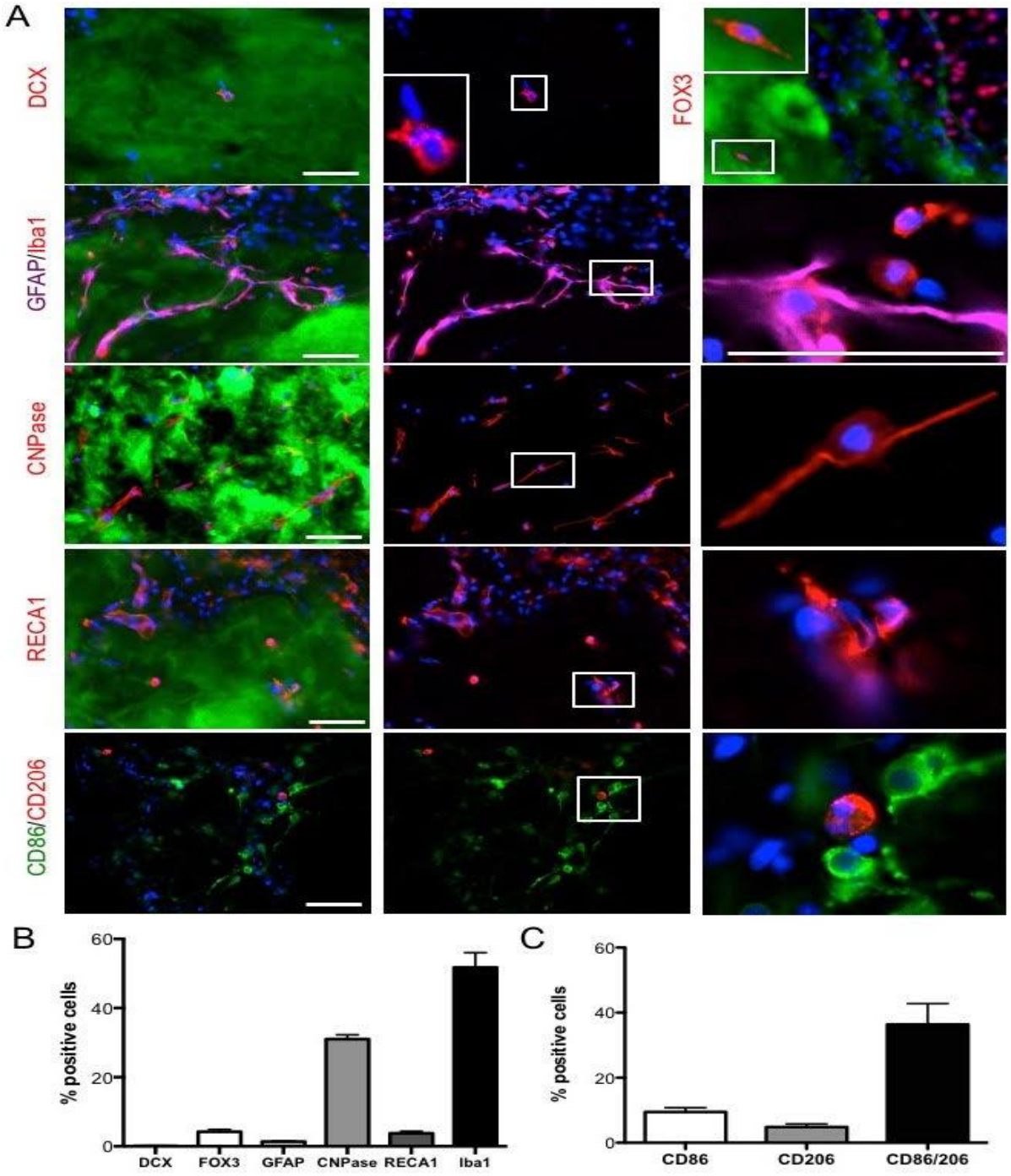

Figure 3.5. Phenotypic characterization of cells in ECM hydrogel.

A. *Immunohistochemical characterization of individual cell phenotypes within the ECM hydrogel at different magnifications.* ***B.*** *A phenotypic analysis of cells present within the hydrogel were predominantly microglia (ionized calcium binding adapter molecule 1, Iba-1), as well as fewer*

(p<0.01) cells from the oligodendrocyte lineage (2',3'-cyclic-nucleotide 3'-phosphodiesterase, CNPase). Significantly (p<0.001) fewer neurons (Fox3), neural progenitors (doublecortin, DCX), astrocytes (glial fibrillary acid protein, GFAP) or endothelial cells (rat endothelial cell antigen 1) were found. ***C.*** *A comparison of monocyte polarization indicated that these mostly co-expressed M1 (CD86) and M2 (CD206) markers, with significantly fewer cell expressing only CD86 (p<0.01) or CD206 (p<0.001). Scale bars 100 μm.*

Neurons (Fox3, 4.2%) and neural progenitors (DCX, 0.15%) were rarely seen within the material at 90 days. A 36.4% co-expression of M1 (CD86)- and M2 (CD206)-like characteristics on monocytes (i.e. microglia/macrophages) was most commonly observed. Significantly fewer cells ($F=20.27$, $p<0.001$) presented with an exclusive M1 (9.5%)- or M2 (4.8%)-like phenotype (Figure 6C).

3.4 DISCUSSION

The formation of a tissue cavity in the brain is commonly the result of a severe acute tissue injury, such as stroke [78] or traumatic brain injury (TBI) [190], but can also be caused by a surgical intervention to evacuate a hematoma [191], or the resection of a neoplasm [192]. The loss of tissue is associated with severe disability and structural deformations of host tissue leading to behavioral dysfunctions through Wallerian degeneration or tissue compacting [193]. As ECM hydrogel can be retained within this tissue cavity [114] and promote the infiltration of site-appropriate phenotypes [112], we here determined that an 8 mg/mL ECM hydrogel was retained long-term (12 weeks) after implantation with only moderate signs of biodegradation. The retention of some host cells that invaded was also evident. These cells were predominantly pro-repair microglia and

oligodendrocytes that were sparsely distributed. There was a significant effect on lesion volume as determined by MRI, but there was no reduction in tissue deformation caused by the stroke. No effect on a battery of behavioral tests was evident, indicating minimal impact on host tissue function. These results therefore indicate that an 8 mg/mL ECM concentration promoted a reduction in lesion volume, but did not undergo a rapid biodegradation as observed in peripheral soft tissue that could support extensive tissue repair.

Biodegradation of ECM bioscaffold in brain

ECM bioscaffolds typically undergo a 50% biodegradation within 30 days and are fully degraded between 75-90 days in volumetric soft tissue defects [194]. Bioscaffolds are often considered to provide the ‘soil’ to seed stem cells from the host organ [195]. Implantation of ECM into the stroke-damaged brain induces a very significant infiltration of host cells within 24 hours, akin to that observed in peripheral organs [112]. This initiation of a constructive remodeling response is essential for tissue repair [196] and is governed by a principle of dynamic reciprocity in which the ECM adapts to the structural, mechanical and functional needs of cells [197]. Although there was a 32% decrease in ECM volume over 12 weeks here, the significant retention of the hydrogel within the tissue cavity indicates that biodegradation of this material in the brain is slower than that in peripheral soft tissue.

Structural elements, such as pore size and fiber orientation, within the ECM hydrogel can influence the biodegradation properties of a scaffold [198]. ECM hydrogels with a denser fiber architecture typically show a slower biodegradation, as evidenced by

dermal ECM hydrogel taking longer to degrade than an equivalent concentration of UBM-ECM [145]. Fiber diameter (0.7 μm), pore size (0.10 μm^2), and node density (6 nodes/μm^2) are well conserved between 2 and 8 mg/mL UBM-ECM concentrations [145]. Pore sizes within these preparations are smaller than NSCs, which we established to have a diameter of ~20 μm [199]. A significant invasion of NSCs was nevertheless observed within 1 day post-implantation suggesting that migration itself was not hindered [112]. Smaller pore size in gelatin scaffolds (50-200 μm) are thought to induce differentiation of chondrocytes, whereas larger pores (250-500 μm) support proliferation [200], potentially indicating that invading NSCs differentiate rather than migrate into the scaffold. Still, little is known about how porosity influences neural stem cell migration and differentiation. It is important to note that cells can change their shape to migrate through smaller pores and pore size can also be enlarged by macrophages pushing apart or degrading fibers [201]. Although pore size provides a geometry that facilitates cell migration, with larger pore size increasing cell migration [200, 202], soluble factors also influence cell behavior by diffusing through these pores [203].

Macrophage infiltration and their activation toward a M2-phenotype have been implicated in ECM remodeling [204] and been identified as a key process for tissue replacement [205, 206]. Cells contained within the matrix here were predominantly macrophages and microglia with a M2-polarization indicating that the scaffold maintained an appropriate biodegradation response. However, there were very few cells present here at 12 weeks (mean=65,050 cells) compared to those reported at 1 day (mean=366,278cells) post-implantation [112]. This difference of 82% fewer cells potentially explains the lack of or extremely slow degradation response. It remains unclear

why the number of cells within the material would decrease so dramatically after 1 day. A time course study investigating the cellular infiltration and degradation response of different ECM concentrations will be required to further address these issues.

The central nervous system is known to be an immune-privileged environment that has limited potential for self-repair [207]. Nevertheless, the host brain response to ECM hydrogel implantation suggests that the bioscaffold can attract significant numbers of host cells to promote structural remodeling by 24 hours [112]. At 12 weeks, oligodendrocytes and microglia/macrophages were the dominant cell phenotypes with very few astrocytes, neural progenitors and neurons present. Still, the presence of neurons within the hydrogel is encouraging. The lack of neovascularization of the bioscaffold through endothelial cell invasion and organization is potentially a major factor impeding the structural remodeling of the implanted material. It remains unclear why revascularization of ECM hydrogel occurs efficiently in peripheral organs, but not in the brain. Improving the neovascularization of the scaffold could hence be a key factor to promote the degradation response and sustain invading brain cells.

Structural support to host brain prevents lesion volume increase

In addition to the release of biochemical factors from the ECM, its rheological properties are also likely to influence cell invasion and phenotypic differentiation. It is known that stiffer material tends to promote astrocytic, rather than neuronal, differentiation [165, 208]. Lower concentration hydrogels that are less stiff could hence undergo a more significant biodegradation and promote invasion of appropriate phenotypes to form a neurovascular environment. The slow biodegradation also maintains a stiffer environment, potentially

limiting further cell invasion [209], as well as morphological cell changes required to align and form a novel vascular structure. Mechanosensing of hydrogels by host tissue also influences the interface with host tissue by creating a glia scar [175]. Nevertheless, cells infiltrated the material upon implantation through the scar. This suggest that neither the stiffness of the material, nor the dense gliosis at the edge of the tissue defect provided a barrier to cell invasion. There was no evidence here that ECM hydrogel impacted the extent of scarring or peri-infarct astrocytosis, further indicating a minimal impact on existing brain tissue.

As the hydrogel maintained its macroscopic structure within the cavity, it can also exert structural support to host brain tissue. The impact of stroke on the host brain is severe with a major loss of tissue leading to ventricular enlargement, progressive atrophy of the ipsilateral parenchyma and an enlargement of the contralateral hemisphere. These tissue deformations are reflected in a midline shift [187, 210], with pressure gradients within tissues producing secondary Wallerian degeneration of axonal connections and poorer outcomes [186, 211]. Reducing tissue deformation is considered beneficial to overall long-term deficits associated with infarction [193, 212]. A slowly degrading bioscaffold implanted into the stroke cavity could exert a supportive function for host tissue. Sufficient stiffness of the hydrogel will be required to ensure a structural support to surrounding tissue. Although there was minimal attenuation of ventricular enlargement and midline shift, a significant reduction in lesion volume compared to baseline and an ~40% difference to the untreated animals revealed structural effects of the hydrogel on the lesion environment. This difference in treated and untreated animals is likely a combination of the cumulative effects of smaller changes in parenchymal volume and

right lateral ventricle. A more acute implantation of hydrogel in combination with the controlled local delivery of therapeutic compounds could provide new treatment approaches in stroke, traumatic brain injury and gliomas [213-216].

ECM hydrogel does not affect behavioral function

ECM implantation has been reported to promote behavioral improvements in animal models of TBI [138, 217, 218]. However, in these cases smaller volumes at lower concentrations of ECM were injected without retention of material within the tissue cavity. We here demonstrated that the retention of urinary bladder ECM within the stroke cavity did not impact behavioral functions. No improvement in deficits was evident, but there was also no indication that the injection led to any deleterious effects. Long-term retention of ECM hydrogel therefore is likely to be safe for physical support and delivery of therapeutic factors, but a concentration of 8 mg/mL is not providing a therapeutic behavioral benefit by itself. It is hence possible that lower concentrations of ECM, which partially gel after injection, would permeate into surrounding tissue to produce beneficial therapeutic effects.

The interface and permeation of ECM into this area might be an important factor in achieving therapeutic efficacy. The implantation of human neural stem cells into the peri-infarct, for instance, has significantly improved the same behavioral deficits as assessed here within a 3 months' time frame [57] and might indicate that repair of pre-infarct tissue is a key process in achieving behavioral recovery. As lower concentrations (3-4 mg/mL) of ECM hydrogel permeate into this peri-infarct tissue [114], these concentrations might provide more favorable conditions to affect behavioral deficits [138],

even though these preparations do not yield as significant a cell invasion after 24 hours of implantation [112]. In this case, the signaling properties of ECM hydrogel would induce the repair of damaged tissue, rather than necessitating a structural scaffold to support the invasion of cells to form a de novo tissue. Although collagen I is the most abundant molecules in UBM- ECM hydrogel and is likely to convey its rheological properties, it also contains a myriad of other proteins, oligopeptides, glycosaminoglycans, proteoglycans, growth factors and other juxtracine/paracrine signaling molecules (including nanovesicles). All of these can influence the repair response by modifying macrophage phenotype, stem cell recruitment and mechanotransduction. However, the variety and complexity of these molecules and their interaction in the damaged brain pose a harrowing challenge to elucidate a specific mechanism of repair. Further exploration of these extensive structure-function relationships is required to achieve a therapeutic efficacy comparable to the implantation of neural stem cells in the peri-infarct area, but also promoting conditions that improve the structural remodeling of ECM inside the lesion cavity to encourage the replacement of lost tissue, as seen in peripheral organs.

3.5 CONCLUSIONS

The tissue loss after a stroke constitutes a major challenge to improve behavioral outcomes. Implantation of a bioscaffold into the cavity can potentially provide physical support to the remaining host brain tissue, but inductive biomaterials can also attract host

cells to invade. We here demonstrated that an 8 mg/mL concentration of UBM-ECM hydrogel can reduce the lesion cavity with minimal impact on host tissue, peri-infarct astrocytosis and glial scarring. The hydrogel was retained within the cavity for 12 weeks suggesting that the biodegradation of the material within the brain does not replicate the typical time course observed in peripheral tissues. Behavioral functions were not affected by the implantation or retention of the material within the cavity indicating that an 8 mg/mL preparation appears safe for the local delivery of therapeutic factors, but by itself does not appear to exert a therapeutic benefit in stroke. Further studies are required using lower concentrations of ECM hydrogel that would afford permeation into the peri-infarct areas and potentially sustain a host response that could reproduce the structural remodeling observed in peripheral organs.

4.0 BIODEGRADATION OF ECM HYDROGEL PROMOTES ENDOGENOUS BRAIN TISSUE RESTORATION

The work in this chapter has been adapted from the following manuscript:

***Ghuman H**, Mauney C, Donnelly J, Massensini AR, Badylak SF, Modo M. Biodegradation of ECM hydrogel promotes endogenous brain tissue restoration in a rat model of stroke. (In peer-review; Acta Biomaterialia)*

4.1 INTRODUCTION

Long-term retention of ECM hydrogel is safe for physical support and delivery of therapeutic factors, but a concentration of 8 mg/mL is not providing a therapeutic behavioral benefit by itself. It is hence possible that lower concentrations of ECM, which partially gel after injection, would partially permeate into surrounding tissue to produce beneficial therapeutic effects. Although a higher concentration 8 mg/mL ECM induces the most cell invasion acutely, we hypothesized that weaker hydrogels will facilitate a more sustained endogenous cell invasion leading to a faster biodegradation that can favor tissue restoration. The aim of the current study was therefore to determine the histological time course (1, 14, 90 days) of cell invasion and biodegradation of different concentrations (3, 4, 8 mg/mL) of ECM hydrogel in a stroke cavity. A time course will allow us to determine if endogenous cells can sufficiently invade and restructure ECM hydrogel to promote the replacement of the scaffold with de novo tissue. Restoration of tissue within

the stroke cavity would indicate that the brain has the capacity to self-repair and create *de novo* tissue, but that appropriate conditions need to be engineered to facilitate this process.

4.2 MATERIALS AND METHODS

4.2.1 Middle cerebral artery occlusion (MCAO)

Please see section 2.2.3. for details.

MCAo rats (n=57) were randomly assigned to one of the following groups, resulting in equivalent lesion volumes between groups.

Table 3. MCAo animals per experimental condition

Conditions	Day 1	Day 14	Day 90
0 mg/mL	3	5	5
3 mg/mL	5	5	4
4 mg/mL	5	5	5
8 mg/mL	5	5	5

4.2.2 Magnetic resonance imaging (MRI) AND infarct volume calculation

Please see section 2.2.4. for details

4.2.3 Perfusion and immunohistochemistry

Please see section 2.2.7. for details

4.2.4 Tissue deformation measurements

Please see section 3.2.3. for details

4.2.5 Statistical analysis

Statistical analyses were performed in SPSS 17 for Mac (IBM) with significance set at $p<0.05$. Specifically, two-way ANOVAs were used to compare group and time effects as independent variables, with tissue volumes, cell invasion and phenotypes as dependent variables. Bonferroni post-hoc tests validated overall significant comparisons. A LOWESS spline curve fitting was performed on the ECM volume data to represent the expected time line of biodegradation. Pearson correlations were calculated to determine associations between two dependent variables. Graphs were drawn in Prism 7 (GraphPad) with data points representing the mean and bars reflecting the standard deviation.

4.3 RESULTS

4.3.1 Weaker ECM hydrogels undergo efficient biodegradation and reduce tissue cavitation

The 8 mg/mL ECM preparation resulted in a stiffer bioscaffold that was consistently still present by 90 days post-implantation while filling the entire lesion cavity (**Figure 4.1.A**).

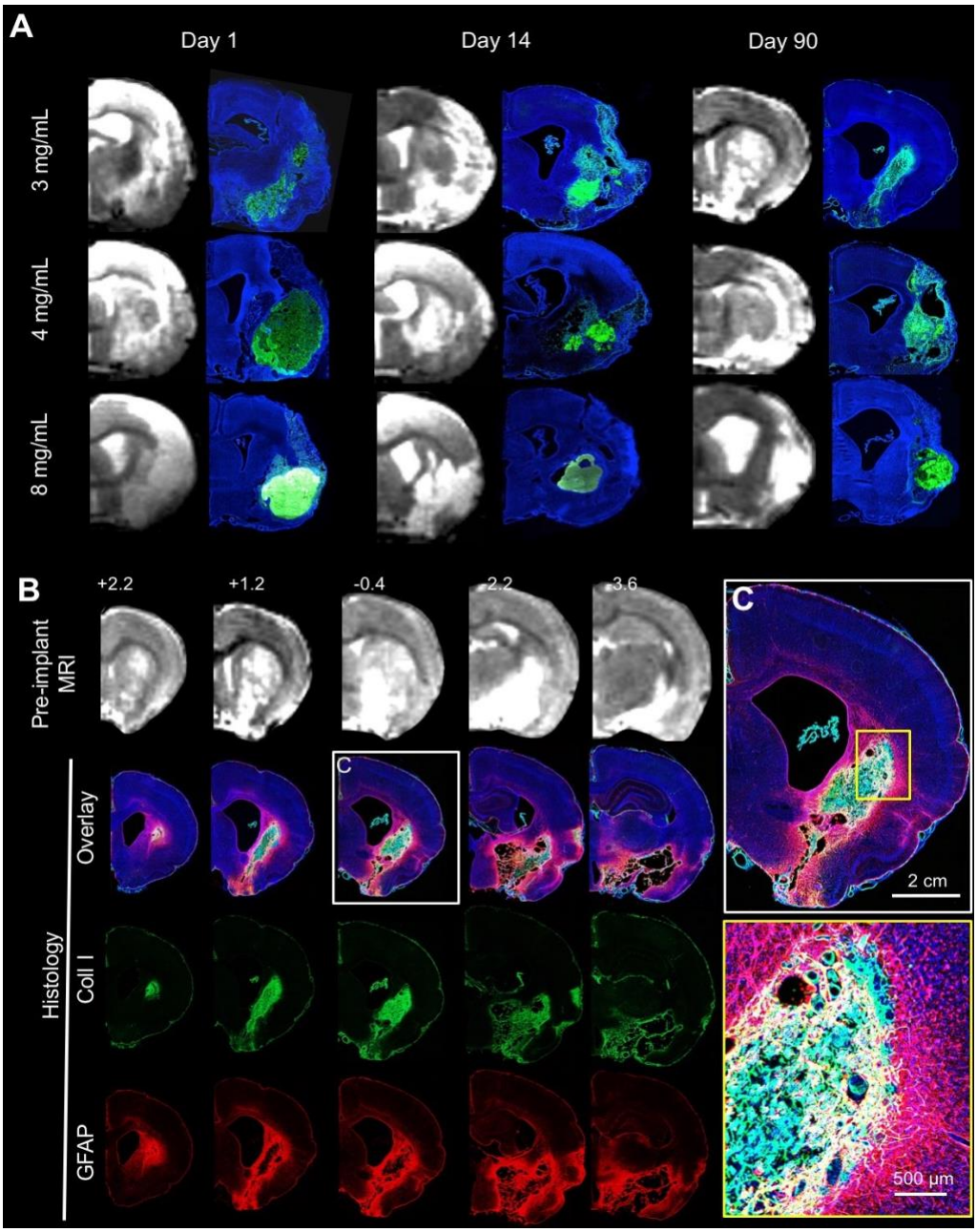

Figure 4.1: Macroscopic distribution of ECM hydrogel in the stroke cavity.

A. *Pre-implantation T_2-weighted magnetic resonance images (MRI) were used to define stereotactic coordinates and calculate volumes of ECM hydrogel precursor for injection. A complete coverage of the lesion cavity with an ECM bioscaffold (Collagen I in green, DAPI in Blue) was achieved with this approach. A concentration of 8 mg/mL ECM shows limited*

degradation over 90 days, whereas 3 and 4 mg/mL show a very efficient structural remodeling, with only a small amount of hydrogel being present at the final time point. ***B.*** *Anterior-Posterior pre-implantation MRI scans revealed the location and volume of the lesion cavity for comparison with 3 mg/mL ECM hydrogel at 90 days post-implantation. Active tissue remodeling inside the ECM bioscaffold and around the lesion cavity is evident (DAPI in Blue, Collagen I in green, GFAP in red).* ***C.*** *At the lesion-tissue boundary, astrocytes (GFAP+ cells) cross the glial scar and invade the bioscaffold that is replacing the stroke cavity. Capillary-like structures were also apparent in ECM remodeling regions.*

A key difference between 3 and 4 mg/mL gels compared to the stiffer 8 mg/mL gels was that the less concentrated ECM hydrogels displaced smaller amounts of damaged tissue and in cases of non-communicating tissue voids, these did not fully cover areas of cavitation. An anterior-posterior view of the lesion cavity pre-implantation showed a distinct delineation of the newly formed tissue inside the original lesion void at 90 days (**Figure 4.1.B**). ECM hydrogel within the tissue void provides a scaffold that bridges the space between host tissue, with cells invading through the substrate to re-colonize the cavity (**Figure 4.1.C**). Lateral ventricles were enlarged in all animals, indicating some degree of hydrocephalus *ex vacuo*, which is known to occur after volumetric tissue loss. In animals with sub-cortical lesions, ECM hydrogel appeared to be pulling tissue together, whereas in large lesions that included cortical regions such contractions of tissue did not occur.

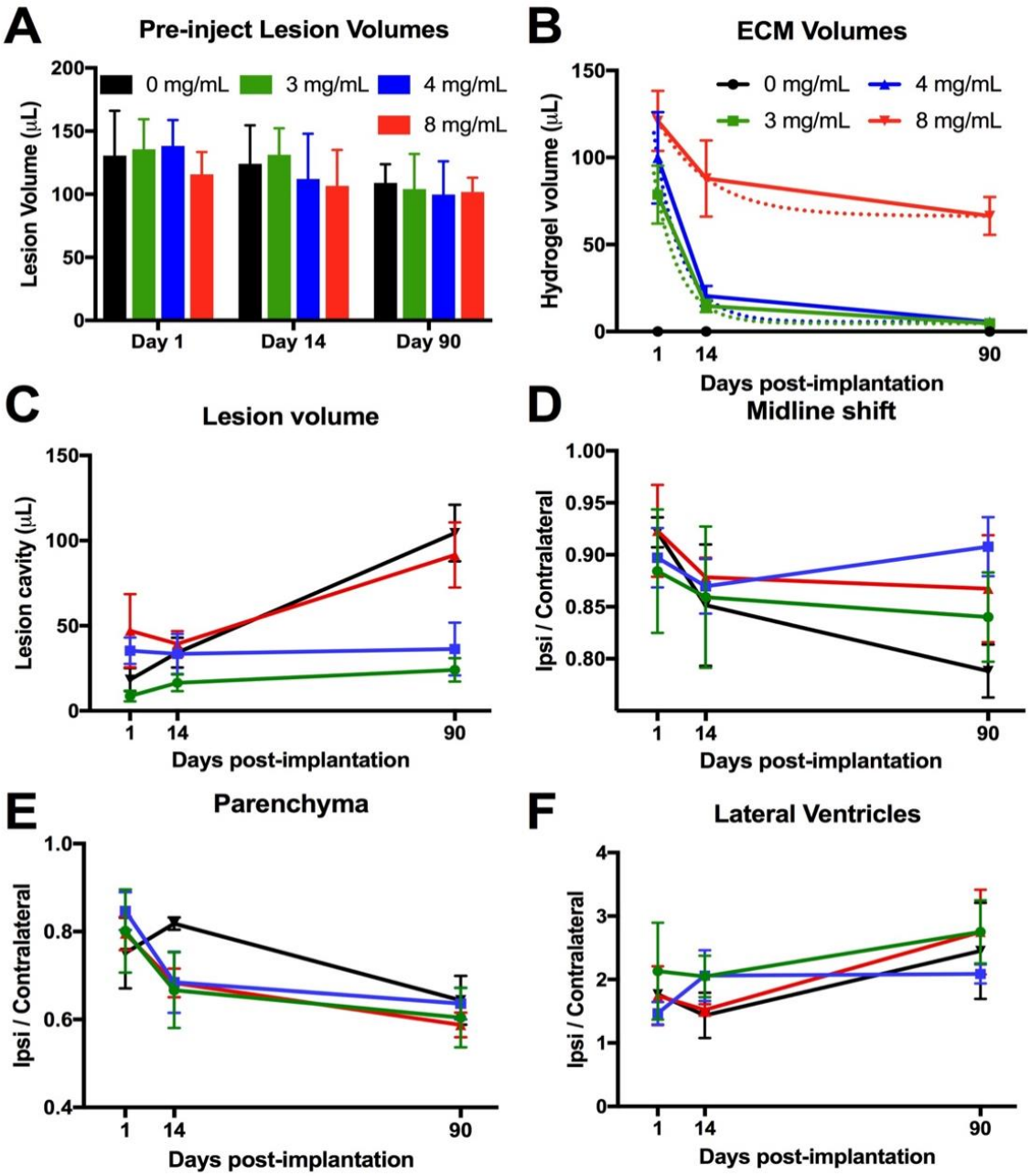

Figure 4.2. ECM biodegradation and tissue deformation.

A. *Lesion volumes calculated from T_2-weighted MR images acquired 4 days before ECM injection (10 days post-stroke) were used to assign rats to groups with equivalent lesion volumes.* ***B.*** *Remaining volume of ECM hydrogel was quantified to determine biodegradation at 1, 14 and 90 days post-implantation. At 90 days post-implantation a decrease in ECM volume of 94.1%, 95%, and 32% was recorded in the 3, 4, and 8 mg/mL. A locally weighted scatter plot smoother*

(LOWESS) fitted curve visualize the anticipated degradation pattern with a 3 mg/mL concentration providing a half-life of 4.5 days, the 4 mg/mL 4.9 days and 8 mg/mL >90 days. A biodegradation plateau is reached for the 3 and 4 mg/mL concentration around 28 days, whereas the 8 mg/mL concentration plateaued at 66 days. ***C.*** *Weaker 3 and 4 mg/mL ECM concentrations halted lesion progression, whereas the 8 mg/mL had a more limited impact on the evolution of the cavity compared to no treatment (0 mg/mL).* ***D.*** *Midline shift was calculated by a ratio between distance of the ipsi- and contralateral hemisphere midpoints. A gradual shift of the midline was evident in all groups. The 4 mg/mL condition exhibited the most promise to reduce tissue deformation.* ***E.*** *Hydrogel implantation did not affect the imbalance in ipsi- and contralateral parenchymal volumes that follows a stroke.* ***F.*** *There was also no effect on the hydrocephalus ex vacuo that ensues stroke damage, as evidence by the ratio of the ipsi- and contralateral lateral ventricles.*

A volumetric MRI comparison of lesion volume prior to implantation of hydrogel showed no significant differences between ECM concentrations ($F=0.23$, n.s.) at different time points ($F=1.032$, n.s.; **Figure 4.2.A**). Animals within each group therefore suffered a similar severity of stroke, with lesion volume pre-implantation ranging between 41-236 µL. The histologic evaluation of hydrogel volume at different time points showed an overall group effect ($F=27.0$, $p<0.001$), with 0 mg/mL (PBS) being significantly different from all other groups (**Figure 4.2.B**). ECM volumes 1 day post-implantation were not significantly different from each other, but 3 and 4 mg/mL volumes were lower compared to 8 mg/mL, further confirming qualitative observations that stiffer gels achieved a greater displacement of damaged tissues within the cavity in addition to filling the tissue voids. A significant interaction ($F=3.085$, $p<0.05$) between ECM concentrations and time was also evident. The 8 mg/mL concentration was significantly ($p<0.01$) different from 3 and 4 mg/mL on day 14 and 90. The 3 and 4 mg/mL groups showed no statistically significant difference in their biodegradation dynamics. The 4 mg/mL hydrogel underwent the fastest

degradation in the first two weeks at a rate of 6.11 µL/day (**Table 4**). In contrast, the 8 mg/mL preparation only saw a biodegradation rate of 2.54 µL/day, i.e. approximately half the rate of the 3 and 4 mg/mL hydrogels.

Table 4. Biodegradation rate of different ECM concentrations

Concentration	3 mg/mL	4 mg/mL	8 mg/mL
1-14 days	4.92 µL/day	6.11 µL/day	2.54 µL/day
14-90 days	0.13 µL/day	0.19 µL/day	0.28 µL/day
1-90 days	0.83 µL/day	1.06 µL/day	0.61 µL/day

A difference between the 8 mg/mL concentration hydrogel and the less concentrated formulations was also evident for its potential to reduce lesion volume (**Figure 4.2.C**). The 3 and 4 mg/mL hydrogel concentrations very effectively reduced lesion progression ($F=9.171$, $p<0.001$). Lesion progression without treatment (0 mg/mL) showed an increase in lesion volume over 90 days. However, an 8 mg/mL concentration reduced this progression. No significant difference between groups was evident at 1 and 14 days post-implantation, but 3 and 4 mg/mL significantly reduced lesion volume at 90 days ($F=5.414$, $p<0.01$). ECM hydrogel-treated animals exhibited no significant overall reduction in midline shift compared to untreated (0 mg/mL) animals (**Figure 4.2.D**). Furthermore, ECM hydrogel treatment did not have a significant effect on parenchymal volume (**Figure 4.2.E**) or lateral ventricle volumes (**Figure 4.2.F**).

4.3.2 Glial scarring and astrocytosis are unaffected by ECM implantation

To evaluate the host tissue glial response to ECM hydrogel implantation, glial scarring was measured in the striatum and cortex (**Figure 4.3.A**). It was noted qualitatively that only minor scarring was evident 1 day post-implantation and that a defined astrocytic barrier was more evident at 14 days (**Figure 4.3.B**). By 90 days in the 3 and 4 mg/mL, no defined line of an astrocytic scar was evident, but this area transformed into a wider area of reactive astrocytes. Quantification of scarring within the striatum showed no significant difference between groups ($F=2.42$, n.s.) or distance ($F=4.53$, n.s.) at day 1 post-implantation (**Figure 4.3.C**). At 14 days, scarring was more pronounced for all groups at the cavity border ($F=90.13$, $p<0.001$), but it was equivalent for all groups ($F=0.09$, n.s.). At 90 days, a wider area of reactive astrocytes defined the cavity border, significantly decreasing in density as a function of distance from the stroke cavity ($F=14.44$, $p<0.001$) in all groups ($F=1.54$, n.s.). A similar pattern of results was also evident in the cortex with a scarring distance effect at 14 ($F=62.05$, $p<0.001$) and 90 days 31.31, $p<0.001$), but no group differences at any time point. In addition to glial scarring, reactive astrocytes were found in the peri-infarct area (**Figure 4.3.D**). A quantification of these revealed a significant increase between day 1 and 14 for all groups ($F=25.23$, $p<0.001$, **Figure 4.3.E**). As ECM concentration was not related to the increase in the number of reactive astrocytes ($F=0.6015$, n.s.), changes in astrocytosis are likely related to the stroke pathology, rather than implantation of ECM hydrogel.

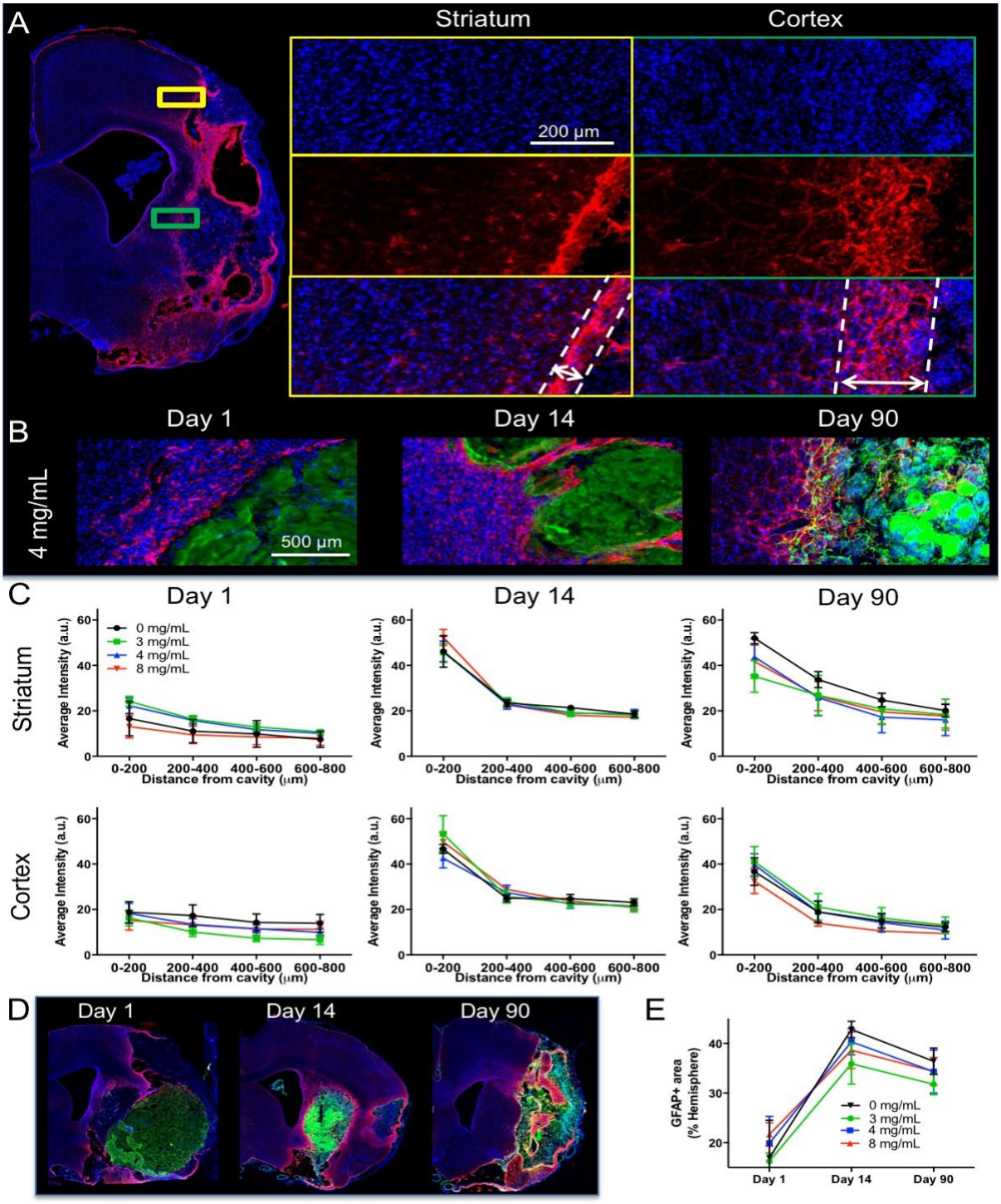

Figure 4.3. Glial scarring and tissue astrocytosis.

A. *To evaluate the impact of ECM hydrogel on glial scarring at the tissue interface, whole brain slices covering the lesion cavity were acquired to measure the level of astrocytic (GFAP) reactivity*

in the striatal and cortical tissues. ***B.*** *However, it is important to note clear morphological difference in astrocytic activity at the different time points is evident with the 14 day time point showing the sharpest interface border, whereas by 90 days post-implantation a complex mesh of astrocytic processes was blurring the line between established and regenerating tissue.* ***C.*** *A quantitative comparison indicated a marked increase in GFAP intensity at the border of cavity 1 day post-implantation that was equivalent for all groups. A gradual decrease of reactivity away from the cavity border was evident. The highest increase in astrocyte reactivity was observed at 14 days post-implantation with a surge in intensity reaching further into both striatum and cortex. By 90 days, the extent and intensity of glial reactivity was reducing, but not back to the level present on day 1.* ***D.*** *Peri-infarct astrocytosis was extensive in areas surrounding the ECM hydrogel implantation at all time points.* ***E****. A quantitative comparison mirrored the results of glial scarring, where an increase occurred in the 14 days post-implantation. This was nevertheless equivalent between all groups, including the 0 mg/mL condition indicating that this astrocytosis is not related to the ECM hydrogel, but either due to lesion progression or the implantation procedure. The 3 mg/mL condition exhibited the lowest level of astrocytosis, potentially revealing a minor effect of ECM permeating into peri-infarct tissue.*

4.3.3 ECM hydrogel efficiently promotes endogenous cell invasion

Although the glial scar is often seen as an obstacle to regeneration, there was a substantial cell invasion into ECM hydrogel for all concentrations (**Figure 4.4**). A quantification of cells within the bioscaffold was achieved by defining the ECM hydrogel using collagen I staining, which is significantly higher in the implanted biomaterial compared to the host brain (**Figure 4.5.A**). Individual cell nuclei were counted across all sections containing ECM hydrogel. In absolute numbers, the 8 mg/mL ECM hydrogel contained the most cells at day 1 (average 366,278), whereas the 3 mg/mL preparation

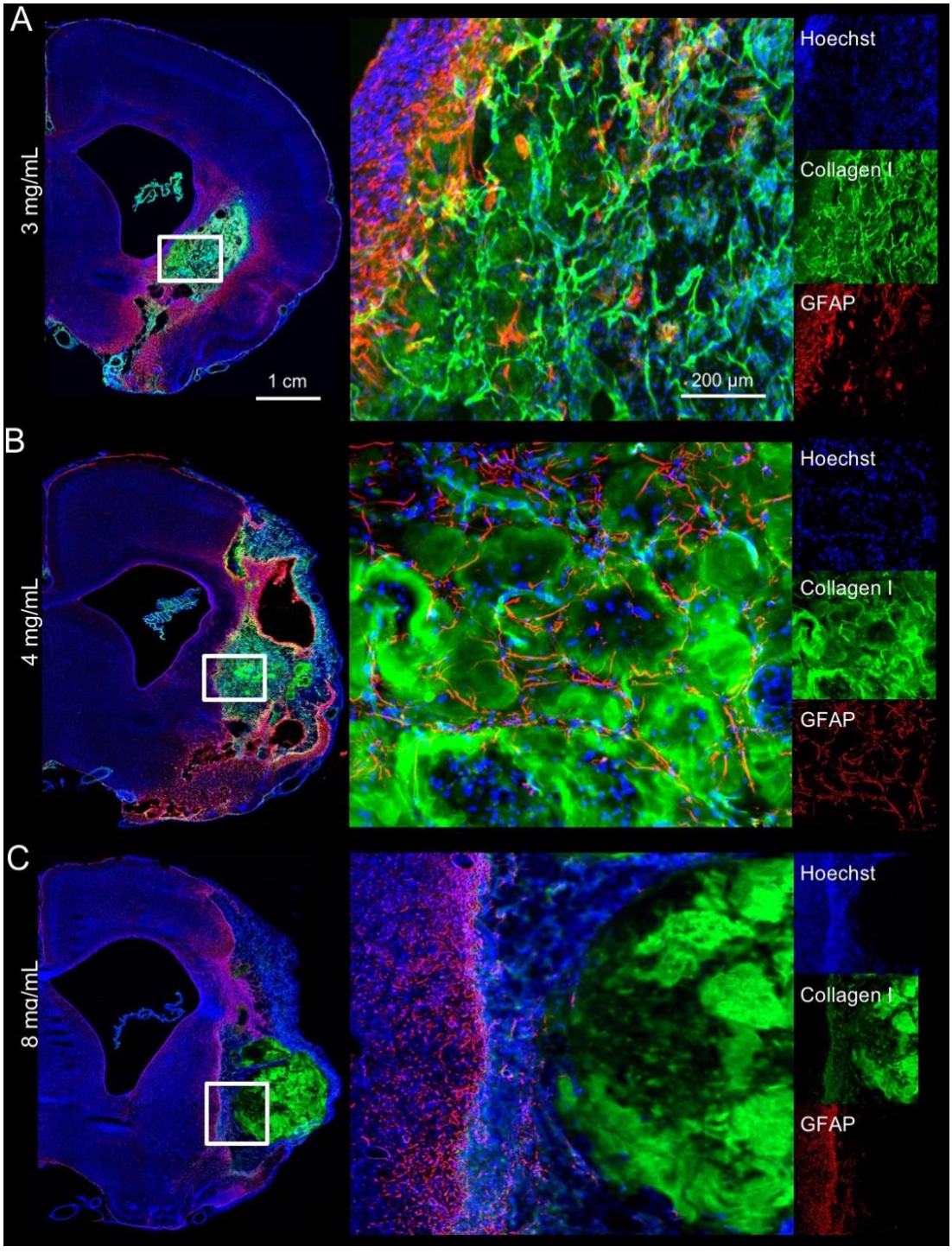

Figure 4.4. Biodegradation of the material is crucial for supporting cell infiltration and tissue remodeling. Biodegradation of ECM hydrogel is concentration dependent with less concentrated 3 and 4 mg/mL bioscaffolds getting efficiently degraded, whereas the 8

mg/mL persist longer. *A.* ***At Day 90, very small amount (5.9 %) of the 3 mg/mL ECM was present with host cells showing an excellent invasion and structural remodeling. An even distribution of the invading GFAP+ cells is seen throughout the remaining hydrogel.*** *B.* ***With 4 mg/mL, chain cell invasion can be seen with GFAP+ cells filling the space in between patches of ECM hydrogel, as identified by collagen I staining.*** *C.* ***In contrast with these less concentrated hydrogels, a sharp boundary between the biomaterial and host was evident in animals injected with 8 mg/mL. Density of cells in the hydrogel at 90 days was much lower compared to the less concentrated gels. These observations highlight key differences in biodegradation and cell infiltration between different concentrations of ECM hydrogel.***

attracted 4x fewer cells (average 96,267, $F=3.522$, $p<0.05$, **Figure 4.5.B**). This pattern was consistent for all time points ($F=6.748$, $p<0.01$) with the 4 mg/mL condition initially attracting more cells and then rapidly decreasing to the level of the 3 mg/mL ECM hydrogels. However, the total number of invading cells is also affected by ECM hydrogel volume. As ECM hydrogel is rapidly degraded in the 3 and 4 mg/mL condition, but not in the 8 mg/mL condition, total cell invasion does not reflect the qualitative impression of cell content within the bioscaffold. Cell density within the ECM reflects this consideration and indicates that for the 8 mg/mL ECM hydrogel, cell density decreases with time, reflecting the slower biodegradation observed by 90 days (**Figure 4.5.C**). In contrast, the 4 mg/mL condition provides a consistent cell density indicating the mode of action for the more rapid biodegradation and tissue replacement ($F=4.065$, $p<0.05$). In the 3 mg/mL condition, cell density increased over time to reach the level of the 4 mg/mL hydrogel, potentially reflecting the lower inductive potential of this concentration and weaker support for cell migration. Efficient cell invasion was typically accompanied by blood vessels in degrading ECM hydrogel (**Figure 4.5.D**), as well as by a large number of astrocytes and macrophages occupying this intermittent space (**Figure 4.5.E**).

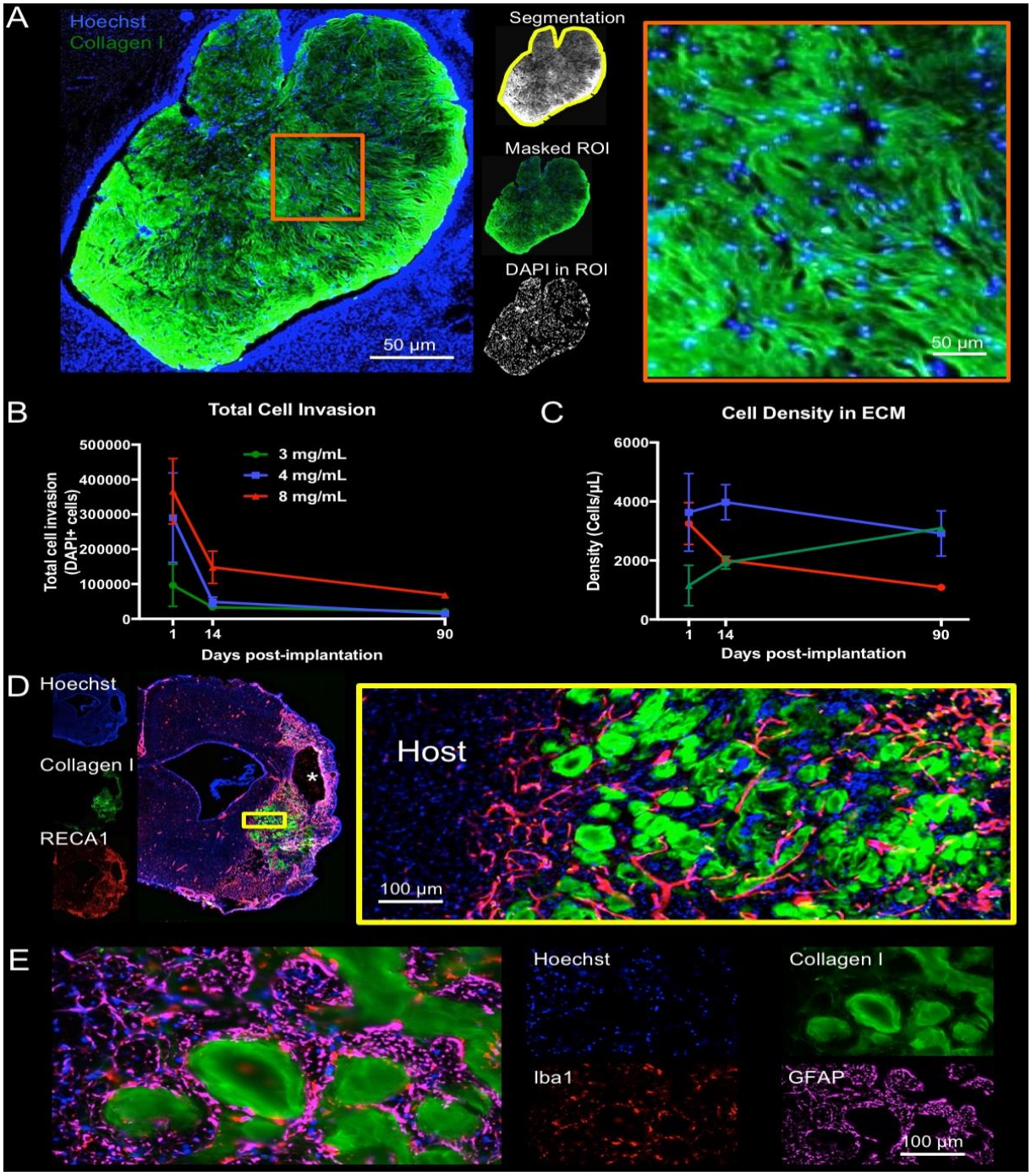

Figure 4.5. Presence of host cells in ECM hydrogel. *A.* ***Using collagen I staining, a region of interest (ROI) was defined around the edges of the biomaterial and applied to the DAPI image to provide a quantification of the number of cells present within the hydrogel.*** *B.* ***Total cell infiltration indicated that the 8 mg/mL hydrogel consistently contained the highest number of cells. In all conditions, a gradual decrease in total number of cells is***

seen that is related to the biodegradation of the scaffold. *C.* ***To account for ECM hydrogel volume changes due to biodegradation, cell density was calculated. The 4 mg/mL hydrogel concentration provided a very consistent density of approximately 4000 cells/µL. Cell density for the 8 mg/mL decreased from a 4 mg/mL comparable level, whereas 3 mg/mL increased to a comparable level at 90 days. These cell density dynamics reveal key differences in the inductive potential of ECM hydrogel concentrations.*** *D.* ***Cell infiltration and density here focus on the bioscaffold content. However, a significant number of cells are evident within the previous cavity in between patches of ECM hydrogel.*** *E.* ***Iba-1+ macrophages and GFAP+ astrocytes are common phenotypes, but no scar or foreign body response was evident.***

4.3.4 Macrophage density affects ECM biodegradation

The invasion of host cells into ECM hydrogel is dominated by macrophages. Invasion of these phagocytic cells occurs through the peri-infarct tissue across the glial scarring (**Figure 4.6.A**). Iba-1 cells are present with distinct morphological characteristics, such as a rounded or amoeboid shape, but also filopodia shapes with processes protruding into their surroundings (**Figure 4.6.B**). M1- (CD86+) and M2-like (CD206+) polarization markers further distinguish macrophage activity within the bioscaffold. A quantification of the proportion of macrophages within the ECM hydrogel showed that the 8 mg/mL concentration consistently contained a higher percentage of Iba-1+ macrophages compared to the other concentrations, increasing to approximately 50% ($F=13.37$, $p<0.001$, **Figure 4.6.C**) over time. The 3 and 4 mg/mL concentrations only contained about 30% macrophages at any time point and showed faster biodegradation than the 8 mg/mL concentration. Total macrophage invasion mirrored the total cell invasion, with 8 mg/mL containing a significantly greater quantity of cells at all time points ($p<0.001$).

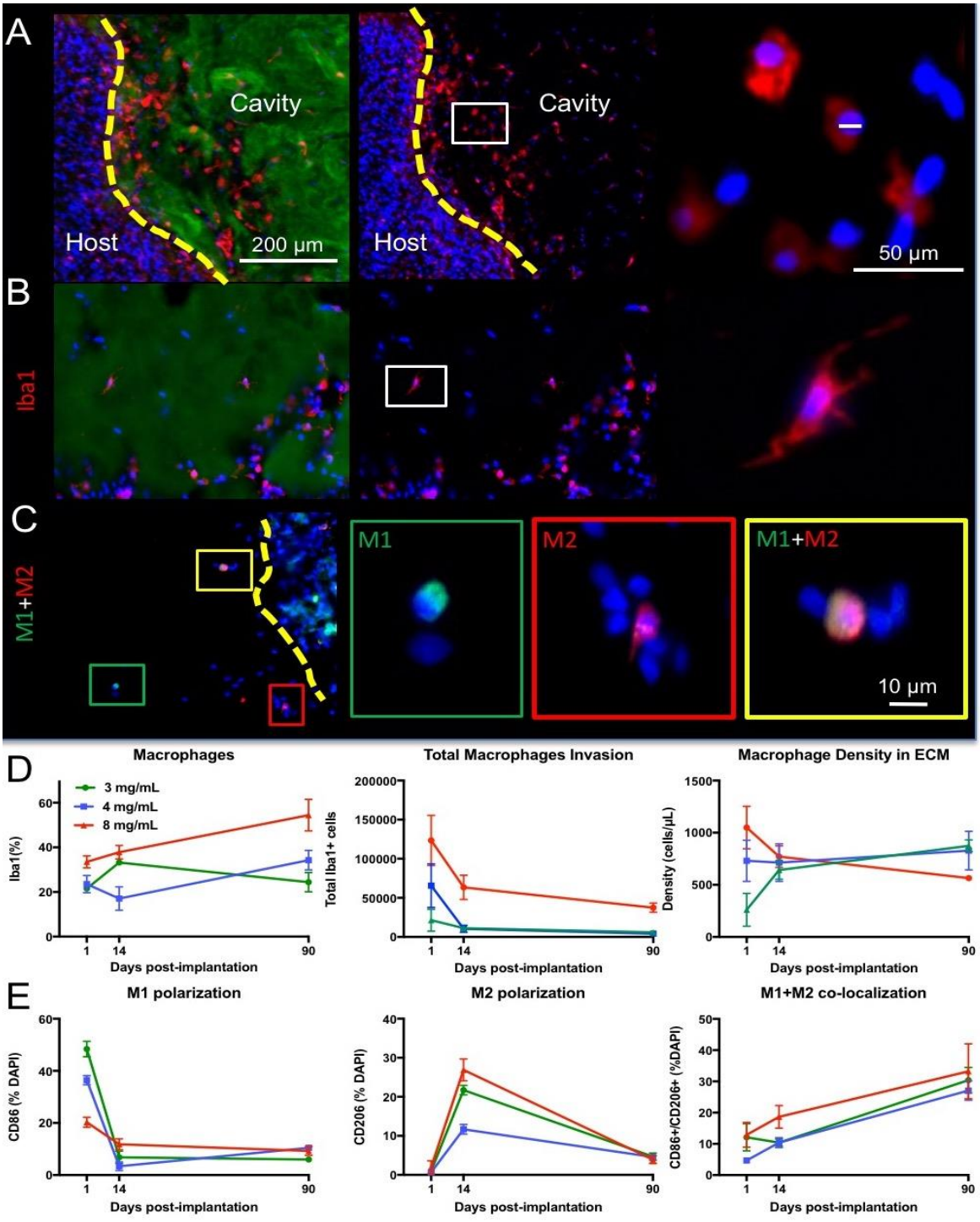

Figure 4.6. Phenotypic characterization of invading immune cells in ECM hydrogel.

A. *Invasion of Iba-1+ macrophage is evident at the tissue/hydrogel interface. Collagen I staining of the ECM hydrogel defined the region of analysis of macrophage invasion. Individual leader*

cells spread through the material, typically with an amoeboid shape 1 day post-implantation. ***B.*** *At 14 days post-implantation, clusters of Iba-1 positive cells were increasingly common, with some macrophages exhibiting an activated and ramified morphology.* ***C.*** *M1-like (CD86) and M2-like (CD206) polarization of macrophages was also evident with some cells expressing both markers, especially at 90 days.* ***D****. The 8 mg/mL ECM concentration invoke the highest proportion of macrophage and this increased with time. However, the total number of macrophage gradually decreased in all conditions. Density of macrophages within efficiently degrading hydrogel was high and persisted at approximately 700-800 cells/ µL. Only in the 8 mg/mL ECM hydrogel was there a decrease in macrophage density.* ***E.*** *Analysis of polarization of macrophages indicated that M1-like phenotypes were predominant 1 day post-implantation, but that M2-like cells were common 14 days post-implantation. By 90 days, both M1 and M2 were commonly found in the same macrophage cell.*

Macrophage density within the ECM hydrogel showed a gradual decrease in the 8 mg/mL condition, while the 4 mg/mL concentration showed a consistent density of 700-800 cells/µL (F-3.297, $p<0.05$). This level was also reached and maintained by the 3 mg/mL preparation at 14 days post-implantation. A phenotypic shift in macrophages was evident with a large proportion (35-48%) showing M1-like characteristics at day 1, especially in the lower ECM concentrations (F=23.21, $p<0.001$, **Figure 4.6.D**). The 8 mg/mL hydrogel had significantly fewer M1-like macrophages at day 1 (~20%) with only a minimal decrease over time to reach the same level (~10%) as the 3 and 4 mg/mL bioscaffolds. A shift in polarization from M1-like macrophages at day 1 to M2-like at day 14 was evident with over 20% of cells showing M2-like characteristics for the 3 and 8 mg/mL group and 11.6% for the 4 mg/mL preparation (F=10.25, $p<0.001$) compared to <4% of cells having only a M2-like marker expression at day 1 and 90 (F=128.8, $p<0.001$). With time (F=15.77, $p<0.001$), co-expression of M1-like and M2-like cell markers increased consistently for all groups, with 27-33% of cells co-expressing both markers (F=2.06, n.s.,

Figure 4.6.E). These results suggest that macrophage density is a key factor driving biodegradation of the ECM hydrogel and that a phenotypic shift in macrophage identify is evident to promote a pro-repair response by 14 days post-implantation.

4.3.5 Neovascularization of implanted hydrogel

Neovascularization is necessary to ensure the long-term survival of invading cells. In the 8 mg/mL ECM hydrogel, very few blood vessels were evident. In contrast, neovascularization was evident in the 3 and 4 mg/mL bioscaffold by 90 days, including branching of different vessels inside and in between the ECM hydrogel (**Figure 4.7.A**). In some cases, very tortuous structures were present (**Figure 4.7.B**), similar to angiogenesis in some peri-infarct areas post-stroke. The number of endothelial (i.e. RECA1+) cells invading the ECM hydrogel (**Figure 4.7.C**) was quantified to determine the cellular basis for neovascularization. The small percentage of endothelial cells that invaded the hydrogel 1 day post-implantation appeared to follow specific trails inside the ECM.

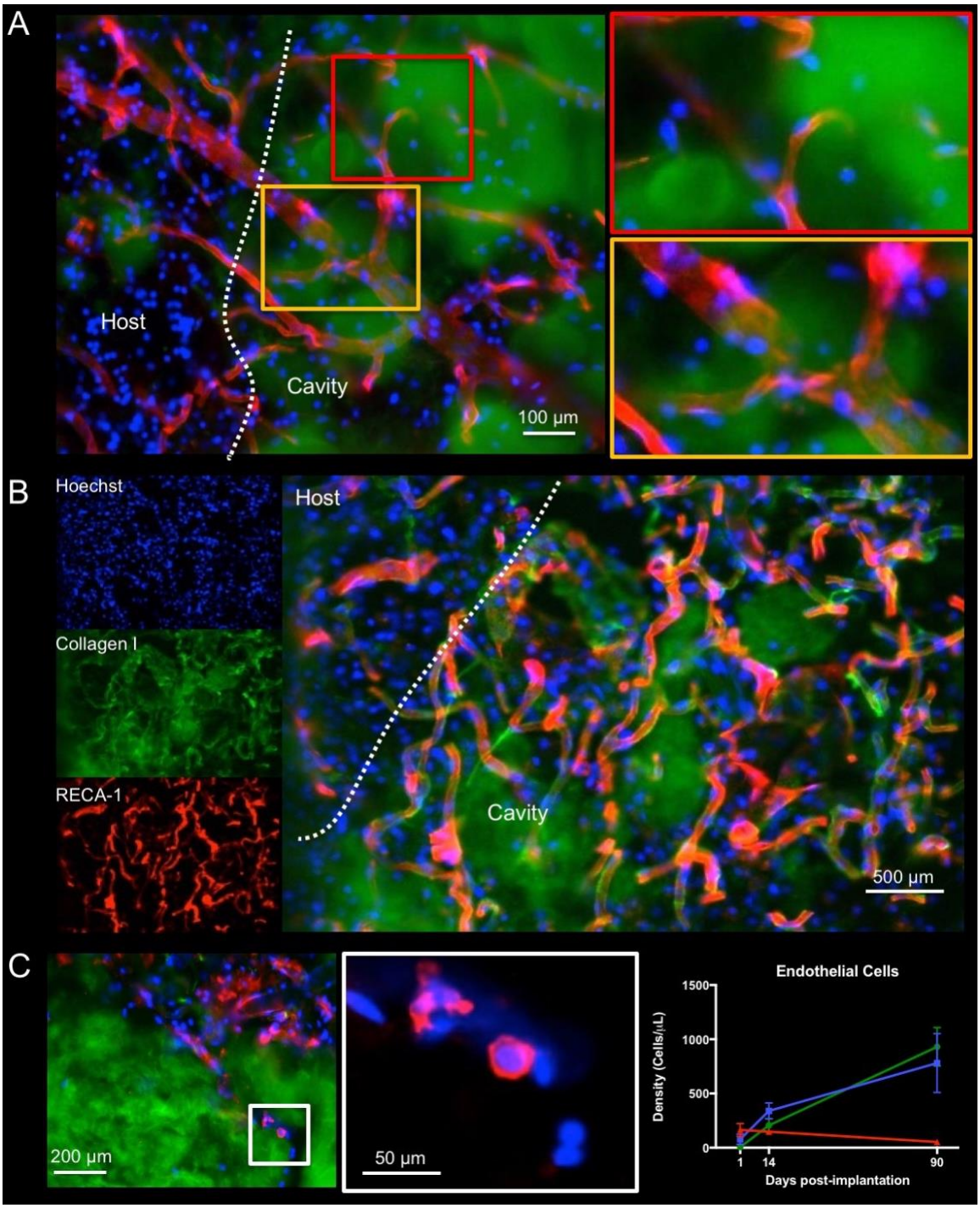

Figure 4.7. Vascularization of the ECM hydrogel.

A. *Neovascularization inside the hydrogel was evident at 14 days if hydrogel underwent an efficient biodegradation, as illustrated here in after implantation a 3 mg/mL ECM bioscaffold. B. However, in some cases very tortuous vessels can be seen.* ***C.*** *Preceding the formation of*

vasculature is the infiltration of endothelial cells. In the 8 mg/mL condition, infiltration of endothelial cells is seen, but there is a lack of vascular formation. A higher magnification of a RECA-1+ cells highlights the early stages of alignment of individual cells that invaded the hydrogel. ***D.*** *A quantification of endothelial cell infiltration indicated a higher infiltration in the 8 mg/mL condition 1 day post-implantation, but a turning point is reached at 14 days where there is decrease of endothelial cells at this concentration. Endothelial cell infiltration was linearly increased in the 3 and 4 mg/mL ECM hydrogel concentration, constituting almost 30% of all cells in the hydrogel at 90 days.*

No significant difference between ECM concentrations was evident at 1 day post-implantation. An inflection point occurred at 14 days, with infiltration peaking for the 8 mg/mL ($F=8.794$, $p<0.001$). An increase to 30% of all cells being endothelial cells occurred in the 3 mg/mL concentration. In contrast, only 4.8% of cells within the 8 mg/mL hydrogel were of an endothelial phenotype by 90 days post-implantation. The lack of endothelial cell invasion beyond 14 days in the 8 mg/mL hydrogel indicates a key shift in the cellular response of cells at this time point. Neovascularization in the 3 and 4 mg/mL concentrations at 90 days contrasts starkly with the lack of new blood vessels in the 8 mg/mL ECM preparation.

4.3.6 Invasion of neural cells

Although macrophages and endothelial cell invasion are associated with biodegradation and vascularization of the ECM hydrogel, neural cells are required to produce *de novo* brain tissue. The infiltration of neural progenitor (DCX+) cells is evident in the peri-infarct area, as well as within the degrading ECM hydrogel (**Figure 4.8.A**). Neural progenitors

were present in the ECM hydrogel as early as 1 day post-implantation. The neural progenitor cells mature into neurons (b-III-tubulin+ and/or NeuN+) and astrocytes (GFAP+) in the degrading bioscaffold (**Figure 4.8.B and 4.8.C**), as well as inside the ECM hydrogel. Small pockets of tissue developed within the degrading bioscaffold and presented conditions that allowed for maturation of brain cells (**Figure 4.8.D**), including the formation of axonal projections as determined by neurofilament staining (**Figure 4.8.E**). Neuronal cells were typically accompanied by astrocytes and oligodendrocytes (**Figure 4.8.F**), even when sparsely distributed in the ECM hydrogel.

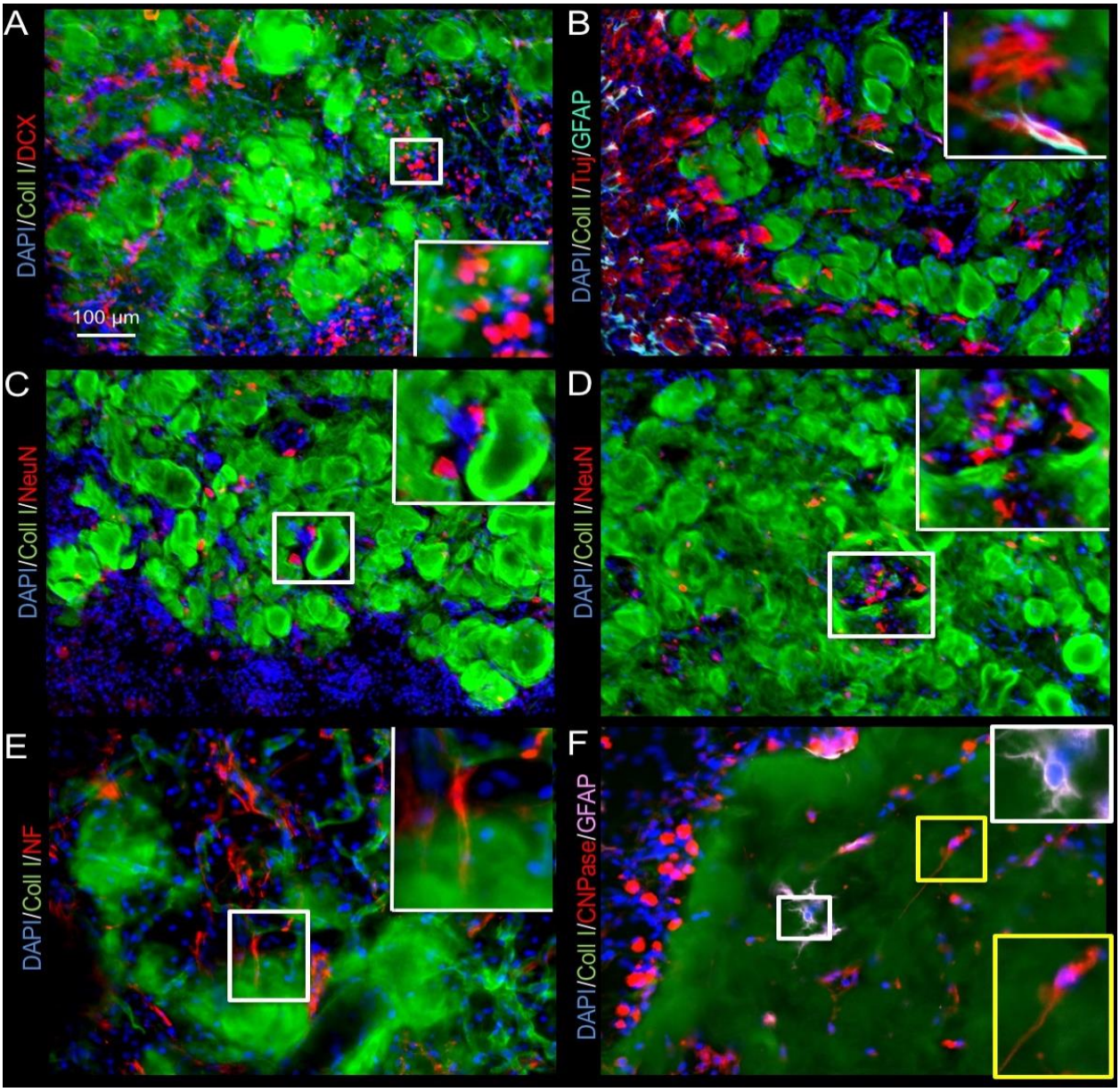

Figure 4.8. Neuronal and glial cell invasion into the ECM hydrogel.

A. *While most of the migrating neural progenitors (doublecortin, DCX) were seen at the host-biomaterial interface, a small number of DCX+ cells could be seen inside the material.* ***B.*** *Immunostaining with beta III-tubulin (Tuj) neuron marker revealed further differentiation of these progenitors inside, as well as in between the remnant of ECM hydrogel. Occasionally GFAP+ astrocytes were adjacent to these neurons, but often these neurons were not paired with astrocytes.* ***C.*** *To verify if mature neurons were being generated in this de novo tissue, NeuN staining was performed to target post-mitotic neurons that typically extend processes for tissue*

integration. Fewer of these were evident, mostly in between ECM hydrogel patches, rather than within the scaffold per se. ***D.*** *Occasional clusters containing NeuN+ cells in between ECM hydrogel were also found, potentially illustrating different stages of development within newly forming tissue.* ***E.*** *Neuron and tissue maturation were evident at 90 days with some neurons extending neurofilament (NF) containing axons.* ***F.*** *Glia lineage cells also invaded the ECM hydrogel. There were surprisingly fewer astrocytes inside the hydrogel, whereas oligodendrocytes efficiently colonized the weaker 3 and 4 mg/mL scaffolds by 90 days post-injection.*

In the 8 mg/mL condition, the ECM appeared to still be present at 90 days with cells contained within the bioscaffold. A quantification of neural phenotypes for comparison between concentrations and time points was focused on cells within ECM hydrogel (**Figure 4.9**). Neural progenitors infiltrated the ECM hydrogel at all concentrations by day 1, with most neural progenitors being attracted by the 8 mg/mL condition ($F=10.96$, $p<0.001$). However, all groups presented with a similar percentage and density of neural progenitors in the bioscaffold at 14 and 90 days, reflecting the further infiltration of host brain cells at all time points. As neural progenitors within the hydrogel differentiated, mature neuronal markers, such as NeuN, became more prominent and steadily increased from <2% to 5% in the 3 and 4 mg/mL condition ($F=32.92$, $p<0.001$). The 8 mg/mL hydrogel contained only 3.6% NeuN+ cells by 90 days. Accounting for ECM volume, density of neurons showed a further distinction between 3 and 4 mg/mL ($F=11.09$, $p<0.001$), with the less concentrated 3 mg/mL hydrogels showing a greater neuron density with an average of 226 neurons per µL ECM hydrogel. The quantity of astrocytes (GFAP+) within the 3 and 4 mg/mL hydrogel also gradually increased with time to approximately 10% cellular content, whereas significantly fewer astrocytes were present within the 8 mg/mL preparation ($F=14.61$, $p<0.001$).

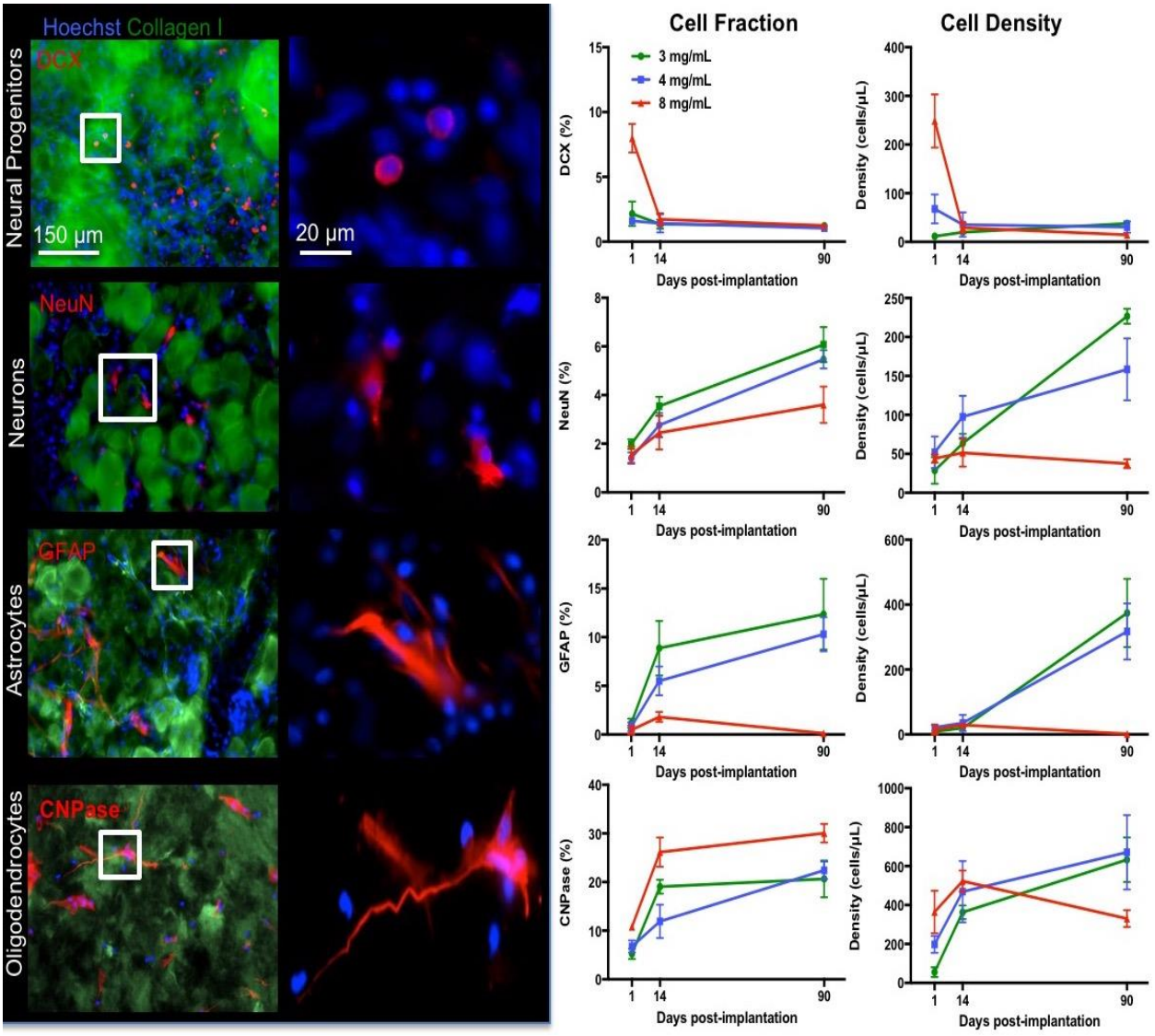

Figure 4.9. Phenotypic characterization and quantification of invading neuronal cells.

The proportion of neural cells 1 day post-implantation was approximately 30% with neural progenitors and oligodendrocytes being the predominant phenotypes. The 8 mg/mL ECM hydrogel was especially efficient in attracting neural progenitors at this time point. However, the proportion of neural progenitor content reduced by 14 days, as more mature phenotypes became more prominent, consistent with differentiation of cells and maturation of tissue. At 90 days, the less concentrated 3 and 4 mg/mL hydrogel contained a higher density of neurons, astrocytes and oligodendrocytes compared to the 8 mg/mL concentration. The 3 and 4 mg/mL ECM concentrations therefore provide favorable conditions for neural tissue formation.

Astrocyte density was approximately twice that of neuronal density and equivalent between both 3 and 4 mg/mL hydrogels. In contrast, oligodendrocytes were significantly increased in the 8 mg/mL condition to almost 30% of cells ($F=13.27$, $p<0.01$). In all ECM concentrations, oligodendrocytes increased with time and were the dominant neural phenotype by 90 days ($F=42.12$, $p<0.001$). However, considering the number of oligodendrocytes in relation to ECM hydrogel volume, a significant lower density of oligodendrocytes was evident in the 8 mg/mL concentration at 90 days compared to the 3 and 4 mg/mL condition ($F= 3.78$, $p<0.01$). Indeed, the density of oligodendrocytes was 3-fold greater than neuron density in the less concentrated gels. This phenotypic analysis of neural cells inside the ECM hydrogel shows an increasing presence of cells that are required to generate neural tissue within the bioscaffold, with predominance of oligodendrocytes. Although neurons are present, they are scarce in numbers and appear insufficient to replace functional brain tissue. Compared to 8 mg/mL hydrogel, the 3 and 4 mg/mL ECM preparations achieved a greater number of neurons and astrocytes, potentially further highlighting the favorable properties of these concentrations for inducing brain tissue restoration.

4.3.7 ECM biodegradation correlates with cellular density

The degree of biodegradation of the ECM hydrogel is related to the stroke cavity and the density of cells with the remaining scaffolding (**Figure 4.10**). At 1 day post-implantation, this the remaining ECM volume was correlated to lesion volume ($r=0.74$, $p<0.01$). This correlation became even stronger at 90 days, with a greater spread between animals, i.e.

degradation of ECM produced smaller lesion volumes, whereas a lack of degradation resulted in larger lesion ($r=0.92$, $p<0.01$). ECM biodegradation is therefore directly correlated with reduced the extent of a lesion cavity. To probe if ECM biodegradation is linked to cell infiltration, ECM volume was correlated with the total number of invading cells. Initially, a non-significant medium correlation ($r=0.49$) was found. However, by 90 days, an inverse relationship ($r=-0.81$, $p<0.001$) was evident indicating that lower amounts of ECM bioscaffolding exhibit higher cell densities.

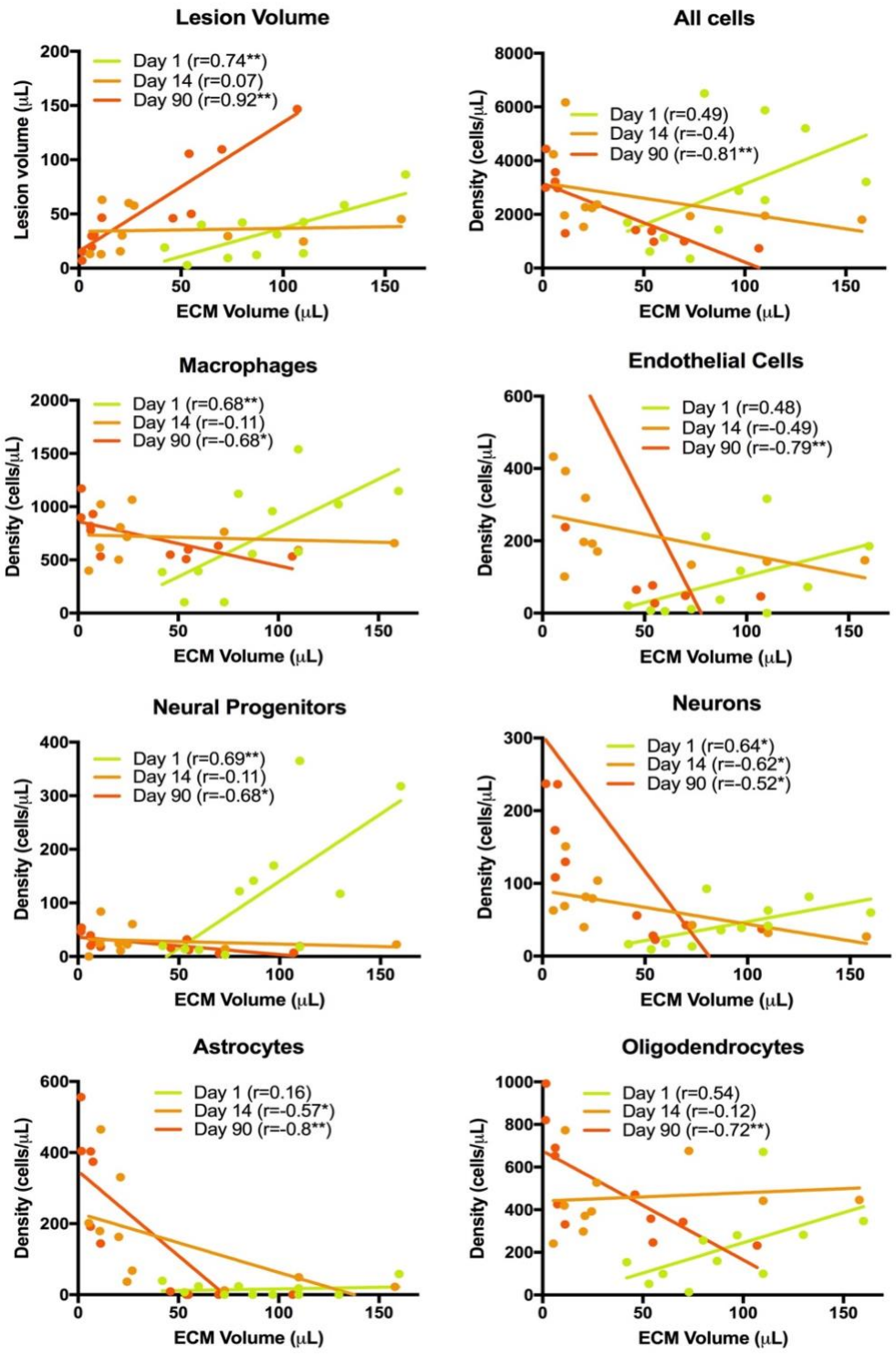

Figure 4.10. Correlations of ECM hydrogel volume and cellular content.

To evaluate the relationship between ECM hydrogel degradation and cellular content, a correlational analysis at each time point was performed. ECM hydrogel volume 1 day post-

implantation revealed a high (r>0.5) positive correlation with the density of cells that invaded. Only astrocytes did not exhibit an association. With time a dramatic inversion of this relationship occurred with cell density being negatively correlated with ECM hydrogel volume. These results indicate that at day 1, the ECM hydrogel volume drives the quantity of cells infiltrating (i.e. large volume of ECM leads to more cells infiltrating), but by 90 days it is the degradation of the ECM hydrogel that is the key determinant of cell density (i.e. good degradation leads to high cell density).

This is consistent with the observation that efficient biodegradation in the 3 and 4 mg/mL conditions was accompanied by a high cell density within the bioscaffold, whereas a low cell density was found in the 8 mg/mL hydrogel, which underwent a limited biodegradation. The gradual shift from a positive to a negative correlation is evident over time, revealing how intertwined the process of ECM biodegradation and cell density within the scaffold is.

Further correlational analyses of cell phenotypes and their relationship to ECM biodegradation also demonstrated this temporal shift (**Figure 4.10**). Macrophage density is initially positively correlated with ECM volume, i.e. the larger the ECM volume, the higher the density of macrophages ($r=0.68$, $p<0.01$). Yet, by 14 days this relationship is no longer evident ($r=-0.11$, n.s.) and by 90 days an inverse association emerged ($r=-0.68$, $p<0.05$), with denser macrophage presence being related to less scaffolding remaining. This temporal shift was also evident for endothelial cells ($r=-0.79$, $p<0.01$ at 90 days), neural progenitors ($r=-0.68$, $p<0.05$ at 90 days), neurons ($r=-0.52$, $p<0.05$ at 90 days) and oligodendrocytes ($r=-0.72$, $p<0.01$ at 90 days). On day 1, astrocytes did not show a strong association with ECM volume ($r=0.16$, n.s.) and by 14 days post-implantation a medium size negative correlation emerged ($r=-0.57$, $p<0.05$) indicating that better biodegradation

produced more astrocytes infiltration. By 90 days, this correlation was even stronger ($r=-0.8$, $p<0.01$). Although correlation does not imply causation, astrocytes and endothelial cells showed stronger correlation with ECM biodegradation at 90 days than macrophages, potentially highlighting their involvement in ECM hydrogel biodegradation in the brain.

4.4 DISCUSSION

The long-held Ramon y Cajal dogma that the brain does not have the capacity to repair [219] was refuted with the discovery of neural stem cells (NSCs) in the subependymal zone and their response to tissue damage [220]. Peri-infarct implantation of NSCs promoting behavioral recovery further demonstrated the potential to promote tissue repair using these cells [57]. However, the dogma that lost brain tissue cannot regenerate (i.e. form new tissue rather than replace cells) has mostly remained unchallenged [221, 222]. Based on our previous work using ECM hydrogel for injection into the stroke cavity [112, 114, 149, 150], the present study suggests that the brain has an endogenous potential to regenerate lost tissue if an inductive and degradable bioscaffold that can support neovascularization and infiltration of neural cells is provided.

4.4.1. Achieving an efficient biodegradation in the brain

A concentration of >3mg/mL ECM is required to achieve gelation and retention of the bioscaffold in a stroke lesion [114]. Increases in ECM concentration produce a stiffer and

denser gel, with 8 mg/mL being equivalent to brain tissue (G' 500-1000 Pa) [223-225]. Acute cellular infiltration in an 8 mg/mL ECM hydrogel was greater than other concentrations [112], but there was limited 28% degradation of this concentration at 90 days [149]. This relatively slow degradation of the ECM contrasts with that of peripheral organs, where ECM bioscaffolds in solid configurations (such as sheets) show complete replacement within 75-90 days [194, 226-229]. Two key questions emerge from the present study: 1) Does the brain have the same capacity to degrade ECM bioscaffolds as other organ systems, and 2) is the biodegradation profile determined by the stiffness of the ECM hydrogel. The biodegradation characteristics in peripheral organs are mostly based on sheets of ECM, rather than hydrogel, and do not address the influence of ECM stiffness on tissue repair [230]. We investigated different concentrations of ECM hydrogels to determine the impact of their rheological properties on biodegradation at different time points. The stiffer 8 mg/mL showed a slow biodegradation, as previously reported [149], whereas the less concentrated and less stiff gels of 3 and 4 mg/mL were resorbed at a rate twice as fast, with an ~80% reduction in volume within 14 days. This biodegradation is faster than the 50% biodegradation reported at 30 days in peripheral soft tissue defects [194], but could be a reflection of differences in product formulation. Importantly, these results show that the brain is capable of ECM hydrogel degradation and that this may be influenced by stiffness of the biomaterial.

The rheological properties of the ECM hydrogel are in part determined by its density and content of inductive material. Higher concentrations of ECM hydrogel package more material into the same space producing a denser scaffold that can limit cell invasion, but also present more biomaterial to degrade for the same volume. The

greater cell invasion at 1 day in the 8 mg/mL higher concentration indicates that density and stiffness of the material is not a barrier for infiltrating cells. In contrast, the results from the 3 and 4 mg/mL conditions, which contain less than half the inductive material of the 8 mg/mL condition, provide a continued cell invasion and biodegradation. Macrophage invasion was positively correlated (r=0.68) with ECM volume at 24 hours after implantation, but over time this relationship inverted (r=-0.68) with lower macrophage density being related to poor ECM degradation (i.e. larger remaining volume). We surmise therefore that stiffness and density, rather than the inductive content, of the 8 mg/mL are the main barriers to macrophage infiltration and hydrogel resorption. Ideally, these two variables (rheological properties and inductive content) can be dissociated to specifically investigate the contribution of each to cell migration and biodegradation. Although this level of experimental control can be readily achieved with synthetic polymers and peptides, the use of natural materials generally does not afford this distinction.

The inductive properties of ECM bioscaffolds remain poorly understood, although the release of chemokine factors, the release of matrix bound nanovesicles, as well matricellular and juxtracrine signaling have been all been thought to play an orchestrated role [196]. These mechanisms have led to the concept that ECM provides the “soil” to seed stem cells from the host organ [195]. However, the most effective constitution of this “soil” remains unknown. A comparison of ECM hydrogel from different organs and their potential to replace lost tissue can provide a pragmatic approach to contrast favorable components [231]. A bottoms-up approach can also investigate different individual components, but it might fail to replicate some of the complexities of co-stimulation that

occur with natural bioscaffolds. The concept of “ground substance” has been proposed as an amorphous gel in extracellular space that contains ECM proteins that induce tissue regeneration in the absence of fibrous materials, such as collagen and elastin, which are mostly require for structural purposes [232]. Although this ground substance might vary depending on the tissue, most cell migration uses similar molecules. Molecules involved in the infiltration of cells might hence be well conserved between organs. In this context, it is interesting to speculate that the repair process observed here follows similar processes to those observed in wound healing [233]. A key difference is that no granulation tissue is formed in the CNS. Granulation tissue (typically rich in type III collagen) is typically weaker than actual tissue containing type I collagen [234]. This would concur with our observation that ECM hydrogels weaker than actual brain tissue performed better in promoting tissue regeneration. Provision of ECM hydrogel, as described here, hence would introduce a “ground substance” that serves as granulation tissue to support the infiltration of host cells and angiogenesis.

4.4.2. Neovascularization of a brain tissue cavity

A quintessential step in tissue engineering is the re- or neovascularization of *de novo* tissue [235]. Transplantation of NSCs attached to poly-lactic acid - co-glycolic acid (PLGA) microparticles is insufficient to efficiently vascularize newly forming tissue [71, 89], but requires the secretion of vascular endothelial growth factor A (VEGF-A) to promote a neovascularization [236]. The inductive properties of ECM hydrogel are in part due to its growth factor content, including VEGF-A [91]. The higher 8 mg/mL ECM

concentration attracted higher numbers of endothelial cells compared to the lower hydrogel concentrations [112], but failed to produce a robust vasculature by 90 days [149] Incorporation of NSCs for co-delivery with ECM hydrogel also did not lead to efficient vascularization [89]. In contrast to these failures of neovascularization of the stroke cavity, here we achieved an efficient and extensive vascularization of ECM hydrogel with 3 and 4 mg/mL weaker bioscaffolds. Although these lower concentrations produced less cell invasion at 24 hours post-implantation, potentially due to their lower inductive potential, the weaker gels afforded a more persistent invasion and greater organization of tubular structures within the scaffold. A neovascularization of the stroke cavity is hence possible without modification of the ECM hydrogel, with scaffold stiffness and density potentially being key determinants in promoting angiogenesis. The precise mechanisms of these processes require further investigation.

One challenge in understanding the processes leading to an efficient vascularization is the changing properties of the bioscaffold due to cell infiltration. The presence of cells, such as macrophages, leads to a greater porosity, secretion of different chemokines, but also deposition of new ECM. The invasion of endothelial cells and formation of blood vessels can also contribute to this process by providing a new route for peripheral macrophages to invade the hydrogel from within rather than through the peri-infarct tissue. At 90 days, endothelial cell density was highly correlated ($r=-0.79$) with the degree of ECM biodegradation indicating the intricate connection between these two processes. It is likely that angiogenesis and biodegradation act in conjunction with each other. It is this interaction that potentially explains the stark dichotomy between very efficiently degraded and vascularized bioscaffolds at 3 and 4 mg/mL and the 8 mg/mL

concentration. Nevertheless, these differences in the time course of cellular behavior in the bioscaffold indicate the complexities of differentiating biomaterial properties and their causal influence on biological processes. Unraveling causal interactions is very challenging, but a time course analysis of cell invasion and their changing phenotypes in relation to ECM biodegradation provides novel insights into these processes and allows for the formulation of specific hypotheses that can be evaluated in more mechanistic studies.

4.4.3. Temporal profile of tissue regeneration after stroke damage

The migration of cells into the ECM hydrogel is a pivotal event to regenerate tissue. Acute cell infiltration indicates that a host response to hydrogel is very rapid. Not only macrophages and endothelial cells infiltrate within 24 hours, but also neural lineage cells that participate in peri-infarct tissue repair. Individual chain cell migration was the predominant method of acute infiltration by “leader cells” into the bioscaffold. This individual cell migration is dependent on cell-matrix interactions involving integrins and proteases [237]. Akin to cancer cell invasion leading to a remodeling of the tissue microenvironment, chains of small files followed leader cells and more extensively remodeled the bioscaffold. Although by 24 hours almost all areas of the scaffold contain individual cells, the density of cells in the scaffold shifted in the opposite directions for the 3 vs. 8 mg/mL concentrations. The less concentrated gels showed a gradual increase in cell density, potentially reflecting the weaker inductive potential at the acute time point and an easier substrate to remodel for secondary chain migration. Eventually these

channels of cell infiltration supported collective sheet cell migration at 14 days that led to a parcellation of the scaffold into smaller patches. This collective migration is more dependent on cell-cell interactions with the chain rather than their interaction with bioscaffold [238]. The 4 mg/mL concentration provided conditions for a very stable cell density within the material, whereas the stiffer and denser 8 mg/mL saw a gradual decline in cell density, although it had the highest inductive potential at 24 hours. If secondary cell migration in the gel is more reliant on interactions with other cells, the stiffer 8 mg/mL might be too dense to allow sufficient cell interactions to promote collective sheet cell migration. A successful cell infiltration pattern and colonialization of the bioscaffold therefore share similarities to cancer cell invasion and tissue remodeling [237], although the composition of cell phenotype is much more diverse and dynamic.

The time course of ECM biodegradation and tissue restoration in peripheral tissues indicates a predominance of macrophages in the first wave of invasion with most of these undergoing a M1-like polarization and being the main source of leader cells observed in individual cell chain migration. However, a shift towards M2-like macrophages is thought to be crucial for tissue remodeling [204]. Indeed, this shift was evident in the present study between the 1 and 14 day time points. Stiffer gels were associated with a higher macrophage response [175], which is consistent with more macrophages invading the 8 mg/mL concentration at 24 hours. Macrophage density within the hydrogel was key to promote a rapid biodegradation. For the 8 mg/mL concentration macrophage density decreased, but it consistently remained over 700 cells/μL for the 4 mg/mL and the 3 mg/mL. A plateau was reached by 14 days and maintained thereafter. The 4 mg/mL condition promoted significantly less M2-like macrophages at the crucial 14 day time

point. However, the peak M2-like polarization for the 4 mg/mL could have occurred between 1 and 14 days. The inductive protein content, as well as scaffold density/stiffness, are likely interacting mechanisms that govern the process of macrophage invasion and density.

In peripheral tissue, this macrophage pro-repair response is followed by host parenchymal cell infiltration. Nevertheless, we have demonstrated that by 24 hours, host cells are already present within the ECM scaffold, especially DCX+ neural progenitors [112]. There is a persistent repair response in the stroke-damaged brain that is ongoing even 1 year post-infarction [239]. It is likely that these neural cells responding to repair in the damaged peri-infarct tissue are being attracted into the ECM hydrogel. Although little is known about the infiltration of neural progenitors into hydrogels, it is likely that most neural and endothelial cells will rely on the soluble SDF-1/CXCR4 signaling axis [240] and/or juxtacrine signaling by integrins (e.g. fibronectin, laminin) in the hydrogel [241]. Further mechanistic studies will be required to determine if there are key functional differences in invasion/migratory behavior between these signaling pathways in scaffold colonization. Although the initial cell infiltration of neural progenitors was higher in the stiffer 8 mg/mL hydrogel, the less concentrated 3 and 4 mg/mL hydrogel supported better neuron and astrocyte differentiation, corroborating in vitro evidence from using cultured neural stem cells [208]. Neuronal (r=-0.52) and astrocytic density (r=-0.8) was negatively correlated with remaining ECM volume by 90 days, further indicating that efficient biodegradation observed in the less concentrated hydrogels is favorable to promote *de novo* neural tissue formation. The temporal profile of tissue regeneration after a stroke in the brain with the 3 and 4 mg/mL concentration ECM hydrogel therefore follows a similar

pattern to that reported in peripheral tissues, with a predominant early macrophage response being gradually superseded by the invasion of neural cells by 14 days with over 80% of scaffolding being degraded. A rapid 2-3 week biodegradation period has been identified as one of the requirements to promote tissue regeneration [242]. However, even at 90 days post-implantation there is still ongoing evidence of structural remodeling within this newly formed tissue. These different phases are reminiscent of the processes described for natural wound healing in other tissues [243], suggesting that ECM hydrogel acts as ground substance fostering a granulation tissue in the stroke cavity.

4.5 CONCLUSIONS

The brain mounts a repair response to damaged tissue, but no spontaneous regeneration of lost tissue occurs [222]. Despite this, the present study suggests that implantation of ECM hydrogel can lead to an induced regeneration of brain tissue. Specifically, the 4 mg/mL hydrogel (G' ~76 Pa) has the most favorable characteristics for brain regeneration. Using this formulation, 80% of the scaffold was degraded by 14 days post-implantation at a speed of 6.11 µL/day with a persistent level of 700-800 macrophages in each µL of ECM hydrogel. The density of mature neural cells consistently increased in the remaining scaffolding, reflecting the structural remodeling phase of tissue regeneration, which was still ongoing at 90 days post-implantation. These measurements provide clear performance benchmarks to compare different scaffolds and their potential for tissue regeneration in the brain [205]. Volumetric tissue loss after a stroke can potentially be treated using this approach, but functional and behavioral studies will be needed to

determine the therapeutic potential. Although further optimization and a better mechanistic understanding is required to afford greater control over the processes involved in tissue regeneration, *in situ* engineering of brain tissue using inductive biomaterials is encouraging and opens new therapeutic avenues.

5.0 NON-INVASIVE IMAGING OF PERIPHERAL MACROPHAGES INVADING BRAIN TISSUE AND IMPLANTED HYDROGEL USING ^{19}F MRI

5.1 INTRODUCTION

Invasion of macrophages into a ECM bioscaffold is the pivotal event that drives its biodegradation through constructive remodeling [205]. Although the immune response to biomaterials was initially considered detrimental to tissue engineering efforts, over the past decade the importance of macrophages has been recognized as a key modulator of scaffold biodegradation and the ensuing tissue repair. Typically, extensive time course studies are required to compare dosing effects, with lesion volume and topology being major co-variates in measurements that are difficult to control for. Longitudinal non-invasive assessments designed to visualize macrophage invasion would hence significantly facilitate our understanding of their role in scaffold degradation and also potentially provide avenues to monitor these therapies in the clinic [244]. Although there is an extensive literature demonstrating the in vivo tracking of macrophages in graft rejection using MRI [245-247], we are not aware of any reports detailing the non-invasive imaging of macrophage activity in scaffolds' biodegradation.

By using the phagocytic activity of circulating macrophages that allows these cells to engulf nano and microparticles, superparamagnetic particles of iron oxide (SPIO) are commonly used in MR imaging to label macrophages in vivo. In an inflammatory

condition, these nanoparticles are internalized by the macrophages and accumulate at the affected site. However, quantification of SPIO labeled cells is complicated since it doesn't follow a linear relationship with concentration and the signal produced by the iron particles interferes with the T_2-weighted analyses of lesion and peri-infarct tissue volumes.

Imaging of macrophages from the reticuloendothelial (RES) system using perfluorcarbon (PFC) labeling and ^{19}F MRI has been first reported 30 years ago [248]. For this, PFC nanoemulsions were systemically injected using the intra-venous route, where the agent is taken up by circulating macrophages [249-252] (**Figure 5.1**).

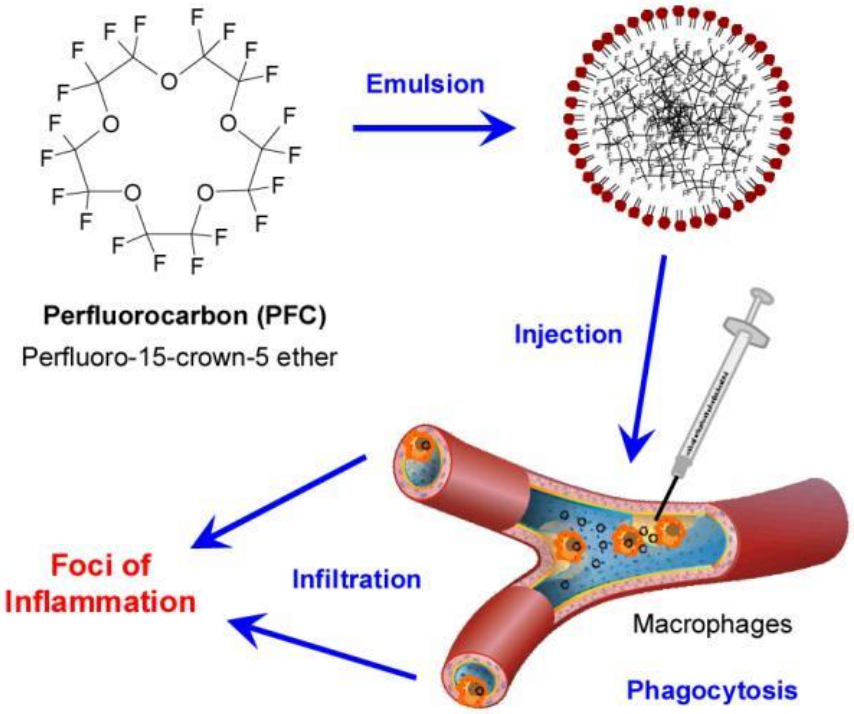

Figure 5.1. Schematic drawing describing the use of PFCs to monitor inflammatory processes. After injection, the nanoparticles are taken up my circulating

monocytes/macrophages and infiltrate the tissues of inflammation. Due to the lack of any endogenous 19F signal, the detected signals are highly specific.

These PFC-tagged macrophages will participate in immune and inflammatory events and afford a visualization of their infiltration into tissues by ^{19}F MRI [245, 253-255]. Although its sensitivity is significantly weaker compared to the detection of SPIO-labeled macrophages [249], major advantages of ^{19}F imaging is that there is no detectable fluorine in native tissue so the signal is directly detected and quantifiable (^{19}F signal is proportional to number of ^{19}F spins per voxel), and hence does not interfere with the visualization of lesion pathology or surrounding peri-infarct tissue. This tissue interface constitutes a crucial distinction to determine if macrophages invade the ECM hydrogel through the peri-infarct tissue. Furthermore, the use of PFC agent has been used in the clinic to detect implanted immunotherapeutic dendtritic cells (DCs), showing the technique is feasible and safe for human use [256]. Unlike PET/SPECT probes, ^{19}F does not undergo radioactive decay and can be used for longitudinal studies without inducing toxicity to the engulfed or surrounding cells. As PFC nanoemulsions can also be prepared to incorporate a fluorescent moiety, it is also possible to monitor the distribution of macrophages in the peri-infarct and ECM hydrogel during biodegradation using immunohistochemistry. This approach therefore will allow us to monitor macrophage activity to refine bioscaffold formulations for the treatment of stroke and eventually to have a method that could be used in patients to evaluate the host response to bioscaffolds.

Although ^{19}F MR imaging has been used to visualize macrophages in peripheral tissues, there is a lack of studies demonstrating the utility of this approach in the brain [249]. The main challenge is the greater anatomical details (high resolution) required in

the brain that typically results in lower regional density of macrophages per voxel that may not be detected and therefore risks underestimating the cell number increases. We have previously used PFC cell labeling and ^{19}F MRI to visualize the distribution of human neural stem cells (NSCs) implanted into a stroke cavity using ECM hydrogel [89]. This produced a homogenous distribution in a large volume area that did not require a narrow distinction of peri infarct tissue and scaffold. In contrast here, we aim to visualize the accumulation of phagocytic cells in the parenchyma and its gradual invasion into the ECM hydrogel. We therefore here optimized ^{19}F MR imaging sequences of PFC to ensure sufficient signal and resolution that will allow us to contrast macrophage activity in the parenchyma and implanted hydrogel.

5.2 MATERIALS AND METHODS

5.2.1 PFC nanoemulsion agent for inflammatory reaction

PFC nanoemulsion V-Sense VS-1000H (Celsense, Inc.) was used as a probe for ^{19}F MRI imaging sequence optimization and comparison. V-sense is available at 129 mM concentration of $CF_3O(CF_2CF_2O)_nCF_3$ producing a 360 mg/mL (30% vol/vol) preparation. The molecular weight of the nanoemulsion is 1380 g/mol, yielding $7.8x10^{16}$ fluorine atoms with a range of 8-14 and average of 10.5 fluorine atoms (i.e. $6.022x10^{23}$ atoms/mol) and an average diameter of 165 nm per nanoparticle. To afford an assessment of co-localization of PFC inside macrophages, a dual-label nanoemulsion containing PFC and

DM Red fluorosence (CelSense) was used for all in vivo animal experiments. The excitation and emission frequencies for DM Red occur at 596/615 nm, respectively.

5.2.2. $^{1}H/^{19}F$ MRI set up and acquisition

^{1}H and ^{19}F MRI was performed on two ^{19}F phantoms, one ex vivo head and five live animals using a 9.4T horizontal bore MR scanner (Bruker) and a 40 mm ($^{1}H/^{19}F$) double resonance coil operating at frequencies of 400.13 MHz for ^{1}H and 376.46 MHz for ^{19}F measurements. For sequence optimization, ^{19}F scans of the phantoms and ex vivo head were acquired using the DOE parameters, as described in the section 5.2.3, with a total scan time of 20 min.

In vivo MR imaging: ^{1}H and ^{19}F imaging were performed at three time points:

(1) 48 hours before ECM injection (prior to PFC injection; to determine endogenous ^{19}F signal)

(2) 24 hours before ECM injection (24 hours after PFC injection; to determine baseline ^{19}F singal and macrophage invasion)

(3) 24 hours after ECM injection

While imaging, MCAo rats were anesthetized with isoflurane (4% induction, 1% maintenance in 30% O_2) and scanned using a T_2-weighted spin-echo MRI sequence (TR = 6000 ms, TE = 8 ms, 8 Averages, FOV 40x40 mm, 128x128 matrix, 5 slices at 1.5 mm thickness). After acquisition of anatomical ^{1}H images, the resonator was then tuned to ^{19}F to acquire morphologically matching ^{19}F images. Fast imaging with steady state

precession (FISP) sequence with 5 slices, 1.5 mm slice thickness, 96x96 matrix size, 40x40 FOV, 4.8 ms TR, 2.4 ms TE, 60 degree flip angle and 30,000 Hz Bandwidth was used to detect ^{19}F with a total scan time of 1 hour. An external phantom vial containing known ^{19}F spins density of 5.6 x 10^{19} spins/mm^3 was placed in the field of view (FOV) and used as a reference during image acquisition and quantification. The FOV, slice geometry, and slice thickness were identical for both ^{1}H and ^{19}F images to allow for image overlay and tissue segmentation.

5.2.3 ^{19}F MRI sequences and optimization

To define optimal imaging parameters, we compared the most commonly used ^{19}F MR sequences using a design-of-experiment (DOE) approach, where we arrayed parameters from a low to high value. An advantage of DOE experiments is that it is possible to investigate interactions between parameters and cover the experimental space in a contour map. This then affords the selection of optimal parameters based on read-out parameters, such as SNR [257].

Sequences: The following sequences have been previously utilized for ^{19}F MRI [250, 258-262], and were compared to select the one with the greatest sensitivity for PFC nanoemulsion detection:

1. Fast low angle shot (FLASH)
2. Multi-slice multi-echo (MSME)

3. Rapid acquisition with relaxation enhancement (RARE)

4. Zero Echo Time (ZTE)

5. Fast imaging with steady-state precession (FISP)

For standard spin echo (SE) sequences (FLASH, MSME, RARE), spins are first excited by a 90^{o} radio frequency (RF) pulse, before applying a second RF pulse some time later (at TE) to refocus the magnetization and flip the direction of spins. This second pulse refocuses all reversible signal and provides optimal signal per excitation. For gradient echo (GE) sequences (ZTE, FISP), an intital RF pulse is applied to excite the spins using a flip angle < 90^{o}, before the frequency encode gradients are applied for dephasing and then reversed in amplitude to form an echo at TE. Despite acquiring less signal per excitation for GE sequences, it allows for lower TR between excitations and more signal averaging for the same scan time period.

19F phantom and concentrations: For sequence optimization, a ^{19}F phantom was prepared by filling eight glass micro-pipet capillaries with PFC nanoemulsions to detect different log10 concentrations (0, 0.01, 0.1, 1, 5, 10, 50, 100 mM, n=3/concentration) (**Figure 5.2**). The capillaries were sealed at both ends and embedded in a 50 mL conical tube containing 2% agarose in H_2O.

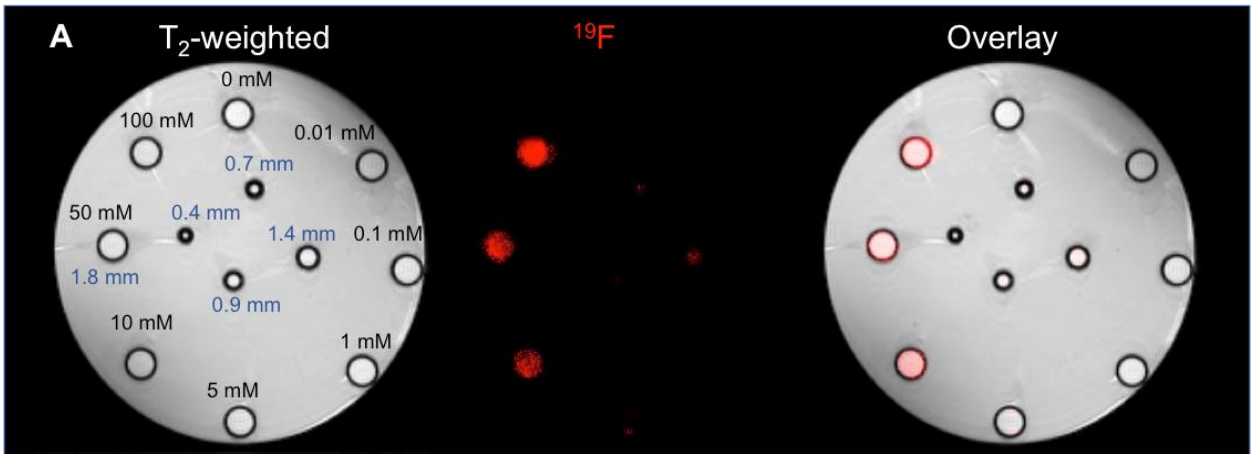

Figure 5.2. 19F phantom for sequence optimization.

A phantom was deisgned to incorporate different concentrations of V-sense for detection using DOE paramaters.

Repetition time (TR): Increasing the repetition time (TR) up to a certain limit increases the SNR, since a high TR will allow the longitudinal magnetization to approach its maximum and produce high signal intensities and low noise. However, high TR values can also produce images with poor tissue contrast and thus an optimized TR is very important to yield good SNR and tissue contrast. To determine the optimal TR that yields highest ^{19}F SNR for each sequence, scans were acquired with varying TR (100 to 2000 ms for FLASH, MSME; 500 to 4000 for RARE, 3.2 to 4 ms for ZTE, 3 to 8 ms for FISP).

Echo time (TE): SE sequences are based on repetition of 90^o and 180^o RF pulses. TE is the time between the 90^o RF pulse and MR signal sampling. A long TE results in reduced signal since the protons are likely to become out of phase, while short TE reduced dephasing and improves SNR. For spin echo sequences (FLASH, MSME, RARE), TR

and TE were arrayed to determine their interactions and effect on SNR. For GE sequences, minimum TE values are used since we do not have to wait for the 180^{o} pulse and shorter TE aloows much shorted TRs to be used, thus allowing us to repeat the pulse sequence more quickly.

Receiver Bandwidth (BW): Receiver bandwidth is the amount of frequencies collected during frequency encoding phase and decreasing the receiver bandwidth increases the SNR. However decreasing the bandwidth beyond a certain level can increase the chemical shift artifacts and thus an optimal bandwidth is needed. To determine the optimal BW for each imaging sequence, scans were acquired with varying BW (10 to 60 kHz for FLASH, MSME, RARE, 15 to 50 kHz for FISP; 40 to 110 kHz for ZTE).

Flip angle (FA): Flip angle is the angle to which the net magnetization is rotated via the application of a RF excitation pulse. For spin echo pulse sequences, increasing the flip angle increases the SNR and thus a 90^{o} flip is most commonly used. For gradient echo pulse sequences which use very short TRs for rapid repetition, using a small flip angle allows for a large fraction of longitudinal magnetization to remain and be available for the next repetition. FA can thus be varied to determine the optimal angle that yields highest SNR. Here we arrayed FA for all sequences (40 to 90° for FLASH, MSME RARE and FISP; 1 to 4° for ZTE) and for each TR to determine its effect on ^{19}F SNR.

Number of averages: Number of averages or excitations is used to represent number of times the data is repeatedly acquired to form the image. Signal averaging sums the signal

intensity together with the superimposed random noise. Increasing the scan time or number of averages directly sums the signal waveforms together and the uncorrelated noise averages out producing a higher SNR. Scans were acquired for each optimized sequence with scan time arrayed as 1 average (0.5 – 2.5 min), 15 min, 30 min, 60 min, 120 min. As signal intensity is dependent on the number of acquired averages in a given time, a comparison of optimized sequences was performed with a maximum in vivo imaging time of 60 minutes.

Voxel size: Increasing the matrix size reduces the volume of individual voxels, and thus reducing the signal received by the individual voxels. Smaller voxels will receive less signal and hence produce a low SNR image. Conversely, decreasing the matrix size will reduce the spatial resolution and increase spillover effects when the FOV is kept constant. Matrix sizes of 32x32 (3.12 mm^3), 64x64 (0.78 mm^3), 96x96 (0.35 mm^3), and 128x128 (0.2 mm^3) were arrayed for each imaging sequence to determine ^{19}F SNR and spillover effects on the ex vivo head.

Slice thickness: Increasing the slice thickness increases the voxel size that results in an increase in the total amount of signal received by individual voxels. Conversely, thinner slices are associated with more noise and reduced SNR. To determine the effect of slice thickness on ^{19}F SNR, scans were acquired with 1, 1.5, and 2 mm thickness for ^{19}F phantom and ex vivo head.

SNR and Contour plots: To define optimal acquisition parameters for each sequence, contour plots were computed based on SNR measurements. To calculate SNR, ROIs were drawn on a T2w image on the cappilary containing the PFC nanoemulsion (i.e. signal) and the surrounding gelatin defines noise. The noise intensity, rather than standard deviation, is used as divisor to avoid introduction of a calculating bias in concentrations below the detection threshold. It is also important to note that the ^{19}F signal is not obeying a normal distribution and hence standard deviation is not an appropriate measure for these types of calculations. An SNR of 1 hence indicates a signal equivalent to noise. Using the DOE approach, parameters for the different sequences were compared based on SNR and contour maps were created to visualize interactions between different imaging parameters and ^{19}F SNR. The optimal values for two independent variables will be defined by the central point of the highest SNR contour.

5.2.4. ^{19}F/fluorescent labeling of peripheral blood mononuclear cells (PBMCs)

Equal volumes of VS-1000H and VS-1000H DM Red (dual probe for MRI and fluorescence imaging) were used to label PBMCs in vivo. Two weeks post-stroke and 48 hours before ECM (4 mg/mL) implantation, rats (n=3) were anesthetized using isoflurane and a single tail vein injection of V-sense (1200mg/kg) was administered to the animal. The baseline (24 hours pre-implantation) ^{19}F scans were acquired 24 hours after PFC administration.

5.2.5. Visualization of sequence optimization on head phantom

DOE acquisition of ex vivo brain images with ^{19}F labeled immune cells will ensure the implementation of the most efficient imaging paradigm to detect macrophages in the ECM hydrogel. Two weeks following stroke and 24 hours before ECM injection, rat (n=1) was injected with 1200 mg/kg V-sense. 24 hours after the ECM injection, the rat was transcardially perfused with 0.9% saline followed by 4% paraformaldehyde (in 0.2 M PBS) to fix brain tissue. The head was post-fixed in 4% paraformaldehyde for 24 hours prior to being vaccum sealed for MR imaging. ^{19}F scans were acquired for each imaging sequence with optimized TR, BW, and FA. Number of averages, slice thickness, and voxel size were also arrayed as discussed in section 5.2.3.

5.2.6. In vivo quantification of ^{19}F signal

^{19}F signal quantification was performed in Voxel tracker software (provided by Celsense, Pittsburgh PA), which fuses ^{1}H and ^{19}F images and enables cell or inflammation quantification in the region of interest. ^{1}H and ^{19}F images were overlayed and ROIs were drawn around the lesion cavity, tissue parenchyma, contralateral hemisphere, reference tube, noise, as well as the scalp incision site. Total number of ^{19}F spins were calculated by comparing the sum of the ^{19}F signal within a ROI to the signal generated by (1) reference tube with known concentration of ^{19}F spins (5.6×10^{19} spins/mm^3), and (2)

noise. Large leukocytes, such as macrophages, have been shown to label with ^{19}F-PFC labeling agents in the high end of 10^{12} to lower end of 10^{13} ^{19}F spins per cell [254, 263]. 10^{13} spins per cell was used to calculate absolute cell number and cell density. A peripheral inflammation site is helpful here to determine if macrophages were labeled, but potentially did not respond to the injected ECM hydrogel or had a delayed infiltration response.

5.2.7 Histological validation of PFC/^{19}F macrophage detection

Post-mortem histology evaluated the overlap between the in vivo ^{19}F imaging of macrophages and the distribution of macrophages within the tissue, as assessed by immunohistochemistry at 24 hours post-implantation. Once tissues were fixed with 4% paraformaldehyde, brains were removed and placed into PFA for overnight post-fixation prior to being transferred to 30% sucrose to provide cryoprotection for histological processing. Brain sections were cut at 50 µm directly onto microscopic slides to preserve the morphology of tissue and stored at -20°C. Immunohistochemical (IHC) analyses involved overnight application of primary antibodies against Iba1 (Monocytes/Macrophages/Microglia), and collagen I to detect ECM hydrogel. To visualize co-localization of macrophages with the dual-label PFC nanoemulsion (red fluorescent), secondary antibodies conjugated to fluorescent dyes (Alexa488 green, and Alexa650 far red) were applied for 60 min prior to counterstaining of cell nuclei with DAPI (in blue). ^{19}F labeled cell count and its overlap with Iba1 was quantified over the whole tissue sections using a semi-automated quantification implemented in CellProfiler.

5.2.8 Statistical analysis

SNR calculated from noise signal rather than standard deviation follows a normal distribution and is linearly related to PFC concentration affording a parametric statistical test. Sequences, as well as parameters can hence be compared using a one-way ANOVAs. In the case of two independent variables, a two-way ANOVA was used.

5.3 RESULTS

5.3.1 DOE approach dictates imaging parameters with highest SNR

Contour plots with SNR as the dependent variable and TR, Bandwidth and flip angle as independent variables were constructed for each imaging sequence (**Figure 5.3**). For all FLASH, MSME and RARE sequences, the SNR increased with increasing TR, lower receiver bandwidths, and higher flip angles. For ZTE, TR had a minimal impact on SNR, while higher flip angles and bandwidth improved SNR. For FISP, DOE interactions revealed a central point with maximum SNR > 250 at low TR, bandwidth and 60^{o} flip angle.

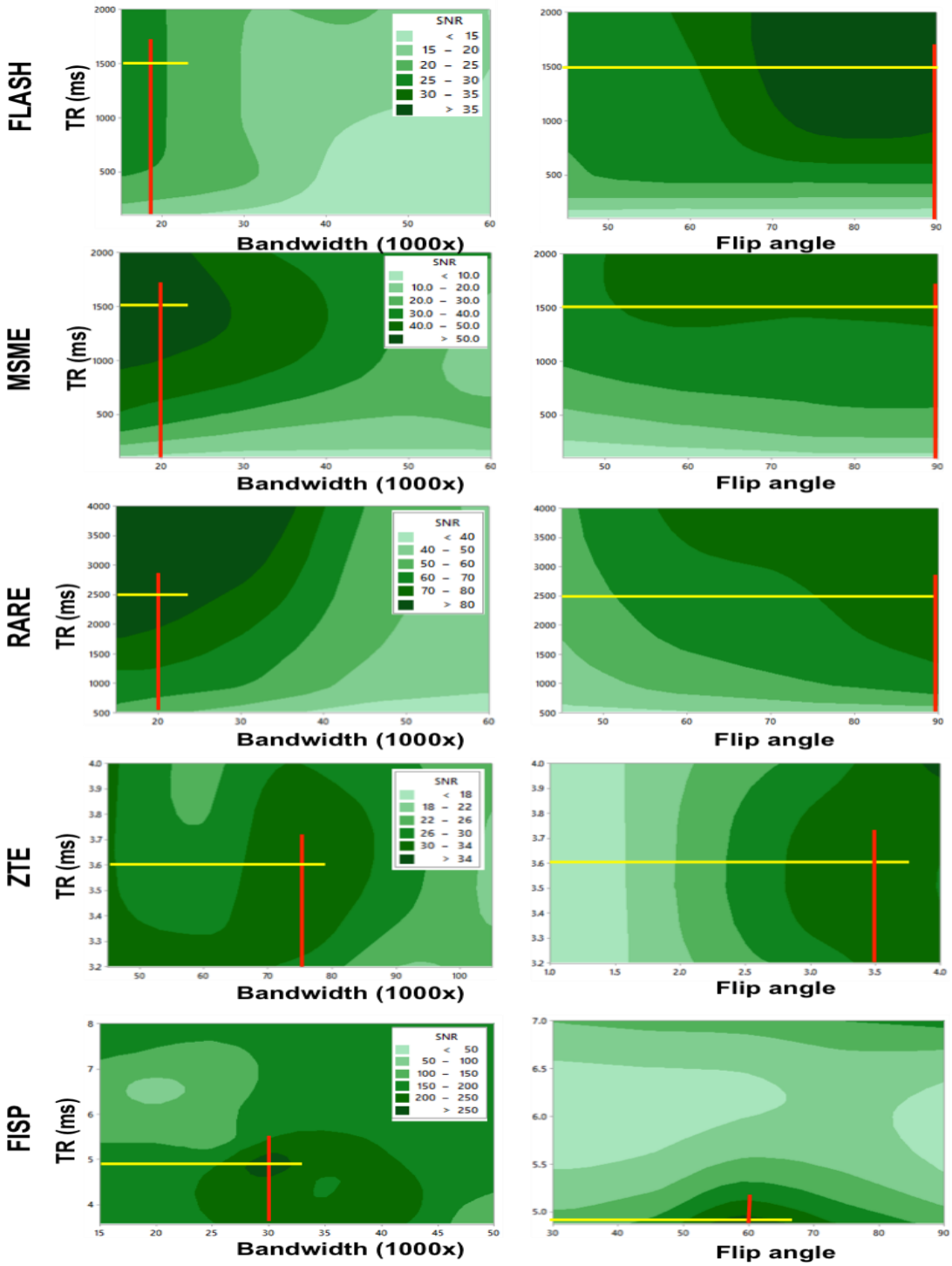

Figure 5.3. Optimization of imaging parameters using DOE approach.

To determine the optimal imaging parameters for different sequences, Repetition time (TR), Bandwidth, and flip angle were arrayed to calculate SNR for each combination. Contour plots

were then generated using SNR as the dependent variable. The optimal parameters for each imaging sequence were defined by the parameters that yielded the highest SNR.

Furthermore, interactions between TR and TE for all SE sequences showed the highest SNR for low TE (5, 10, 20 ms for FLASH, MSME, RARE) and high TR values (1500, 1500, 2500 for FLASH, MSME, RARE) (**Figure 5.4**). For MSME, a small range of optimal TR and TE was evident from the contour plots that yielded the maximum SNR.

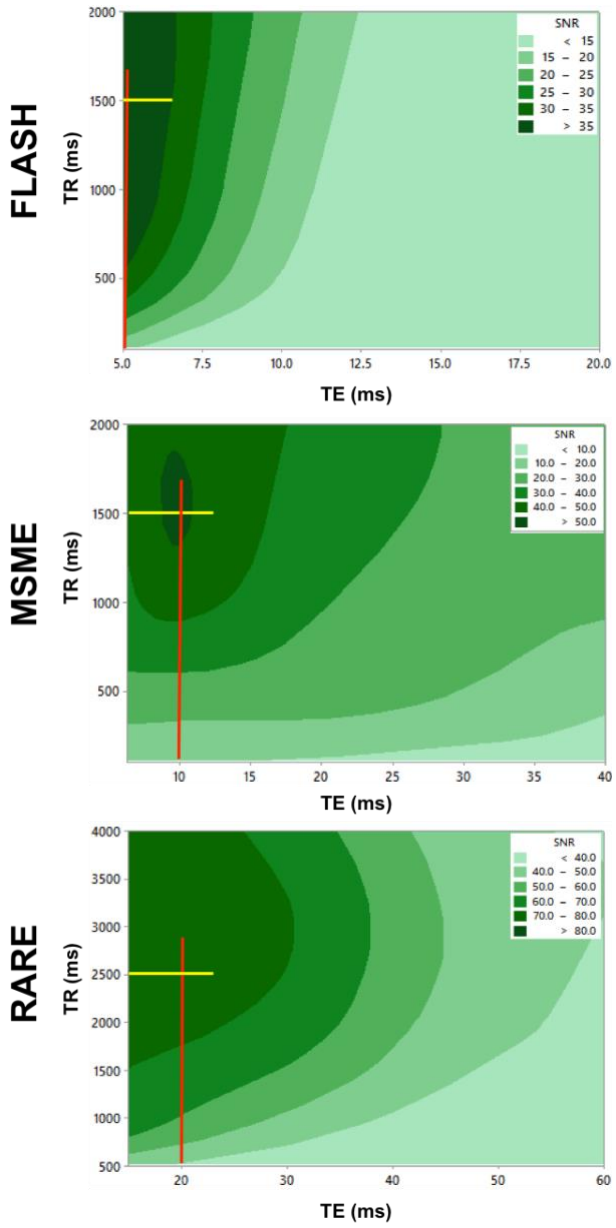

Figure 5.4. Low TE improves SNR.

To determine the effect of varying TR/TE on SNR, TR and TE values were arrayed to calculate SNR for each combination. Contour plots were then generated using SNR as the dependent variable. High TR and low TE values resulted in the highest SNR for all sequences.

Optimal imaging parameters (TR, TE, BW, FA) were then deduced from the central points of regions with maximum SNR. **Table 5** provides optimal imaging parameters for each sequence that resulted in the highest SNR. These optimal parameters were used for all subsequent sequence comparison analysis.

Table 5. Overview of optimized imaging parameters that yield the highest SNR for each sequence.

Sequence	Repetition time (TR, ms)	Echo time (TE, ms)	Bandwidth (BW, kHz)	Flip angle (FA, Degrees)	Scan time for 1 average (s)
FLASH	1500	5	18	90	150
MSME	1500	10	20	90	150
RARE	2500	20	20	90	30
ZTE	3.6	_	75	3.5	100
FISP	4.8	2.4	30	60	0.5

5.3.2 Optimized FISP sequence produces highest SNR

Comparison of optimized sequences for 50 mM PFC nanoemulsion reveals FISP achieving the highest SNR of 217 followed by RARE sequence with SNR of 66. MSME resulted in the lowest SNR of 28 (**Figure 5.5.A**). Although the FISP sequence produced 4.5x more noise than RARE, the signal intensity for FISP was 15x higher than RARE resulting in 3.3x higher SNR.

The optimized sequences were also then used to acquire ^{19}F images from the ex vivo head to compare signal quality across sequences. High noise levels and low SNR were evident in MSME, ZTE and FLASH sequences resulting in poor localization of the invading macrophages (**Figure 5.5.B**). A robust signal at the scalp indicates accumulation of macrophages at peripheral injury site (incision made during ECM delivery) and serves as a positive control. As the signal intensity increased with increasing ^{19}F concentrations, robust visualization of the signal can be seen with concentrations above 5mM (**Figure 5.5.C**). For all concentrations (0-100 mM), FISP achieved the highest SNR, with the minimum detectable concentration at 0.1mM with SNR of 2.3 (**Figure 5.5.D**). All other sequences at concentrations of 0.1 mM and lower were undetectable and similar to noise intensity yielding a SNR of ~1. For the highest concentration of 100 mM, FISP achieved a SNR of 420 (2.8x RARE, 5.9x FLASH, 6.9x MSME and 8.7x ZTE).

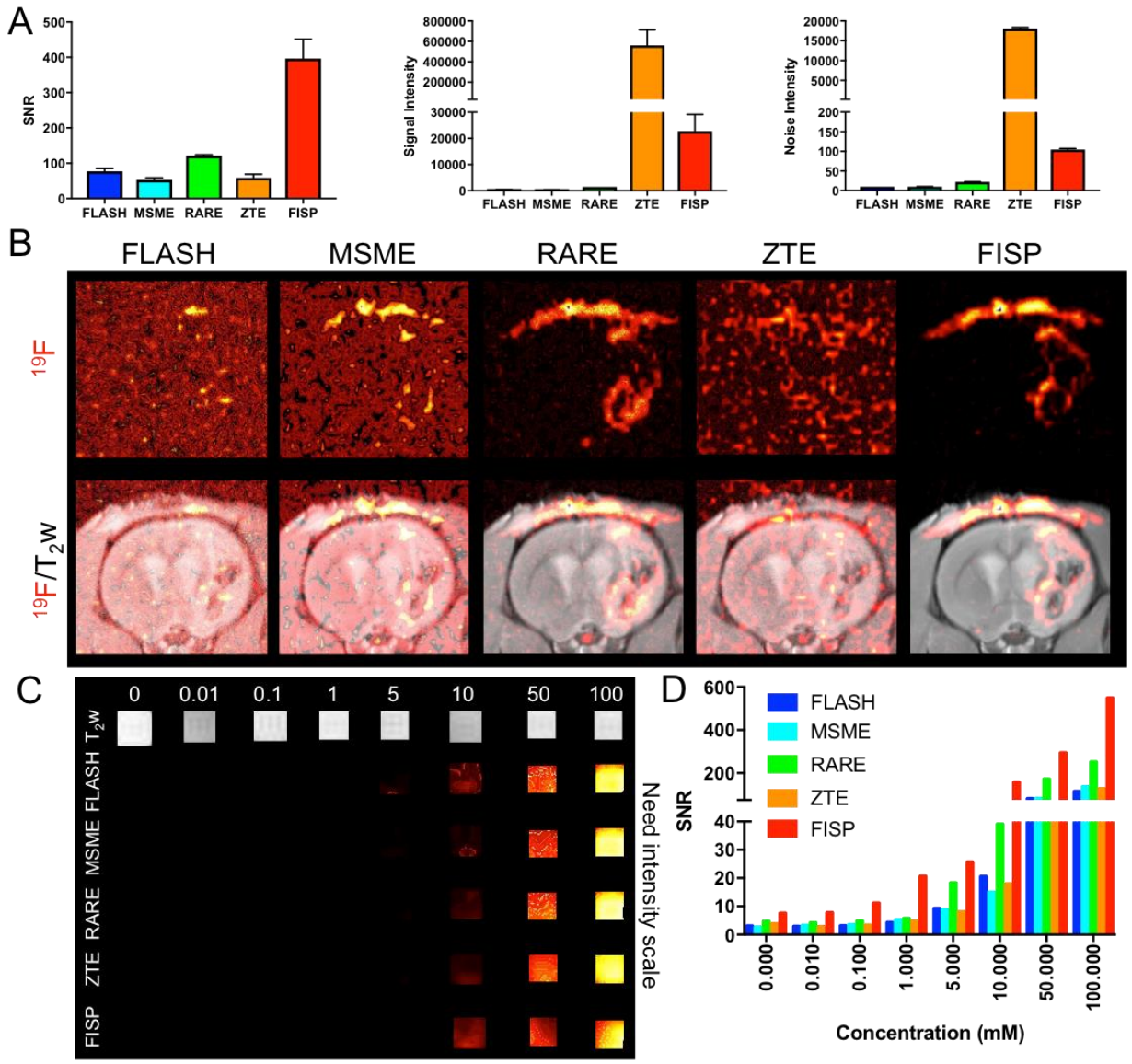

Figure 5.5. Comparison of optimized sequences.

A. *For 50mM ^{19}F nanoemulsion, FISP achieved the highest SNR, followed by RARE and FLASH sequences.* ***B.*** *The optimized sequences were also then used to acquire ^{19}F images of the ex vivo head implanted with ECM hydrogel. FISP sequence provides a robust SNR and spatial resolution required to localize the ^{19}F labeled macrophages. The peripheral inflammation from scalp incision serves as a positive control for macrophage response.* ***C.*** *A significant increase in signal intensity and,* ***D.*** *SNR was determined for ^{19}F concentrations greater than 1mM. FISP achieved the highest SNR across all sequences and concentrations.*

5.3.3 Increasing signal averaging improves SNR

For all optimized sequences increasing the signal averaging or scan time from 15 mins to 120 mins (8x) increased the SNR by at least 2.5 times (**Figure 5.6.A**). At high concentrations (>10mM), the ^{19}F signal was detectable (SNR >3) for all sequences using only 1 average (0.5 - 2.5 min scan time). Comparison of sequences for a 60 min scan duration revealed FISP achieving the highest SNR for all concentrations, followed by RARE and FLASH sequences (**Figure 5.6.B**).

Effect of signal averaging on the ex vivo head was also determined by arraying scan times (0.5 min – 120 min) for each sequence (**Figure 5.6.C**). FISP and RARE achieved a robust localization of the ^{19}F signal, while FLASH, MSME and ZTE showed poor localization and SNR inside the brain tissue as well as on the scalp incision.

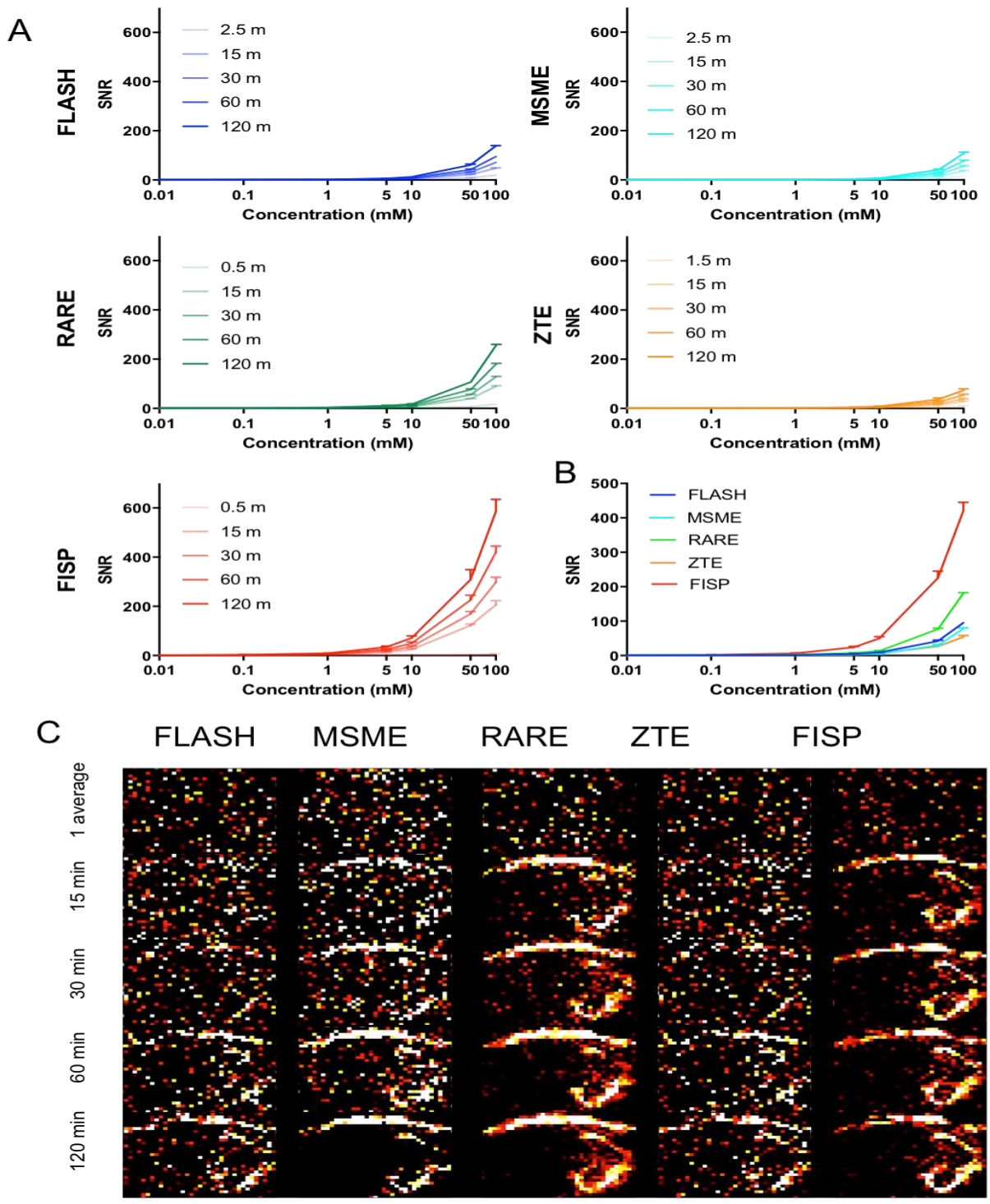

Figure 5.6. Signal averaging improves ^{19}F SNR. *A.* ***To determine the effects of signal averaging on SNR, scans were acquired for a range of scan times (0.5 min to 120 min). Increasing the scan times improved the SNR for all sequences and concentrations.*** *B.* ***A***

comparison of optimized sequences for 60 min scan time indicated FISP achieving the highest SNR for all concentrations, followed by RARE and FLASH. *C.* ***19F imaging of ex vivo head with different scan times reveal improved SNR and macrophage localization with increasing scan times.***

5.3.4 Increasing voxel size improves SNR but affords poor spatial resolution

With all sequences and ^{19}F concentrations, the SNR increased with increasing voxel size from 0.2 mm^3 (128x128) to 3.12 mm^3 (32x32) (**Figure 5.7.A**). A comparison of sequences using 96x96 matrix size (0.35 mm^3) revealed FISP achieving the highest SNR (2.8x RARE, 5.9x FLASH), followed by RARE and FLASH sequences (**Figure 5.7.B**).

^{19}F imaging of ex vivo head using different matrix sizes showed the spillover effects in smaller matrix size (32x32) resulting in poor localization of signal (**Figure 5.7.C**). On the other hand, 128x128 matrix size resulted in a lower SNR, but high spatial resolution allowing improved localization of the acquired signal. Thus 96x96 matrix size (i.e. 0.42 mm in plane resolution, 0.35 mm^3 volume) using a FISP sequence will provide imaging conditions that allow sufficient SNR and scanning time (1-2 hours) in vivo, as well as resolution of structural detail to provide biologically relevant information (e.g. resolve tissue/scaffold interface)

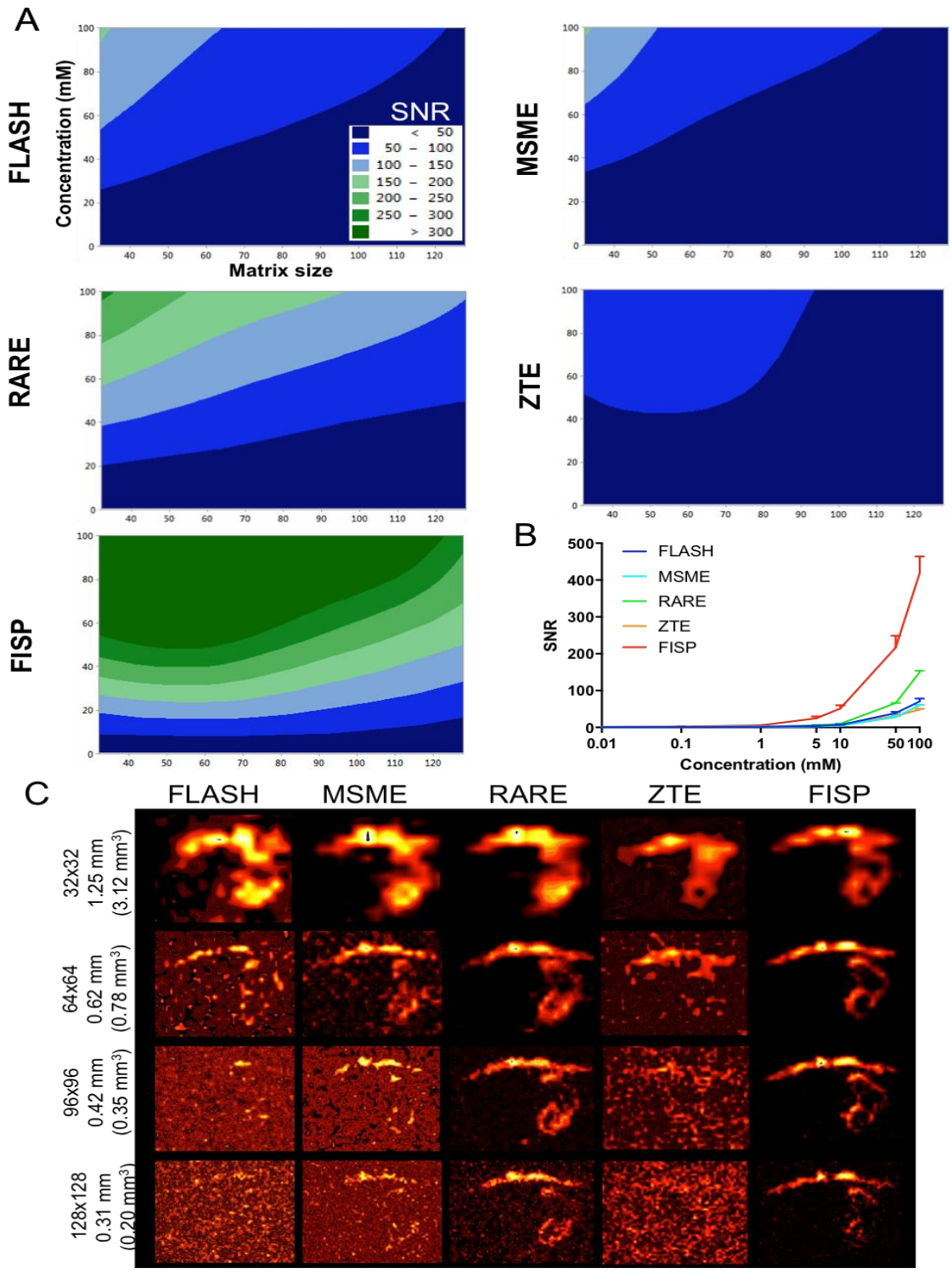

Figure 5.7. Decreasing voxel size reduces SNR, but improves macrophage localization. *To determine the effect of varying voxel size on SNR, scans were acquired with different matrix sizes 128x128 – 32x32 (0.2 mm^3 – 3.12 mm^3).* ***A.*** *For all sequences and ^{19}F concentrations,*

increasing the voxel size improved SNR. ***B.*** *Comparison of optimized sequences using 96x96 matrix (0.35 mm3) reveals FISP achieving the highest SNR across all sequences and concentrations.* ***C.*** *19F ex vivo images reveal spillover effects in larger voxel sizes. Although decreasing voxel size decreases SNR, robust localization of macrophages and minimal spillover effects were evident for voxel sizes < 1mm^3.*

5.3.5 Increasing slice thickness improves SNR

Increasing the slice thickness for all sequences increased the SNR. Specifically, increasing the slice thickness from 1 mm to 2 mm increased the SNR by at least 1.8x (**Figure 5.8.A**). For comparison of optimized sequences with 1.5 mm slice thickness, FISP achieved the highest SNR (1.2, 2.4, 2.8, and 4.2 times higher than RARE, FLASH, MSME, and ZTE sequences) (**Figure 5.8.B**). An ex vivo ^{19}F scan on head with different slice thickness shows higher SNR and signal localization for thicker slices (**Figure 5.8.C**).

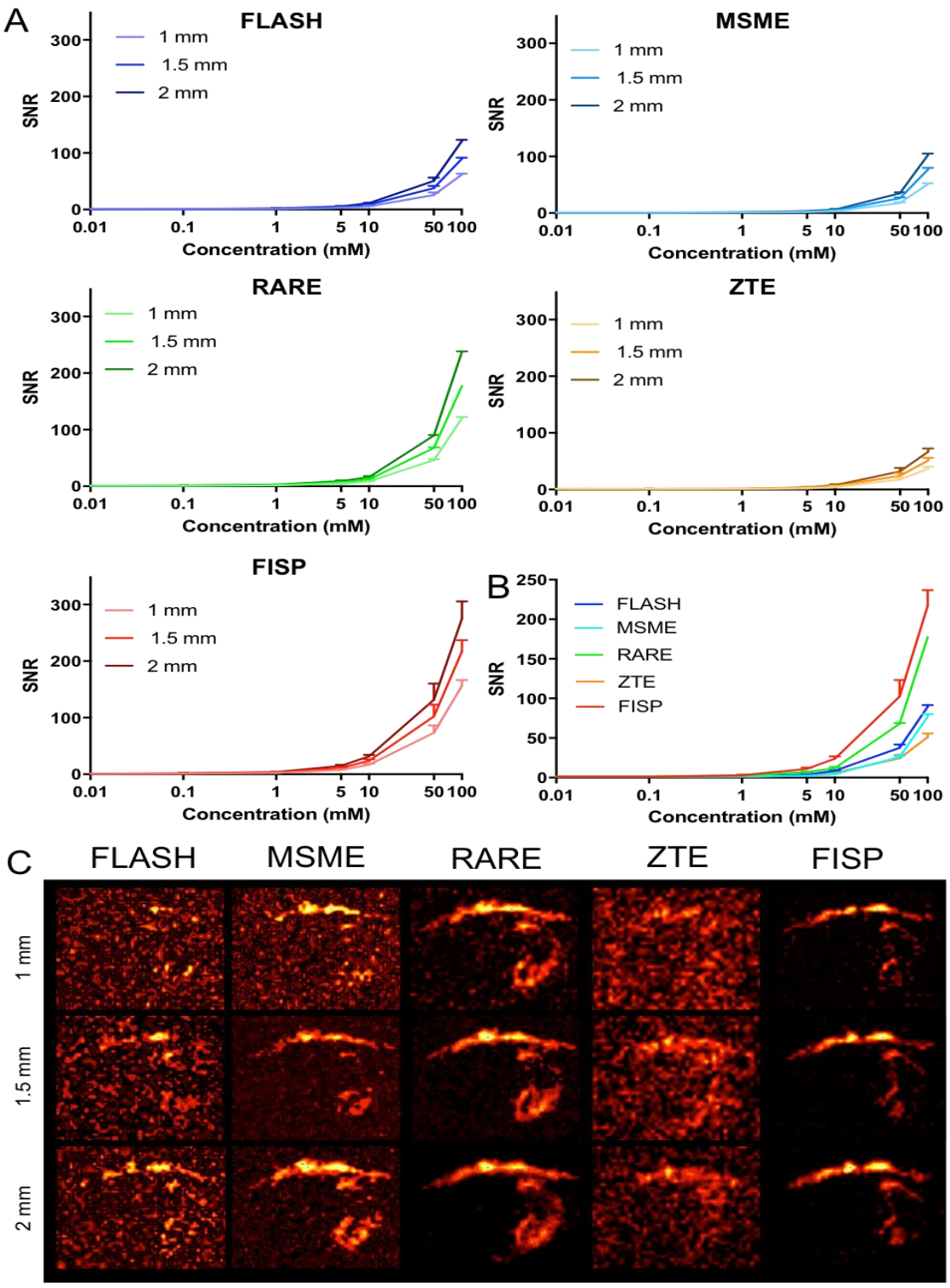

Figure 5.8. Slice thickness and SNR. To determine the effect of slice thickness on ^{19}F SNR, scans were acquired with 1, 1.5, and 2 mm slice thicknesses. *A.* ***Increasing slice thickness***

improves SNR for all sequences, with FISP achieving the highest SNR for all ^{19}F concentrations. *B.* ***Comparison of optimized sequences with 1.5mm slice thickness achieved the highest SNR for FISP, followed by RARE and FLASH.*** *C.* ***Ex vivo scan with different slice thicknesses show improved SNR and macrophage localization with increasing slice thicknesses.***

5.3.6 PFC/^{19}F infiltration into the brain at 24 hours post-implant

24 hours after tail vein ^{19}F injection, animals were scanned to acquire baseline $^{1}H/^{19}F$ images before ECM implantation. Merging the ^{1}H and ^{19}F scans in the pre-implantation (**Figure 5.9.A**) image shows the presence of ^{19}F signal in the major arteries and veins in head, including macillary artery and linguinal vein. Minimal ^{19}F signal is detected inside the brain prior to ECM injection. 24 hours after ECM injection, rats were scanned again to acqire $^{1}H/^{19}F$ images using the same acquisition paramaters. Post-implant images show extensitve accumulation of PFCs insdie the lesion cavity or ECM hydrogel, as well as on the peripheral scalp injury indicating active inflammatory response. Anterior-posterior $^{1}H/^{19}F$ images of the stroke-damaged ECM treated brain shows infiltration of PFCs throughout the lesion cavity, with most signal detected at the central slice of ECM implant (**Figure 5.9.B**).

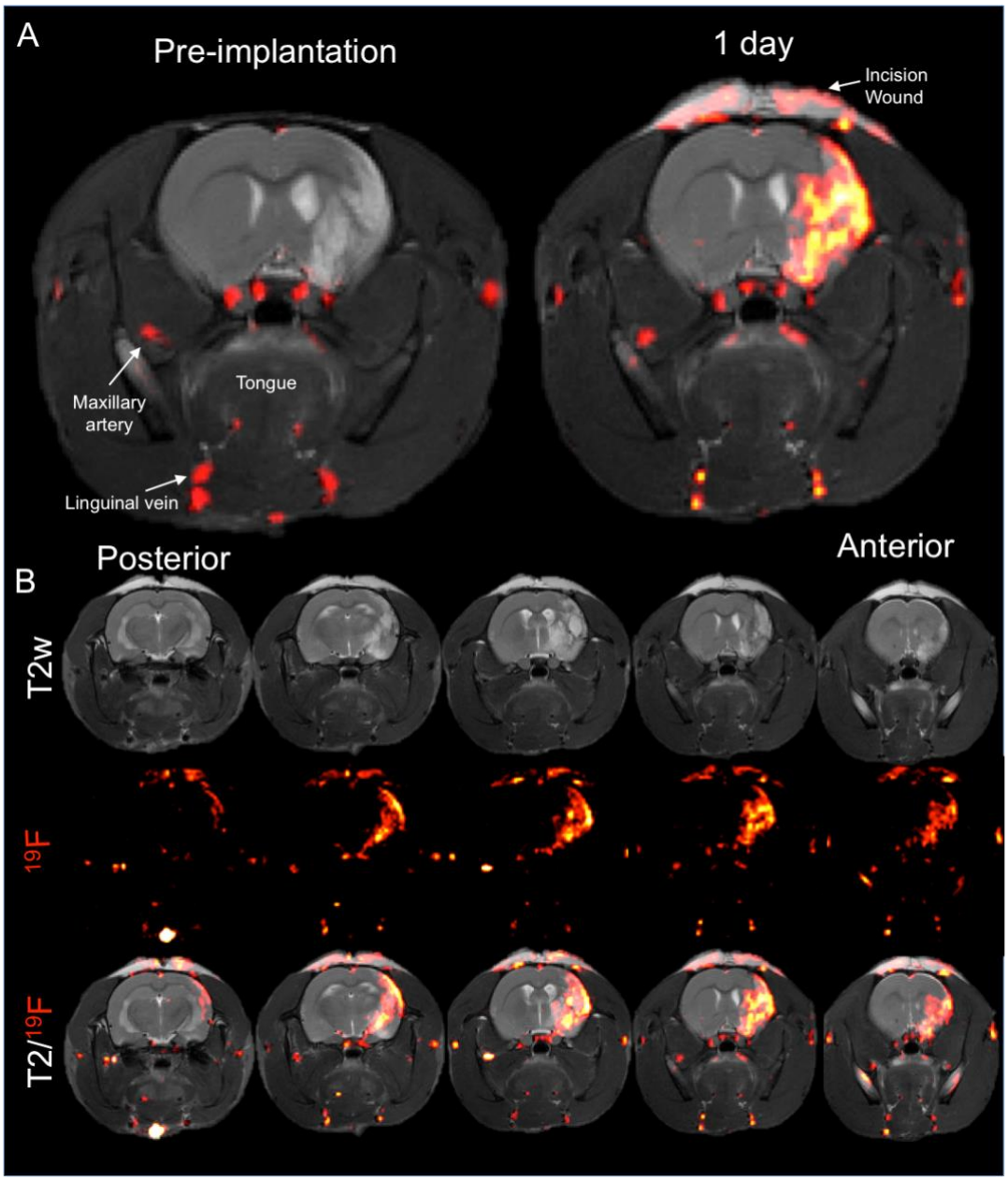

Figure 5.9. Infiltration of PFCs after ECM implantation as detected by in vivo ^{19}F MRI.

A. *Anatomically matching ^{1}H and ^{19}F images from the stroke brain shows an accumulation of PFCs in the lesion cavity after ECM implantation. ^{19}F signal can also be detected in the major arteries and veins in the head, indicating the presence and detection of PFC in the blood for upto 48 hours after PFC injection. ^{19}F signal from the peripheral scalp insision site provides a positive control for inflammation and PFC accumulation.* ***B.*** *Anterior-posterior ^{1}H (T2w) and ^{19}F images of the brain shows extensive infiltration and distribution of 19F signal inside the lesion cavity or ECM hydrogel.*

5.3.7 In vivo quantification of ^{19}F signal

^{19}F imaging before the tail vein PFC injection (48 hours before ECM implantation) revealed no endogenous ^{19}F signal present in tissues or arteries. A ratio of ^{19}F signal to noise signal revealed an SNR of 1 for all regions (**Figure 5.10**). An increase in SNR was evident 24 hours post-PFC injection indicating active flow of PFC nanoemulsions through various arteries and veins in brain tissue as well as in the scalp. ^{19}F imaging 24 hours post-ECM implantation showed significantly increased SNRs for scalp incision site (98.3% increase) as well as lesion cavity (72% increase). Minor changes in SNRs (16% and 8% increase) were observed for the tissue parenchyma and contralateral hemisphere.

A ratio of total ^{19}F spins to volume of different regions revealed total number of ^{19}F spins/μL or spin density within the ROI. The peripheral scalp incision site showed extensive accumulation of ^{19}F labeled cells with a spin density of 5.4×10^{17} (4x spin density inside lesion cavity). The lesion cavity had a spin density of 1.3×10^{17}, which was 4x and 7x higher than spin density inside tissue parenchyma and contralateral hemisphere. Conversion of spin density to cell density using known number of ^{19}F spins per cell (1×10^{13} spins per cell) revealed ^{19}F labeled cell density in the different regions. The peripheral scalp incision site showed the most accumulation of ^{19}F labeled cells with an average cell density of 53,852 cells/μL. Within the brain tissue, lesion cavity revealed the highest cell density of 13,300 cells/μL, while tissue parenchyma and contralateral hemisphere had a cell density of 3256 and 1880 cells/μL.

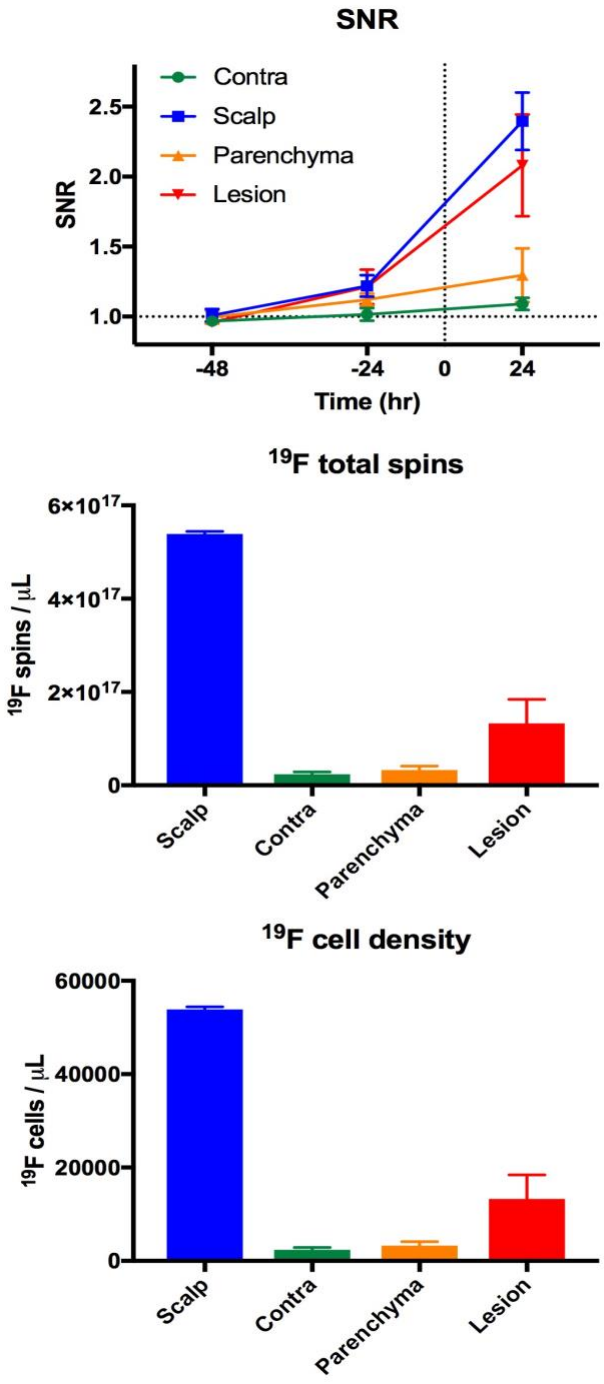

Figure 5.10. In vivo quantification of 19F signal.

A. *SNR comparison reveals no endogenous 19F signal present at 48 hours before ECM implantation (pre-PFC injection). 24 hours after PFC injection, SNR increased reflecting active flow of PFC in various blood vessels insdie and outside brain tissue. 24 hours after ECM*

implantation, scalp and lesion cavity showed increased SNRs indicating detection of infiltrating macrophages. B and C. Quantification of 19F signal revealed maximum 19F cell density at the scalp incision site, followed by lesion cavity.

5.3.8 Histological validation of ECM invading peripheral macrophages

Whole hemispehere Iba1 images of the animal injected with PFC and ECM hydrogel at 1 day post-injection shows colocalization of iba1+ cells (microglia/macrophage) and of ^{19}F signal inside and around the lesion cavity (**Figure 5.11**). A strong signal in the peri-infarct is evident indicating a higher density of ^{19}F labeled macrophages in this region.

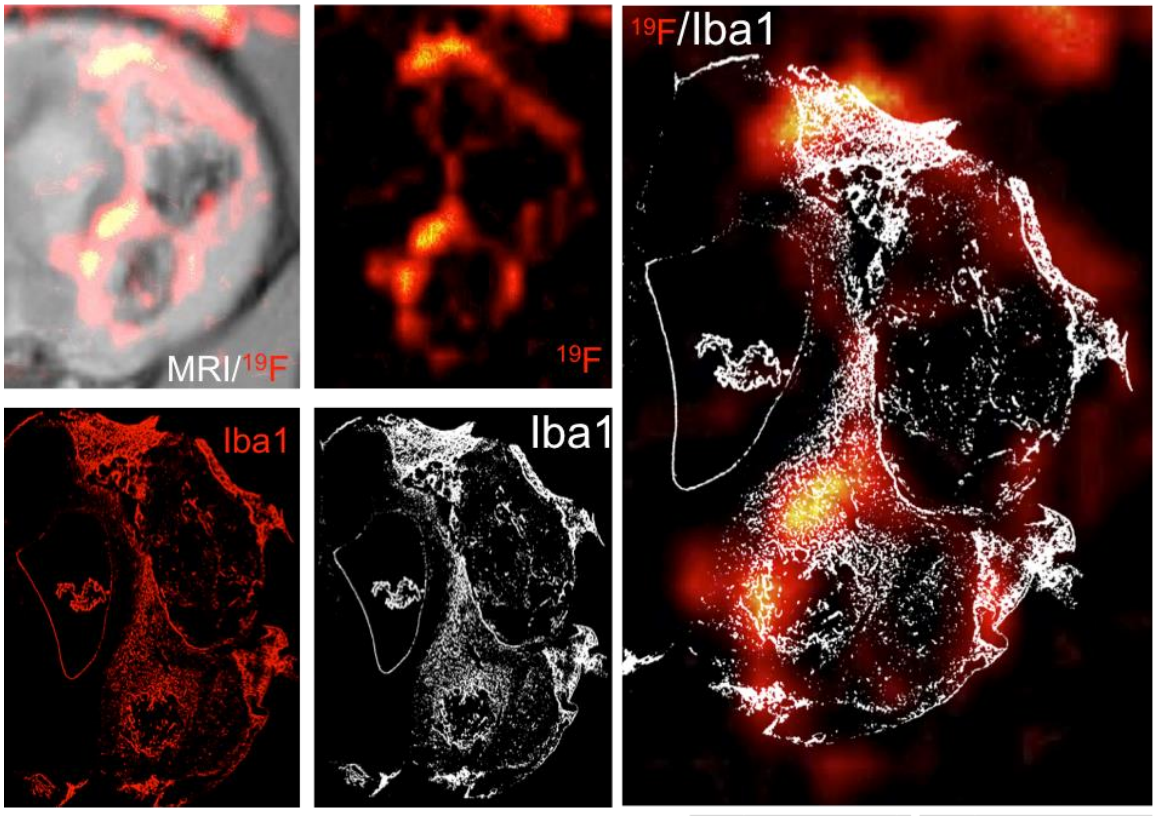

Figure 5.11. 19F signal and histology overlay.

A comparison of 19F images with histology revealed areas with high 19F intensity also contained high density of Iba1+ cells.

Tissue sections were also stained with collagen I to show infiltration of ^{19}F/DM Red labeled macrophages into the ECM hydrogel. ^{19}F/DM Red labeled macrophages can be seen accumulating at a sharp boundary between the ECM and host tissue and crossing into the ECM hydrogel (white arrows, **Figure 5.12.A**). Staining with Iba1 shows co-labeling of Dm Red and Iba1 for all ^{19}F labeled cells. It is noteworthy to notice that although Iba1 stained cells can be seen in the tissue parenchyma, peripheral macrophages were largely accumulated in the damaged tissue.

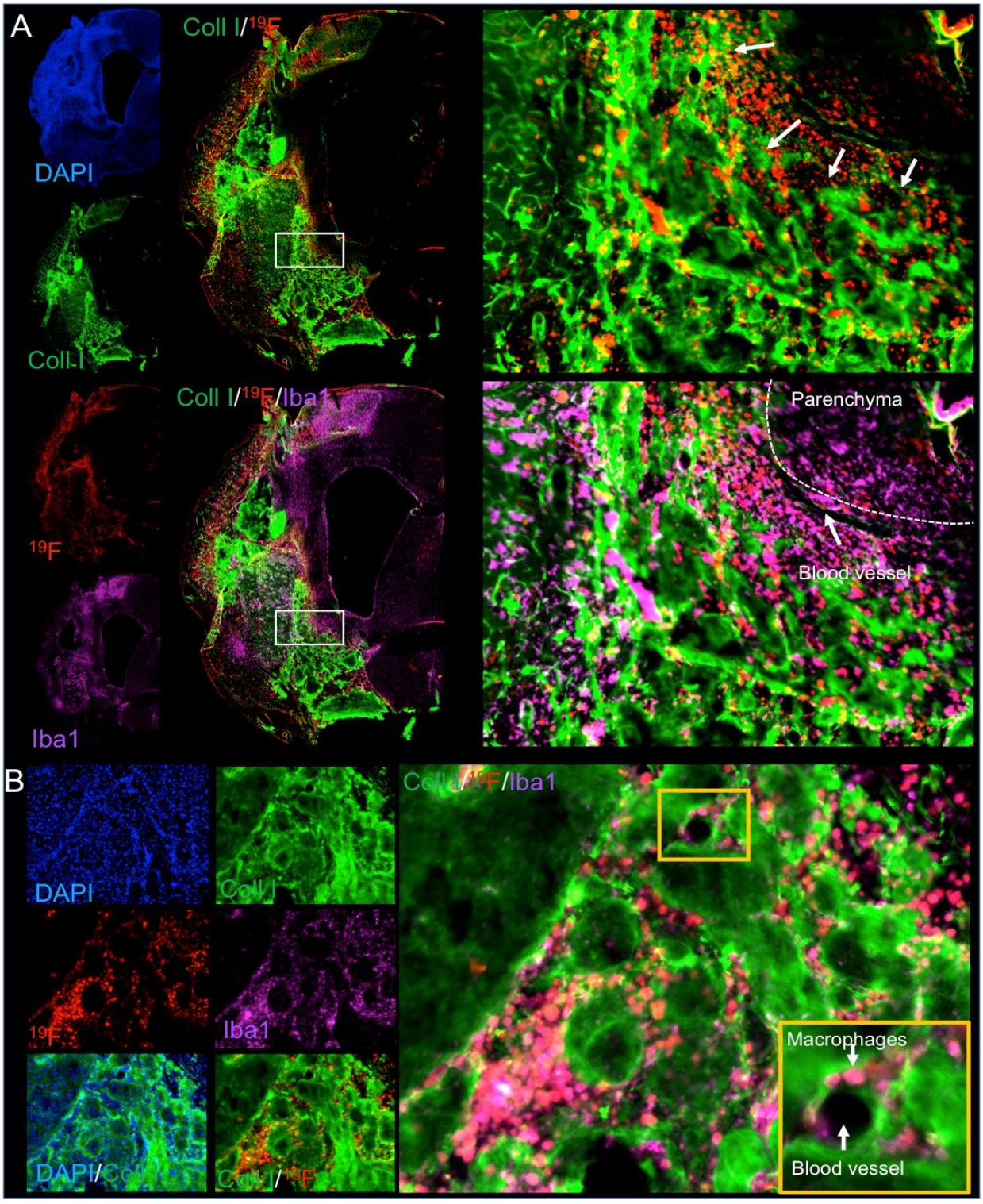

Figure 5.12. Histological validation of brain invading macrophages. *A.* ***Peripheral macrophages tagged with DM Red were seen accumulating at the peri-infarct tissue with***

gradual invasion into the ECM hydrogel. DM Red tagged macrophages also showed co labeling with Iba1+ cells indicating that the infiltrating cells are peripheral macrophages rather than brain derived microglia. B. 19F labeled macrophages were also seen in very close proximity to blood vessels reflecting their active recruitment into the brain tissue from blood.

^{19}F labeled macrophages were also found in close proximity of blood vessels indicating that these cells indeed migrated into the brain tissue from vessels in the peri-infarct region (**Figure 5.12.B**).

5.3.9 Characterization and quantification of ^{19}F/DM Red labeled cells

Immunostaining of brain tissue sections confirmed co-labeling of ^{19}F/DM Red labeled cells with Iba1 indicating that all the ^{19}F labeled cells were peripheral macrophages/monocytes that engulfed the ^{19}F label in blood and infiltrated the brain tissue and ECM hydrogel (**Figure 5.13**).

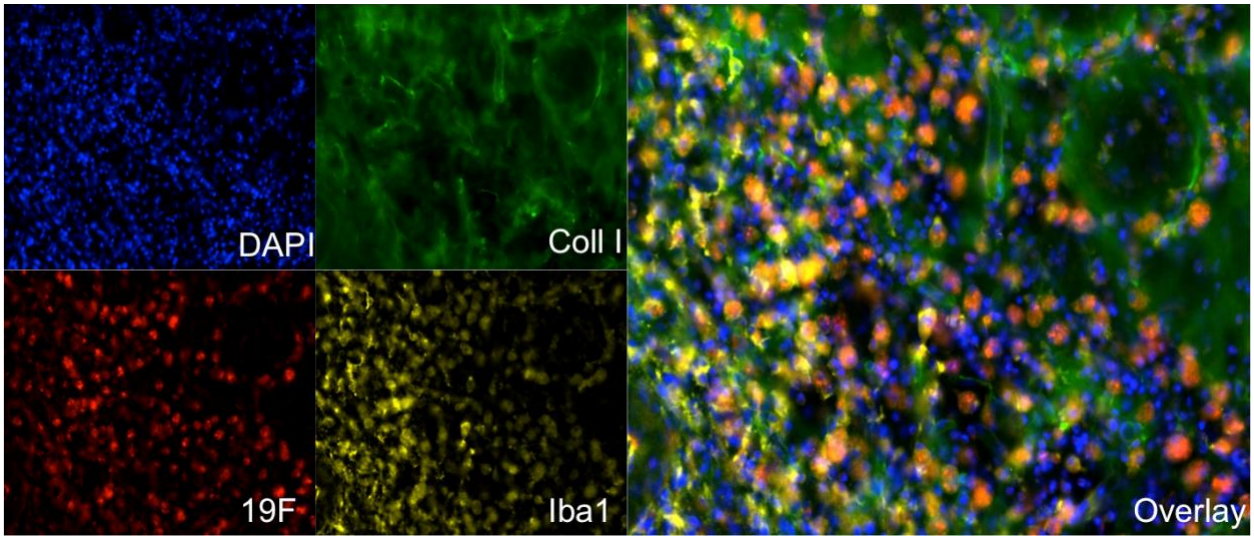

Figure 5.13. Immunohistochemistry confirmed the colabeling of 19F and Iba1 indicating that all the 19F labeled cells are peripheral macrophages.

A quantitative analysis of 19F/DM Red cells revealed a cell density of 1086 and 14,845 cells/µL inside the ECM hydrogel and peri-infarct tissue (**Figure 5.14**).

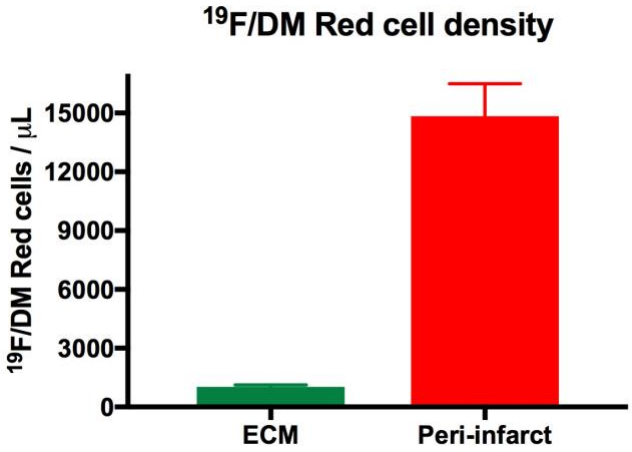

Figure 5.14. Quantitative analysis of ^{19}F/DM red labeled cells shows extensive accumulation of these cells in the peri-infarct area and ECM hydrogel with a cell density of 14845 and 1086 cells/uL.

5.4 DISCUSSION

The aim of this study was to describe a novel approach to visualize the local inflammatory responses by ^{19}F MRI using in vivo tagging of circulating macrophages with biochemically inert ^{19}F agent. Our results show that the intravenous administration of PFCs in stroke rats results in accumulation of ^{19}F labeled cells within the ECM hydrogel and peri-infarct tissue. Thus, PFCs can serve as reliable contrast agent for inflammatory processes revealing high specificity due to lack of any endogenous ^{19}F signal.

DOE provides optimal imaging paramters

We compared the most commonly used ^{19}F MR sequences using a design-of-experiment (DOE) approach, where we arrayed parameters from a low to high value and investigated interactions between parameters and cover the experimental space in a contour map. This resulted in regions in the contour map with maximum SNR that was used to define optimal imaging parameters for each sequence. A comparison of the optimized sequences revealed FISP achieving the the most sensitivity to detect PFCs, followed by RARE and FLASH sequences. Effects of changing slice thickness, scan time and voxel size were also measured for each sequence and showed improved SNRs for thicker slices, longer scan time, and larger voxel size. Although thinner slices results in a decrease in signal intensity or SNR, it offers more number of slices that can be acquired for a region of interest (stroke cavity in our case). Thus, a slice thickness of 1.5 mm was used for in vivo experiments to cover the entire lesion area, while affording sufficient SNR to delineate cavity from tissue parenchyma. Similarly, as longer acquisition times improve SNR, we are limited by in vivo scan time. Thus, a 60 min scan time was used for animal experiments. In general, increasing the voxel size improves ^{19}F SNR, since larger voxels contain more atoms and thus generates higher signal. However, if the source of ^{19}F signal (eg. implanted cell graft) is orders of magnitude smaller than the voxel size, it would not lead to an increased SNR since there are no additional ^{19}F atoms to excite in the surrounding tissue. Indeed, when the FOV is kept constant larger voxels tend to decrease SNR sue to increased under-sampling artifact.

In vivo detection of peripheral macrophages

This study demonstrated the ability to use ^{19}F MRI cell tracking to detect and measure signal from peripheral immune cells in vivo. Numerous studies have reported the challenges associated with quantifying signal loss due to iron-labeled cells. The use of ^{19}F MRI overcomes these issues and provides a direct measure of labeled cells without interfering with other scans (eg. T2). Iron-based contrast agents are readily metabolized in vivo, while PFC emulsions have a very stable C-F bond this is biologically inert and does not degrade easily [252]. Additionaly, there have not been any indications of cellular toxicity or effect on the viability of cells even at very hight PFC loading doses [264]. Indeed we did not observe any adverse effects on animals after PFC injections. Recent ^{19}F MRI studies of cells loaded with PFCs ex vivo and injected into mice required long acquisition times (upto 3 hours) [254], and limited spacial resolution with voxel size of 26 uL (compared to 0.35 uL in this present work) [265]. The significantly higher sensitivity seen in our study is likely due to the efficient in vivo uptake of PFCs through the RES compared to stem cells that were incubated ex vivo.

The in vivo imaging of rats implanted with ECM hydrogel revealed a ^{19}F cell density of 13,300 cells/μL in the lesion cavity. This lesion area includes the area with ECM hydrogel, but also the peri-infarct areas since we currently lack the tools needed to discriminate area of ECM vs peri-infarct tissue in the MR scans. Ex vivo labeling of ECM hydrogel with contrast agents such as Gadolinium could resolve this issue and afford a direct comparison of ^{19}F cell density inside ECM vs peri-inafrct tissue. Histological analysis of the brain tissues revelaed ^{19}F labeled cell density to be much higher in the peri-infarct areas (14,845 cells/μL) compared to labeled cells inside the ECM (1086

cells/μL). This supports the idea that the peripheral macrophages enter the brain through the peri-infarct tissue with gradual invasion into the ECM hydrogel. All the ^{19}F labeled cells inside as well as outside the ECM hydrogel were also positive for Iba1 indicating that these cells are peripheral macrophages rather than brain derived microglia. The spatial distribution of the ^{19}F signal is covering the area of ECM hydrogel and indicates that macrophage activity is not only regulated by the presence of ECM, but ECM distribution defines the pattern of macrophage activity while avoiding invasion in other areas of the brain

5.5 CONCLUSIONS

At present, the evaluation of bioscaffolds to promote tissue repair relies on tedious time point histological studies, which require large numbers of animals due to the heterogeneity of lesions, as well as the biomaterial implants. Non-invasive imaging of macrophage dynamics will constitute a major advance to visualize the time point of invasion and longitudinally monitor macrophage distribution in small cohorts of animals. As PFC nanomeulsions and ^{19}F MRI can be used in both animals and patients, it also provides a unique translational measure to monitor an efficient biodegradation and accelerate the clinical development of bioscaffolds.

6.0 DISSERTATION SYNOPSIS

This work is the first implementation of ECM hydrogel implantation showing tissue restoration in a large stroke cavity and ^{19}F MRI for immune cell tracking in a stroke-damaged brain implanted with ECM hydrogel. In chapter 2, we describe an innovative minimally invasive technique to implant ECM hydrogel while simultaneously draining ECF from stroke cavity, as well as characterizing the in vivo gelation and retention properties of the ECM with phenotypes of infiltrating cells quantified at 1 day post-ECM implantation. In Chapter 3, we demonstrate that long term retention of a stiffer 8 mg/mL ECM hydrogel in a stroke cavity reduces lesion volume, but allows insuccifient cell invasion and biodegradation of the ECM to restore tissue cavity and improve behavioral outcomes. In chapter 4, we showed that a softer 4 mg/mL ECM affords almost a complete biodegradation by 3 months, and restores tissue within the cavity. The density of macrophages in the ECM hydrogel is a key modulator that affects biodegradation. Finally, in chapter 5 we optimized ^{19}F MRI sequences to non-invasively visualize and quantify brain infiltrating macrophages to monitor the cellular aspects of ECM biodegradation in vivo.

Although cell infiltration into the lesion cavity is the first step in regenerating the lost tissue, robust cell invasion and axonal growth alone may not necessarily ensure functional restoration [266], as researchers were unable to restore visual function even after inducing the mouse retinal axons to regrow and form synapses in the superior colliculus [267]. Further analysis revealed that the newly formed axons were not properly myelinated, and the addition of a voltage gated potassium channel blocker improved the

conduction of action potentials allowing functional restoration. For more complex behavioral functions, targeted behavioral training will need to accompany the period of increased plasticity following treatment [268], since not all plasticity is known to be beneficial (ex. seizures, spasticity).

6.1 MAJOR FINDINGS

The following are the major findings of the presented work:

Specific Aim 1

- Using the injection-drainage approach, ECM hydrogel can be reliably delivered to the stroke cavity without causing further damage to the surrounding tissue
- Implanted ECM hydrogel shows robust concentration-dependent gelation and retention properties in situ
- ECM hydrogel induces host tissue response that leads to cell infiltration
- Structural support is required for cell invasion in the cavity
- Microglia/Macrophages are the dominant infiltrating cells with concentration-dependent polarization towards an M2-like phenotype
- 8 mg/mL UBM ECM (rheological properties akin to intact tissue) promotes the most significant cell invasion and attracts large numbers of neural and oligodendrocytes progenitor cells within 24 hours

Specific Aim 2

- Long-term structural support inside the stroke cavity prevents the lesion size from increasing

- Poor degradation of ECM leads to long term retention in stroke cavity
- Large ECM volume injection and poor biodegradation does not impact behavioral outcomes
- Poor biodegradation of ECM hydrogel significantly reduces the total number and density of infiltrating cells including macrophages
- Microglia/macrophages and oligodendrocytes are the dominant cell types invading the ECM hydrogel at 90 day post-implantation

Specific Aim 3

- Biodegradation of ECM hydrogel is essential for recruting host cells and restoring stroke cavity
- Softer ECM hydrogels (3 and 4 mg/mL) undergo efficient biodegradation and reduce tissue cavitation
- Glial scarring and astrocytosis is not impacted by ECM implantation
- Biodegradation of ECM hydrogel promotes neovascularization of stroke cavity
- Microglia/macrophage density affects ECM biodegradation
- Mature neurons are found inside around the softer ECM hydrogels at 90 day post-injection

Specific Aim 4

- DOE approach allows visualization of interactions between imaging parameters and SNR to define optimal imaging parameters
- FISP sequence is the most efficent in detecting PFC nanoemulsion
- PFC nanoemulsions are engulfed by circulating macrophages before migrating to the site of ECM implantation

- In vivo ^{19}F MRI at 1 day post-ECM injection provides a robust localization of infiltrating immune cells cells inside the stroke lesion cavity post transplant

6.2 LIMITATIONS AND FUTURE WORK

A major limitation of this work was detection of the implanted ECM hydrogel using immunohistochemistry and MRI. Since approximately 70% of the UBM ECM is collagen I, we have demonstrated that collagen I is a good surrogate marker for histologial distribution at early time points post-implantation. However, as the material gets degraded (especially 3 mg/mL at 3 months), it is unclear if this is still the case. The use of additional markers and morphological characteristics at later time points can further aid to identify the implanted material. Ex vivo covalent pre-labeling of the material prior to injection with florescent tetramethylrhodamine (TRITC) would allow researchers to histologically detect the implanted material without the need for any surrogate histoloigical markers like collagen I. In addition, MRI detection of the implanted hydrogel using Gadolinium-Gold nanoparticles tagging would allow us to delineate the ^{19}F signal from the ECM hydrogel vs peri-infarct tissue.

A second limitation of this study is lack of understanding of the identity of the invading neurons. Brain is highly specialized and neurons are defined by their regional identity, which is defined during differentiation through positional specification. Future experiments will evaluate the positional specification using immunohistochemistry for striatal (eg. Dlx2, NKX2.1) and cortical markers (eg. Pax6) to determine if the invading neurons express the regional positional specification markers in the striatum and cortex.

Another potential limitation is the homogenous delivery of ECM hydrogel in non-communicating stroke cavities. We have seen this issue mostly with the 3 mg/mL hydrogel which is weaker and does not displace remnants of scar tissue that seperates cavity pockets. At 4 mg/mL concentration, these weak tissues are displaced and more homogenous distribution is observed. Using diffusion MRI scans instead of T2w scans would allow us to identify separate cavity pockets and target injection to individual pockets.

The final limitation in this study is the time of delivery of ECM hydrogel to stroke cavity. Our current time of delivery is based on studies using fetal tissue transplants that show improved survival between 2-3 weeks post-stroke compared to more acute or chronic phases [269]. Nevertheless, it is possible here that improved structural remodeling is observed at an earlier time point. An earlier injection time point (eg. 7 days post-stroke) using a less concentrated hydrogel will allow researchers to investigate this and guide future approaches based on solid evidence.

6.3 OVERALL CONCLUSIONS

The work contained in this dissertation demonstrates that implantation of ECM hydrogel in a stroke cavity induces cellular infiltration to support endogenous repair processes. The novel injection-drainage approach described herein allowed us to inject large ECM volumes into the brain cavity without causing additional damage to the peri-infarct tissue. While the implantation of the stiffer 8 mg/mL hydrogel did not alter the behavioral outcomes, it provided a permissive microenvironment for the host cells to infiltrate into

the lesion cavity and reduce the lesion size by 28%. Injection of softer 3 and 4 mg/mL ECM showed robust biodegradation and infiltration of host cells including neurons, and resulted in a 50% decrease in cavity size by 3 months. In addition, the noninvasive imaging of brain infiltrating monocytes/macrophages using ^{19}F MRI allowed us to selectively visualize and quantify the number of infiltrating cells that participate in the biodegradation of the ECM hydrogel. This combination of in situ gel formation that modulates the inflammatory and neural cell responses, and its non-invasive visualization using ^{19}F MRI sets the foundation for future evaluation of biomaterials in acute brain injuries like stroke.

APPENDIX

PUBLICATION LIST

10. **Ghuman H**, Hitchens K, Modo M. A systematic optimization of ^{19}F MR image acquisition to detect macrophage invasion into an ECM hydrogel implanted in the stroke-damaged brain. (In prep, 2018)

9. **Ghuman H**, Mauney C, Donnelly J, Massensini AR, Badylak SF, Modo M. Biodegradation of ECM hydrogel promotes endogenous brain tissue restoration in a rat model of stroke. (Accepted, Acta Biomaterialia, 2018)

8. Wahlberg B*, **Ghuman H***, Liu JR, Modo M. Ex vivo biomechanical characterization of syringe-needle ejections for intracerebral cell delivery. Scientific Reports. 2018; 8(1):9194. ***Contributed equally

7. **Ghuman H**, Gerwig M, Nicholls FJ, Liu JR, Donnelly J, Badylak SF, Modo M. Long-term retention of ECM hydrogel after implantation into a sub-acute stroke cavity reduces lesion volume. Acta Biomater. 2017; 63:50-63

6. Dalise S*, Cavalli L*, **Ghuman H***, Wahlberg B*, Gerwig M, Chisari C, Ambrosio F, Modo M. Biological effects of dosing aerobic exercise and neuromuscular electrical stimulation in rats. Sci Rep. 2017; 7(1):10830. ***Contributed equally

5. Jin T, Nicholls FJ, Crum WR, **Ghuman H**, Badylak SF, Modo M. Diamagnetic chemical exchange saturation transfer (diaCEST) affords magnetic resonance imaging of extracellular matrix hydrogel implantation in a rat model of stroke. Biomaterials. 2017; 113:176-190.

4. **Ghuman H**, Modo M. Biomaterial applications in neural therapy and repair. Chinese Neurosurgical Journal. 2016; 2:34.

3. **Ghuman H**, Massensini AR, Donnelly J, Kim S, Badylak SF, Modo M. ECM Hydrogel injection for the treatment of chronic stroke: Characterization of the acute host cells invasion. Biomaterials. 2016; 91:166-181.

2. Nicholls FJ, Rotz MW, **Ghuman H**, Macrenaris KW, Meade TJ, Modo M. DNA-gadolinium-gold nanoparticles for in vivo T1 MR imaging of transplanted human neural stem cells. Biomaterials. 2016; 77:291-306.

1. Massensini AR[*], **Ghuman H**[*], Saldin LT, Medberry CJ, Keane TJ, Nicholls FJ, Velankar SS, Badylak SF, Modo M. Concentration-dependent rheological properties of ECM hydrogel for intracerebral delivery to a stroke cavity. Acta Biomater. 2015; 27:116-30. *****Contributed equally

BIBLIOGRAPHY

[1] A.G. Thrift, H.M. Dewey, R.A. Macdonell, J.J. McNeil, G.A. Donnan, Incidence of the major stroke subtypes: initial findings from the North East Melbourne stroke incidence study (NEMESIS), Stroke 32(8) (2001) 1732-8.

[2] R.J. Winquist, S. Kerr, Cerebral ischemia-reperfusion injury and adhesion, Neurology 49(5 Suppl 4) (1997) S23-6.

[3] H.P. Adams, Jr., G. del Zoppo, M.J. Alberts, D.L. Bhatt, L. Brass, A. Furlan, R.L. Grubb, R.T. Higashida, E.C. Jauch, C. Kidwell, P.D. Lyden, L.B. Morgenstern, A.I. Qureshi, R.H. Rosenwasser, P.A. Scott, E.F. Wijdicks, A. American Heart, C. American Stroke Association Stroke, C. Clinical Cardiology, R. Cardiovascular, C. Intervention, D. Atherosclerotic Peripheral Vascular, G. Quality of Care Outcomes in Research Interdisciplinary Working, Guidelines for the early management of adults with ischemic stroke: a guideline from the American Heart Association/American Stroke Association Stroke Council, Clinical Cardiology Council, Cardiovascular Radiology and Intervention Council, and the Atherosclerotic Peripheral Vascular Disease and Quality of Care Outcomes in Research Interdisciplinary Working Groups: the American Academy of Neurology affirms the value of this guideline as an educational tool for neurologists, Stroke 38(5) (2007) 1655-711.

[4] G.C. Fonarow, E.E. Smith, J.L. Saver, M.J. Reeves, D.L. Bhatt, M.V. Grau-Sepulveda, D.M. Olson, A.F. Hernandez, E.D. Peterson, L.H. Schwamm, Timeliness of tissue-type plasminogen activator therapy in acute ischemic stroke: patient characteristics, hospital factors, and outcomes associated with door-to-needle times within 60 minutes, Circulation 123(7) (2011) 750-8.

[5] J.P. Broderick, William M. Feinberg Lecture: stroke therapy in the year 2025: burden, breakthroughs, and barriers to progress, Stroke 35(1) (2004) 205-11.

[6] S. Dalise, F. Ambrosio, M. Modo, Brain plasticity and recovery in preclinical models of stroke, Arch Ital Biol 152(4) (2014) 190-215.

[7] M.A. Dimyan, L.G. Cohen, Neuroplasticity in the context of motor rehabilitation after stroke, Nat Rev Neurol 7(2) (2011) 76-85.

[8] D. Lloyd-Jones, R. Adams, M. Carnethon, G. De Simone, T.B. Ferguson, K. Flegal, E. Ford, K. Furie, A. Go, K. Greenlund, N. Haase, S. Hailpern, M. Ho, V. Howard, B. Kissela, S. Kittner, D. Lackland, L. Lisabeth, A. Marelli, M. McDermott, J. Meigs, D. Mozaffarian, G. Nichol, C. O'Donnell, V. Roger, W. Rosamond, R. Sacco, P. Sorlie, R. Stafford, J. Steinberger, T. Thom, S. Wasserthiel-Smoller, N. Wong, J. Wylie-Rosett, Y. Hong, C. American Heart Association Statistics, S. Stroke Statistics, Heart disease and stroke statistics--2009 update: a report from the American Heart Association Statistics Committee and Stroke Statistics Subcommittee, Circulation 119(3) (2009) 480-6.

[9] L.C. Case, M. Tessier-Lavigne, Regeneration of the adult central nervous system, Curr Biol 15(18) (2005) R749-53.

[10] B.D. Watson, W.D. Dietrich, R. Busto, M.S. Wachtel, M.D. Ginsberg, Induction of reproducible brain infarction by photochemically initiated thrombosis, Ann Neurol 17(5) (1985) 497-504.

[11] C. Kleinschnitz, S. Braeuninger, M. Pham, M. Austinat, I. Nolte, T. Renne, B. Nieswandt, M. Bendszus, G. Stoll, Blocking of platelets or intrinsic coagulation pathway-driven thrombosis does not prevent cerebral infarctions induced by photothrombosis, Stroke 39(4) (2008) 1262-8.

[12] V.M. Lee, N.G. Burdett, A. Carpenter, L.D. Hall, P.S. Pambakian, S. Patel, N.I. Wood, M.F. James, Evolution of photochemically induced focal cerebral ischemia in the rat. Magnetic resonance imaging and histology, Stroke 27(11) (1996) 2110-8; discussion 2118-9.

[13] M. Yanagisawa, H. Kurihara, S. Kimura, K. Goto, T. Masaki, A novel peptide vasoconstrictor, endothelin, is produced by vascular endothelium and modulates smooth muscle Ca2+ channels, J Hypertens Suppl 6(4) (1988) S188-91.

[14] M.J. Robinson, I.M. Macrae, M. Todd, J.L. Reid, J. McCulloch, Reduction of local cerebral blood flow to pathological levels by endothelin-1 applied to the middle cerebral artery in the rat, Neurosci Lett 118(2) (1990) 269-72.

[15] P.M. Hughes, D.C. Anthony, M. Ruddin, M.S. Botham, E.L. Rankine, M. Sablone, D. Baumann, A.K. Mir, V.H. Perry, Focal lesions in the rat central nervous system induced by endothelin-1, J Neuropathol Exp Neurol 62(12) (2003) 1276-86.

[16] K. Fuxe, B. Bjelke, B. Andbjer, H. Grahn, R. Rimondini, L.F. Agnati, Endothelin-1 induced lesions of the frontoparietal cortex of the rat. A possible model of focal cortical ischemia, Neuroreport 8(11) (1997) 2623-9.

[17] J. Biernaskie, D. Corbett, J. Peeling, J. Wells, H. Lei, A serial MR study of cerebral blood flow changes and lesion development following endothelin-1-induced ischemia in rats, Magn Reson Med 46(4) (2001) 827-30.

[18] M. Uesugi, Y. Kasuya, K. Hayashi, K. Goto, SB209670, a potent endothelin receptor antagonist, prevents or delays axonal degeneration after spinal cord injury, Brain Res 786(1-2) (1998) 235-9.

[19] K.A. Hossmann, Cerebral ischemia: models, methods and outcomes, Neuropharmacology 55(3) (2008) 257-70.

[20] K. Overgaard, T. Sereghy, G. Boysen, H. Pedersen, S. Hoyer, N.H. Diemer, A rat model of reproducible cerebral infarction using thrombotic blood clot emboli, J Cereb Blood Flow Metab 12(3) (1992) 484-90.

[21] F. Niessen, T. Hilger, M. Hoehn, K.A. Hossmann, Differences in clot preparation determine outcome of recombinant tissue plasminogen activator treatment in experimental thromboembolic stroke, Stroke 34(8) (2003) 2019-24.

[22] T. Gerriets, F. Li, M.D. Silva, X. Meng, M. Brevard, C.H. Sotak, M. Fisher, The macrosphere model: evaluation of a new stroke model for permanent middle cerebral artery occlusion in rats, J Neurosci Methods 122(2) (2003) 201-11.

[23] K. Fukuchi, H. Kusuoka, Y. Watanabe, T. Nishimura, Correlation of sequential MR images of microsphere-induced cerebral ischemia with histologic changes in rats, Invest Radiol 34(11) (1999) 698-703.

[24] M. Ren, Z.J. Lin, H. Qian, G.R. Choudhury, R. Liu, H. Liu, S.H. Yang, Embolic middle cerebral artery occlusion model using thrombin and fibrinogen composed clots in rat, J Neurosci Methods 211(2) (2012) 296-304.

[25] J.S. Beech, S.C. Williams, C.A. Campbell, P.M. Bath, A.A. Parsons, A.J. Hunter, D.K. Menon, Further characterisation of a thromboembolic model of stroke in the rat, Brain Res 895(1-2) (2001) 18-24.

[26] J. Bogousslavsky, G. Van Melle, F. Regli, The Lausanne Stroke Registry: analysis of 1,000 consecutive patients with first stroke, Stroke 19(9) (1988) 1083-92.

[27] J.H. Garcia, K.F. Liu, K.L. Ho, Neuronal necrosis after middle cerebral artery occlusion in Wistar rats progresses at different time intervals in the caudoputamen and the cortex, Stroke 26(4) (1995) 636-42; discussion 643.

[28] D.W. Howells, M.J. Porritt, S.S. Rewell, V. O'Collins, E.S. Sena, H.B. van der Worp, R.J. Traystman, M.R. Macleod, Different strokes for different folks: the rich diversity of animal models of focal cerebral ischemia, J Cereb Blood Flow Metab 30(8) (2010) 1412-31.

[29] P. Lipton, Ischemic cell death in brain neurons, Physiol Rev 79(4) (1999) 1431-568.

[30] J. Yuan, Neuroprotective strategies targeting apoptotic and necrotic cell death for stroke, Apoptosis 14(4) (2009) 469-77.

[31] E.H. Lo, A new penumbra: transitioning from injury into repair after stroke, Nat Med 14(5) (2008) 497-500.

[32] K.M. Baeten, K. Akassoglou, Extracellular matrix and matrix receptors in blood-brain barrier formation and stroke, Dev Neurobiol 71(11) (2011) 1018-39.

[33] T. Bliss, R. Guzman, M. Daadi, G.K. Steinberg, Cell transplantation therapy for stroke, Stroke 38(2 Suppl) (2007) 817-26.

[34] A. Bakshi, C.A. Keck, V.S. Koshkin, D.G. LeBold, R. Siman, E.Y. Snyder, T.K. McIntosh, Caspase-mediated cell death predominates following engraftment of neural progenitor cells into traumatically injured rat brain, Brain Res 1065(1-2) (2005) 8-19.

[35] M. Lalancette-Hebert, G. Gowing, A. Simard, Y.C. Weng, J. Kriz, Selective ablation of proliferating microglial cells exacerbates ischemic injury in the brain, J Neurosci 27(10) (2007) 2596-605.

[36] A. Denes, R. Vidyasagar, J. Feng, J. Narvainen, B.W. McColl, R.A. Kauppinen, S.M. Allan, Proliferating resident microglia after focal cerebral ischaemia in mice, J Cereb Blood Flow Metab 27(12) (2007) 1941-53.

[37] F.C. Barone, B. Arvin, R.F. White, A. Miller, C.L. Webb, R.N. Willette, P.G. Lysko, G.Z. Feuerstein, Tumor necrosis factor-alpha. A mediator of focal ischemic brain injury, Stroke 28(6) (1997) 1233-44.

[38] K.L. Lambertsen, M. Meldgaard, R. Ladeby, B. Finsen, A quantitative study of microglial-macrophage synthesis of tumor necrosis factor during acute and late focal cerebral ischemia in mice, J Cereb Blood Flow Metab 25(1) (2005) 119-35.

[39] M. Minami, Y. Kuraishi, K. Yabuuchi, A. Yamazaki, M. Satoh, Induction of interleukin-1 beta mRNA in rat brain after transient forebrain ischemia, J Neurochem 58(1) (1992) 390-2.

[40] G.J. Harry, C.A. McPherson, R.N. Wine, K. Atkinson, C. Lefebvre d'Hellencourt, Trimethyltin-induced neurogenesis in the murine hippocampus, Neurotox Res 5(8) (2004) 623-7.

[41] W.J. Streit, Microglia as neuroprotective, immunocompetent cells of the CNS, Glia 40(2) (2002) 133-9.

[42] Y. Ziv, N. Ron, O. Butovsky, G. Landa, E. Sudai, N. Greenberg, H. Cohen, J. Kipnis, M. Schwartz, Immune cells contribute to the maintenance of neurogenesis and spatial learning abilities in adulthood, Nat Neurosci 9(2) (2006) 268-75.

[43] P. Thored, U. Heldmann, W. Gomes-Leal, R. Gisler, V. Darsalia, J. Taneera, J.M. Nygren, S.E. Jacobsen, C.T. Ekdahl, Z. Kokaia, O. Lindvall, Long-term accumulation of microglia with proneurogenic phenotype concomitant with persistent neurogenesis in adult subventricular zone after stroke, Glia 57(8) (2009) 835-49.

[44] N.M. Walton, B.M. Sutter, E.D. Laywell, L.H. Levkoff, S.M. Kearns, G.P. Marshall, 2nd, B. Scheffler, D.A. Steindler, Microglia instruct subventricular zone neurogenesis, Glia 54(8) (2006) 815-25.

[45] K.S. Panickar, M.D. Norenberg, Astrocytes in cerebral ischemic injury: morphological and general considerations, Glia 50(4) (2005) 287-98.

[46] H. Li, N. Zhang, G. Sun, S. Ding, Inhibition of the group I mGluRs reduces acute brain damage and improves long-term histological outcomes after photothrombosis-induced ischaemia, ASN Neuro 5(3) (2013) 195-207.

[47] G.E. Barreto, X. Sun, L. Xu, R.G. Giffard, Astrocyte proliferation following stroke in the mouse depends on distance from the infarct, PLoS One 6(11) (2011) e27881.

[48] Y. Chen, R.A. Swanson, Astrocytes and brain injury, J Cereb Blood Flow Metab 23(2) (2003) 137-49.

[49] B. Ransom, T. Behar, M. Nedergaard, New roles for astrocytes (stars at last), Trends Neurosci 26(10) (2003) 520-2.

[50] C. Iadecola, M. Nedergaard, Glial regulation of the cerebral microvasculature, Nat Neurosci 10(11) (2007) 1369-76.

[51] H.K. Kimelberg, Astrocytic swelling in cerebral ischemia as a possible cause of injury and target for therapy, Glia 50(4) (2005) 389-97.

[52] C.M. Anderson, M. Nedergaard, Astrocyte-mediated control of cerebral microcirculation, Trends Neurosci 26(7) (2003) 340-4; author reply 344-5.

[53] M.V. Sofroniew, Reactive astrocytes in neural repair and protection, Neuroscientist 11(5) (2005) 400-7.

[54] J. Liauw, S. Hoang, M. Choi, C. Eroglu, M. Choi, G.H. Sun, M. Percy, B. Wildman-Tobriner, T. Bliss, R.G. Guzman, B.A. Barres, G.K. Steinberg, Thrombospondins 1 and 2 are necessary for synaptic plasticity and functional recovery after stroke, J Cereb Blood Flow Metab 28(10) (2008) 1722-32.

[55] M.D. Laird, J.R. Vender, K.M. Dhandapani, Opposing roles for reactive astrocytes following traumatic brain injury, Neurosignals 16(2-3) (2008) 154-64.

[56] G.K. Steinberg, D. Kondziolka, L.R. Wechsler, L.D. Lunsford, M.L. Coburn, J.B. Billigen, A.S. Kim, J.N. Johnson, D. Bates, B. King, C. Case, M. McGrogan, E.W. Yankee, N.E. Schwartz, Clinical Outcomes of Transplanted Modified Bone Marrow-Derived Mesenchymal Stem Cells in Stroke: A Phase 1/2a Study, Stroke 47(7) (2016) 1817-24.

[57] E.J. Smith, R.P. Stroemer, N. Gorenkova, M. Nakajima, W.R. Crum, E. Tang, L. Stevanato, J.D. Sinden, M. Modo, Implantation site and lesion topology determine efficacy of a human neural stem cell line in a rat model of chronic stroke, Stem Cells 30(4) (2012) 785-96.

[58] D. Tornero, O. Tsupykov, M. Granmo, C. Rodriguez, M. Gronning-Hansen, J. Thelin, E. Smozhanik, C. Laterza, S. Wattananit, R. Ge, J. Tatarishvili, S. Grealish, O. Brustle, G. Skibo, M. Parmar, J. Schouenborg, O. Lindvall, Z. Kokaia, Synaptic inputs from stroke-injured brain to grafted human stem cell-derived neurons activated by sensory stimuli, Brain 140(3) (2017) 692-706.

[59] L. Zai, C. Ferrari, S. Subbaiah, L.A. Havton, G. Coppola, S. Strittmatter, N. Irwin, D. Geschwind, L.I. Benowitz, Inosine alters gene expression and axonal projections in neurons contralateral to a cortical infarct and improves skilled use of the impaired limb, J Neurosci 29(25) (2009) 8187-97.

[60] D. Kim, L. Zai, P. Liang, C. Schaffling, D. Ahlborn, L.I. Benowitz, Inosine enhances axon sprouting and motor recovery after spinal cord injury, PLoS One 8(12) (2013) e81948.

[61] S. Jarvis, S.R. Schultz, Prospects for Optogenetic Augmentation of Brain Function, Front Syst Neurosci 9 (2015) 157.

[62] I.C. Maier, R.M. Ichiyama, G. Courtine, L. Schnell, I. Lavrov, V.R. Edgerton, M.E. Schwab, Differential effects of anti-Nogo-A antibody treatment and treadmill training in rats with incomplete spinal cord injury, Brain 132(Pt 6) (2009) 1426-40.

[63] P. Freund, E. Schmidlin, T. Wannier, J. Bloch, A. Mir, M.E. Schwab, E.M. Rouiller, Nogo-A-specific antibody treatment enhances sprouting and functional recovery after cervical lesion in adult primates, Nat Med 12(7) (2006) 790-2.

[64] P. Dibajnia, C.M. Morshead, Role of neural precursor cells in promoting repair following stroke, Acta Pharmacol Sin 34(1) (2013) 78-90.

[65] T.M. Bliss, R.H. Andres, G.K. Steinberg, Optimizing the success of cell transplantation therapy for stroke, Neurobiol Dis 37(2) (2010) 275-83.

[66] D. Drago, C. Cossetti, N. Iraci, E. Gaude, G. Musco, A. Bachi, S. Pluchino, The stem cell secretome and its role in brain repair, Biochimie 95(12) (2013) 2271-85.

[67] K. Tureyen, R. Vemuganti, K.K. Bowen, K.A. Sailor, R.J. Dempsey, EGF and FGF-2 infusion increases post-ischemic neural progenitor cell proliferation in the adult rat brain, Neurosurgery 57(6) (2005) 1254-63; discussion 1254-63.

[68] M. Bacigaluppi, S. Pluchino, L. Peruzzotti-Jametti, E. Kilic, U. Kilic, G. Salani, E. Brambilla, M.J. West, G. Comi, G. Martino, D.M. Hermann, Delayed post-ischaemic neuroprotection following systemic neural stem cell transplantation involves multiple mechanisms, Brain 132(Pt 8) (2009) 2239-51.

[69] M. Modo, R.P. Stroemer, E. Tang, S. Patel, H. Hodges, Effects of implantation site of stem cell grafts on behavioral recovery from stroke damage, Stroke 33(9) (2002) 2270-8.

[70] O.K. Bitzer-Quintero, I. Gonzalez-Burgos, Immune system in the brain: a modulatory role on dendritic spine morphophysiology?, Neural Plast 2012 (2012) 348642.

[71] E. Bible, D.Y. Chau, M.R. Alexander, J. Price, K.M. Shakesheff, M. Modo, The support of neural stem cells transplanted into stroke-induced brain cavities by PLGA particles, Biomaterials 30(16) (2009) 2985-94.

[72] K. Jin, X. Mao, L. Xie, V. Galvan, B. Lai, Y. Wang, O. Gorostiza, X. Wang, D.A. Greenberg, Transplantation of human neural precursor cells in Matrigel scaffolding improves outcome from focal cerebral ischemia after delayed postischemic treatment in rats, Journal of cerebral blood flow and metabolism : official journal of the International Society of Cerebral Blood Flow and Metabolism 30(3) (2010) 534-44.

[73] T. Osanai, S. Kuroda, H. Yasuda, Y. Chiba, K. Maruichi, M. Hokari, T. Sugiyama, H. Shichinohe, Y. Iwasaki, Noninvasive transplantation of bone marrow stromal cells for ischemic stroke: preliminary study with a thermoreversible gelation polymer hydrogel, Neurosurgery 66(6) (2010) 1140-7; discussion 1147.

[74] F. Meng, M. Modo, S.F. Badylak, Biologic scaffold for CNS repair, Regenerative medicine 9(3) (2014) 367-83.

[75] M. Modo, F. Ambrosio, R.M. Friedlander, S.F. Badylak, L.R. Wechsler, Bioengineering solutions for neural repair and recovery in stroke, Current opinion in neurology 26(6) (2013) 626-31.

[76] J. Zhong, A. Chan, L. Morad, H.I. Kornblum, G. Fan, S.T. Carmichael, Hydrogel matrix to support stem cell survival after brain transplantation in stroke, Neurorehabil Neural Repair 24(7) (2010) 636-44.

[77] A. Encarnacion, N. Horie, H. Keren-Gill, T.M. Bliss, G.K. Steinberg, M. Shamloo, Long-term behavioral assessment of function in an experimental model for ischemic stroke, J Neurosci Methods 196(2) (2011) 247-57.

[78] F. Moreau, S. Patel, M.L. Lauzon, C.R. McCreary, M. Goyal, R. Frayne, A.M. Demchuk, S.B. Coutts, E.E. Smith, Cavitation after acute symptomatic lacunar stroke depends on time, location, and MRI sequence, Stroke 43(7) (2012) 1837-42.

[79] M. Zhang, D. Methot, V. Poppa, Y. Fujio, K. Walsh, C.E. Murry, Cardiomyocyte grafting for cardiac repair: graft cell death and anti-death strategies, J Mol Cell Cardiol 33(5) (2001) 907-21.

[80] R.S. Lappalainen, S. Narkilahti, T. Huhtala, T. Liimatainen, T. Suuronen, A. Narvanen, R. Suuronen, O. Hovatta, J. Jolkkonen, The SPECT imaging shows the accumulation of neural progenitor cells into internal organs after systemic administration in middle cerebral artery occlusion rats, Neurosci Lett 440(3) (2008) 246-50.

[81] J.M. Mountz, Nuclear medicine in the rehabilitative treatment evaluation in stroke recovery. Role of diaschisis resolution and cerebral reorganization, Eura Medicophys 43(2) (2007) 221-39.

[82] Y. Ma, A. Zechariah, Y. Qu, D.M. Hermann, Effects of vascular endothelial growth factor in ischemic stroke, J Neurosci Res 90(10) (2012) 1873-82.

[83] R.A. Asher, D.A. Morgenstern, L.D. Moon, J.W. Fawcett, Chondroitin sulphate proteoglycans: inhibitory components of the glial scar, Prog Brain Res 132 (2001) 611-9.

[84] J. Silver, J.H. Miller, Regeneration beyond the glial scar, Nat Rev Neurosci 5(2) (2004) 146-56.

[85] X. Yu, R.V. Bellamkonda, Dorsal root ganglia neurite extension is inhibited by mechanical and chondroitin sulfate-rich interfaces, J Neurosci Res 66(2) (2001) 303-10.

[86] H. Yu, B. Cao, M. Feng, Q. Zhou, X. Sun, S. Wu, S. Jin, H. Liu, J. Lianhong, Combinated transplantation of neural stem cells and collagen type I promote functional recovery after cerebral ischemia in rats, Anat Rec (Hoboken) 293(5) (2010) 911-7.

[87] R.A. Sobel, The extracellular matrix in multiple sclerosis lesions, J Neuropathol Exp Neurol 57(3) (1998) 205-17.

[88] K.I. Park, Y.D. Teng, E.Y. Snyder, The injured brain interacts reciprocally with neural stem cells supported by scaffolds to reconstitute lost tissue, Nat Biotechnol 20(11) (2002) 1111-7.

[89] E. Bible, F. Dell'Acqua, B. Solanky, A. Balducci, P.M. Crapo, S.F. Badylak, E.T. Ahrens, M. Modo, Non-invasive imaging of transplanted human neural stem cells and ECM scaffold remodeling in the stroke-damaged rat brain by (19)F- and diffusion-MRI, Biomaterials 33(10) (2012) 2858-71.

[90] S.Z. Guo, X.J. Ren, B. Wu, T. Jiang, Preparation of the acellular scaffold of the spinal cord and the study of biocompatibility, Spinal Cord 48(7) (2010) 576-81.

[91] P.M. Crapo, C.J. Medberry, J.E. Reing, S. Tottey, Y. van der Merwe, K.E. Jones, S.F. Badylak, Biologic scaffolds composed of central nervous system extracellular matrix, Biomaterials 33(13) (2012) 3539-47.

[92] P.M. Crapo, S. Tottey, P.F. Slivka, S.F. Badylak, Effects of biologic scaffolds on human stem cells and implications for CNS tissue engineering, Tissue engineering. Part A 20(1-2) (2014) 313-23.

[93] U. Novak, A.H. Kaye, Extracellular matrix and the brain: components and function, J Clin Neurosci 7(4) (2000) 280-90.

[94] M.S. Viapiano, R.T. Matthews, From barriers to bridges: chondroitin sulfate proteoglycans in neuropathology, Trends Mol Med 12(10) (2006) 488-96.

[95] C.J. Medberry, P.M. Crapo, B.F. Siu, C.A. Carruthers, M.T. Wolf, S.P. Nagarkar, V. Agrawal, K.E. Jones, J. Kelly, S.A. Johnson, S.S. Velankar, S.C. Watkins, M. Modo, S.F. Badylak, Hydrogels derived from central nervous system extracellular matrix, Biomaterials 34(4) (2013) 1033-40.

[96] R.K. Mittapalli, X. Liu, C.E. Adkins, M.I. Nounou, K.A. Bohn, T.B. Terrell, H.S. Qhattal, W.J. Geldenhuys, D. Palmieri, P.S. Steeg, Q.R. Smith, P.R. Lockman, Paclitaxel-hyaluronic nanoconjugates prolong overall survival in a preclinical brain metastases of breast cancer model, Mol Cancer Ther 12(11) (2013) 2389-99.

[97] J. Lam, W.E. Lowry, S.T. Carmichael, T. Segura, Delivery of iPS-NPCs to the Stroke Cavity within a Hyaluronic Acid Matrix Promotes the Differentiation of Transplanted Cells, Adv Funct Mater 24(44) (2014) 7053-7062.

[98] A.J. Hyatt, D. Wang, J.C. Kwok, J.W. Fawcett, K.R. Martin, Controlled release of chondroitinase ABC from fibrin gel reduces the level of inhibitory glycosaminoglycan chains in lesioned spinal cord, J Control Release 147(1) (2010) 24-9.

[99] B.G. Ballios, M.J. Cooke, L. Donaldson, B.L. Coles, C.M. Morshead, D. van der Kooy, M.S. Shoichet, A Hyaluronan-Based Injectable Hydrogel Improves the Survival and Integration of Stem Cell Progeny following Transplantation, Stem Cell Reports 4(6) (2015) 1031-45.

[100] N.B. Skop, F. Calderon, S.W. Levison, C.D. Gandhi, C.H. Cho, Heparin crosslinked chitosan microspheres for the delivery of neural stem cells and growth factors for central nervous system repair, Acta Biomater 9(6) (2013) 6834-43.

[101] Y. Wu, W. Wei, M. Zhou, Y. Wang, J. Wu, G. Ma, Z. Su, Thermal-sensitive hydrogel as adjuvant-free vaccine delivery system for H5N1 intranasal immunization, Biomaterials 33(7) (2012) 2351-60.

[102] T. Nakaji-Hirabayashi, K. Kato, H. Iwata, In vivo study on the survival of neural stem cells transplanted into the rat brain with a collagen hydrogel that incorporates laminin-derived polypeptides, Bioconjug Chem 24(11) (2013) 1798-804.

[103] V.L. Cross, Y. Zheng, N. Won Choi, S.S. Verbridge, B.A. Sutermaster, L.J. Bonassar, C. Fischbach, A.D. Stroock, Dense type I collagen matrices that support cellular remodeling and microfabrication for studies of tumor angiogenesis and vasculogenesis in vitro, Biomaterials 31(33) (2010) 8596-607.

[104] D. Jiang, J. Liang, P.W. Noble, Hyaluronan in tissue injury and repair, Annu Rev Cell Dev Biol 23 (2007) 435-61.

[105] D.F. Emerich, M.A. Tracy, K.L. Ward, M. Figueiredo, R. Qian, C. Henschel, R.T. Bartus, Biocompatibility of poly (DL-lactide-co-glycolide) microspheres implanted into the brain, Cell Transplant 8(1) (1999) 47-58.

[106] G.M. Zentner, R. Rathi, C. Shih, J.C. McRea, M.H. Seo, H. Oh, B.G. Rhee, J. Mestecky, Z. Moldoveanu, M. Morgan, S. Weitman, Biodegradable block copolymers for delivery of proteins and water-insoluble drugs, J Control Release 72(1-3) (2001) 203-15.

[107] C. Gouhier, S. Chalon, M.C. Venier-Julienne, S. Bodard, J. Benoit, J. Besnard, D. Guilloteau, Neuroprotection of nerve growth factor-loaded microspheres on the D2 dopaminergic receptor positive-striatal neurones in quinolinic acid-lesioned rats: a quantitative autoradiographic assessment with iodobenzamide, Neurosci Lett 288(1) (2000) 71-5.

[108] P. Menei, J.M. Pean, V. Nerriere-Daguin, C. Jollivet, P. Brachet, J.P. Benoit, Intracerebral implantation of NGF-releasing biodegradable microspheres protects striatum against excitotoxic damage, Exp Neurol 161(1) (2000) 259-72.

[109] J.E. Rinholm, N.B. Hamilton, N. Kessaris, W.D. Richardson, L.H. Bergersen, D. Attwell, Regulation of oligodendrocyte development and myelination by glucose and lactate, J Neurosci 31(2) (2011) 538-48.

[110] M.J. Cooke, Y. Wang, C.M. Morshead, M.S. Shoichet, Controlled epi-cortical delivery of epidermal growth factor for the stimulation of endogenous neural stem cell proliferation in stroke-injured brain, Biomaterials 32(24) (2011) 5688-97.

[111] K. Duncan, G.S. Gonzales-Portillo, S.A. Acosta, Y. Kaneko, C.V. Borlongan, N. Tajiri, Stem cell-paved biobridges facilitate stem transplant and host brain cell interactions for stroke therapy, Brain Res 1623 (2015) 160-5.

[112] H. Ghuman, A.R. Massensini, J. Donnelly, S.M. Kim, C.J. Medberry, S.F. Badylak, M. Modo, ECM hydrogel for the treatment of stroke: Characterization of the host cell infiltrate, Biomaterials 91 (2016) 166-181.

[113] H.T. Ta, C.R. Dass, D.E. Dunstan, Injectable chitosan hydrogels for localised cancer therapy, J Control Release 126(3) (2008) 205-16.

[114] A.R. Massensini, H. Ghuman, L.T. Saldin, C.J. Medberry, T.J. Keane, F.J. Nicholls, S.S. Velankar, S.F. Badylak, M. Modo, Concentration-dependent rheological properties of ECM hydrogel for intracerebral delivery to a stroke cavity, Acta Biomater 27 (2015) 116-130.

[115] D. Gupta, C.H. Tator, M.S. Shoichet, Fast-gelling injectable blend of hyaluronan and methylcellulose for intrathecal, localized delivery to the injured spinal cord, Biomaterials 27(11) (2006) 2370-9.

[116] M.L. Brady, R. Raghavan, A. Alexander, K. Kubota, K. Sillay, M.E. Emborg, Pathways of infusate loss during convection-enhanced delivery into the putamen nucleus, Stereotactic and functional neurosurgery 91(2) (2013) 69-78.

[117] F. Valles, M.S. Fiandaca, J. Bringas, P. Dickinson, R. LeCouteur, R. Higgins, M. Berger, J. Forsayeth, K.S. Bankiewicz, Anatomic compression caused by high-volume convection-enhanced delivery to the brain, Neurosurgery 65(3) (2009) 579-85; discussion 585-6.

[118] E. Fournier, C. Passirani, C.N. Montero-Menei, J.P. Benoit, Biocompatibility of implantable synthetic polymeric drug carriers: focus on brain biocompatibility, Biomaterials 24(19) (2003) 3311-31.

[119] K.J. Lampe, K.B. Bjugstad, M.J. Mahoney, Impact of degradable macromer content in a poly(ethylene glycol) hydrogel on neural cell metabolic activity, redox state, proliferation, and differentiation, Tissue Eng Part A 16(6) (2010) 1857-66.

[120] C.G. Williams, A.N. Malik, T.K. Kim, P.N. Manson, J.H. Elisseeff, Variable cytocompatibility of six cell lines with photoinitiators used for polymerizing hydrogels and cell encapsulation, Biomaterials 26(11) (2005) 1211-8.

[121] K.S. Anseth, A.T. Metters, S.J. Bryant, P.J. Martens, J.H. Elisseeff, C.N. Bowman, In situ forming degradable networks and their application in tissue engineering and drug delivery, J Control Release 78(1-3) (2002) 199-209.

[122] C.C. Lin, K.S. Anseth, PEG hydrogels for the controlled release of biomolecules in regenerative medicine, Pharm Res 26(3) (2009) 631-43.

[123] P.J. Martens, S.J. Bryant, K.S. Anseth, Tailoring the degradation of hydrogels formed from multivinyl poly(ethylene glycol) and poly(vinyl alcohol) macromers for cartilage tissue engineering, Biomacromolecules 4(2) (2003) 283-92.

[124] G. De Santis, A.B. Lennon, F. Boschetti, B. Verhegghe, P. Verdonck, P.J. Prendergast, How can cells sense the elasticity of a substrate? An analysis using a cell tensegrity model, Eur Cell Mater 22 (2011) 202-13.

[125] N.D. Leipzig, M.S. Shoichet, The effect of substrate stiffness on adult neural stem cell behavior, Biomaterials 30(36) (2009) 6867-78.

[126] A.J. Engler, S. Sen, H.L. Sweeney, D.E. Discher, Matrix elasticity directs stem cell lineage specification, Cell 126(4) (2006) 677-89.

[127] M.D. Tang-Schomer, J.D. White, L.W. Tien, L.I. Schmitt, T.M. Valentin, D.J. Graziano, A.M. Hopkins, F.G. Omenetto, P.G. Haydon, D.L. Kaplan, Bioengineered functional brain-like cortical tissue, Proc Natl Acad Sci U S A 111(38) (2014) 13811-6.

[128] M.C. Murphy, G.L. Curran, K.J. Glaser, P.J. Rossman, J. Huston, 3rd, J.F. Poduslo, C.R. Jack, Jr., J.P. Felmlee, R.L. Ehman, Magnetic resonance elastography of the brain in a mouse model of Alzheimer's disease: initial results, Magn Reson Imaging 30(4) (2012) 535-9.

[129] A.F. Christ, K. Franze, H. Gautier, P. Moshayedi, J. Fawcett, R.J. Franklin, R.T. Karadottir, J. Guck, Mechanical difference between white and gray matter in the rat cerebellum measured by scanning force microscopy, J Biomech 43(15) (2010) 2986-92.

[130] S.K. Seidlits, Z.Z. Khaing, R.R. Petersen, J.D. Nickels, J.E. Vanscoy, J.B. Shear, C.E. Schmidt, The effects of hyaluronic acid hydrogels with tunable mechanical properties on neural progenitor cell differentiation, Biomaterials 31(14) (2010) 3930-40.

[131] R. Biran, D.C. Martin, P.A. Tresco, Neuronal cell loss accompanies the brain tissue response to chronically implanted silicon microelectrode arrays, Exp Neurol 195(1) (2005) 115-26.

[132] M. Ashioti, J.S. Beech, A.S. Lowe, M.B. Hesselink, M. Modo, S.C. Williams, Multi-modal characterisation of the neocortical clip model of focal cerebral ischaemia by MRI, behaviour and immunohistochemistry, Brain research 1145 (2007) 177-89.

[133] D. Kondziolka, G.K. Steinberg, S.B. Cullen, M. McGrogan, Evaluation of surgical techniques for neuronal cell transplantation used in patients with stroke, Cell transplantation 13(7-8) (2004) 749-54.

[134] M.J. Caicco, M.J. Cooke, Y. Wang, A. Tuladhar, C.M. Morshead, M.S. Shoichet, A hydrogel composite system for sustained epi-cortical delivery of Cyclosporin A to the brain for treatment of stroke, Journal of controlled release : official journal of the Controlled Release Society 166(3) (2013) 197-202.

[135] D. Klose, M. Laprais, V. Leroux, F. Siepmann, B. Deprez, R. Bordet, J. Siepmann, Fenofibrate-loaded PLGA microparticles: effects on ischemic stroke, European journal of pharmaceutical sciences : official journal of the European Federation for Pharmaceutical Sciences 37(1) (2009) 43-52.

[136] D.F. Emerich, E. Silva, O. Ali, D. Mooney, W. Bell, S.J. Yu, Y. Kaneko, C. Borlongan, Injectable VEGF hydrogels produce near complete neurological and anatomical protection following cerebral ischemia in rats, Cell transplantation 19(9) (2010) 1063-71.

[137] D.O. Freytes, J. Martin, S.S. Velankar, A.S. Lee, S.F. Badylak, Preparation and rheological characterization of a gel form of the porcine urinary bladder matrix, Biomaterials 29(11) (2008) 1630-7.

[138] L. Zhang, F. Zhang, Z. Weng, B.N. Brown, H. Yan, X.M. Ma, P.S. Vosler, S.F. Badylak, C.E. Dixon, X.T. Cui, J. Chen, Effect of an inductive hydrogel composed of urinary bladder matrix upon functional recovery following traumatic brain injury, Tissue Eng Part A 19(17-18) (2013) 1909-18.

[139] K. Saha, A.J. Keung, E.F. Irwin, Y. Li, L. Little, D.V. Schaffer, K.E. Healy, Substrate modulus directs neural stem cell behavior, Biophys J 95(9) (2008) 4426-38.

[140] E. Bible, D.Y. Chau, M.R. Alexander, J. Price, K.M. Shakesheff, M. Modo, Attachment of stem cells to scaffold particles for intra-cerebral transplantation, Nature protocols 4(10) (2009) 1440-53.

[141] A.V. Naumova, M. Modo, A. Moore, C.E. Murry, J.A. Frank, Clinical imaging in regenerative medicine, Nature biotechnology (2014).

[142] P.M. Crapo, T.W. Gilbert, S.F. Badylak, An overview of tissue and whole organ decellularization processes, Biomaterials 32(12) (2011) 3233-43.

[143] H. Marcal, T. Ahmed, S.F. Badylak, S. Tottey, L.J. Foster, A comprehensive protein expression profile of extracellular matrix biomaterial derived from porcine urinary bladder, Regenerative medicine 7(2) (2012) 159-66.

[144] L. Huleihel, G.S. Hussey, J.D. Naranjo, L. Zhang, J.L. Dziki, N.J. Turner, D.B. Stolz, S.F. Badylak, Matrix-bound nanovesicles within ECM bioscaffolds, Sci Adv 2(6) (2016) e1600502.

[145] M.T. Wolf, K.A. Daly, E.P. Brennan-Pierce, S.A. Johnson, C.A. Carruthers, A. D'Amore, S.P. Nagarkar, S.S. Velankar, S.F. Badylak, A hydrogel derived from decellularized dermal extracellular matrix, Biomaterials 33(29) (2012) 7028-38.

[146] M. Modo, Long-term survival and serial assessment of stroke damage and recovery - practical and methodological considerations, J Exp Stroke Transl Med 2(2) (2009) 52-68.

[147] M. Modo, R.P. Stroemer, E. Tang, T. Veizovic, P. Sowniski, H. Hodges, Neurological sequelae and long-term behavioural assessment of rats with transient middle cerebral artery occlusion, J Neurosci Methods 104(1) (2000) 99-109.

[148] M. Stille, E.J. Smith, W.R. Crum, M. Modo, 3D reconstruction of 2D fluorescence histology images and registration with in vivo MR images: Application in a rodent stroke model, J Neurosci Methods 219(1) (2013) 27-40.

[149] H. Ghuman, M. Gerwig, F.J. Nicholls, J.R. Liu, J. Donnelly, S.F. Badylak, M. Modo, Long-term retention of ECM hydrogel after implantation into a sub-acute stroke cavity reduces lesion volume, Acta Biomater 63 (2017) 50-63.

[150] T. Jin, F.J. Nicholls, W.R. Crum, H. Ghuman, S.F. Badylak, M. Modo, Diamagnetic chemical exchange saturation transfer (diaCEST) affords magnetic resonance imaging of extracellular matrix hydrogel implantation in a rat model of stroke, Biomaterials 113 (2017) 176-190.

[151] D. Ito, K. Tanaka, S. Suzuki, T. Dembo, Y. Fukuuchi, Enhanced expression of Iba1, ionized calcium-binding adapter molecule 1, after transient focal cerebral ischemia in rat brain, Stroke 32(5) (2001) 1208-15.

[152] S. Tan, J.Y. Fang, Z. Yang, M.E. Nimni, B. Han, The synergetic effect of hydrogel stiffness and growth factor on osteogenic differentiation, Biomaterials 35(20) (2014) 5294-306.

[153] A.E. Wilkinson, L.J. Kobelt, N.D. Leipzig, Immobilized ECM molecules and the effects of concentration and surface type on the control of NSC differentiation, Journal of biomedical materials research. Part A (2013).

[154] N.H. Qureshi, K.S. Bankiewicz, D.N. Louis, F.H. Hochberg, E.A. Chiocca, G.R.t. Harsh, Multicolumn infusion of gene therapy cells into human brain tumors: technical report, Neurosurgery 46(3) (2000) 663-8; discussion 668-9.

[155] D. Yin, R.M. Richardson, M.S. Fiandaca, J. Bringas, J. Forsayeth, M.S. Berger, K.S. Bankiewicz, Cannula placement for effective convection-enhanced delivery in the nonhuman primate thalamus and brainstem: implications for clinical delivery of therapeutics, Journal of neurosurgery 113(2) (2010) 240-8.

[156] D. Yin, J. Forsayeth, K.S. Bankiewicz, Optimized cannula design and placement for convection-enhanced delivery in rat striatum, Journal of neuroscience methods 187(1) (2010) 46-51.

[157] K. Agashi, D.Y. Chau, K.M. Shakesheff, The effect of delivery via narrow-bore needles on mesenchymal cells, Regenerative medicine 4(1) (2009) 49-64.

[158] D. Kondziolka, G.T. Gobbel, W. Fellows-Mayle, Y.F. Chang, M. Uram, Injection parameters affect cell viability and implant volumes in automated cell delivery for the brain, Cell transplantation 20(11-12) (2011) 1901-6.

[159] A.I. Brooks, M.W. Halterman, C.A. Chadwick, B.L. Davidson, M. Haak-Frendscho, C. Radel, C. Porter, H.J. Federoff, Reproducible and efficient murine CNS gene delivery using a microprocessor-controlled injector, Journal of neuroscience methods 80(2) (1998) 137-47.

[160] G.T. Gobbel, D. Kondziolka, W. Fellows-Mayle, M. Uram, Manual vs automated delivery of cells for transplantation: accuracy, reproducibility, and impact on viability, Neurosurgery 67(6) (2010) 1662-8; discussion 1668.

[161] K.M. Chan, R.H. Li, J.W. Chapman, E.M. Trac, J.B. Kobler, S.M. Zeitels, R. Langer, S.S. Karajanagi, Functionalizable hydrogel microparticles of tunable size and stiffness for soft-tissue filler applications, Acta Biomater 10(6) (2014) 2563-73.

[162] R.S. Stowers, S.C. Allen, L.J. Suggs, Dynamic phototuning of 3D hydrogel stiffness, Proc Natl Acad Sci U S A 112(7) (2015) 1953-8.

[163] K. Ziv, H. Nuhn, Y. Ben-Haim, L.S. Sasportas, P.J. Kempen, T.P. Niedringhaus, M. Hrynyk, R. Sinclair, A.E. Barron, S.S. Gambhir, A tunable silk-alginate hydrogel scaffold for stem cell culture and transplantation, Biomaterials 35(12) (2014) 3736-43.

[164] E.R. Aurand, J.L. Wagner, R. Shandas, K.B. Bjugstad, Hydrogel formulation determines cell fate of fetal and adult neural progenitor cells, Stem cell research 12(1) (2014) 11-23.

[165] E.R. Aurand, K.J. Lampe, K.B. Bjugstad, Defining and designing polymers and hydrogels for neural tissue engineering, Neurosci Res 72(3) (2012) 199-213.

[166] B.R. Simona, L. Hirt, L. Demko, T. Zambelli, J. Voros, M. Ehrbar, V. Milleret, Density gradients at hydrogel interfaces for enhanced cell penetration, Biomater Sci 3(4) (2015) 586-91.

[167] K.B. Bjugstad, K. Lampe, D.S. Kern, M. Mahoney, Biocompatibility of poly(ethylene glycol)-based hydrogels in the brain: an analysis of the glial response across space and time, J Biomed Mater Res A 95(1) (2010) 79-91.

[168] Y. Ma, J. Wang, Y. Wang, G.Y. Yang, The biphasic function of microglia in ischemic stroke, Prog Neurobiol (2016).

[169] J.R. Mauney, R.M. Adam, Dynamic reciprocity in cell-scaffold interactions, Adv Drug Deliv Rev 82-83 (2015) 77-85.

[170] M. Bracher, D. Bezuidenhout, M.P. Lutolf, T. Franz, M. Sun, P. Zilla, N.H. Davies, Cell specific ingrowth hydrogels, Biomaterials 34(28) (2013) 6797-803.

[171] S.F. Badylak, Decellularized allogeneic and xenogeneic tissue as a bioscaffold for regenerative medicine: factors that influence the host response, Ann Biomed Eng 42(7) (2014) 1517-27.

[172] S. Plantman, Proregenerative properties of ECM molecules, Biomed Res Int 2013 (2013) 981695.

[173] F.W. Meng, P.F. Slivka, C.L. Dearth, S.F. Badylak, Solubilized extracellular matrix from brain and urinary bladder elicits distinct functional and phenotypic responses in macrophages, Biomaterials 46 (2015) 131-40.

[174] Y. Hosseini, M. Agah, S.S. Verbridge, Endothelial cell sensing, restructuring, and invasion in collagen hydrogel structures, Integr Biol (Camb) 7(11) (2015) 1432-41.

[175] A.K. Blakney, M.D. Swartzlander, S.J. Bryant, The effects of substrate stiffness on the in vitro activation of macrophages and in vivo host response to poly(ethylene glycol)-based hydrogels, J Biomed Mater Res A 100(6) (2012) 1375-86.

[176] M.T. Wolf, C.L. Dearth, C.A. Ranallo, S.T. LoPresti, L.E. Carey, K.A. Daly, B.N. Brown, S.F. Badylak, Macrophage polarization in response to ECM coated polypropylene mesh, Biomaterials 35(25) (2014) 6838-49.

[177] T.J. Keane, R. Londono, N.J. Turner, S.F. Badylak, Consequences of ineffective decellularization of biologic scaffolds on the host response, Biomaterials 33(6) (2012) 1771-81.

[178] N. Mokarram, A. Merchant, V. Mukhatyar, G. Patel, R.V. Bellamkonda, Effect of modulating macrophage phenotype on peripheral nerve repair, Biomaterials 33(34) (2012) 8793-801.

[179] B.N. Brown, J.E. Valentin, A.M. Stewart-Akers, G.P. McCabe, S.F. Badylak, Macrophage phenotype and remodeling outcomes in response to biologic scaffolds with and without a cellular component, Biomaterials 30(8) (2009) 1482-91.

[180] L. Roll, A. Faissner, Influence of the extracellular matrix on endogenous and transplanted stem cells after brain damage, Front Cell Neurosci 8 (2014) 219.

[181] S.E. Stabenfeldt, G. Munglani, A.J. Garcia, M.C. LaPlaca, Biomimetic microenvironment modulates neural stem cell survival, migration, and differentiation, Tissue engineering. Part A 16(12) (2010) 3747-58.

[182] M.C. Tate, D.A. Shear, S.W. Hoffman, D.G. Stein, D.R. Archer, M.C. LaPlaca, Fibronectin promotes survival and migration of primary neural stem cells transplanted into the traumatically injured mouse brain, Cell transplantation 11(3) (2002) 283-95.

[183] T.W. Hsiao, P.A. Tresco, V. Hlady, Astrocytes alignment and reactivity on collagen hydrogels patterned with ECM proteins, Biomaterials 39 (2015) 124-30.

[184] D.J. Macaya, K. Hayakawa, K. Arai, M. Spector, Astrocyte infiltration into injectable collagen-based hydrogels containing FGF-2 to treat spinal cord injury, Biomaterials 34(14) (2013) 3591-602.

[185] P.C. Georges, W.J. Miller, D.F. Meaney, E.S. Sawyer, P.A. Janmey, Matrices with compliance comparable to that of brain tissue select neuronal over glial growth in mixed cortical cultures, Biophys J 90(8) (2006) 3012-8.

[186] W. Goldsmith, The state of head injury biomechanics: past, present, and future: part 1, Crit Rev Biomed Eng 29(5-6) (2001) 441-600.

[187] H.W. Soon, A. Qiu, Individualized diffeomorphic mapping of brains with large cortical infarcts, Magn Reson Imaging 33(1) (2015) 110-23.

[188] F. Faul, E. Erdfelder, A.G. Lang, A. Buchner, G*Power 3: a flexible statistical power analysis program for the social, behavioral, and biomedical sciences, Behav Res Methods 39(2) (2007) 175-91.

[189] D. Lakens, Calculating and reporting effect sizes to facilitate cumulative science: a practical primer for t-tests and ANOVAs, Front Psychol 4 (2013) 863.

[190] B. Lee, A. Newberg, Neuroimaging in traumatic brain imaging, NeuroRx 2(2) (2005) 372-83.

[191] P. Vespa, D. Hanley, J. Betz, A. Hoffer, J. Engh, R. Carter, P. Nakaji, C. Ogilvy, J. Jallo, W. Selman, A. Bistran-Hall, K. Lane, N. McBee, J. Saver, R.E. Thompson, N. Martin, I. Investigators, ICES (Intraoperative Stereotactic Computed Tomography-Guided Endoscopic Surgery) for Brain Hemorrhage: A Multicenter Randomized Controlled Trial, Stroke 47(11) (2016) 2749-2755.

[192] S. Bette, J. Gempt, T. Huber, C. Delbridge, B. Meyer, C. Zimmer, J.S. Kirschke, T. Boeckh-Behrens, FLAIR signal increase of the fluid within the resection cavity after glioma surgery: generally valid as early recurrence marker?, J Neurosurg (2016) 1-9.

[193] M.M. Breteler, N.M. van Amerongen, J.C. van Swieten, J.J. Claus, D.E. Grobbee, J. van Gijn, A. Hofman, F. van Harskamp, Cognitive correlates of ventricular enlargement and cerebral white matter lesions on magnetic resonance imaging. The Rotterdam Study, Stroke 25(6) (1994) 1109-15.

[194] R.D. Record, D. Hillegonds, C. Simmons, R. Tullius, F.A. Rickey, D. Elmore, S.F. Badylak, In vivo degradation of 14C-labeled small intestinal submucosa (SIS) when used for urinary bladder repair, Biomaterials 22(19) (2001) 2653-9.

[195] S.J. Forbes, N. Rosenthal, Preparing the ground for tissue regeneration: from mechanism to therapy, Nat Med 20(8) (2014) 857-69.

[196] I.T. Swinehart, S.F. Badylak, Extracellular matrix bioscaffolds in tissue remodeling and morphogenesis, Dev Dyn 245(3) (2016) 351-60.

[197] M.J. Bissell, J. Aggeler, Dynamic reciprocity: how do extracellular matrix and hormones direct gene expression?, Prog Clin Biol Res 249 (1987) 251-62.

[198] Q.L. Loh, C. Choong, Three-dimensional scaffolds for tissue engineering applications: role of porosity and pore size, Tissue Eng Part B Rev 19(6) (2013) 485-502.

[199] T. Rossetti, F. Nicholls, M. Modo, Intra-cerebral cell implantation: Preparation and characterization of cell suspensions, Cell Transplant (2015).

[200] S.M. Lien, L.Y. Ko, T.J. Huang, Effect of pore size on ECM secretion and cell growth in gelatin scaffold for articular cartilage tissue engineering, Acta Biomater 5(2) (2009) 670-9.

[201] P.S. Ciano, R.B. Colvin, A.M. Dvorak, J. McDonagh, H.F. Dvorak, Macrophage migration in fibrin gel matrices, Lab Invest 54(1) (1986) 62-70.

[202] K. Wolf, M. Te Lindert, M. Krause, S. Alexander, J. Te Riet, A.L. Willis, R.M. Hoffman, C.G. Figdor, S.J. Weiss, P. Friedl, Physical limits of cell migration: control by ECM space and nuclear deformation and tuning by proteolysis and traction force, J Cell Biol 201(7) (2013) 1069-84.

[203] P.F. Slivka, C.L. Dearth, T.J. Keane, F.W. Meng, C.J. Medberry, R.T. Riggio, J.E. Reing, S.F. Badylak, Fractionation of an ECM hydrogel into structural and soluble components reveals distinctive roles in regulating macrophage behavior, Biomater Sci 2(10) (2014) 1521-34.

[204] B.N. Brown, R. Londono, S. Tottey, L. Zhang, K.A. Kukla, M.T. Wolf, K.A. Daly, J.E. Reing, S.F. Badylak, Macrophage phenotype as a predictor of constructive remodeling following the implantation of biologically derived surgical mesh materials, Acta Biomater 8(3) (2012) 978-87.

[205] J.M. Aamodt, D.W. Grainger, Extracellular matrix-based biomaterial scaffolds and the host response, Biomaterials 86 (2016) 68-82.

[206] B.N. Brown, S.F. Badylak, Extracellular matrix as an inductive scaffold for functional tissue reconstruction, Transl Res 163(4) (2014) 268-85.

[207] I. Bechmann, Failed central nervous system regeneration: a downside of immune privilege?, Neuromolecular Med 7(3) (2005) 217-28.

[208] A. Banerjee, M. Arha, S. Choudhary, R.S. Ashton, S.R. Bhatia, D.V. Schaffer, R.S. Kane, The influence of hydrogel modulus on the proliferation and differentiation of encapsulated neural stem cells, Biomaterials 30(27) (2009) 4695-9.

[209] M. Ahearne, Introduction to cell-hydrogel mechanosensing, Interface Focus 4(2) (2014) 20130038.

[210] M. Modo, J.S. Beech, T.J. Meade, S.C. Williams, J. Price, A chronic 1 year assessment of MRI contrast agent-labelled neural stem cell transplants in stroke, Neuroimage 47 Suppl 2 (2009) T133-42.

[211] W. Qiu, Q. Jiang, G. Xiao, W. Wang, H. Shen, Changes in intracranial pressure gradients between the cerebral hemispheres in patients with intracerebral hematomas in one cerebral hemisphere, BMC Anesthesiol 14 (2014) 112.

[212] S.B. Jeon, S.U. Kwon, J.C. Park, D.H. Lee, S.C. Yun, Y.J. Kim, J.S. Ahn, B.D. Kwun, D.W. Kang, H.A. Choi, K. Lee, J.S. Kim, Reduction of Midline Shift Following Decompressive Hemicraniectomy for Malignant Middle Cerebral Artery Infarction, J Stroke 18(3) (2016) 328-336.

[213] J. Tao, J. Zhang, Y. Hu, Y. Yang, Z. Gou, T. Du, J. Mao, M. Gou, A conformal hydrogel nanocomposite for local delivery of paclitaxel, J Biomater Sci Polym Ed 28(1) (2017) 107-118.

[214] D.J. Cook, C. Nguyen, H.N. Chun, L.L. I, A.S. Chiu, M. Machnicki, T.I. Zarembinski, S.T. Carmichael, Hydrogel-delivered brain-derived neurotrophic factor promotes tissue repair and recovery after stroke, J Cereb Blood Flow Metab 37(3) (2017) 1030-1045.

[215] A. Tuladhar, C.M. Morshead, M.S. Shoichet, Circumventing the blood-brain barrier: Local delivery of cyclosporin A stimulates stem cells in stroke-injured rat brain, J Control Release 215 (2015) 1-11.

[216] Y. Wang, M.J. Cooke, N. Sachewsky, C.M. Morshead, M.S. Shoichet, Bioengineered sequential growth factor delivery stimulates brain tissue regeneration after stroke, J Control Release 172(1) (2013) 1-11.

[217] J.Y. Wang, A.K. Liou, Z.H. Ren, L. Zhang, B.N. Brown, X.T. Cui, S.F. Badylak, Y.N. Cai, Y.Q. Guan, R.K. Leak, J. Chen, X. Ji, L. Chen, Neurorestorative effect of urinary bladder matrix-mediated neural stem cell transplantation following traumatic brain injury in rats, CNS Neurol Disord Drug Targets 12(3) (2013) 413-25.

[218] Y. Wu, J. Wang, Y. Shi, H. Pu, R.K. Leak, A.K. Liou, S.F. Badylak, Z. Liu, J. Zhang, J. Chen, L. Chen, Implantation of Brain-derived Extracellular Matrix Enhances Neurological Recovery after Traumatic Brain Injury, Cell Transplant (2016).

[219] S. Ramon y Cajal, Degeneration and regeneration of the nervous system., Haffner Publishing, New York City, NY, 1928.

[220] A.F. Hallbergson, C. Gnatenco, D.A. Peterson, Neurogenesis and brain injury: managing a renewable resource for repair, J Clin Invest 112(8) (2003) 1128-33.

[221] E.J. Fry, Central nervous system regeneration: mission impossible?, Clin Exp Pharmacol Physiol 28(4) (2001) 253-8.

[222] L.S. Illis, Central nervous system regeneration does not occur, Spinal Cord 50(4) (2012) 259-63.

[223] E.R. Aurand, J. Wagner, C. Lanning, K.B. Bjugstad, Building biocompatible hydrogels for tissue engineering of the brain and spinal cord, J Funct Biomater 3(4) (2012) 839-63.

[224] A. Gefen, S.S. Margulies, Are in vivo and in situ brain tissues mechanically similar?, J Biomech 37(9) (2004) 1339-52.

[225] Z. Taylor, K. Miller, Reassessment of brain elasticity for analysis of biomechanisms of hydrocephalus, J Biomech 37(8) (2004) 1263-9.

[226] J.E. Valentin, A.M. Stewart-Akers, T.W. Gilbert, S.F. Badylak, Macrophage participation in the degradation and remodeling of extracellular matrix scaffolds, Tissue Eng Part A 15(7) (2009) 1687-94.

[227] T.W. Gilbert, A.M. Stewart-Akers, S.F. Badylak, A quantitative method for evaluating the degradation of biologic scaffold materials, Biomaterials 28(2) (2007) 147-50.

[228] C.L. Dearth, P.F. Slivka, S.A. Stewart, T.J. Keane, J.K. Tay, R. Londono, Q. Goh, F.X. Pizza, S.F. Badylak, Inhibition of COX1/2 alters the host response and reduces ECM scaffold mediated constructive tissue remodeling in a rodent model of skeletal muscle injury, Acta Biomater 31 (2016) 50-60.

[229] L.E. Carey, C.L. Dearth, S.A. Johnson, R. Londono, C.J. Medberry, K.A. Daly, S.F. Badylak, In vivo degradation of 14C-labeled porcine dermis biologic scaffold, Biomaterials 35(29) (2014) 8297-304.

[230] S.F. Badylak, D.O. Freytes, T.W. Gilbert, Extracellular matrix as a biological scaffold material: Structure and function, Acta Biomater 5(1) (2009) 1-13.

[231] D. Tukmachev, S. Forostyak, Z. Koci, K. Zaviskova, I. Vackova, K. Vyborny, I. Sandvig, A. Sandvig, C.J. Medberry, S.F. Badylak, E. Sykova, S. Kubinova, Injectable Extracellular Matrix Hydrogels as Scaffolds for Spinal Cord Injury Repair, Tissue Eng Part A 22(3-4) (2016) 306-17.

[232] D.N. Wheatley, Diffusion, perfusion and the exclusion principles in the structural and functional organization of the living cell: reappraisal of the properties of the 'ground substance', J Exp Biol 206(Pt 12) (2003) 1955-61.

[233] K.S. Midwood, L.V. Williams, J.E. Schwarzbauer, Tissue repair and the dynamics of the extracellular matrix., International Journal of Biochemistry & Cell Biology 36(6) (2004) 1031-1037.

[234] L. Hakkinen, H. Larjava, L. Koivisto, Granulation tissue formation and remodeling., Endodontic Topics 24(1) (2011) 94-129.

[235] M.M. Martino, S. Brkic, E. Bovo, M. Burger, D.J. Schaefer, T. Wolff, L. Gurke, P.S. Briquez, H.M. Larsson, R. Gianni-Barrera, J.A. Hubbell, A. Banfi, Extracellular matrix and growth factor engineering for controlled angiogenesis in regenerative medicine, Front Bioeng Biotechnol 3 (2015) 45.

[236] E. Bible, O. Qutachi, D.Y. Chau, M.R. Alexander, K.M. Shakesheff, M. Modo, Neo-vascularization of the stroke cavity by implantation of human neural stem cells on VEGF-releasing PLGA microparticles, Biomaterials 33(30) (2012) 7435-46.

[237] P. Friedl, S. Alexander, Cancer invasion and the microenvironment: plasticity and reciprocity, Cell 147(5) (2011) 992-1009.

[238] P. Friedl, J.A. Zallen, Dynamics of cell-cell and cell-matrix interactions in morphogenesis, regeneration and cancer, Curr Opin Cell Biol 22(5) (2010) 557-9.

[239] I. Kazanis, N. Gorenkova, J.W. Zhao, R.J. Franklin, M. Modo, C. Ffrench-Constant, The late response of rat subependymal zone stem and progenitor cells to stroke is restricted to directly affected areas of their niche, Exp Neurol 248 (2013) 387-97.

[240] S. Prokoph, E. Chavakis, K.R. Levental, A. Zieris, U. Freudenberg, S. Dimmeler, C. Werner, Sustained delivery of SDF-1alpha from heparin-based hydrogels to attract circulating pro-angiogenic cells, Biomaterials 33(19) (2012) 4792-800.

[241] J. Lam, N.F. Truong, T. Segura, Design of cell-matrix interactions in hyaluronic acid hydrogel scaffolds, Acta Biomater 10(4) (2014) 1571-1580.

[242] I.V. Yannas, Emerging rules for inducing organ regeneration, Biomaterials 34(2) (2013) 321-30.

[243] R. Shechter, M. Schwartz, CNS sterile injury: just another wound healing?, Trends Mol Med 19(3) (2013) 135-43.

[244] E.T. Ahrens, J.W. Bulte, Tracking immune cells in vivo using magnetic resonance imaging, Nat Rev Immunol 13(10) (2013) 755-63.

[245] T.K. Hitchens, Q. Ye, D.F. Eytan, J.M. Janjic, E.T. Ahrens, C. Ho, 19F MRI detection of acute allograft rejection with in vivo perfluorocarbon labeling of immune cells, Magn Reson Med 65(4) (2011) 1144-53.

[246] C. Ho, T.K. Hitchens, A non-invasive approach to detecting organ rejection by MRI: monitoring the accumulation of immune cells at the transplanted organ, Curr Pharm Biotechnol 5(6) (2004) 551-66.

[247] H.E. Daldrup-Link, C. Chan, O. Lenkov, S. Taghavigarmestani, T. Nazekati, H. Nejadnik, F. Chapelin, A. Khurana, X. Tong, F. Yang, L. Pisani, M. Longaker, S.S. Gambhir, Detection of Stem Cell Transplant Rejection with Ferumoxytol MR Imaging: Correlation of MR Imaging Findings with Those at Intravital Microscopy, Radiology 284(2) (2017) 495-507.

[248] A.V. Ratner, R. Hurd, H.H. Muller, B. Bradley-Simpson, W. Pitts, D. Shibata, C. Sotak, S.W. Young, 19F magnetic resonance imaging of the reticuloendothelial system, Magn Reson Med 5(6) (1987) 548-54.

[249] S. Temme, F. Bonner, J. Schrader, U. Flogel, 19F magnetic resonance imaging of endogenous macrophages in inflammation, Wiley Interdiscip Rev Nanomed Nanobiotechnol 4(3) (2012) 329-43.

[250] U. Flogel, Z. Ding, H. Hardung, S. Jander, G. Reichmann, C. Jacoby, R. Schubert, J. Schrader, In vivo monitoring of inflammation after cardiac and cerebral ischemia by fluorine magnetic resonance imaging, Circulation 118(2) (2008) 140-8.

[251] G. Weise, T.C. Basse-Luesebrink, C. Wessig, P.M. Jakob, G. Stoll, In vivo imaging of inflammation in the peripheral nervous system by (19)F MRI, Exp Neurol 229(2) (2011) 494-501.

[252] M.P. Krafft, Fluorocarbons and fluorinated amphiphiles in drug delivery and biomedical research, Adv Drug Deliv Rev 47(2-3) (2001) 209-28.

[253] C. Jacoby, S. Temme, F. Mayenfels, N. Benoit, M.P. Krafft, R. Schubert, J. Schrader, U. Flogel, Probing different perfluorocarbons for in vivo inflammation imaging by 19F MRI: image reconstruction, biological half-lives and sensitivity, NMR Biomed 27(3) (2014) 261-71.

[254] E.T. Ahrens, R. Flores, H. Xu, P.A. Morel, In vivo imaging platform for tracking immunotherapeutic cells, Nat Biotechnol 23(8) (2005) 983-7.

[255] F. Bonner, M.W. Merx, K. Klingel, P. Begovatz, U. Flogel, M. Sager, S. Temme, C. Jacoby, M. Salehi Ravesh, C. Grapentin, R. Schubert, J. Bunke, M. Roden, M. Kelm, J. Schrader, Monocyte imaging after myocardial infarction with 19F MRI at 3 T: a pilot study in explanted porcine hearts, Eur Heart J Cardiovasc Imaging 16(6) (2015) 612-20.

[256] E.T. Ahrens, B.M. Helfer, C.F. O'Hanlon, C. Schirda, Clinical cell therapy imaging using a perfluorocarbon tracer and fluorine-19 MRI, Magn Reson Med 72(6) (2014) 1696-701.

[257] R. Colotti, J.A.M. Bastiaansen, A. Wilson, U. Flogel, C. Gonzales, J. Schwitter, M. Stuber, R.B. van Heeswijk, Characterization of perfluorocarbon relaxation times and their influence on the optimization of fluorine-19 MRI at 3 tesla, Magn Reson Med 77(6) (2017) 2263-2271.

[258] A. Mastropietro, E. De Bernardi, G.L. Breschi, I. Zucca, M. Cametti, C.D. Soffientini, M. de Curtis, G. Terraneo, P. Metrangolo, R. Spreafico, G. Resnati, G. Baselli, Optimization of rapid acquisition with relaxation enhancement (RARE) pulse sequence parameters for (1)(9)F-MRI studies, J Magn Reson Imaging 40(1) (2014) 162-70.

[259] L.C. Rose, D.K. Kadayakkara, G. Wang, A. Bar-Shir, B.M. Helfer, C.F. O'Hanlon, D.L. Kraitchman, R.L. Rodriguez, J.W. Bulte, Fluorine-19 Labeling of Stromal Vascular Fraction Cells for Clinical Imaging Applications, Stem Cells Transl Med 4(12) (2015) 1472-81.

[260] L. Mignion, J. Magat, O. Schakman, E. Marbaix, B. Gallez, B.F. Jordan, Hexafluorobenzene in comparison with perfluoro-15-crown-5-ether for repeated monitoring of oxygenation using 19F MRI in a mouse model, Magn Reson Med 69(1) (2013) 248-54.

[261] F. Schmid, C. Holtke, D. Parker, C. Faber, Boosting (19) F MRI-SNR efficient detection of paramagnetic contrast agents using ultrafast sequences, Magn Reson Med 69(4) (2013) 1056-62.

[262] M. Srinivas, A. Heerschap, E.T. Ahrens, C.G. Figdor, I.J. de Vries, (19)F MRI for quantitative in vivo cell tracking, Trends Biotechnol 28(7) (2010) 363-70.

[263] F. Bonetto, M. Srinivas, A. Heerschap, R. Mailliard, E.T. Ahrens, C.G. Figdor, I.J. de Vries, A novel (19)F agent for detection and quantification of human dendritic cells using magnetic resonance imaging, Int J Cancer 129(2) (2011) 365-73.

[264] J.M. Janjic, M. Srinivas, D.K. Kadayakkara, E.T. Ahrens, Self-delivering nanoemulsions for dual fluorine-19 MRI and fluorescence detection, J Am Chem Soc 130(9) (2008) 2832-41.

[265] K.C. Partlow, J. Chen, J.A. Brant, A.M. Neubauer, T.E. Meyerrose, M.H. Creer, J.A. Nolta, S.D. Caruthers, G.M. Lanza, S.A. Wickline, 19F magnetic resonance imaging for stem/progenitor cell tracking with multiple unique perfluorocarbon nanobeacons, FASEB J 21(8) (2007) 1647-54.

[266] P. Assinck, G.J. Duncan, B.J. Hilton, J.R. Plemel, W. Tetzlaff, Cell transplantation therapy for spinal cord injury, Nat Neurosci 20(5) (2017) 637-647.

[267] F. Bei, H.H.C. Lee, X. Liu, G. Gunner, H. Jin, L. Ma, C. Wang, L. Hou, T.K. Hensch, E. Frank, J.R. Sanes, C. Chen, M. Fagiolini, Z. He, Restoration of Visual Function by Enhancing Conduction in Regenerated Axons, Cell 164(1-2) (2016) 219-232.

[268] R.J. Nudo, E.J. Plautz, S.B. Frost, Role of adaptive plasticity in recovery of function after damage to motor cortex, Muscle Nerve 24(8) (2001) 1000-19.

[269] M. Grabowski, B.B. Johansson, P. Brundin, Survival of fetal neocortical grafts implanted in brain infarcts of adult rats: the influence of postlesion time and age of donor tissue, Exp Neurol 127(1) (1994) 126-36.